PhD Thesis

Submitted in partial fulfillment of the requirements
of the Degree of Doctor of Philosophy

Numerical Modelling of Composite Materials Based on a Combined Manufacturing-Crash Simulation

André Berger

School of Engineering and Materials Science
Queen Mary University of London

Supervisor:
Fabian Duddeck

May 2014

I, André Berger, confirm that the research included within this thesis is my own work or that where it has been carried out in collaboration with, or supported by others, that this is duly acknowledged below and my contribution indicated. Previously published material is also acknowledged below.

I attest that I have exercised reasonable care to ensure that the work is original, and does not to the best of my knowledge break any UK law, infringe any third party's copyright or other Intellectual Property Right, or contain any confidential material.

I accept that the College has the right to use plagiarism detection software to check the electronic version of the thesis.

I confirm that this thesis has not been previously submitted for the award of a degree by this or any other university.

5th May 2014

Abstract

Fibre reinforced plastics are widely used for energy dissipating parts. Due to their superior strength to density ratio they provide a high performance and are ideal for lightweight design for crashworthiness. For this, it is essential that the mechanical behaviour of fibre reinforced composites can be predicted correctly by simulation. However, due to the complex inner structure, this is still a challenging task, in particular in case of highly nonlinear crash loading.
In this work, a new purely virtual method is developed, which derives the complex fibre structure of a filament wound tube by a chain of numerical simulations. Thereby a finite element simulation of the fibre placement, taking into account the occurring physical effects, constitutes the fundamental base. Based on the results of the manufacturing simulation, a 3D fibre architecture is generated and compared to the real existing structure. The fibre structure, combined with an automatic matrix implementation algorithm, subsequently provides a finite element model of the composite on meso-scale. Using micro-scale analysis, effective material properties for the roving structure, based on filament-matrix interaction, are derived. Incorporation of the effective properties in a USER MATERIAL model completes the finite element model generation. The meso-scale model is subsequently used to analyse the filament wound tube in terms of quasi-static and crash loading. Finally, the obtained results are compared to experimental observations.

Contents

Chapter 1

Introduction

1.1 Problem Statement

Following the activities of the automotive industry in recent years shows one major topic which everybody everywhere frequently encounters: electro mobility. The reason for the huge amount of developments realised by the car manufacturers related to this topic is also well known and obvious every day: the reduction of the CO_2 emission caused by cars. Using electric engines will strongly improve this issue, but also provide new challenges for the automotive industry. For instance, the power supply of batteries is still not effective and sufficient enough today for standard car construction from the past to get cruising ranges comparable to vehicles with conventional combustion engines. As a consequence the car manufacturers started to develop more and more constructions based on light weight materials a few years ago. As examples Volkswagen XL1 [46] or the BMW I3 [44] concept are named here. However, these new type of cars have to satisfy also a certain number of requirements based on safety regulations. In particular, in terms of a crash scenario the structure of a car must be able to dissipate the kinetic energy to protect the occupants. The conflict between safety and light weight strongly restricts the number of appropriate materials. One of them are fibre reinforced plastics which can be classified in the domain of composite materials. Due to their good strength to density ratio, they provide high performance by light weight. In order to effectively use this advantage it is essential that the mechanical behaviour of such a material is predictable by simulation. However, due to the complex structure of composites, which is also influenced by the manufacturing process, this is still a challenge and often provides difficulties in the scope of Computer Aided Engineering (CAE). As a consequence today many industrial components made by fibre reinforced plastic are over designed. In particular for energy dissipating parts, the prediction of the crushing behaviour by finite element simulation is quite difficult. In the past, several approaches have been developed to be able to simulate composite structures in impact loading cases [26, 34, 94]. However, none of these approaches has directly considered the complete internal geometrical fibre structure, the surrounding matrix and the related mechanical properties of the whole composite part to capture e.g. combined fibre loading

or inter laminar failure. As a consequence, the validity of the results of such finite element based simulations is limited.

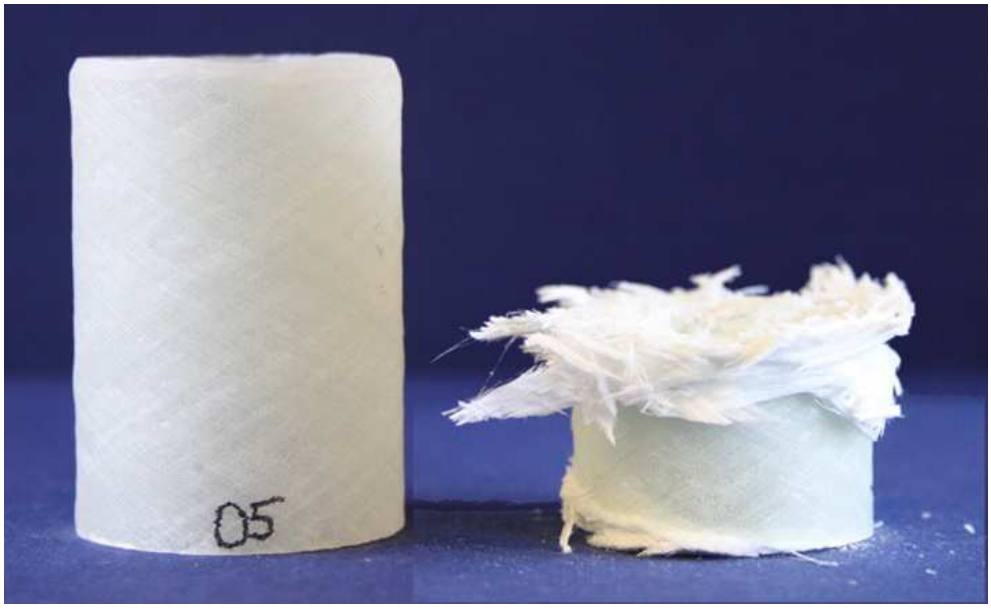

Figure 1.1: Filament wound tube before and after impact.

To overcome these limitations, a combination of virtual manufacturing simulation and subsequent crash analysis based on the finite element method is proposed within this work. Thereby, the manufacturing process provides the fundamental base to gather detailed information about the geometrical constitution of the composite structure. In addition the detailed geometrical information is supplied by material properties based on filament-matrix consideration on micro-scale. In order to assess quality and limitations, the proposed method is applied and evaluated for a filament wound tube shown in Fig. 1.1 in terms of impact loading.

1.2 State-of-the-Art

Generally, composite materials can be derived by combining two or more materials to use the benefit of the characteristics of each material and especially their interaction. Thus, the properties of a composite are normally better than those of its individual constituents. Considering fibre reinforced plastics, the following distribution of the individual tasks can be given: the fibre provides the strength and stiffness, whereas the matrix gives rigidity and environmental resistance. Thereby, the main advantage over traditional engineering materials is given by the superior ratio of strength to density. In addition a high fatigue strength and a good impact behaviour characterise these materials. However, the combination of individual materials also provides difficulties due to inhomogeneous stress states and various strength. In the following sections, fibre

reinforced plastics are briefly reviewed with respect to their properties relevant for this work, e.g. classification, manufacturing and failure, including advices to existing simulation approaches. In addition a short introduction to the crushing phenomena of composite tubes and related approaches in the scope of finite element simulation is given at the end.

Classification of Fibre Reinforced Plastics

Fibre reinforced composites can exist in many different forms. For instance, the fibre can be long continuous, woven fabric or short chopped. The latter can additionally be related to a random orientation of the individual fibres. In Fig. 1.2 the aforementioned is summarised by classification of composite materials with respect to the type of reinforcements [3]. For sake of completeness the particle reinforced composites are also represented.

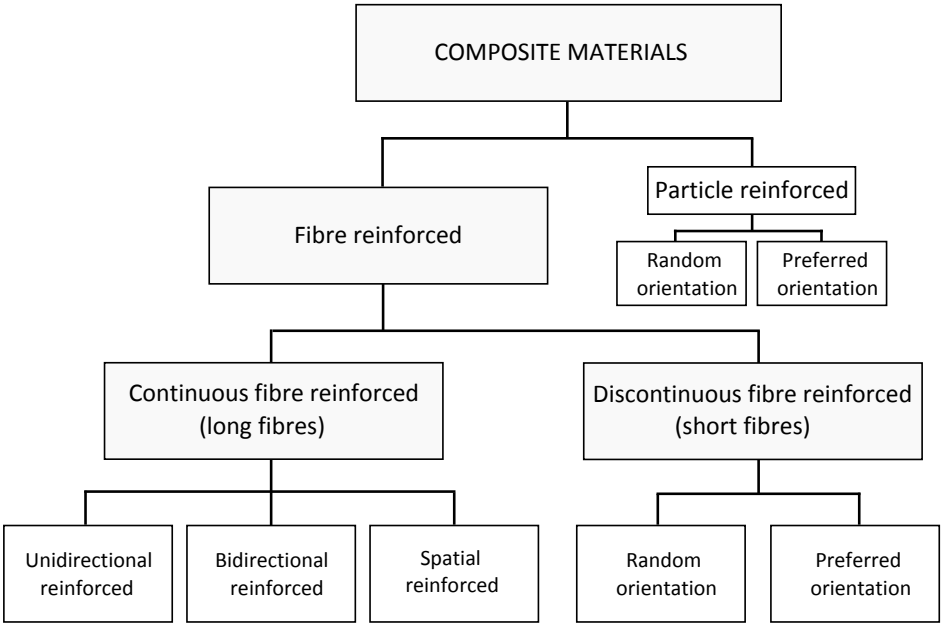

Figure 1.2: Classification of composite materials with respect to reinforcement [3].

Moreover, a composite fibre can be made by different materials such as glass, carbon or aramid and can be incorporated in single or multiple plies. Also the fibre surrounding matrix and its way of integration can vary strongly. For instance the matrix can consist of a thermoset epoxy resin or of a thermoplastic polypropylene and can be integrated directly with the fibre placements process or can be inserted by an additional subsequent process. Consequently, the individual fibre reinforced plastics differ in their way of manufacturing. In the following, only continuous fibre reinforced plastics are considered because this thesis is focused on wound composite tubes.

Manufacturing of Continuous Fibre Reinforced Plastics

In terms of continuous fibre reinforced plastics a number of industrial manufacturing processes exist. For instance the fibre placement can be realised by filament winding, braiding or by tailored fibre placement. In Fig. 1.3, two different examples for the fibre placement are illustrated: a) the braiding of a tube and b) the tailored fibre placement of given pattern.

Figure 1.3: Manufacturing of composite structures by a) braiding and b) tailored fibre placement.

In addition, the draping shall be mentioned here, where the fibres are placed by a forming process. This procedure can be characterised as a two-step process since the forming procedure is based on preforms (e.g. various layers of unidirectional fibre clutches) which again can be manufactured by a tailored fibre placement procedure. As example for the direct matrix integration, the resin moulding transfer (RTM) process is named here. Alternatives are the use of pre-impregnated fibres or a resin bath before the fibre placement procedure. Finally, most of the manufacturing processes of fibre reinforced composites are completed by a curing procedure. In order to get more detailed information about the individual composite materials as well as the corresponding manufacturing processes a comprehensive summary can be found in [61] for example.

The mechanical properties of fibre reinforced plastics are related to a certain number of parameters of the manufacturing process. For example stiffness and strength are strongly dependent on the fibre volume content and fibre architecture which are in turn influenced by the manufacturing process used. In the filament winding process considered in this work, the strength, the stiffness and also the failure of the composite are significantly affected by the stacking sequence, the winding tension and the winding tension gradient [11]. Additionally, there is a strong relationship between the fibre failure strain and the fibre volume content which is shown by Cohen et al. [12] for filament wound pressure vessels. Moreover Mertiny and Ellyin [64] show the close relation between the winding tension and the fibre volume content for filament wound tubes based

on experimental investigations and point out the dependency of the structural failure to the winding tension.
The publications mentioned above are only a small selection of the existing literature which shall reveal here the importance of the consideration of manufacturing issues for the prediction of mechanical properties for composite structures. The existing approaches for the simulation of the filament winding process are quite different. Most of them are concerned with the prediction of the fibre path or fibre placement. De Carvalho et al. [16] for example use a finite element analysis for the determination of the ideal fibre orientation in combination with a non-geodesic fibre path generation to obtain feasible fibre paths. Park et al. [71] use the semi-geodesic fibre path equation for the determination of the fibre angle distribution, combined with a finite element analysis for the consideration of the change of the fibre angles through the thickness. Kim et al. [49] use semi-geodesic path algorithm to calculate possible winding patterns by taking into account the windability and slippage between fibre and mandrel. Koussios et al. [51,52] show a method based on kinematic equations and generic geometry for the representation of the filament winding process under the assumption of geodesic tow path. Furthermore they provide a fast and simplified approach for collision control based on a complete set of analytical kinematic equations for a lathe winder [53].
The existing approaches for the fibre path prediction can be roughly classified into two groups. Those using geodesic algorithm and the others which are based on non or semi-geodesic methods. The latter require more elaborated calculations and are more time consuming but permit more flexibility and appropriate fibre path generation. For example Zu et al. [102] conclude in their work that non-geodesic trajectories can increase the performance of a winding structure. Furthermore they show the influence and benefit of using non-geodesic roving trajectories in comparison to the geodesic method for a pressure vessel dome in another publication [101]. As a consequence the existing commercial software [45, 55] is nowadays able to use the benefit of non-geodesic trajectories.
A different approach taking into account another manufacturing issue for filament wound structures is proposed by Zhao et al. [96], which is mainly focused on the prediction of the radial change of the fibre volume fraction of a wound cylinder based on a fibre consolidation model. As can be seen by this representative selection, there is a huge number of publications regarding the simulation of the filament winding process which are partly summarised by Mackerle in [59]. However, the path fibre methods mentioned above do not consider the influence of fibre waviness or fibre undulation which occur during filament winding in terms of helical or polar pattern. Already Hsiao and Daniel [43] have shown that Young's modulus and strength decrease strongly as the fibre waviness increases for unidirectional composite structures under compressive loading. Gramoll and Ramaprasad [33] demonstrate the influence of undulated fibre bands to the ultimate failure strength. Furthermore they point out that fibre undulations follow generally a sinusoidal pattern in filament wound structures and identify the wave cycle length and amplitude as critical parameters. Pai and Jensen [70] improve the accuracy for the prediction of buckling loading by using a stiffness model based on a modified classical laminate theory approach for the crossover

regions. And finally Zindel and Bakis [97] show the influence of the winding pattern and the related fibre undulation regions for the axial modulus of filament wound tubes. As presented above there are a number of parameters related to the manufacturing process which influence the mechanical behaviour of wound composite structures and consequently have to be taken into account. In particular fibre placement, fibre undulation and stacking as well as fibre tension are finally summarised here.

Failure of Continuous Fibre Reinforced Plastics

Separating the main mechanical functions of the fibres and the matrix in a composite structure provides the following functionalities. The fibres carry the main load while the matrix binds the fibres and transfers the load between the fibres. In addition, the matrix isolates the fibres, so that individual fibres can act separately which slows or even stops crack propagation [61]. Furthermore, the failure is strongly affected by the type of the used material, the fibre distribution and the applied load. Since a composite material can consist of multiple layers, failure may occur within a single ply (intralaminar fracture) or between two plies (interlaminar fracture). The latter is also known as delamination of the bonded plies. Furthermore, a fracture oriented transversely to a ply is called translaminar fracture, e.g. [3].

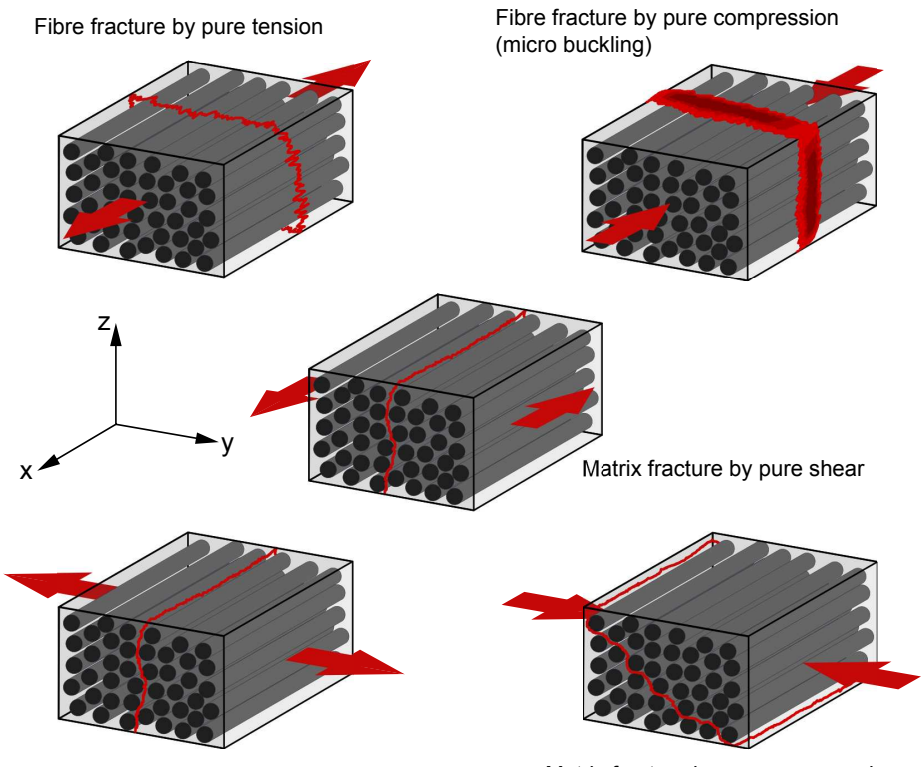

Figure 1.4: Fracture modes in single unidirectional composite layer based on [3].

Within a single ply of a composite structure, various local failure modes can appear. These local mechanisms lead to a redistribution of the stresses in the laminate and finally provide a gradual decrease of the complete structural stiffness. Considering an unidirectional layer, the fracture is caused by the accumulation of following elementary mechanisms: fibre fracture, transverse or longitudinal matrix fracture, fibre-matrix interface fracture.
In Fig. 1.4 the failure modes for an unidirectional composite layer are illustrated in which the applied load is represented by bold arrows and the red sketched lines reveal the fracture location. In the upper row of Fig. 1.4, the loading in fibre direction is shown. Consequently, these modes result in a fibre tensile or compressive fracture (micro buckling), respectively. The former, propagates rapidly and is related to tensile strength of the fibre. In the lower row of Fig. 1.4, the load is applied perpendicular to the fibre direction. Thereby, the fracture in terms of tensile loading can be related to the matrix tensile strength, the fibre tensile strength across the diameter or to the failure of the fibre-matrix interface. The fracture of the matrix under compression is dominated by the shear strength of the matrix material. In accordance, the shear loading resistance longitudinal to the fibres is also related to the shear strength of the matrix material. Often, the failure modes within a single ply are summarised by: the inter fibre fracture which is related to a matrix failure and the intra fibre fracture which reflects the failure of the fibre.
Using high performance electron micrographs and in recent years also computer tomographs, these effects can be demonstrated in more detail and visualised on small scales e.g. [37, 57, 81]. An example is shown in Fig. 1.5, where the inter fibre fracture of the matrix and the interface fracture surface in terms of transverse compressive loading are illustrated on micro-scale.

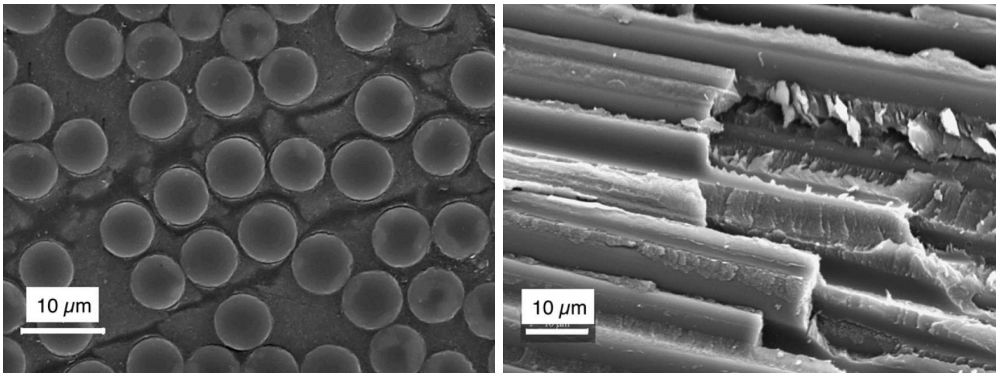

Figure 1.5: Example for a) inter fibre fracture and b) fracture surface under transverse compression [4].

In addition, Fig. 1.6 and 1.7 represent the occurring fracture of two laminates consisting of eight single plies under a given load on meso-scale. Consideration of these two images reveals the statements given above. In Fig. 1.6 inter fibre cracks due to transverse tensile loading can be observed in the lateral plies. Moreover, a stop of the crack can be observed at the layer border due to the change of the fibre orientation in the second ply. In contrast a crack propagation

can be seen in the middle layer which causes the start of the delamination of two plies.

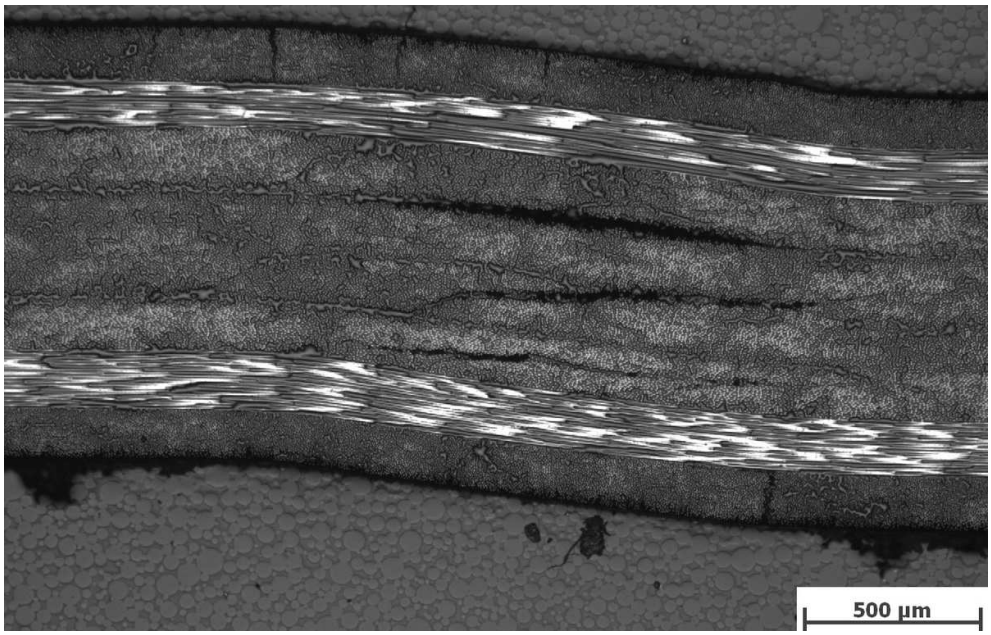

Figure 1.6: Failure and crack propagation in fibre reinforced laminate (A).[1]

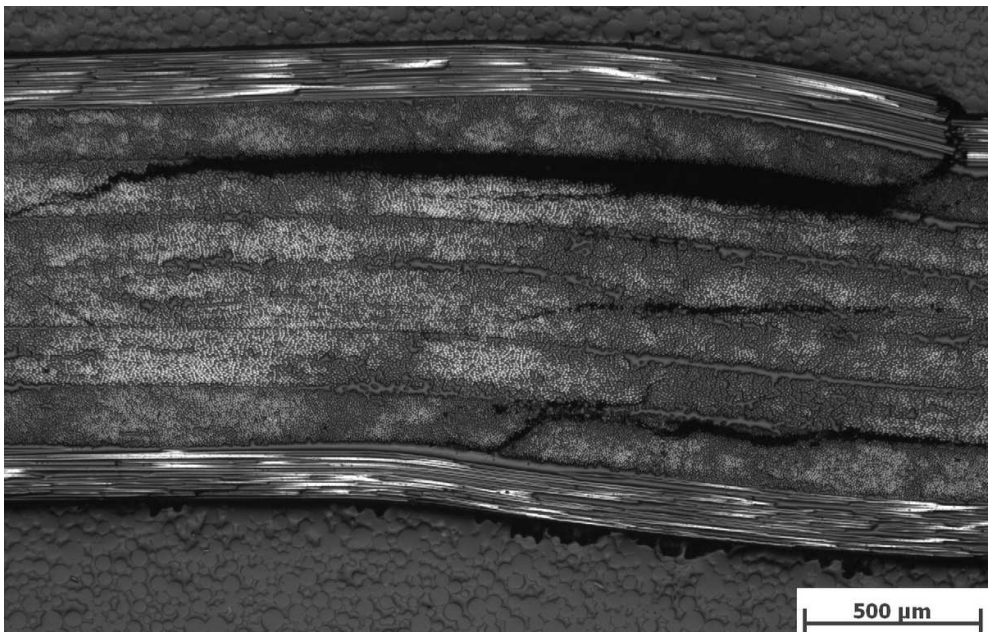

Figure 1.7: Failure and crack propagation in fibre reinforced laminate (B).[1]

[1]Micrograph records provided within COMET K2 project, a joint research project between Virtual Vehicle Research Center, ESI GmbH, Audi AG, Institut für Werkstoffkunde und Schweißtechnik at Graz University of Technology, Fachgebiet Konstruktiver Leichtbau und Bauweisen at Technische Universität Darmstadt.

In Fig. 1.7 this effect can be observed even better in the lower ply where the relation between inter fibre failure and delamination becomes directly apparent. Finally, a chain of different failures can be seen in the upper three plies of the laminate. Here, the redistribution of the stresses finally causes a fibre fracture (intra fibre failure) in the upper row, which is also initiated by the effects mentioned above, inter fibre failure and delamination. This directly reveals the gradual process of decrease in strength and stiffness within fibre reinforced plastics.

The mentioned publications as well as the illustrations reveal that there are different kinds of failure which have to be taken into account to calculate the strength of a composite material. In particular a mixture of the individual effects in combination with the appearing damage of matrix material provides difficulties for the virtual failure prediction of such materials. Consequently, a lot of studies from the past and the present are addressed to this scope of research. Thereby, the used approaches are quite different. Some are based on stress criteria other on strain or energy theories. Some are taking into account single plies other the complete laminate. And of course there are methods which use the benefits of the individual approaches in a mixed form. There is a large body of existing literature. A comprehensive overview about some of the main existing approaches are included in the *World Wide Failure Exercise* (WWFE) [41]. Apart from the theoretical foundation this exercise also contains the evaluation of each method with respect to the failure prediction of fibre reinforced plastics for pre-defined load cases. Thereby one of the main objectives was to gain input from different classes of approaches predicting failure in fibre reinforced plastics. A group of them are the *Interactive Failure Theories* which are based on the theories for the description of yielding of metals. Most of them have been adapted with respect to anisotropic behaviour and distinction between tensile and compressive loading. The benefits of those approaches are the reduction to simple equations and the inherent possibility of the generation of efficient algorithms. A second class represents the *Physically Based Failure Criteria* where separate equations for the specific failure modes are defined, for instance one for the fibre failure and one for the matrix failure. The *Damage Mechanics* based approaches constitutes the third class. Here analytical approaches are developed which describe the initiation and evolution of damage for the representation of the complete failure process. The last considered class contains the approaches used in local, national or international guidelines. All of the theories mentioned above are covered by the WWFE and a few of them are briefly summarised below.
For example Puck and Schürmann [74, 75] use a mechanistic theory which distinguishes between various failure modes. Their theory consists of two independent failure criteria, one for the fibre fracture and one for the inter fibre fracture. In addition a gradually degradation of the stiffness of the ply after crack initiation is applied. This approach is widely used within the domain of composite failure prediction. In the work of Deuschle [17] Puck's criterion is applied to three-dimensional stress space and incorporated to the finite element analysis. Cuntze [13, 14] considers two fibre failures and three inter fibre

failure mechanisms and his theory is mainly based on Puck's. However, unlike Puck, his work contains an assumption based on probabilistic effects for the interaction between the failure mechanisms. Also Rotem [78, 79] is using two separate failure criteria: one for matrix and one for the fibre. In contrary Tsai and Liu are using a quadratic failure criterion with linear terms based on single valued function which is well known in the community as Tsai-Wu failure criterion [86]. By applying degradation they also suggest a progressive quadratic failure criterion [87, 88].
Another possibility for failure prediction constitutes the use of strain based criteria. This is done for example by Bogetti et al. [6, 7], who employed the Maximum Strain Theory in full 3D form taking into account nonlinear effects. Also Hart-Smith is applying the maximum strain theory. In addition he is using a truncated form of this approach [38]. It has to be mentioned here, that Hart-Smith is also the founder of the Ten Percent Rule [39] which has been used widely in the aerospace industry for many years. Finally, Wolfe and Butalia [9, 90] use a strain energy based criterion for the prediction of failure. A further widely used failure criterion is the Maximum Stress Theory. For instance Zinoviev et al. [98, 99] are applying this method in combination with consideration of geometrical nonlinearity caused by changes of the ply angle with increasing deformation. However, also approaches based on damage mechanics are presented within the scope of the WWFE. Within this context McCartney [62,63] can be mentioned who employed a method based on damage mechanics using a fracture energy approach for the failure prediction.
However, there are also additional theories which have not been represented within the scope of the WWFE. For example theories which are purely based on probabilistic effects. These approaches use a statistical distribution for the prediction of failure and are mainly appropriate for brittle material behaviour. As examples here [73, 82, 95] are named. A summary of the existing stochastic modelling approaches in combination with a quantification of uncertainty in fibre reinforced plastics can be found in [83].
Models based on Continuum Damage Mechanics constitute a further group in the large scope of theories for fibre reinforced plastics failure. Talerja and Li are two important representatives using this theory. Finally, the group using micro mechanics shall close this review. These methods are often combined with numerical methods such as Finite Element Analysis (FEA) or Boundary Element Method (BEM). Examples are provided by LLorca and González [56] who investigated the behaviour of fibre reinforced polymers under transverse compression by FEA or Paris et al. [72] who use BEM for the matrix failure prediction. Another example using micro mechanics is the Strain Invariant Failure Theory (SIT) developed by Gosse and Christensen [32]. In contrary to the other methods, this is an analytical approach. However, it becomes apparent that the main focus of these methodologies is set to the prediction of the matrix failure, in particular in terms of transverse loading.

Multi-Scale Analysis and Homogenisation

The initiation of failure as well as the global stiffness of fibre reinforced plastics are related to effects occurring in the micro-structure. In contrast the composite component and its boundary conditions are represented on macro-level. In order to take into account micro-structure effects, the multi-scale modelling approach offers the possibility to consider the material behaviour on individual scales. Different techniques can be used to link the scales. Since there is a large body of existing literature, only a few methods are briefly considered here. The simplest case of a multi-scale approach is the *submodelling technique*, where a small subdomain of a smaller scale is taken to analyse the material behaviour on larger level. Submodelling techniques are often used to analyse the mechanical behaviour of materials with complex multilevel structures, for example [66, 67] are listed here.

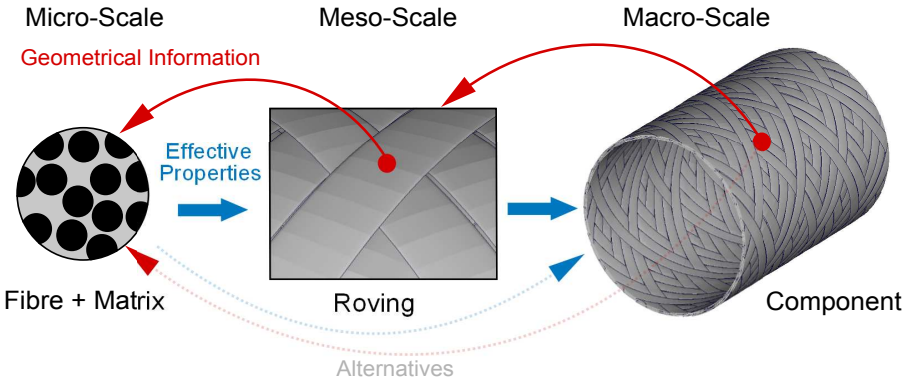

Figure 1.8: Example of a multi-scale consideration for a filament wound tube.

In Fig. 1.8 this approach is illustrated for a filament wound tube structure, using three different scales: micro-scale, meso-scale and macro-scale. The geometrical information on smaller scale is used to provide effective properties to the larger one. Thereby, the boundary conditions on the smaller scale are defined by the larger one. The intermediate meso-scale is not mandatory and consequently the subdomain technique can also be applied between micro- and macro-scale. However, an additional scale enriches the amount of information. The subdomain technique is an one-directional approach which implies, for instance, that the macro-scale provides the boundary conditions for the micro-scale model, but not vice-versa, e.g. the micro-scale model will not influence the modelling on macro-scale and will only provide material properties. Consequently an interaction between the different levels does not exist in a one-sided approach. It has to be mentioned that using the submodelling technique, the problem of impedance occur at the interface of the individual domains [93] in which high frequencies of propagating signals are reflected. Therefore the usage of submodelling is limited.
Another group of multi-scale analyses is the *domain decomposition technique* where a macro-scopic domain is decomposed in connected subdomains. An

example of this method can be found in [100] where a global problem is decomposed in a set of smaller decoupled problems. The *superposition methods* constitute a further class of multi-scale analyses. For example Takano and Okuno [85] combine mesh superposition methods with the asymptotic homogenisation method. Another example of superposition techniques is the *composite grid method* suggested by Fish et al. [30], which uses the decomposition of a hybrid system into a global-local problem. The *multi-scale finite element approach* provides also the possibility to consider and link the mechanical behaviour on different scales. For example Feyel and Chaboche [28] use this approach to introduce the micro-structure of materials into the material model on macro-scale at Gauss point level.
Multi-scale analyses are very often combined with homogenisation methods in order to provide effective properties of a heterogeneous structure for a larger scale. With respect to Fig. 1.8 this implies that the filament-matrix combination on micro-scale provides effective material properties for the meso-scale. From another point of view, a homogenisation procedure needs at least the consideration of two scales and therefore a multi-scale analysis. According to Fish and Shek [31], a homogenisation is related to three main assumptions: the macro-structure can be built of representative volume elements (RVE), the solution is locally periodic in a statistical sense and the occurring macro-scopic fields in the RVE are constant. Furthermore, according to Hori and Nemat-Nasser [42] two basic strategies for homogenisation exist, namely *mean field theory* and *asymptotic homogenisation theory*. In the mean field theory, also known as average field theory, macro-scopic fields are defined as volume averages of the corresponding micro-fields. Contrary, the asymptotic homogenisation theory is based on asymptotic expansion of displacement and strain fields about macro-scale values. However, both theories define a relation between two scales e.g. macro- and micro-field, only in a different manner. Further information about the individual theories can be found in [40, 80]. In addition a hybrid formulation taking into account both approaches is shown by Hori and Nemat-Nasser in [42]. An overview about homogenisation methods and inherent techniques for the estimation of effective properties and its limitations are given in [65].

Crushing of Fibre Reinforced Composite Tubes

The interaction of manufacturing issues, geometrical properties as well as local and global failure can be found in high dynamic loading of composite tube structures. The high potential of such tubes with respect to the energy dissipation has been demonstrated for example by Marsolek [60]. In this work he compares amongst others different fibre reinforced tube structures with traditional metal tubes in terms of high dynamic loading. Thereby, different types of laminates and load applications have been investigated and the corresponding energy dissipation has been discussed. In order to get an optimal energy dissipation by fibre reinforced structures, a progressive deformation with a constant force level should be assured. This procedure is called crushing and the related

force-displacement behaviour is illustrated in Fig. 1.9, where F_C denotes the crushing force level, F_{max} the initial maximum force and s the displacement. In order to get a maximum of energy dissipation, the difference between these quantities should be minimised. The perfect energy absorber is represented in the same figure by the dotted line rectangle. The provided energy dissipation of a component can be determined by integration of the occurring forces over the displacements. The maximum force level is limited by the requirement of low acceleration of the occupants to reduce injury risks, see for example [27].

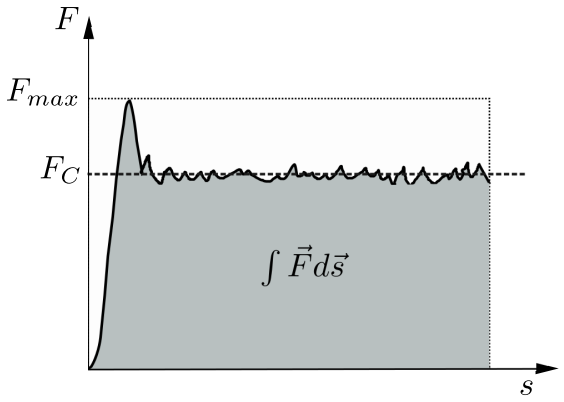

Figure 1.9: Progressive crushing behaviour of composite structures.

The prediction of the crushing behaviour of composite tube structures by finite element simulation is quite difficult. Considering the occurring failure mechanism in a crushing load case makes the complexity apparent. Farley and Jones investigated intensively the response of composite tubes structures under axial impact loading and provided a characterisation of the occurring crushing modes [25]. The main modes are:

(1) The **transverse shearing crushing mode** which is controlled by the inter laminar crack growth and the laminate bundle fracture.

(2) The **lamina bending crushing mode** which is controlled by inter and intra laminar crack growth (also parallel to the fibre) and friction.

(3) The **local buckling crushing mode** which is controlled by plastic yielding of the fibre and/or the matrix.

Since the **brittle fracturing crushing mode** is a combination of the transverse shearing and lamina bending mode, it is not denoted as single crushing mode by Farley and Jones. The mechanism controlling the different crushing modes is related to the mechanical properties of the constituent materials which implies also a possible strain rate dependency. In addition the crushing modes are a function of the specimen structure.
In order to capture these effects by finite element simulation many attempts have been conducted in recent years. Thereby, many approaches are related to

macro-scale representations and specialised techniques to capture phenomenological effects. For instance, hybrid finite element meshes, consisting of shell and volume elements, or highly sophisticated material models, containing special treatments for the degradation of composite materials, are used. Also special modelling techniques for the delamination, the incorporation of meshless methods or a mix of the approaches can be found in publications within the scope of finite element crushing simulation. Thereby, the various methods are combined with failure prediction or multi-scale approaches mentioned above. Since the possibility of combining these techniques for the prediction of fracture in composites is extensive only a few publications dealing directly with composite tube crushing are listed here [1,26,34,69,94]. However, none of these approaches take into account directly the complete internal geometrical structure and the related mechanical properties of the composite tubes. Since the quality of parallelisation in finite element codes and the hardware performance are continuously increasing, the possibility of direct modelling on a small or medium scale e.g. meso-scale has to be considered.

1.3 Scope of Work

The main objective of this work is the virtual chain of a manufacturing simulation to a subsequent crash analysis for the prediction of the energy absorption behaviour of a composite structure. Thereby, the filament wound tube illustrated in Fig. 1.1 is representing the demonstration component which is used within the entire work. This considered structure is made by a wet winding process and consists of two layers of glass fibre covered by an epoxy resin. Thereby the fibre placement orientation angle of each layer amounts to $\pm 60^\circ$ with respect to the global longitudinal tube axis.
In the work a new, purely virtual method is shown, which derives the fibre architecture of the filament wound tube by numerical simulation. Thereby the finite element simulation of the fibre placement, taking into account the occurring physical effects, constitutes the fundamental base. Also fibre tension, inter fibre contact, the related fibre undulations as well as friction effects are fully represented by the approach. Based on the results of the simulation of the winding process, a 3D fibre architecture is generated and compared to the real existing structure. In order to automatically incorporate the fibre surrounding matrix in a subsequent step, an algorithm using the calculated fibre structure has been developed. Applying this, finally provides the finite element geometry of the complete composite structure on meso-scale including the fibre-matrix connection. By the use of a multi-scale analysis, effective material properties for the filament-matrix interaction are derived in the second major step. Thereby, a numerical homogenisation procedure is used to determine the effective stiffness tensor. In addition an embedded unit cell approach is applied to evaluate failure parameters for the filament-matrix interaction. This will be supported by the calibrated finite element material models of the individual material constituents, based on experimental investigations. Using the derived material properties in a developed orthotropic USER MATERIAL routine in

combination with the generated meso-scale geometry completes the finite element model. Finally, structure analyses, including the simulation of the crash event, of the filament wound tube are conducted and the obtained results are compared to the experimental observations.
The content of this work is structured in the following way. The subsequent Chapter 2 summarises the relevant theoretical aspect for the USER MATERIAL model and the applied homogenisation procedure. In Chapter 3 the experimental base of this work is presented and the results are discussed briefly. In the main part of this work, Chapter 4, the finite element meso-model generation is described. Finally, in Chapter 5 the generated model is used for finite element simulations of the wound tube structure in terms of quasi-static and crash loading. Thereby, a comparison to the experiments and an assessment of the quality are given, which are summarised in the conclusions. In the following Fig.1.10 the subsequent chapters are illustrated with respect to the flow of information to reveal the dependencies among each other and to show the base of validation.

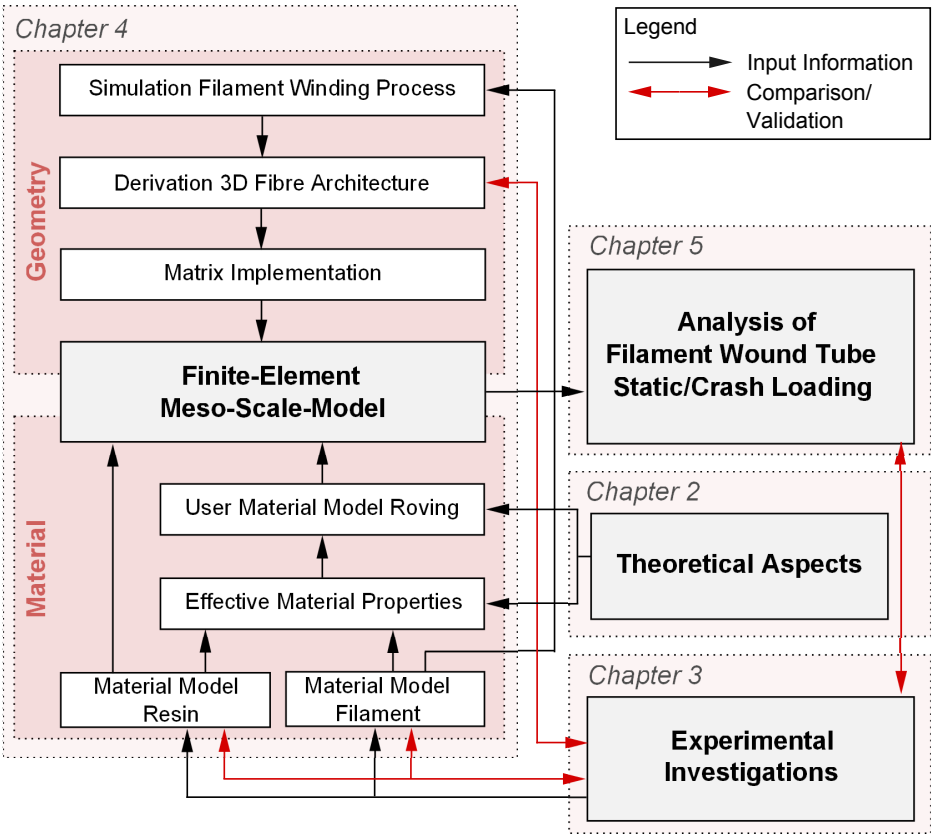

Figure 1.10: Scheme of information flow and chapter dependencies as well as base of validation.

Chapter 2

Theoretical Aspects for Wound Composite Modelling

Within this chapter a constitutive material model for large elastic deformation is described which is used in this work for the representation of an unidirectional composite layer in finite element simulations. Since fibre undulations and orientations are captured by a very detailed geometrical finite element mesh, the material modelling approach can be based on unidirectional composite layer considerations.
Firstly, some main aspects from the continuum mechanics of large deformation are briefly summarised, to introduce the necessary quantities for the constitutive law. As a consequence, not all dependencies and derivatives are given within this chapter. For more detailed explanations and relations of the used equations and quantities it is referred to the existing literature. As examples here [2, 8, 91] are provided. In the second step the numerical implementation method for an explicit finite element USER MATERIAL routine is shown. In this state, the model is extended to orthotropic material behaviour including a failure treatment and the initialisation of the material frame axis based on prescribed orientations. Finally, in the last section of this chapter one method for numerical homogenisation is introduced to provide effective composites properties directly applicable to the constitutive model.

2.1 General Aspects

2.1.1 Notation

In order to simplify the reading and understanding of the following sections and subsequent chapters, the used notation is briefly summarised below. In general the symbolic notation is used to express the quantities and mathematical relations within this work. However, sometimes it is useful to express a quantity or relation by coordinates and corresponding base. As a consequence this notation, known as component or index notation, can also be found in this work.

Referring to the symbolic notation, scalars are represented by lower italic case. Also vectors are expressed in lower italic case, however with an additional arrow denotation. Higher order tensors are represented in boldface letters, denoted by a superscript if the order is higher than two.
In terms of index notation all considerations are with respect to a Cartesian basis in $\mathbb{R}^3$, which represents an orthogonal normalised vector system satisfying the condition

$$\vec{e_i} \cdot \vec{e_j} = \delta_{ij} \qquad (i,j = 1,2,3) \quad . \tag{2.1}$$

Here $\vec{e}_1$, $\vec{e}_2$, $\vec{e}_3$ express the three base unit vectors and δ_{ij} represents the Kronecker delta which is defined by

$$\delta_{ij} = \begin{cases} 1 & \text{if } i = j \\ 0 & \text{if } i \neq j \end{cases} \quad . \tag{2.2}$$

In addition the summation convention by Einstein is used for the index tensor notation. This implies that e.g. a first order tensor (vector) can be expressed by

$$\vec{a} = a_i \vec{e_i} \quad \equiv \quad \vec{a} = \sum_{i=1}^{3} a_i \vec{e}_i \tag{2.3}$$

and its derivative with respect to the spatial coordinates x_j is represented by

$$\frac{\partial a_i}{\partial x_j} = a_{i,j} \quad . \tag{2.4}$$

Since most of the existing literature for continuum mechanics include a section dealing in detail with tensor algebra and amongst others the handling of this convention, no deeper introduction is done here. A very comprehensive summary concerning tensor algebra and analysis can be found in the introduction of [3]. Taking into account the conventions mentioned above, the notation for this work can be summarised as follows in Table 2.1 where $i,j,k,l = 1,2,3$. If not mentioned otherwise this is valid for the complete work without restrictions.

Order	Description	Symbol	Index Notation
0	Scalar	a, b	
1	Vector	$\vec{a}$	$= a_i \vec{e_i}$
		$\vec{b}$	$= b_i \vec{e_i}$
2	2nd Order Tensor	$\mathbf{A}$	$= A_{ij}\ \vec{e_i} \otimes \vec{e_j}$
		$\mathbf{b}$	$= b_{ij}\ \vec{e_i} \otimes \vec{e_j}$
4	4th Order Tensor	$\mathbf{A}^{(4)}$	$= A_{ijkl}\ \vec{e_i} \otimes \vec{e_j} \otimes \vec{e_k} \otimes \vec{e_l}$
		$\mathbf{b}^{(4)}$	$= b_{ijkl}\ \vec{e_i} \otimes \vec{e_j} \otimes \vec{e_k} \otimes \vec{e_l}$

Table 2.1: Tensor notation with respect to tensor order.

2.1.2 Motion and Configuration

Consideration of a deformable body Ω, consisting of continuously connected particles, in two different states is used to introduce the topic of motion and configuration as shown in Fig. 2.1. The initial location ($t = 0$) of the body is denoted by Ω_0 and named initial or reference configuration. Ω_t expresses the current position of the body in three-dimensional space for the time t and is consequently named as current configuration. The motion between the two configurations is defined by ϕ. In addition, each particle of the body in the initial configuration can be represented by the coordinates X_i with respect to the Cartesian basis system described by Eq. (2.1). The current configuration of the same particle with respect to the same basis system $\vec{e}_i$ can be expressed by the coordinates x_i. This implies that e.g. the point P of the body Ω is represented in the initial configuration by $\mathrm{P}(X_1, X_2, X_3)$ and by $\mathrm{p}(x_1, x_2, x_3)$ in the current configuration. From mathematical point of view, the motion can be described by the following equation

$$\vec{x} = \vec{x}(\vec{X}, t) \tag{2.5}$$

which represents a mapping between the initial and current configuration for each particle. This means that each particle is defined by a spatial point for each time. In terms of a constant value for t it represents a mapping between an undeformed and deformed body, $\vec{x} = \vec{x}(\vec{X})$. In terms considering a fixed particle, it expresses the motion as a function of time, $\vec{x} = \vec{x}(t)$. The latter is shown in Fig. 2.1 by the representation of the trajectories (dotted lines) of P and Q.

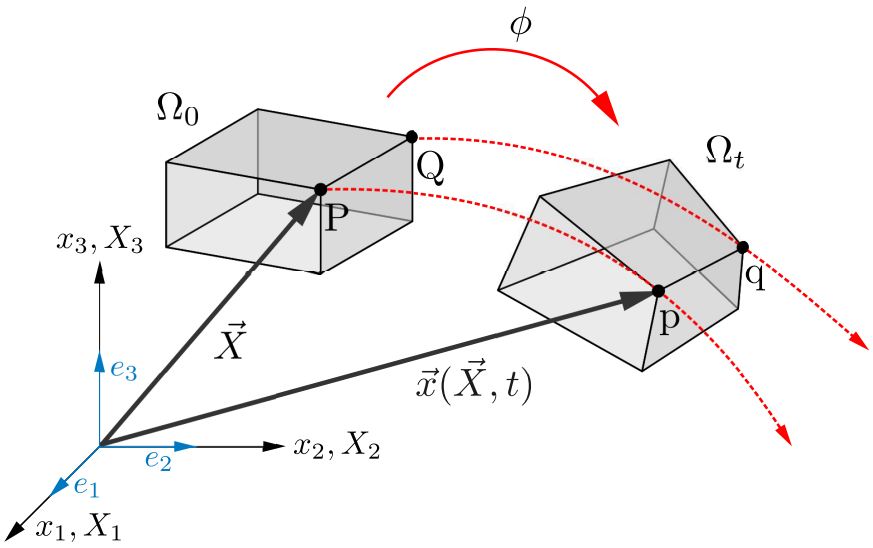

Figure 2.1: General motion of a deformable body Ω.

In terms of expressing quantities as a function of the coordinates X_i of the initial configuration, in continuum mechanics the definition *Lagrangian* or *ma-*

terial description is used. The reference to the coordinates x_i of the current configuration is denoted *Eulerian* or *spatial description*. Within this work all tensors which are expressed with respect to a material description are denoted by boldface upper cases. A tensor reference to a spatial description is expressed by boldface lower cases.

2.2 Strain and Stress Measure

2.2.1 Deformation Gradient

One key quantity in continuum mechanics constitutes the deformation gradient **F**. It appears, directly or indirectly, in many equations which are used in finite deformation analysis. Consequently, this quantity is introduced here in more detail.

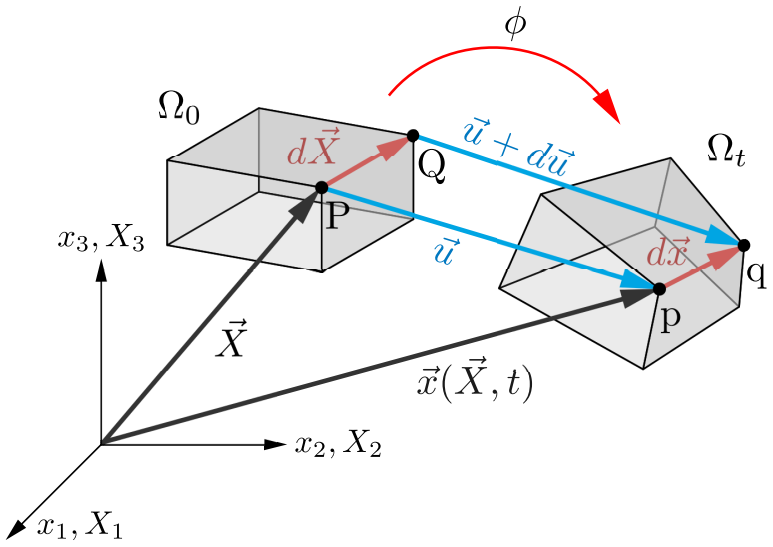

Figure 2.2: Initial and current configuration of a deformable body Ω.

In Fig. 2.2, two configurations of the deformable body Ω are shown. Additionally, this sketch illustrates the definition of the differential line elements $d\vec{X}$ and $d\vec{x}$ in the initial and current configuration, respectively. The relation between those two quantities is described by the deformation gradient

$$d\vec{x} = \mathbf{F} d\vec{X} \quad . \tag{2.6}$$

This implies that the deformation gradient transforms a material line element $d\vec{X}$ from the initial to the current configuration. The complete definition of this second order tensor is given by Eq. (2.7).

$$\mathbf{F} = \frac{\partial \vec{x}}{\partial \vec{X}} = \frac{\partial x_i}{\partial X_j} \, \vec{e_i} \otimes \vec{e_j} \tag{2.7}$$

The determinant of the deformation gradient is know as the Jacobian J

$$\det\mathbf{F} = J \neq 0 \quad . \tag{2.8}$$

With the condition $J \neq 0$ the mapping Eq. (2.6) is bijective and the existence of the inverse of the deformation gradient $\mathbf{F^{-1}}$ is given. Consequently, a backward transformation of $d\vec{x}$ to $d\vec{X}$ can be applied. J also defines the relation between a differential volume element in initial and current configuration.
Another expression of the deformation gradient is based on displacements, e.g. the distance $d\vec{u}$ between a particle in the initial and current configuration (Fig. 2.2). With the relation

$$d\vec{x} = d\vec{X} + d\vec{u} \tag{2.9}$$

and Eq. (2.7) as well as the second order identity $\mathbf{I}$ the deformation gradient can be represented by the displacement gradient $\mathbf{H}$ in the following way

$$\mathbf{F} = \frac{\partial\vec{X} + \partial\vec{u}}{\partial\vec{X}} = \mathbf{I} + \mathbf{H} \quad \text{with} \quad \mathbf{H} = \frac{\partial\vec{u}}{\partial\vec{X}} \quad . \tag{2.10}$$

2.2.2 Strain Tensor

The deformation gradient can now be used to define a general strain measure for finite deformation. Therefore, firstly the Right Cauchy-Green deformation tensor $\mathbf{C}$ is defined, which can be derived from the representation of the square of $d\vec{x}$ expressed in terms of $d\vec{X}$ and is defined by

$$\mathbf{C} = \mathbf{F}^T\mathbf{F} \quad . \tag{2.11}$$

Thereby, $\mathbf{C}$ is a positive definite tensor where the rigid rotation has been eliminated. Based on the difference of the square of the differential line elements, expressed in terms of $d\vec{X}$ and the use of Eq. (2.11) the Green-Lagrange strain tensor $\mathbf{E}$ can be defined by

$$\mathbf{E} = \frac{1}{2}(\mathbf{C} - \mathbf{I}) \quad . \tag{2.12}$$

As already implied by the name, this tensor is a Lagrangian or material tensor referring to $\vec{X}$ and consequently to the initial configuration. For completeness here also the Eulerian or Almansi strain tensor $\mathbf{e}$ is mentioned which is referring to $\vec{x}$ and defined by

$$\mathbf{e} = \frac{1}{2}(\mathbf{I} - \mathbf{b}^{-1}) \quad \text{with} \quad \mathbf{b} = \mathbf{F}\mathbf{F}^T \quad . \tag{2.13}$$

Here, $\mathbf{b}$ defines the Left Cauchy-Green deformation tensor, also known as Finger tensor [8].

Expression of Eq. (2.12) by the displacement gradient $\mathbf{H}$ provides

$$\mathbf{E} = \frac{1}{2}(\mathbf{H} + \mathbf{H}^T + \mathbf{H}^T\mathbf{H}) \quad . \tag{2.14}$$

In terms of small displacements, $\| \mathbf{H} \| \ll 1$, the term $\mathbf{H}^T\mathbf{H}$ vanishes and the Green-Lagrange strain tensor becomes identical with linear strain tensor $\boldsymbol{\varepsilon}$ and can be presented by the following

$$\varepsilon_{ij} = \frac{1}{2}\left(u_{i,j} + u_{j,i}\right) \quad . \tag{2.15}$$

Thus, it can been seen that a general strain measure formulation for large deformation will automatically provide the equations derived by the linear elasticity theory [35].

2.2.3 Rate of Deformation and Spin Tensor

The rate of deformation $\mathbf{d}$ and the spin tensor $\mathbf{w}$ are spatial quantities which can be directly derived by splitting the velocity gradient $\mathbf{l}$ in a symmetric and antisymmetric part. Thereby, the velocity gradient constitutes a mapping between the differential element $d\vec{x}$ and $d\vec{v}$ in the current configuration which is illustrated in Fig 2.3.

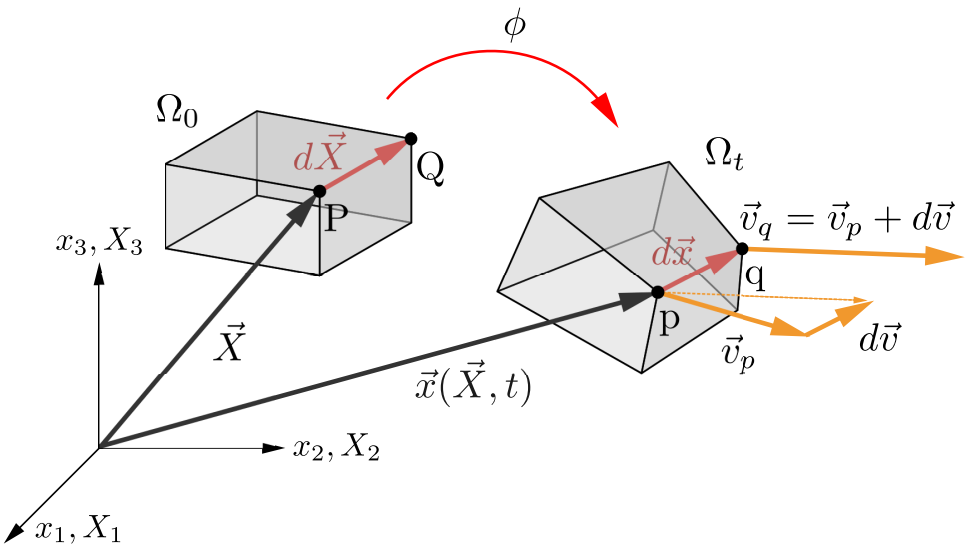

Figure 2.3: Initial and current configuration of a deformable body Ω incl. velocities.

Consequently, the velocity gradient can be expressed by

$$\mathbf{l} = \frac{\partial \vec{v}}{\partial \vec{x}} = \frac{\partial v_i}{\partial x_j}\, \vec{e_i} \otimes \vec{e_j} \quad . \tag{2.16}$$

It addition it can be shown, that substituting $d\vec{v}$ by the time derivative of $d\vec{x}$ and expression in terms of $d\vec{X}$ provide a description in dependency of the deformation gradient by

$$\mathbf{l} = \dot{\mathbf{F}}\mathbf{F}^{-1} \quad . \tag{2.17}$$

As mentioned above the velocity gradient is split into two terms in order to provide the rate of deformation and the spin tensor (Eq. (2.18)).

$$\mathbf{l} = \mathbf{l}_{sym} + \mathbf{l}_{asym} = \mathbf{d} + \mathbf{w} \tag{2.18}$$

Consequently, $\mathbf{d}$ and $\mathbf{w}$ can be defined by Eq. (2.19) and Eq. (2.20), respectively.

$$\mathbf{d} = \frac{1}{2}(\mathbf{l} + \mathbf{l}^T) \tag{2.19}$$

$$\mathbf{w} = \frac{1}{2}(\mathbf{l} - \mathbf{l}^T) \tag{2.20}$$

Finally, some relations between the main quantities for the description of deformation are given. The derivation of the relations presented in Eq. (2.21) can be found in the literature mentioned in the introduction of this chapter. However, it can be seen that each quantity transformation is based on the deformation gradient $\mathbf{F}$. Thereby, the denotations *push forward* and *pull back* are often used in the existing literature [8], e.g. $\mathbf{d}$ is the push forward of $\dot{\mathbf{E}}$ whereas $\mathbf{E}$ represents the pull back of $\mathbf{e}$.

$$\begin{aligned} \mathbf{E} &= \mathbf{F}^T\mathbf{e}\ \mathbf{F} \quad , \quad \mathbf{e} = \mathbf{F}^{-T}\mathbf{E}\ \mathbf{F}^{-1} \\ \dot{\mathbf{E}} &= \mathbf{F}^T\mathbf{d}\ \mathbf{F} \quad , \quad \mathbf{d} = \mathbf{F}^{-T}\dot{\mathbf{E}}\ \mathbf{F}^{-1} \end{aligned} \tag{2.21}$$

The formulation of constitutive laws in the domain of explicit finite elements is mainly based on $\mathbf{d}$.

2.2.4 Stress Tensor

In this section the different stress measures used in Section 2.3 will be introduced briefly. Thereby, all considerations are based on the Cauchy stress tensor $\boldsymbol{\sigma}$, which relates the normal vector $\vec{n}$ to the traction vector $\vec{t}$ by following equation

$$\vec{t} = \boldsymbol{\sigma}\vec{n} \quad , \tag{2.22}$$

which is often denoted as the Cauchy theorem. The Cauchy stress tensor in its index notation is given by

$$\boldsymbol{\sigma} = \sigma_{ij}\ \vec{e_i} \otimes \vec{e_j} \quad , \tag{2.23}$$

and represents a symmetric second order tensor. Thereby, the symmetry condition, $\sigma_{ij} = \sigma_{ji}$, can be derived by the conservation of angular momentum [2]. Fig. 2.4 represents the contribution of each component of the stress tensor to the traction with respect to an infinitesimal cube for an orthogonal basis system.

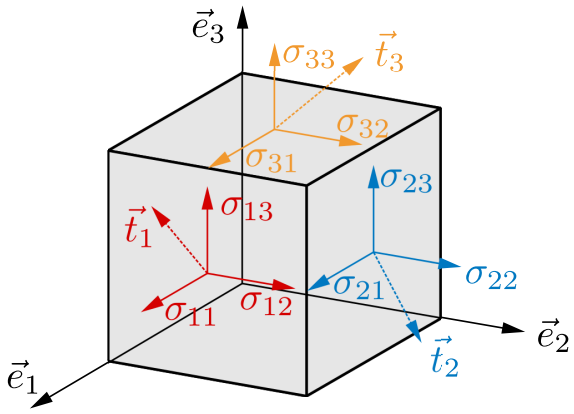

Figure 2.4: Cauchy stress tensor for infinitesimal cube.

In addition the Cauchy stress tensor expresses a quantity in the current configuration. In order to have a stress measure referring to the initial configuration, the second Piola-Kirchhoff stress tensor $\mathbf{S}$ is defined by

$$\mathbf{S} = J\mathbf{F}^{-1}\boldsymbol{\sigma}\mathbf{F}^{-T} \quad . \tag{2.24}$$

Also $\mathbf{S}$ represents a symmetric second order tensor and can be considered as a pure mathematical quantity since it has no physical meaning. Replacing $J\boldsymbol{\sigma}$ by $\boldsymbol{\tau}$, the Kirchhoff stress, provides

$$\mathbf{S} = \mathbf{F}^{-1}\boldsymbol{\tau}\mathbf{F}^{-T} \quad . \tag{2.25}$$

and reveals that $\mathbf{S}$ can be considered as a pull back operation of $J\boldsymbol{\sigma}$ or $\boldsymbol{\tau}$, respectively.

2.2.5 Objectivity and Rate of Stress

The objectivity constitutes an important role in continuum mechanics. In order to reveal and briefly introduce this concept an example from [8] is taken. In Fig. 2.5 a deformed body Ω, with a given Cauchy stress state $\vec{t}$ in point p is considered in two different configurations Ω and Ω'. The only difference between both configurations constitutes a rigid body rotation represented by the orthogonal, second order tensor $\mathbf{R}$. Consideration of the traction $\vec{t}$ from different points of view provides the following statement. Seen from of an observer directly located in p, the traction $\vec{t}$ remains constant during the rotation (material point based consideration). In contrary $\vec{t}$ changes for an observer located in the origin O of the coordinate system (spatial point based consideration) by

$$\vec{t}\,' = \mathbf{R}\,\vec{t} \quad . \tag{2.26}$$

However, although the vector $\vec{t}\,'$ is different to $\vec{t}$, the magnitude remains equal. In this sense $\vec{t}$ can be considered objective under rigid body motion. Generally

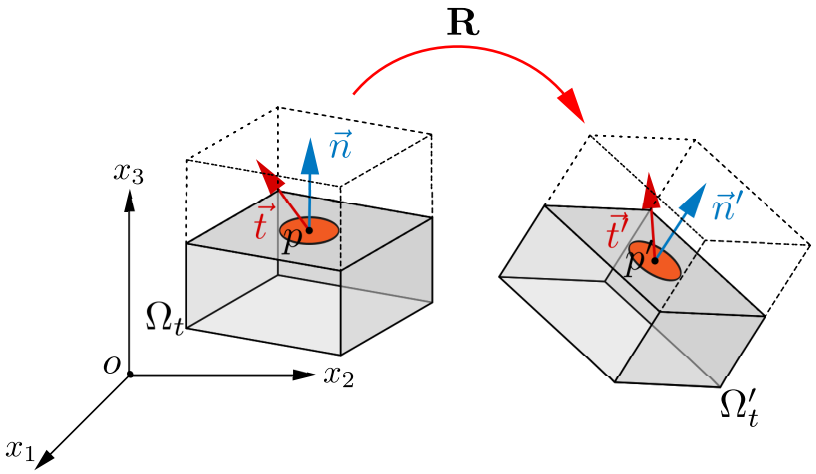

Figure 2.5: Body under rigid body rotation.

this implies, that a vector can be considered as objective if it transforms accordingly to Eq. (2.26). In addition it can be shown that, by using Eq. (2.22) in combination with $\vec{n}\,' = \mathbf{R}\,\vec{n}$, Eq. (2.26) can be extended to an expression for the Cauchy stress tensor by

$$\boldsymbol{\sigma}\,' = \mathbf{R}\,\boldsymbol{\sigma}\mathbf{R}^T \quad , \tag{2.27}$$

which represents the general transformation relation for an objective second order tensor. Consequently, each second order tensor satisfying Eq. (2.27) can be said to be objective, thus also the Cauchy stress tensor. In addition, it has to be mentioned that a tensor which is defined with respect to the material configuration is always objective. This implies that e.g. $\mathbf{S}$ and $\mathbf{E}$ are objective tensors. For $\mathbf{S}$ the complete independence of any rigid body motion is shown for example in [8].

In the second part of this section the definition of the stress rate is treated. The stress rate tensor is defined by the material time derivative of the stress tensor. In terms of the Cauchy stress tensor this implies

$$\dot{\boldsymbol{\sigma}} = \frac{D\boldsymbol{\sigma}}{Dt} = \frac{\partial \boldsymbol{\sigma}}{\partial t} + \frac{\partial \boldsymbol{\sigma}}{\partial x}\frac{\partial x}{\partial t} \quad . \tag{2.28}$$

It can be shown that the stress rate tensor of the Cauchy stress, contrary to the Cauchy stress tensor, does not satisfy Eq. (2.27) and is consequently not objective [2]. Since objectivity is a necessary property to take into account rigid body motion correctly in finite deformation, an objective stress rate quantity has to be defined. Amongst others, therefore the Truesdell Stress Rate $\boldsymbol{\sigma}^{\blacktriangledown}$ and Jaumann Stress Rate $\boldsymbol{\sigma}^{\triangledown}$ exist.

$$\boldsymbol{\sigma}^{\blacktriangledown} = \dot{\boldsymbol{\sigma}} - \mathbf{l}\boldsymbol{\sigma} - \boldsymbol{\sigma}\mathbf{l}^T + \boldsymbol{\sigma}(\mathrm{tr}\ \mathbf{l}) \tag{2.29}$$

$$\boldsymbol{\sigma}^{\triangledown} = \dot{\boldsymbol{\sigma}} - \mathbf{w}\boldsymbol{\sigma} - \boldsymbol{\sigma}\mathbf{w}^T \tag{2.30}$$

As can be seen, in both equations additional terms based on the velocity gradient $\mathbf{l}$ are added to the material time derivative of the Cauchy stress, whereas for the Jaumann Stress Rate only the spin tensor is taken into account. A detailed derivation and the proof of objectivity for the equations mentioned above can be found in [2, 8].

2.3 Constitutive Modelling

2.3.1 Elasticity for Large Deformation

The introduced quantities of the previous section are used now to describe a constitutive law, in which the stresses and strains are related in terms of large elastic deformation. Therefore, a hyperelastic material formulation is used. In such an elastic stress-strain relationship, the stress can be obtained from a potential function of the strains [5]. However, due to the conservation of energy, the stress and strain measure must be conjugated in power. This condition is satisfied by $\mathbf{S}$ and $\dot{\mathbf{E}}$ as well as $\boldsymbol{\sigma}$ and $\mathbf{d}$ [5]. The simplest form of a hyperelastic material is represented by a Saint Venant-Kirchhoff material, which is defined by

$$\mathbf{S} = \mathbf{C}^{(4)} : \mathbf{E} \quad , \tag{2.31}$$

and based on the strain energy per volume w in the following way

$$w = \frac{1}{2}\mathbf{E} : \mathbf{C}^{(4)} : \mathbf{E} \quad , \quad \mathbf{S} = \frac{\partial w}{\partial \mathbf{E}} \quad , \quad \mathbf{C}^{(4)} = \frac{\partial^2 w}{\partial \mathbf{E} \partial \mathbf{E}} \quad . \tag{2.32}$$

Here $\mathbf{C}^{(4)}$ is the fourth order tensor of the elastic moduli related to the initial configuration, having minor and major symmetry ($C_{ijkl} = C_{jikl} = C_{ijlk}$, $C_{ijkl} = C_{klij}$). In general, this constitutive law can be considered as an extension to large deformation of Hooke's law of elasticity. It is expressed in Lagrangian description and can incorporate fully anisotropic material response [5]. In order to get a formulation based on the Cauchy stress Eq. (2.31) must be transformed to the spatial description. Therefore, firstly Eq. (2.31) is represented in terms of rates and subsequently multiplied by the deformation gradient $\mathbf{F}$ from the left-hand and right-hand side as follows

$$\dot{\mathbf{S}} = \mathbf{C}^{(4)} : \dot{\mathbf{E}} \quad , \tag{2.33}$$

$$\mathbf{F}\dot{\mathbf{S}}\mathbf{F}^T = \mathbf{F}\mathbf{C}^{(4)} : \dot{\mathbf{E}}\mathbf{F}^T \quad . \tag{2.34}$$

Taking into account the relation

$$\mathbf{F}\dot{\mathbf{S}}\mathbf{F}^T = \boldsymbol{\tau}^{\blacktriangledown} = J\boldsymbol{\sigma}^{\blacktriangledown} \quad , \tag{2.35}$$

which will be provided by the Lie derivative of the Kirchhoff stress [8, 91], and the substitution of $\dot{\mathbf{E}}$ by $\mathbf{d}$ from Eq. (2.21) the following expression is given

$$\boldsymbol{\sigma}^{\blacktriangledown} = J^{-1}\mathbf{F}\mathbf{F}^T\mathbf{C}^{(4)}\mathbf{F}^T\mathbf{F} : \mathbf{d} \quad . \tag{2.36}$$

The transformation of the Lagrangian elasticity tensor can be now expressed by the Eulerian elasticity tensor $\mathbf{c}^{(4)}$

$$\mathbf{c}^{(4)} = J^{-1}\mathbf{F}\mathbf{F}^T\mathbf{C}^{(4)}\mathbf{F}^T\mathbf{F} \quad . \tag{2.37}$$

Thus, the constitutive law from Eq.(2.31) can be expressed in terms of the Truesdell stress rate of the Cauchy stress, the spatial elasticity tensor and the rate of deformation by

$$\boldsymbol{\sigma}^{\blacktriangledown} = \mathbf{c}^{(4)} : \mathbf{d} \quad . \tag{2.38}$$

Such a formulation which relates the stress rate to the rate of deformation is called Hypoelastic material law [5].

2.3.2 Numerical Implementation

The incorporation of the constitutive law in an explicit finite element USER MATERIAL routine can be done as described below. In contrast to Eq. (2.38) here the Jaumann stress rate $\boldsymbol{\sigma}^{\triangledown}$ is used instead of the Truesdell $\boldsymbol{\sigma}^{\blacktriangledown}$ stress rate. In terms of small strains and dominating rotation the differences are negligible (see Eq. (2.29), (2.30)). Due to the explicit time integration scheme and the resulting small increments it is assumed that the strains are also small and the condition fulfilled.

Consequently, the constitutive law written in terms of the Jaumann stress rate is expressed by

$$\boldsymbol{\sigma}^{\triangledown} = \mathbf{c}^{(4)} : \mathbf{d} \quad , \quad \text{with} \quad \boldsymbol{\sigma}^{\triangledown} = \dot{\boldsymbol{\sigma}} - \mathbf{w}\boldsymbol{\sigma} - \boldsymbol{\sigma}\mathbf{w}^T \quad , \tag{2.39}$$

and provides the base for an incremental formulation. As mentioned above explicit time integration is related to small time steps and therefore the time derivative of the Cauchy stress can be approximated by the difference quotient by

$$\dot{\boldsymbol{\sigma}} = \frac{\Delta\boldsymbol{\sigma}}{\Delta t} = \frac{\boldsymbol{\sigma}_{t+\Delta t} - \boldsymbol{\sigma}_t}{\Delta t} \quad . \tag{2.40}$$

Substitution of $\dot{\boldsymbol{\sigma}}$ by the difference quotient in Eq. (2.39) yields

$$\frac{\boldsymbol{\sigma}_{t+\Delta t} - \boldsymbol{\sigma}_t}{\Delta t} = \mathbf{c}^{(4)} : \mathbf{d} + \mathbf{w}\boldsymbol{\sigma}_t + \boldsymbol{\sigma}_t\mathbf{w}^T \quad . \tag{2.41}$$

Finally, the expression with respect to $\boldsymbol{\sigma}_{t+\Delta t}$ provides an incremental formulation for the Cauchy stress, including objectivity, by

$$\underbrace{\boldsymbol{\sigma}_{t+\Delta t}}_{\text{new stress}} = \underbrace{\mathbf{c}^{(4)} : \mathbf{d}\Delta t}_{\text{new stress increment}} + \underbrace{\boldsymbol{\sigma}_t + (\mathbf{w}\boldsymbol{\sigma}_t + \boldsymbol{\sigma}_t\mathbf{w}^T)\Delta t}_{\text{old stress in current configuration}} \quad , \tag{2.42}$$

which can be summarised in three main terms: $\boldsymbol{\sigma}_{\text{NEW}}$, the new total stress, $\Delta\boldsymbol{\sigma}$, the new stress increment and $\boldsymbol{\sigma}^{\text{ROT}}_{\text{OLD}}$, the old stress rotated to the current configuration. In Fig. 2.8 the general scheme of implementation of such an incremental formulation with respect to a USER MATERIAL routine in an explicit finite element code is represented. Here in terms of PAM-CRASH [23]. Thereby, the elasticity tensor will be determined during initialisation. In terms of isotropic material behaviour, $\mathbf{c}^{(4)}$ can be determined based on engineering constants (Young's modulus E, shear modulus G, Poisson's ratio ν) or Lamé parameters (λ, μ).

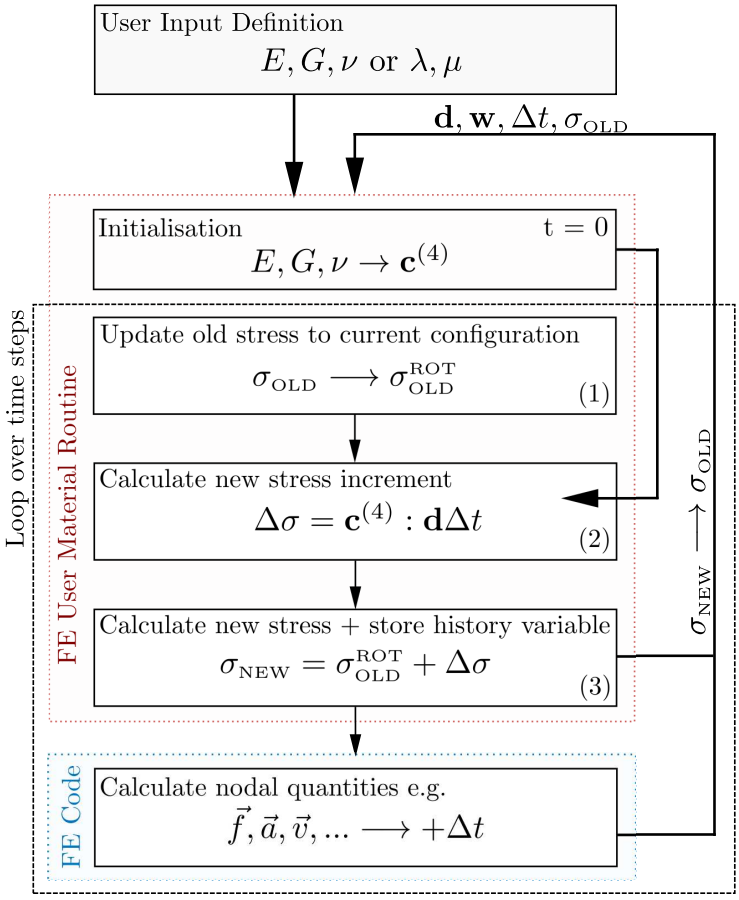

Figure 2.6: Flowchart material routine isotropic elasticity in terms of explicit finite element analysis.

2.3.3 Extension to Composite Material

In order to describe an unidirectional composite material including failure, the finite element material routine for general isotropic behaviour is extended. Thereby, the modifications are only related to the stress increment $\Delta\boldsymbol{\sigma}$ defined by

$$\Delta\boldsymbol{\sigma} = \mathbf{c}^{(4)} : \mathbf{d}\Delta t \quad . \tag{2.43}$$

In terms of an unidirectional composite material, the change of the material response with respect to the fibre orientation has to be taken into account. Therefore, the constitutive law is extended to an orthotropic elasticity. Firstly, a notation, which is known as the Voigt notation [5], is used to represent Eq. (2.43) in terms of a matrix-vector arrangement (Eq. (2.44)).

$$\begin{Bmatrix} \Delta\sigma_{11} \\ \Delta\sigma_{22} \\ \Delta\sigma_{33} \\ \Delta\sigma_{23} \\ \Delta\sigma_{13} \\ \Delta\sigma_{12} \end{Bmatrix} = \begin{bmatrix} c_{1111} & c_{1122} & c_{1133} & c_{1123} & c_{1113} & c_{1112} \\ & c_{2222} & c_{2233} & c_{2223} & c_{2213} & c_{2212} \\ & & c_{3333} & c_{3323} & c_{3313} & c_{3312} \\ & & & c_{2323} & c_{2313} & c_{2312} \\ & \text{sym} & & & c_{1313} & c_{1312} \\ & & & & & c_{1212} \end{bmatrix} \begin{Bmatrix} d_{11}\Delta t \\ d_{22}\Delta t \\ d_{33}\Delta t \\ d_{23}\Delta t \\ d_{13}\Delta t \\ d_{12}\Delta t \end{Bmatrix} \tag{2.44}$$

This is possible since the number of constants of the general anisotropic elasticity tensor can be reduced from 81 to 21 due to symmetry properties [5]. In terms of orthotropic material behaviour represented by three mutually orthogonal planes of symmetry, the number of elastic constants further decreases in following way [2]:

$$\begin{Bmatrix} \Delta\sigma_{11} \\ \Delta\sigma_{22} \\ \Delta\sigma_{33} \\ \Delta\sigma_{23} \\ \Delta\sigma_{13} \\ \Delta\sigma_{12} \end{Bmatrix} = \begin{bmatrix} \frac{1-\nu_{23}\nu_{32}}{E_{22}E_{33}\square} & \frac{\nu_{21}+\nu_{31}\nu_{23}}{E_{22}E_{33}\square} & \frac{\nu_{31}+\nu_{21}\nu_{32}}{E_{22}E_{33}\square} & 0 & 0 & 0 \\ \frac{\nu_{21}+\nu_{31}\nu_{23}}{E_{22}E_{33}\square} & \frac{1-\nu_{13}\nu_{31}}{E_{11}E_{33}\square} & \frac{\nu_{32}+\nu_{12}\nu_{31}}{E_{11}E_{33}\square} & 0 & 0 & 0 \\ \frac{\nu_{31}+\nu_{21}\nu_{32}}{E_{22}E_{33}\square} & \frac{\nu_{32}+\nu_{12}\nu_{31}}{E_{11}E_{33}\square} & \frac{1-\nu_{12}\nu_{21}}{E_{11}E_{22}\square} & 0 & 0 & 0 \\ 0 & 0 & 0 & G_{23} & 0 & 0 \\ 0 & 0 & 0 & 0 & G_{13} & 0 \\ 0 & 0 & 0 & 0 & 0 & G_{12} \end{bmatrix} \begin{Bmatrix} d_{11}\Delta t \\ d_{22}\Delta t \\ d_{33}\Delta t \\ d_{23}\Delta t \\ d_{13}\Delta t \\ d_{12}\Delta t \end{Bmatrix} \tag{2.45}$$

with

$$\square = \frac{1 - \nu_{12}\nu_{21} - \nu_{23}\nu_{32} - \nu_{13}\nu_{31} - 2\nu_{21}\nu_{32}\nu_{13}}{E_{11}E_{22}E_{33}}$$

Here E_{11}, E_{22}, E_{33} represent the elastic moduli in three directions of an orthogonal base system. G_{23}, G_{13}, G_{12} and ν_{23}, ν_{32}, ν_{13}, ν_{31}, ν_{12}, ν_{21} are the

shear moduli and Poisson's ratios, respectively. Thereby, the first index refers to the acting plane and the second one to acting direction. Since each ν_{ij} can be expressed by ν_{ji}, E_{ii} and E_{jj} (no summation here) the orthotropic elasticity tensor can be fully determined by 9 engineering constants.
In addition it is defined that the orientation of the three mutually orthogonal planes of symmetry is based on the coincidence of the normal of the fibre cross-section and the first material axis vector. In order to evaluate Eq. (2.45) correctly, the spatial quantities have to be transformed into this configuration.

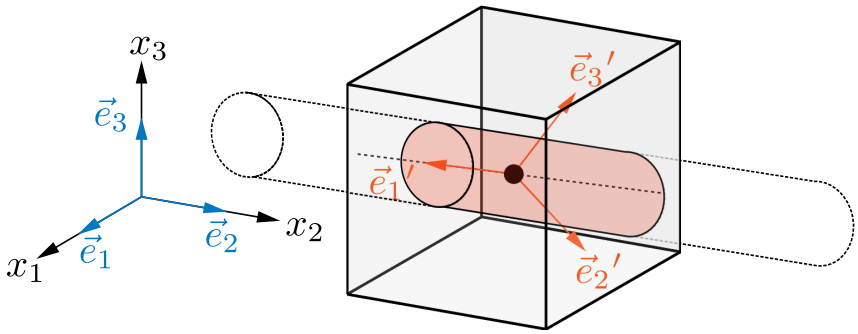

Figure 2.7: Local material axis with respect to fibre direction.

In Fig. 2.7 this situation is illustrated for one finite element and a crossing fibre. Thereby, $\vec{e}_i$ expresses a base system, coinciding with the global coordinate system, and $\vec{e}_j\,'$ the material frame axis. Both systems define an orthogonal, normalised base systems. Consequently, the second order transformation tensor $\mathbf{R}$ can be determined by

$$\mathbf{R} = \vec{e}_i \otimes \vec{e}_j\,' \quad . \tag{2.46}$$

Based on $\mathbf{R}$, $\mathbf{d}$ can be transformed to $\mathbf{d}'$ and the local stress increment $\Delta\boldsymbol{\sigma}'$ can be calculated by

$$\Delta\boldsymbol{\sigma}' = \mathbf{c}^{(4)}\mathbf{d}'\Delta t \quad \text{with} \quad \mathbf{d}' = \mathbf{R}\,\mathbf{d}\,\mathbf{R}^T \quad . \tag{2.47}$$

The new spatial stress increment will be obtained by backward transformation of $\Delta\boldsymbol{\sigma}'$ in the following way

$$\Delta\boldsymbol{\sigma} = \mathbf{R}^{-1}\Delta\boldsymbol{\sigma}'\mathbf{R}^{-T} \quad , \tag{2.48}$$

and can subsequently be used to calculate the total new stress as defined by Eq. (2.42).

Finally, an element elimination criterion is implemented to represent the fracture within an unidirectional composite layer. In this work a maximum stress criterion is used where the occurring local stresses are compared to user defined limits. Thereby, the compared quantities are considered separately without taking into account any interaction. The failure occurs if one of the quotients in Eq. (2.49) provides a value greater than one whereas the stresses are evaluated with respect to the local material frame axis.

$$f = \max\left(\left|\frac{\sigma'_{11}}{\sigma_{11}^{\mathrm{FAIL}}}\right|, \left|\frac{\sigma'_{22}}{\sigma_{22}^{\mathrm{FAIL}}}\right|, \left|\frac{\sigma'_{33}}{\sigma_{33}^{\mathrm{FAIL}}}\right|, \left|\frac{\sigma'_{23}}{\sigma_{23}^{\mathrm{FAIL}}}\right|, \left|\frac{\sigma'_{13}}{\sigma_{13}^{\mathrm{FAIL}}}\right|, \left|\frac{\sigma'_{12}}{\sigma_{12}^{\mathrm{FAIL}}}\right|\right) > 1 \qquad (2.49)$$

$$\sigma_{11}^{\mathrm{FAIL}} = \begin{cases} \sigma_{11+}^{\mathrm{FAIL}} & \text{if } \sigma'_{11} \geq 0 \\ \sigma_{11-}^{\mathrm{FAIL}} & \text{if } \sigma'_{11} < 0 \end{cases}$$

$$\sigma_{22}^{\mathrm{FAIL}} = \begin{cases} \sigma_{22+}^{\mathrm{FAIL}} & \text{if } \sigma'_{22} \geq 0 \\ \sigma_{22-}^{\mathrm{FAIL}} & \text{if } \sigma'_{22} < 0 \end{cases}$$

$$\sigma_{33}^{\mathrm{FAIL}} = \begin{cases} \sigma_{33+}^{\mathrm{FAIL}} & \text{if } \sigma'_{33} \geq 0 \\ \sigma_{33-}^{\mathrm{FAIL}} & \text{if } \sigma'_{33} < 0 \end{cases}$$

$\sigma_{ij}^{\mathrm{FAIL}}$ represent the limits of the unidirectional composite layer which have to be provided by user input. In addition $\sigma_{ii+}^{\mathrm{FAIL}}$ are related to limits in tension, $\sigma_{ii-}^{\mathrm{FAIL}}$ referring to limits in compression. Within this work these values are determined by micro-scale analysis described in Section 4.3.

In Fig. 2.8 the extension of the USER MATERIAL described above has been integrated in the previous illustration and finally presents the complete USER MATERIAL model which is used for the roving structure in the finite element simulation of the wound tube in terms of static and impact loading in Chapter 5.

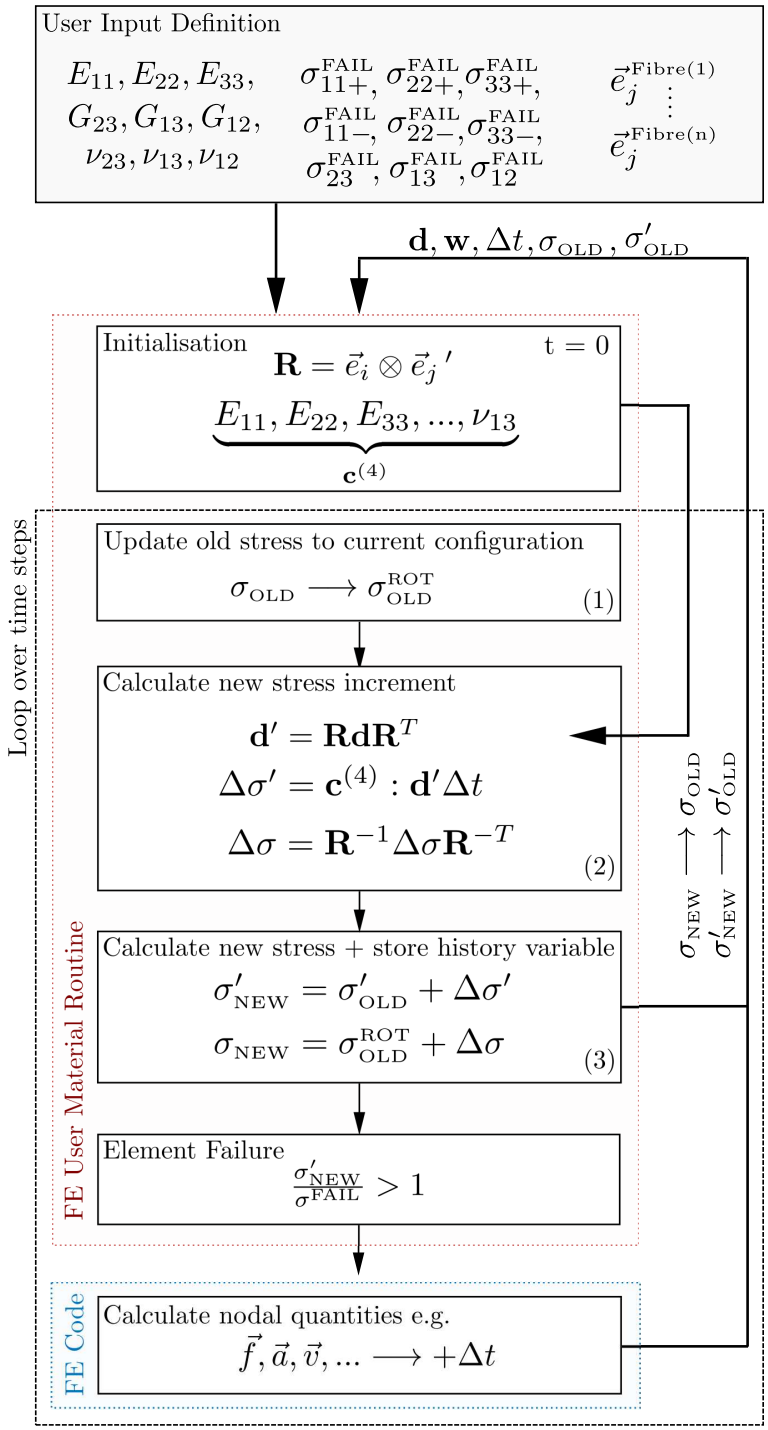

Figure 2.8: Flowchart material routine orthotropic elasticity with failure in terms of explicit finite element analysis.

2.4 Numerical Homogenisation Procedure for the Determination of Elastic Constants

In order to derive effective elastic material properties from an inhomogeneous structure, a numerical homogenisation procedure based on the finite element method is described below. The procedure is used in Section 4.3 to provide input parameters for the constitutive model described above. The applied method can be sub-divided into two parts. The first one is based on an analytical relation between a homogeneous and a periodic inhomogeneous structure, the second part is related to the determination of the unknown quantities based on finite element simulations. For the representation of the relations it is more convenient using index notation in one common Cartesian base system. In addition, it has to be mentioned that contrary to the previous sections the spatial elasticity tensor is denoted by C_{ijkl} instead of c_{ijkl} here. The change is conducted in order to be in accordance with the literature dealing with homogenisation and effective properties, e.g. [36].

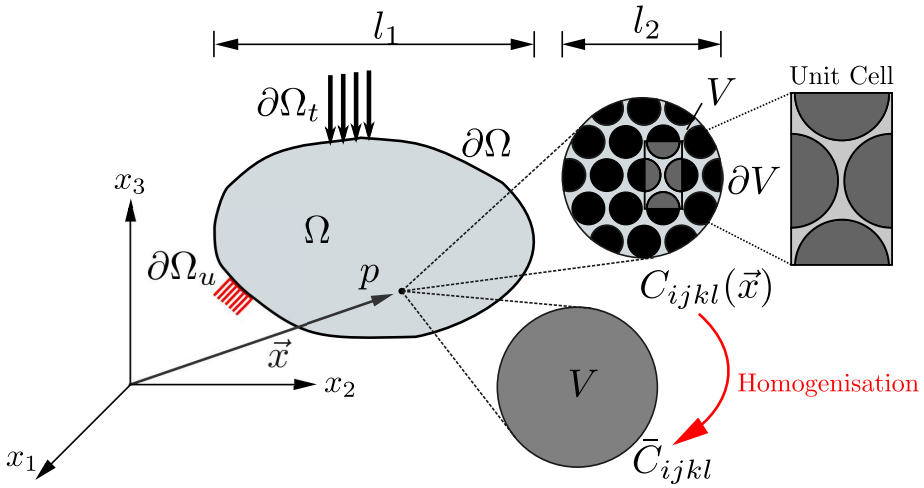

Figure 2.9: Boundary value problem and scheme of homogenisation approach.

The homogenisation approach presented here is based on an average energy theorem [40] which considers the elastic strain energy density w. It implies that the strain energy density $\bar{w}$ for a homogeneous continuum is identical with the average of the strain energy density $\{w\}$ of the inhomogeneous structure for a representative volume V.

$$\bar{w} = \{w\} \quad \text{with} \quad \{...\} = \frac{1}{V}\int_V ...\, dV \tag{2.50}$$

Considering Fig. 2.9, Ω represents a domain of continuously connected points in the current configuration and $\partial\Omega$ its boundary surface where $\partial\Omega_u \cup \partial\Omega_t = \partial\Omega$ and $\partial\Omega_u \cap \partial\Omega_t = \varnothing$. The linear elastic boundary value problem of this configuration can be expressed by

$$\sigma_{ij,j} + f_i = 0 \quad \forall x_i \in \Omega \quad , \tag{2.51}$$

$$\varepsilon_{ij} = \frac{1}{2}\left(u_{i,j} + u_{j,i}\right) \quad \forall x_i \in \Omega \quad , \tag{2.52}$$

$$\sigma_{ij} = C_{ijkl}\varepsilon_{kl} \quad \forall x_i \in \Omega \quad . \tag{2.53}$$

Also here σ_{ij} represents the Cauchy stress, ε_{ij} the linear strain tensor and C_{ijkl} the elasticity tensor. f_i refers to the volume load vector and u_i to the displacement vector. Moreover, Eq. (2.51) expresses the static equilibrium, Eq. (2.52) the relation between deformations and displacements and Eq. (2.53) provides the constitutive law. The latter represents Hooke's law of elasticity and can be obtained by reducing Eq. (2.31) to infinitesimal displacements. In addition, appropriate boundary conditions for displacements ($\tilde{u}_i$) or tractions $\tilde{t}_i$ have to be applied by

$$u_i = \tilde{u}_i \quad \forall x_i \in \partial\Omega_u \quad , \tag{2.54}$$

$$\sigma_{ij} n_j = \tilde{t}_i \quad \forall x_i \in \partial\Omega_t \quad . \tag{2.55}$$

Contrary to a homogeneous material, in a heterogeneous material the elasticity tensor is depending on the location (Fig. 2.9). Due to the homogenisation approach the elasticity tensor $C_{ijkl}(\vec{x})$ is replaced by an effective stiffness tensor $\bar{C}_{ijkl}$, for a representative structure. Consequently, the original boundary value problem can now be expressed as

$$\left.\begin{aligned} &\bar{\sigma}_{ij,j} + \bar{f}_i = 0 \\ &\bar{\varepsilon}_{ij} = \tfrac{1}{2}\left(\bar{u}_{i,j} + \bar{u}_{j,i}\right) \\ &\bar{\sigma}_{ij} = \bar{C}_{ijkl}\bar{\varepsilon}_{kl} \end{aligned}\right\} \quad \forall x_i \in \Omega \quad , \tag{2.56}$$

where the bar over a quantity, e.g. $\bar{\sigma}_{ij}$ and $\bar{\varepsilon}_{ij}$, refers to the larger scale of consideration. In the example of Fig. 2.9, two different scales, macro-scale (l_1) and micro-scale (l_2), are considered. In order to get a sufficient approximation by Eq. (2.56) the condition $l_1 \gg l_2$ must be satisfied. In accordance with Eq. (2.55) the boundary conditions are given by

$$\bar{u}_i = \tilde{u}_i \quad \forall x_i \in \partial\Omega_u \tag{2.57}$$

$$\bar{\sigma}_{ij} n_j = \tilde{t}_i \quad \forall x_i \in \partial\Omega_t. \tag{2.58}$$

Combining Eq. (2.53) and Eq. (2.56) with the initially postulated condition of Eq. (2.50) as well as the definition of the strain energy in terms of small strains by

$$w = \frac{1}{2} C_{ijkl} \varepsilon_{ij} \varepsilon_{kl} = \frac{1}{2} \sigma_{ij} \varepsilon_{ij} \quad , \tag{2.59}$$

yields to an expression, where stress and strain fields of different scales are related by

$$\{\sigma_{ij} \varepsilon_{ij}\} = \bar{\sigma}_{ij} \bar{\varepsilon}_{ij} \quad . \tag{2.60}$$

In addition, the so called Hill-Mandel condition [76] provides

$$\{\sigma_{ij} \varepsilon_{ij}\} = \{\sigma_{ij}\} \{\varepsilon_{ij}\} \tag{2.61}$$

and expresses that for arbitrary statically admissible stress or kinematic deformation fields the volume average of the stress strain product is equal to the product of the individual volume averaged stress and strain, respectively. However, Eq. (2.61) is only fulfilled if one of the following boundary conditions is satisfied

$$t_i = \bar{\sigma}_{ij} n_j \quad \forall x_i \in \partial V \quad , \tag{2.62}$$

$$u_i = \bar{\varepsilon}_{ij} x_j \quad \forall x_i \in \partial V \quad , \tag{2.63}$$

where ∂V is the boundary of the representative volume (Fig. 2.9). In addition from Eq. (2.61) and Eq. (2.60) the identity $\{\sigma_{ij}\} = \bar{\sigma}_{ij}$ and $\{\varepsilon_{ij}\} = \bar{\varepsilon}_{ij}$ becomes apparent, respectively.

Taking into account the Hill-Mandel condition, Eq. (2.60) can be rewritten by

$$\{\sigma_{ij}\} \{\varepsilon_{ij}\} = \bar{\sigma}_{ij} \bar{\varepsilon}_{ij} \quad . \tag{2.64}$$

The combination with the constitutive law from Eq. (2.56), under the consideration of $\{\varepsilon_{ij}\} = \bar{\varepsilon}_{ij}$, provides a relation between the volume average of the stress field and the volume average of strain field, based on the effective elasticity tensor (Eq. 2.65).

$$\{\sigma_{ij}\} = \bar{C}_{ijkl} \{\varepsilon_{kl}\} \tag{2.65}$$

In order to further decrease the number of unknowns in Eq. (2.65), the average strain theorem is used [15, 36]. It postulates that the average strain in V can be expressed by a given constant strain field $\bar{\varepsilon}^0_{ij}$ in terms of

$$u_i = \bar{\varepsilon}^0_{ij} x_j \quad \forall x_i \in \partial V \quad , \tag{2.66}$$

and it is defined by

$$\{\varepsilon_{ij}\} = \bar{\varepsilon}^0_{ij} \quad . \tag{2.67}$$

This implies that by a given constant boundary condition $\bar{\varepsilon}^0_{ij}$ on an arbitrary body, the average strain in the body $\{\varepsilon_{ij}\}$ is equal to the prescribed strain tensor $\bar{\varepsilon}^0_{ij}$. Consequently, using Eq. (2.67) in Eq. (2.65) provides the final equation for the determination of the effective stiffness tensor for a representative heterogeneous volume by

$$\bar{C}_{ijkl} = \frac{1}{V\bar{\varepsilon}^0_{kl}} \int_V \sigma_{ij}\, dV \quad , \tag{2.68}$$

expressed in terms of the volume average of the occurring stresses σ_{ij} due to a prescribed strain field $\bar{\varepsilon}^0_{ij}$. The finite element method can now be used to obtain the stress state of an inhomogeneous structure based on a defined deformation. It has to be mentioned that using the average stress theorem $\{\sigma_{ij}\} = \bar{\sigma}^0_{ij}$ [15,36], the effective stiffness tensor also can be determined by the occurring strains ε_{kl} due to an applied stress field $\bar{\sigma}^0_{ij}$. However, in this work only the approach discussed here will be used.

In order to fully determine $\bar{C}_{ijkl}$ by Eq. (2.68), six deformation modes are sufficient, due to the symmetry properties of the stiffness tensor. Thereby, only one component of the imposed strain tensor may be different from zero. By using the Voigt notation the six deformation modes are defined by

$$\bar{\boldsymbol{\varepsilon}}^0_{11} = \begin{Bmatrix} \alpha \\ 0 \\ 0 \\ 0 \\ 0 \\ 0 \end{Bmatrix} \quad , \bar{\boldsymbol{\varepsilon}}^0_{22} = \begin{Bmatrix} 0 \\ \alpha \\ 0 \\ 0 \\ 0 \\ 0 \end{Bmatrix} \quad , \bar{\boldsymbol{\varepsilon}}^0_{33} = \begin{Bmatrix} 0 \\ 0 \\ \alpha \\ 0 \\ 0 \\ 0 \end{Bmatrix} \quad , \tag{2.69}$$

$$\bar{\boldsymbol{\varepsilon}}^0_{23} = \begin{Bmatrix} 0 \\ 0 \\ 0 \\ 0 \\ \frac{\alpha}{2} \\ 0 \end{Bmatrix} \quad , \bar{\boldsymbol{\varepsilon}}^0_{13} = \begin{Bmatrix} 0 \\ 0 \\ 0 \\ 0 \\ 0 \\ \frac{\alpha}{2} \end{Bmatrix} \quad . \bar{\boldsymbol{\varepsilon}}^0_{12} = \begin{Bmatrix} 0 \\ 0 \\ 0 \\ \frac{\alpha}{2} \\ 0 \\ 0 \end{Bmatrix} \quad , \tag{2.70}$$

Here α is a scalar which reflects the magnitude of non zero strain components. Note, the curly brackets here relate to vectors based on the Voigt notation and do not refer to volume average.

An essential requirement to the representative structure, which will often be defined in terms of representative unit cells and denoted as representative volume element (RVE), is the periodicity. It implies that stress and strain fields between adjacent representative volumes must be compatible. In order to ensure this compatibility requirement for the homogenisation procedure, the boundary conditions of Eq. (2.63) have to be enhanced. This is realised by an additional periodic term u_i^p, which describes a deviation with respect to the linear displacement. Thus, boundary conditions ensuring a periodicity of the representative structure can be defined by

$$u_i = \bar{\varepsilon}_{ij} x_j + u_i^p \quad \forall x_i \in \partial V \quad . \tag{2.71}$$

The periodic displacement term will provide anti-periodic tractions and will not affect the average strain. In Fig. 2.10 periodic displacement boundary conditions are illustrated with respect to an imposed strain in $\bar{\varepsilon}_{22}$ direction. The representation of such boundary conditions in the numerical model will be described in Section 4.3.2 within the scope of the determination of effective material properties.

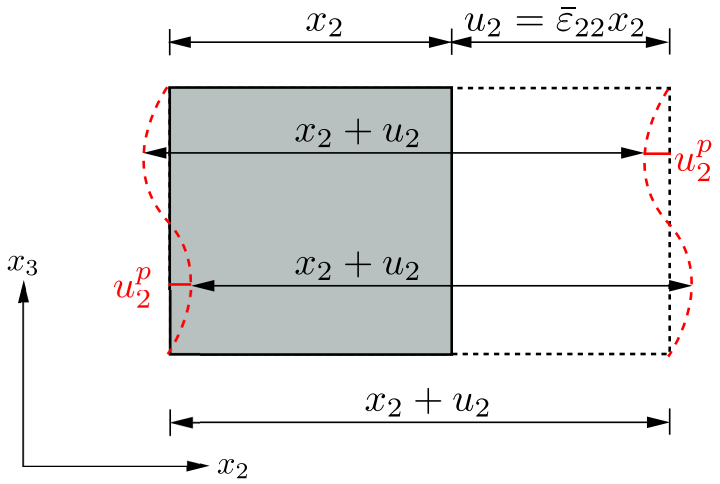

Figure 2.10: Example of periodic displacements boundary conditions for $\bar{\varepsilon}_{22}$.

In terms of using the finite element method an alternative approach can be used. Keeping linear displacement boundary conditions in combination with the consideration of an embedded representative structure, the periodicity condition can also be satisfied. However, the boundary of the additional surrounding representative structure must be sufficiently far away from the periodic boundary. This requirement will strongly affect the computational effort and is therefore only of restricted usability. Nevertheless, due to limitations of the used finite element code this approach is also applied and discussed in Section 4.3.2 for the determination of failure properties.

Using the finite element method, the occurring stresses in a heterogeneous structure, due to prescribed strain fields, can be determined for each element in each deformation mode. In addition, the respective volume of an element can be computed. Consequently, the effective constants of the elasticity tensor, according to Eq. (2.68), can be calculated by summation of the stresses over the domain dV for each deformation mode. Thereby the considered homogenisation domain must be representative and fulfil the length scale relation $l_1 \gg l_2$.

It has to be mentioned that the stress and volume evaluation in Eq. (2.68) by finite element analysis may depend on the element type used. This must be taken into account in particular for automatic homogenisation procedures. In order to be independent of the element type an alternative is shown in [10]. Based on the same homogenisation approach, the effective properties of a periodic heterogeneous structure are calculated by the occurring reaction forces. Nevertheless, if the same element type is used for the complete structure for the homogenisation, e.g. eight node hexahedron, this limitation disappears. Within this work this is ensured by using a voxel mesh, consisting of pure hexahedrons, for the representation of the heterogeneous structure in terms of homogenisation.

Chapter 3

Experimental Analysis of Wound Composites

Within this chapter the real filament wound tube structure is analysed from different point of views. Firstly, the base materials, epoxy resin and glass fibre, are investigated with respect to their mechanical properties. In the second section the demonstration component, made by these main materials by the filament winding procedure, is characterised. Thereby, the section is sub-divided in a geometrical and in a mechanical analysis. The first will present the results of Computer Tomography analyses. The latter will provide information about the mechanical behaviour in terms of static loading as well as the ability of energy dissipation during crash scenarios.

3.1 Individual Material Testing

The characterisation of the base materials, epoxy resin and glass fibre, constitutes an important role within this work. Based on the evaluated individual mechanical properties, different material models for the description of the complete component structure are supplied. Consequently, the method proposed in Chapter 4 is strongly influenced by these results.

3.1.1 Epoxy Resin

The used matrix system Epoxy Resin L1100 EPH294 consists of a standard laminate, adhesive resin combined with a low curing hardener of type EPH 294. All experiments related to the determination of the characteristics of the resin have been conducted in the frame of a collaboration by the University of Applied Science Mittelhessen [48]. Thereby, special tools and devices for the generation of appropriate resin specimens have been developed by this institute. Within this work two experimental series are used to characterise the mechanical properties of the resin: a tension and a compression test series. The evaluation of these experiments can be sub-divided in a primary and a secondary part. The first one is related to the data recorded directly by the test device and provided by the laboratory (force and displacement over time). The sec-

ond part is based on equations and optical evaluation procedures. The latter are derived quantities such as stress-strain relation and their determination is a part of this work.

Uniaxial Tension Tests

The tension tests are conducted on a standard measurement device (Zwick zwickiLine Z2.5, max. F=2.5 kN) with a velocity of v=0.001 m/s. During testing all specimens are unidirectionally loaded (y-direction) up to total failure. Thereby the occurring forces as well as displacements are recorded by the machine by a frequency of 500 Hz. In addition, each test is recorded by a camera in front of the specimen in order to provide high resolution images for a subsequent optical analysis. Also here a frame rate of 500 Hz is used. The data record frequency, machine and video, is related to the test velocity and is chosen to ensure sufficient number of data points for the respective quantities. However, it is also restricted by the control unit of each device.

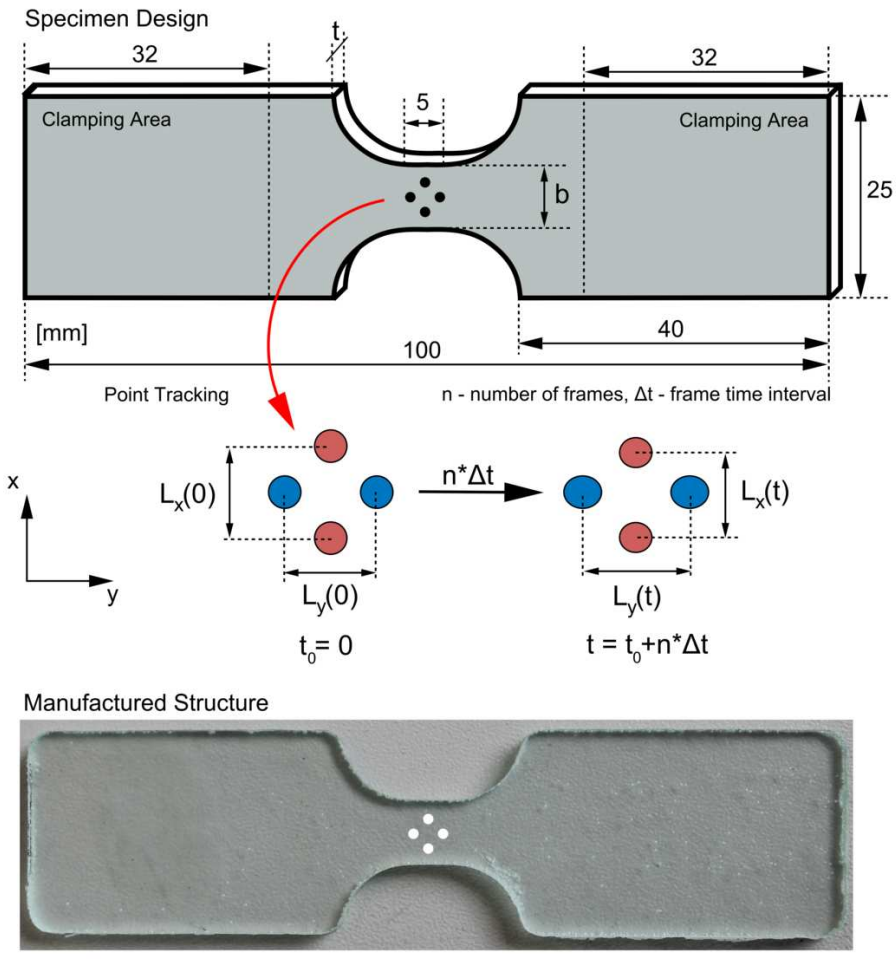

Figure 3.1: Specimen for uniaxial tension testing of resin (all dimensions in [mm]).

Specimen Identifier	t [mm]	b [mm]	A_0 [mm^2]
ZW-TE-L1100EPH294-102	2.49	8.00	19.92
ZW-TE-L1100EPH294-110	2.49	8.00	19.92
ZW-TE-L1100EPH294-111	2.48	8.00	19.84
ZW-TE-L1100EPH294-113	2.47	8.00	19.76
Mean Value	2.48	8.00	19.86

Table 3.1: Geometrical properties of the resin specimens for uniaxial tension tests.

The uniaxial tension test specimen geometry is shown in Fig. 3.1, where the upper part represents the design including dimension and the lower part shows one real manufactured and tested specimen. The geometrical properties of the four tested specimens are summarised in Table 3.1. Considering both illustrations, Fig. 3.1 shows that each specimen is equipped with a point pattern. This pattern is used for an optical post strain analysis based on the image records. By determining the distance L_x and L_y between two points for each frame, the occurring true strains ε_x and ε_y can directly be calculated over the time t by

$$\varepsilon_x(t) = \ln\left(\frac{L_x(t)}{L_x(0)}\right) \quad , \tag{3.1}$$

$$\varepsilon_y(t) = \ln\left(\frac{L_y(t)}{L_y(0)}\right) \quad . \tag{3.2}$$

Based on Eq.(3.1) and Eq. (3.2) the Poisson's ratio will be obtained over the the same time period by

$$\nu(t) = -\frac{\varepsilon_x(t)}{\varepsilon_y(t)} \quad . \tag{3.3}$$

Consequently, all of the quantities mentioned above are available as functions of the evaluated time. As example, the test ZW-TE-L1100EPH294-111 is considered here. In Fig. 3.2 on the left-hand side the optical strain evaluation is represented. It becomes apparent that the obtained strain values are significantly lower than the one which would be obtained based on the displacements captured by the test device. This indicates an influence by the testing environment and reveals the importance of an optical strain evaluation procedure. The corresponding Poisson's ratio over the time, including the mean value, is shown on the right-hand side of Fig. 3.2.

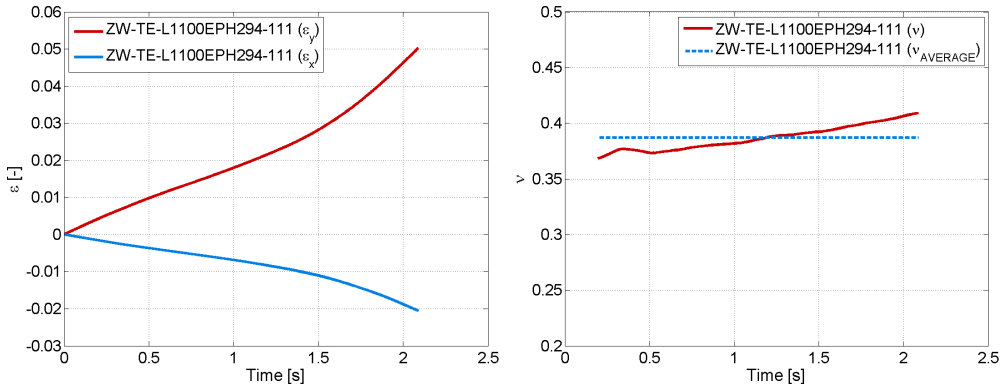

Figure 3.2: Example results for the optical strain and Poisson's ratio evaluation.

It can be seen that the Poisson's ratio is not constant during the complete test procedure. In addition a maximum deviation of about 17% is detected within the four tested samples (Table 3.2). In order to get one common constant value, firstly the mean value within one test is determined and finally the average over all tests is calculated.
Under the assumption of a homogeneous state of strain and an unrestricted deformation in the evaluation region, as well as an isotropic material behaviour, the initial cross-section $A(0)$, the Poisson ratio ν and the strain $\varepsilon_y(t)$ in loading direction can be used to calculate the current state of the cross-section $A(t)$ by

$$A(t) = A(0) \cdot e^{(-2\nu\varepsilon_y(t))} \quad . \tag{3.4}$$

The derivation of Eq. (3.4) is provided in the Appendix A. Dividing the measured force $F(t)$ in loading direction by the conjugated current cross-section yields to the Cauchy stress for the respective time (Eq.(3.5)).

$$\sigma(t) = \frac{F(t)}{A(t)} \tag{3.5}$$

The procedure mentioned above can be summarised in four steps, which are realised in a MATLAB procedure:

(1) Determination of mean value Poisson's ratio ν

(2) Evaluation of local strains $\varepsilon_y(t)$ in loading direction

(3) Calculation of effective cross-section $A(t)$

(4) Calculation of the Cauchy Stress $\sigma(t)$

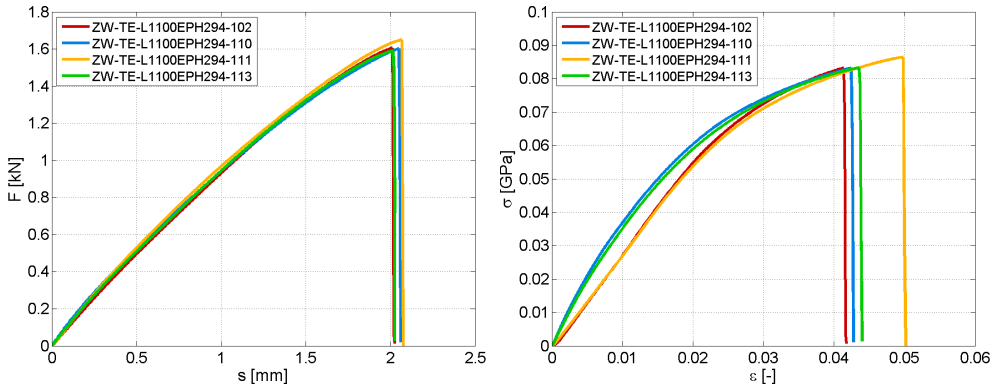

Figure 3.3: Results tension testing resin a) force-displacement b) stress-strain.

In Fig.3.3 on the left-hand side the primary results provided by the test device are represented in terms of force over displacement. A good repeatability over all conducted tests can be seen here. Also the very brittle behaviour of the resin becomes apparent. Additionally, the right-hand side of the same figure depicts the derived stress-strain relation based on the method described before for each of the four tests. Here, a higher scatter between the individual tests can be seen. This is related to the optical evaluation procedure. In contrast to the global displacement measurement by the machine, local effects are captured and environmental influences such as sliding at the fixation points are eliminated. Consequently, these results can be considered as more precise for the characterisation of a material. A closer consideration of the stress-strain curves shows that in particular the initial slope and the related stiffness differ. This may be caused by different local small air inclusions which could not be eliminated completely during the manufacturing process. However, with respect to the tensile failure strength R_t and the corresponding tensile failure strain $\varepsilon\,(R_t)$ a clear tendency can also be observed within these curves.

Specimen Identifier	E [GPa]	ν [-]	R_t [GPa]	$\varepsilon\,(R_t)$ [-]
ZW-TE-L1100EPH294-102	2.688	0.42	0.083	0.041
ZW-TE-L1100EPH294-110	3.324	n.a.	0.083	0.042
ZW-TE-L1100EPH294-111	2.721	0.39	0.086	0.050
ZW-TE-L1100EPH294-113	3.185	0.37	0.083	0.044
Mean Value	2.980	0.39	0.084	0.044

Table 3.2: Mechanical properties of the resin based on uniaxial tension tests.

In Table 3.2 the mechanical properties based on the optical evaluation in combination with Eq. (3.1-3.5) are summarised. The determination of the Young's modulus of each test is based on the global assumption of a linear elastic behaviour up to stress of 0.050 GPa, which can be observed in test ZW-TE-

L1100EPH294-111 and ZW-TE-L1100EPH294-102 here and also in the compression tests of the following section. Consequently, this limit is used for each Young's modulus calculation within the characterisation of the resin.
Finally, all determined values in case of tensile loading are averaged in the last line of Table 3.2. It has to be mentioned, that for calculating the mean values of ν only three test are available due to the failure of the point tracking in transverse direction (x) for test ZW-TE-L1100EPH294-110.

Uniaxial Compression Tests

The characterisation of the resin by uniaxial compression tests is part of the second series in the scope of material testing. The test device used, a screw press, is a development of the University of Applied Science Mittelhessen. The maximum force of this device is limited to F=20 kN by a maximum testing velocity of v=0.1 m/s. The machine is equipped with three piezoelectric load cells (between a massive steel bottom plate and the ground of the test device) and an electromagnetic measurement system to capture the displacements.

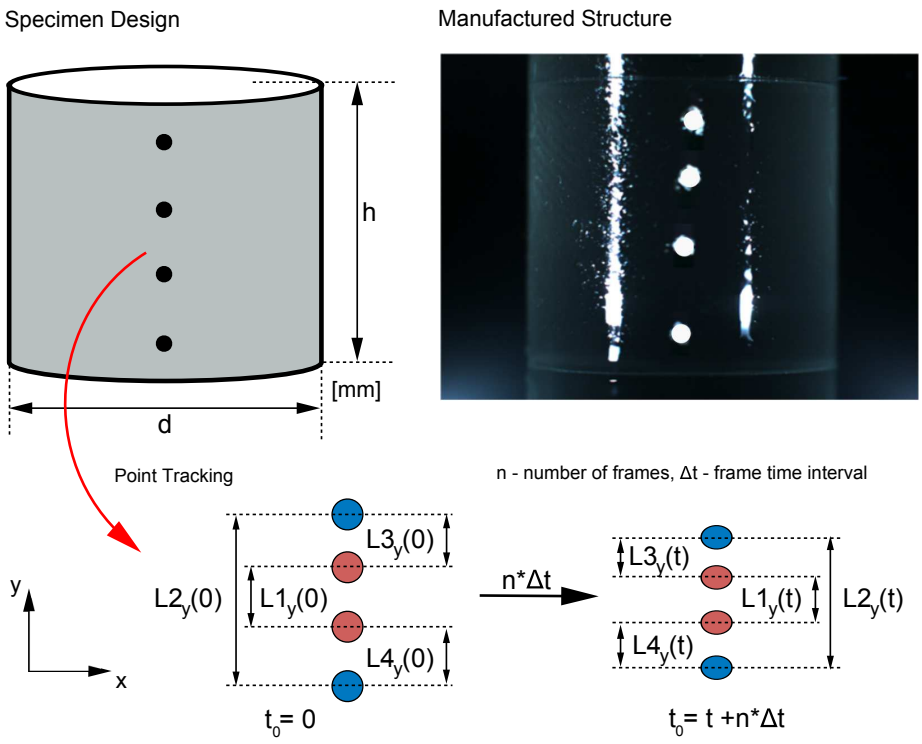

Figure 3.4: Specimen for uniaxial compression testing of resin.

The tests have been conducted on cylindrical specimens with a velocity of v=0.01 m/s. This implies an increase by ten times in comparison to the uniaxial tension tests and is related to the limitation of the control unit of the screw press, which is designed for a velocity range of 0.01-0.1 m/s. Since alternative testing devices have not been available and no significantly influence is expected for the considered range, the higher testing velocity for the compressive loading can be accepted.
During testing, the forces and displacements have been recorded by a frequency of 5000 Hz. Taking into account the testing velocity this implies an identical sampling rate in comparison to the tension tests. Also in this series each test has been captured by a high speed camera in front of the specimen. Here with a frame rate of 2000 Hz. Due to a more ductile behaviour of the resin in terms of compressive loading this frequency is appropriate to provide sufficient images for a post evaluation procedure. In Fig. 3.4 the design of the specimen as well as a real manufactured one is illustrated. Here, d and h represent the diameter and the height of the specimen, respectively. In total six samples have been tested and the individual geometrical properties are summarised in Table 3.3. It becomes apparent that d and h are almost identical. Consequently the slenderness ratio for the chosen specimen geometry is very small and the occurrence of buckling can be excluded.

Specimen Identifier	d [mm]	h [mm]	A_0 [mm^2]
SP-CO-L1100EPH294-130	15.77	15.10	195.32
SP-CO-L1100EPH294-131	15.77	15.08	195.32
SP-CO-L1100EPH294-132	15.72	15.02	194.09
SP-CO-L1100EPH294-133	15.91	15.17	198.81
SP-CO-L1100EPH294-134	15.74	15.00	194.58
SP-CO-L1100EPH294-135	15.81	15.04	196.32
Mean Value	15.79	15.07	195.74

Table 3.3: Geometrical properties of specimens for uniaxial compression resin tests.

In accordance with the tension tests, also in this series an optical evaluation procedure based on point tracking and Eq. (3.2) is conducted. Contrary to the tension tests the evaluation of the deformation in transverse direction (x direction) is not possible with the same procedure here. This is related to the cylindrical shape of the specimen and the resulting not existing flat plane view for the transverse direction. Consequently, only markers in loading direction are available for the point tracking and no information about the Poisson's ratio can be provided by this experiment. Thus, the value obtained by the tension test is used for the calculation of the current cross-section area by Eq. (3.4) in this test series. Also here a homogeneous state of strain is assumed and identical strains (ε_x=ε_z) perpendicular to the loading direction are postulated. In order to ensure an appropriate optical evaluation in loading direction, the occurrence of cambers of the specimen has to be avoided. Since this effect can

be related to the Poisson's ratio and the transverse forces at the contact surfaces due to friction, specimen and contact plates have been polished for this experiment. In addition this provides an unrestricted deformation of the specimen. In Fig. 3.5 six different states of deformation for test SP-CO-L1100EPH294-135 are depicted.

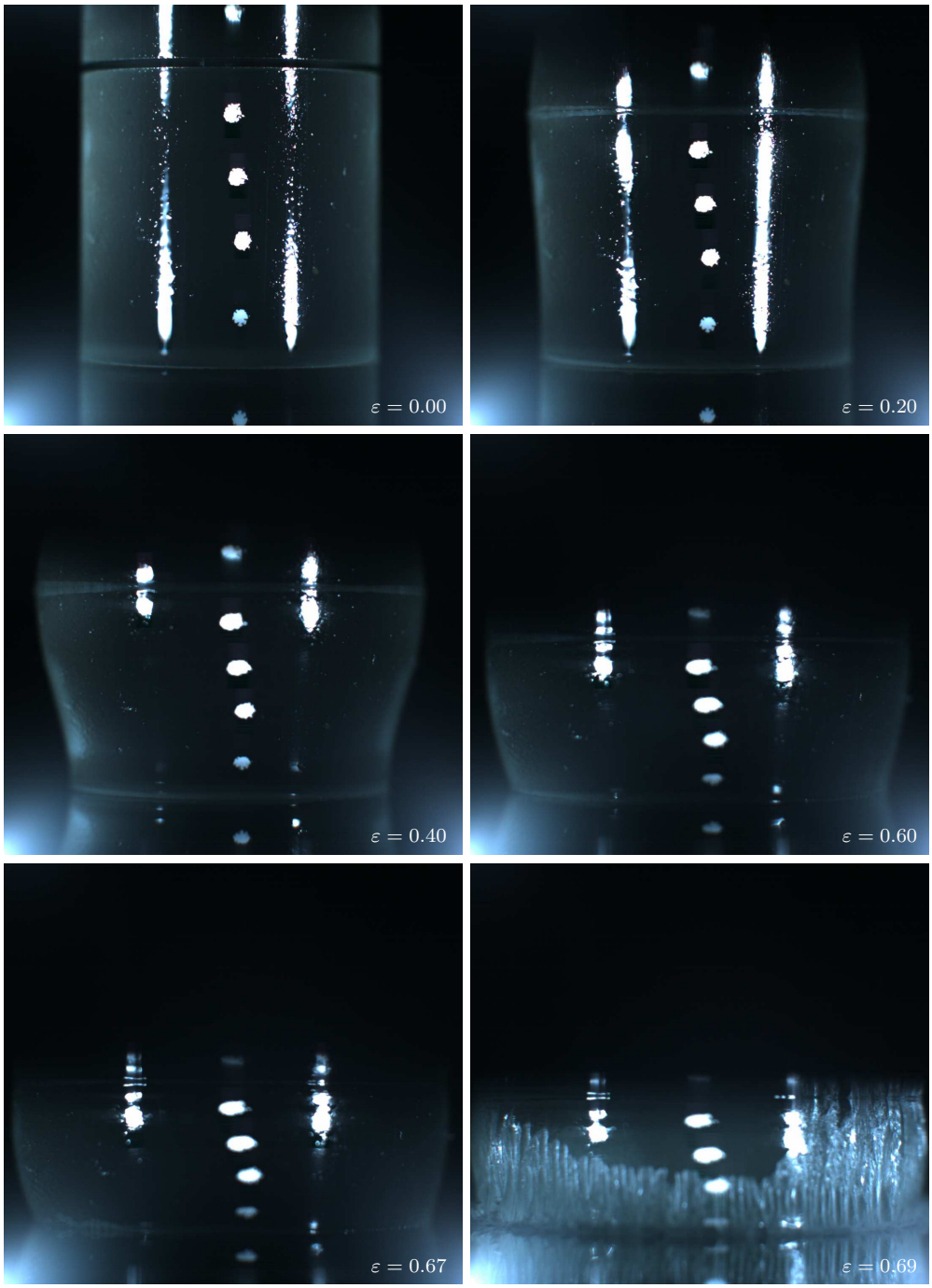

Figure 3.5: States of deformation for ε=0.00, ε=0.20, ε=0.40, ε=0.60, ε=0.67 and ε=0.69 for compression test SP-CO-L1100EPH294-135.

Considering the individual states between ε=0.20 and ε=0.60 shows that the camber effect cannot completely be avoided during the whole testing procedure. However, this is related to localisation effects and not to the one mentioned above. Since the effect remains small for the region of evaluation, the procedure used for the tension tests can be applied also in this load case.
In order to further quantify the influence of the localisation, the optical evaluation procedure has been conducted for different domains of the specimen (L1, L2, L3 and L4 from Fig. 3.4) for test SP-CO-L1100EPH294-135. The corresponding stress-strain relations are given in Fig. 3.6 in which the stresses have been determined in exact the same manner done for the tension tests.

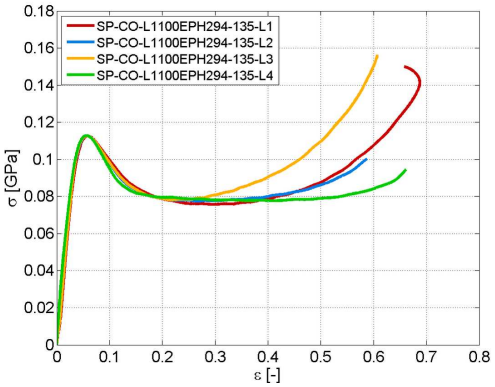

Figure 3.6: Stress-strain relation for test SP-CO-L1100EPH294-135 for evaluation domains L1, L2, L3 and L4.

The dependency of the evaluation domain becomes directly apparent within this diagram. A stiffer response can be observed for the top domain (L3) and a softer behaviour for the bottom (L4) which emphasises a non-homogeneous state of strain for the complete specimen under the given loading condition. However, it is also visible that the evaluation of the domains L1 and L2 give almost identical results and additionally represent a mean value over all considered domains. Therefore it is assumed for this work that an average homogeneous state of strain can be represented by the domain L1 or L2. In addition, it has to be mentioned that for domains including the bottom point (L2, L4) a reduced evaluation period occurs. This is related to the fail of the point tracking procedure based on a strong change of lightening conditions at the bottom point in terms of high deformation. As a consequence the optical evaluation procedure is conducted for domain L1 for all compression tests.
Considering finally the last state of deformation in Fig. 3.5 shows the failure of the specimen in terms of uniaxial compression. Under the assumption of a homogeneous state of strain the associated strength can be addressed to the compressive strength R_c and $\varepsilon\,(R_c)$ to the corresponding compressive failure strain.

In the following Fig. 3.7 the results obtained by the compression test series are represented, again sub-divided in primary and secondary results. On the left-hand side of Fig.3.7 the force-displacement relation based on the machine data is shown. The diagram on the right-hand side illustrates the Cauchy stresses over true strains based on optical evaluation for the L1 domain as well as Eq. (3.5) and Eq. (3.2).

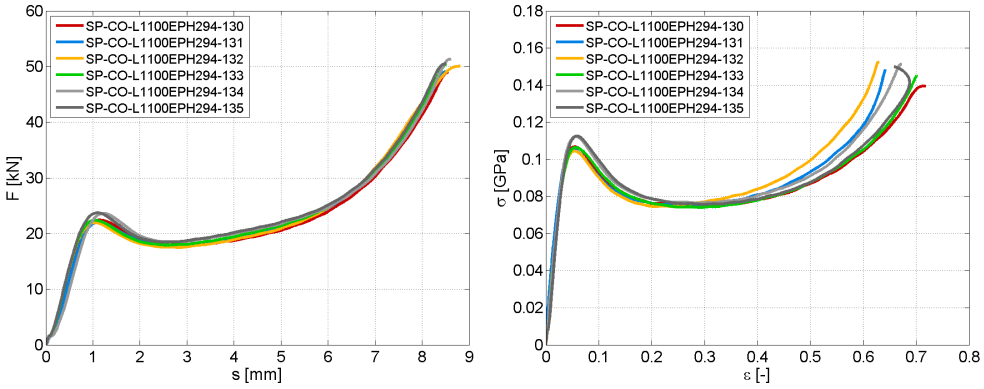

Figure 3.7: Results compression testing resin: force-displacement and stress-strain relation.

It is obviously, that this test series shows also a good repeatability in case of the force-displacement behaviour. However, an increase of the scatter for the stress-strain relation is visible for higher strains. In particular variations of the final failure stress and strain appear. This is again caused by capturing local effects in terms of an optical evaluation procedure as mentioned in the tension test section. In addition here, the results may also be impacted by another issue. Due to the larger specimen size and the corresponding volume, the probability of more influential inhomogeneities is higher in the compression tests than in the tension experiments. Finally, the mechanical properties derived by this series are summarised in Table 3.4 where again in the last row the mean values are given.

Specimen Identifier	E [GPa]	ν [-]	R_c [GPa]	$\varepsilon\,(R_c)$ [-]
SP-CO-L1100EPH294-130	3.372	n.a	0.139	0.71
SP-CO-L1100EPH294-131	3.876	n.a	0.148	0.64
SP-CO-L1100EPH294-132	3.009	n.a	0.152	0.63
SP-CO-L1100EPH294-133	3.261	n.a	0.145	0.70
SP-CO-L1100EPH294-134	3.212	n.a	0.151	0.67
SP-CO-L1100EPH294-135	2.872	n.a	0.140	0.69
Mean value	3.267	n.a	0.146	0.67

Table 3.4: Mechanical properties of the resin based on uniaxial compression tests.

Comparison of the compression and tension results in absolute values in a single stress-strain diagram (Fig. 3.8) shows that the initial slope of all curves for both loading conditions is very similar. In addition the summaries in Table 3.2 and Table 3.4, respectively, show that the scatter for the Young's modulus is within the same range. Apart from one test in compression all values are in the range of about 2.7-3.4 GPa. Generating the average over all conducted tests provides a mean value of 3.152 GPa. Finally, all obtained mechanical properties based on the static testing series are represented in Table 3.5.

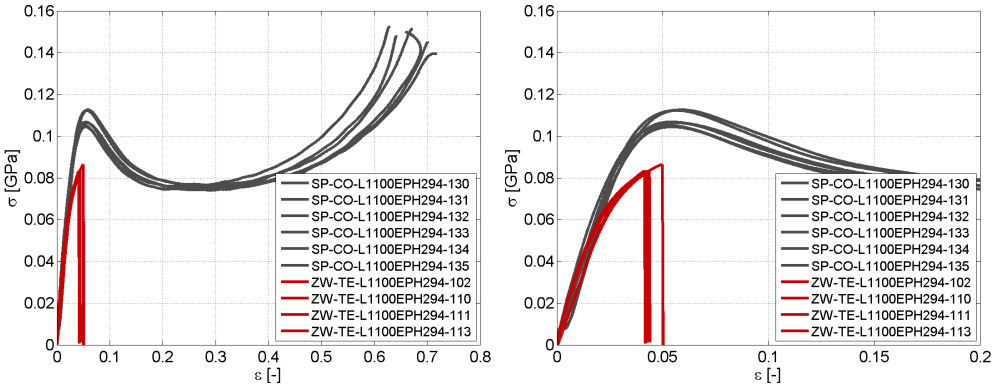

Figure 3.8: Comparison of the stress-strain relations for tension and compression test series for two different abscissa ranges.

Epoxy Resin L1100 EPH294			
Density	ρ	1.34e-6	[kg/mm^3]
Poisson's Ratio	ν	0.39	[-]
Young's Modulus	E	3.152	[GPa]
Tensile Strength	R_t	0.084	[GPa]
Compressive Strength	R_c	0.146	[GPa]
Tensile Failure Strain	$\varepsilon\,(R_t)$	0.042	[-]
Compressive Failure Strain	$\varepsilon\,(R_c)$	0.670	[-]

Table 3.5: Summary of the mechanical properties of the epoxy resin L1100 EPH294.

It has to be mentioned, that also a high dynamic test series for both experimental configuration has been conducted. However, the result quality obtained in these tests was not sufficient to generate any additional benefit for the mechanical characterisation of the epoxy resin. In particular the occurrence of high oscillations is responsible for the lack of quality in these tests. Therefore the behaviour under dynamic loading is not further considered and consequently no strain rate dependency for the resin is taken into account within this work.

3.1.2 Glass Fibre

In contrast to the epoxy resin, the testing of pure single glass filaments is a more complex procedure. Due to the very small size of a filament, the testing procedure is a challenging task and special devices are needed. In particular the determination of the occurring local strains and strengths under a given load are very difficult. As a consequence no experiments have been conducted for the determination of mechanical properties for glass fibres. Instead the properties provided by the manufacturer are used within this work. The considered filament wound tube consists of glass fibre of the type E-Glass EC 1200-315 whose main data are summarised in Table 3.6.

E-Glass EC 1200-315			
Density	ρ	2.54e-6	[kg/mm^3]
Poisson's Ratio	ν	0.25	[-]
Young's Modulus	E	75	[GPa]
Tensile Strength	R_t	1.141	[GPa]
Filament Diameter	d_F	0.017	[mm]
Yarn Count (Roving)	$-$	1200	[tex]
Number of Filaments (Roving)*	n_F	2081	[-]

Table 3.6: Mechanical properties E-Glass EC 1200-315 based on manufacturer data sheet [92], *number of filaments calculated based on yarn count, density and single filament diameter.

3.2 Component Testing of Tubes

3.2.1 Geometrical Characterisation

The geometrical characterisation of the real tube structure from Fig. 1.1 constitutes a major role within this work, since these data will provide a base for the assessment of the numerical results in terms of the fibre placements. In order to capture as much as possible geometrical information, this investigation has been conducted by Computer Tomography (CT). In the considered case the sample has been scanned by a v|tome|x L 450 CT within a collaboration with the Technical University Dresden by two different resolutions. The subsequent evaluation of the raw data has been conducted as a part of this work and is presented in the following illustrations. The first CT analysis is applied to the complete tube structure and represents a voxel size resolution of L_{xyz}=0.025 mm. In Fig. 3.9 this CT record is depicted after the evaluation procedure. As can be seen in the figure a global overview of the placement of the individual roving is provided by this analysis. In addition, the occurring local undulation of the single rovings can be captured as well.

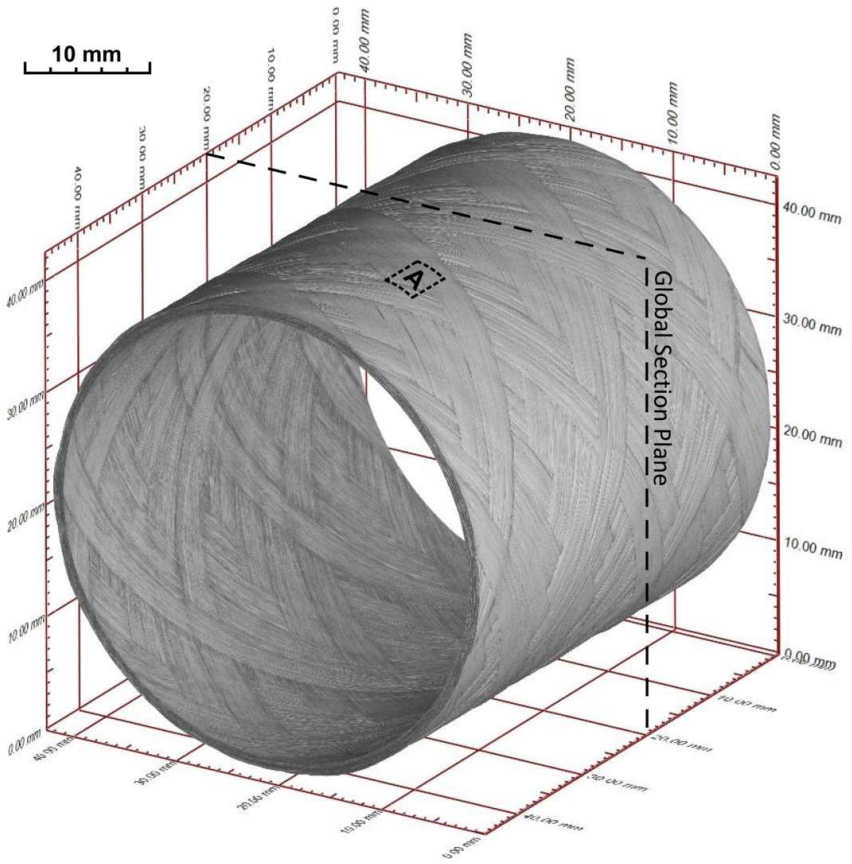

Figure 3.9: CT record of complete component (filament wound tube specimen for dynamic testing).

Furthermore the illustration is equipped with a scale raster in order to give a classification with respect to the dimensions of the component sample. A second analysis of the first record is depicted in Fig. 3.10. It represents the upper part from a section cut perpendicular to the global section plane illustrated in Fig. 3.9.

Figure 3.10: CT record of complete component (filament wound tube specimen for dynamic testing) - section cut upper part.

Here, the white pixels present the pure epoxy resin and the grey-scaled a mixture of the glass fibre and resin. In contrast to the other images in this case the rendering settings for the fibre-matrix differentiation were changed for a better visibility. It can be directly seen that the chosen resolution it not well suited to provide sufficient information of the individual rovings. However, it shows that the used winding pattern will lead to a variation of the outer radius of the component, whereas the inner radius remains constant due to the smooth mandrel surface. In addition, this figure gives a first impression about the layer stack of the individual rovings. In order to get more detailed information about the roving shape itself, the second CT scan has been performed with a higher resolution (L_{xyz}=0.005 mm). However, due to limitations by data size and recording time the observed domain has been reduced to a smaller sub-domain A (see Fig. 3.9).

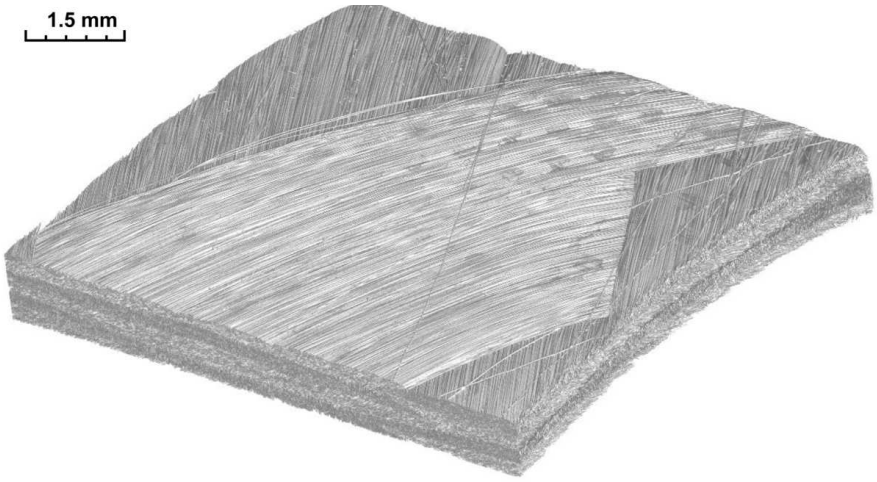

Figure 3.11: CT record of detailed sub-domain A (1) - global view.

Thereby, the condition of representing a main undulation point was taken into account. The chosen sub-domain A is illustrated in Fig. 3.11. It has to be mentioned here, that due to costs restrictions only one sub-domain could be investigated within this work. It can directly be seen that within this high resolution record even single filaments of the glass roving (d=0.017 mm) can be captured. In order to get additional appropriate information about the roving shape, a certain number of cuts perpendicular to the roving longitudinal axis have been applied to the existing sub-domain A. The result of this evaluation is shown in Fig. 3.12. Here, the layer stack of the composite structure becomes apparent. Although the component was manufactured by only two layers a stack up to five layers can be observed in the illustration. This is related to the permanent occurring undulation due to the chosen winding pattern.

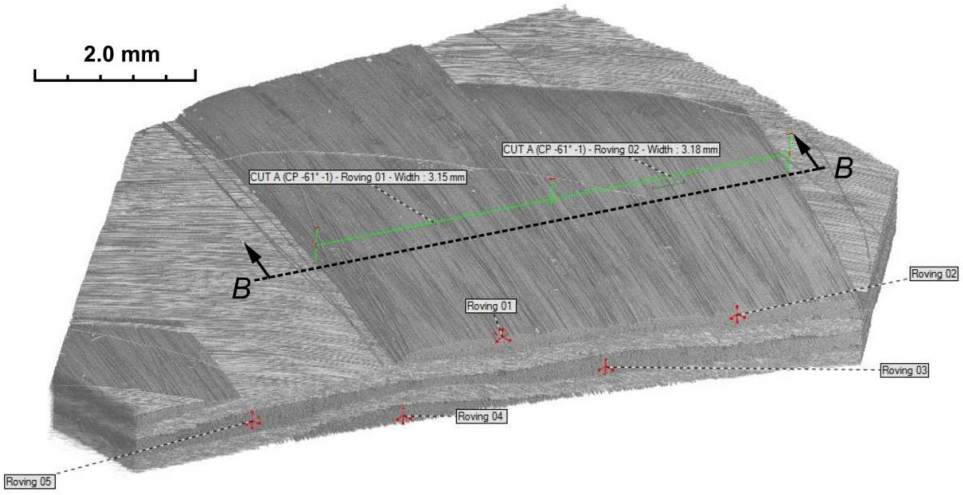

Figure 3.12: CT record of detailed sub-domain A (2) - cut off perpendicular to individual roving directions.

Applying an additional section cut to the existing sub-domain A at position B-B (perpendicular to the roving axis) provides Fig. 3.13. Here, opposed to Fig. 3.10 the resin is represented by black colour whereas the filaments possess grey colour values. This section cut constitutes the base for a detailed analysis of the individual roving shapes. Therefore, the orthogonal cut rovings have been measured with respect to their width and height. It has to be mentioned, that only the top and the middle layer of the stack are appropriate candidates for the evaluation of the roving shapes, since all other rovings are not cut orthogonally to their longitudinal axis in this record. An average roving height of h=0.28 mm and average roving width of b=3.17 mm are determined by this record. It is obviously that this number of values cannot be considered as representative for the complete existing component structure. However, due to the limited number of available sub-domain CT records within this work, it will be assumed that these values are representative. At least an analysis of additional section cuts in sub-domain A has shown that the shape, width and height remain nearly constant in longitudinal roving axis. Considering finally

the shape of the individual rovings, reveals some differences in height and width in the various layers. This is mainly related to compression and friction effects caused by the manufacturing process. In particular the bottom layer of the stack shows a lower height in comparison to the other ones. However, a non-ambiguous tendency cannot be detected within this one record. It can only be seen that all rovings in orthogonal direction may fit approximately an elliptical shape.

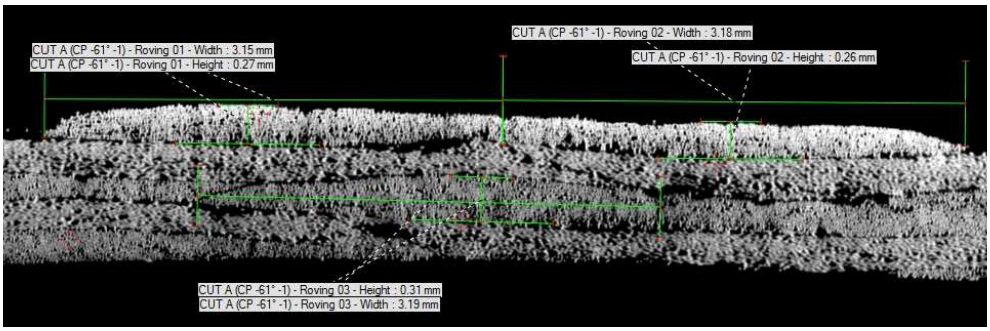

Figure 3.13: CT record of detailed sub-domain A (3) - section cut B-B.

3.2.2 Fibre Volume Content

The stiffness and strength of fibre reinforced composites are directly related to the fibre volume content. In order to get a high accuracy for this important value, the CT records from Section 3.2.1 are used. The determination of the fibre volume content has been conducted for different scales: micro- and meso-scale. Therefore, the sub-domain A is sub-divided in a number of section cuts in the global direction of the tube. Each generated section cut is stored in an individual picture, which is subsequently evaluated by an image analysing script, written in MATLAB, for a prescribed area. Within this program a pixel is converted into 8 bit grey-scale value (0-255) and subsequently evaluated with respect to a defined threshold. Pixels having a value over the threshold are set to a constant grey value and assigned as fibre. All other pixels are automatically identified as matrix and represented by pure black colour. The percentage of fibre pixels with respect to all pixels of the selected area represents the fibre volume content. In this work 130 section cuts have been created in order to determine the fibre volume content on micro-scale and meso-scale, respectively. In the upper row of Fig. 3.14 an example for the evaluation of one image is shown. Here, on the left-hand side the source image is depicted and on the right-hand side the converted one. The boxes represent the chosen area before and after the analysis, respectively. Since this domain covers almost the complete width and height of the component structure, it will represent a value for the meso-scale. In addition the lower row of Fig. 3.14 illustrates the same scenario for the micro-scale analysis. The only difference between the procedures is the size of the evaluation box, which is much smaller here.
Applying the algorithm to all extracted images provides the fibre volume contribution shown in Fig. 3.15 on the left- and right-hand side, respectively. The

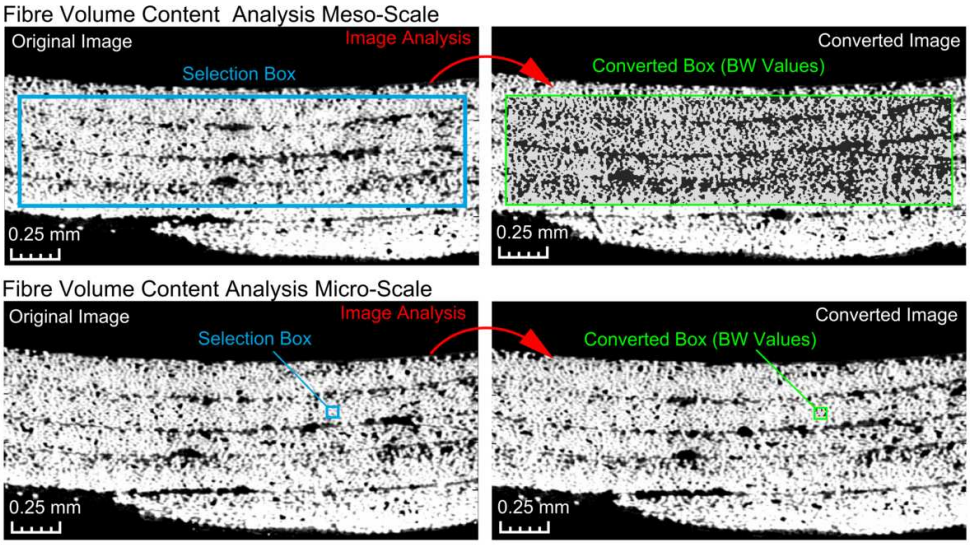

Figure 3.14: Fibre volume content (v_f) image analysis on meso- and micro-scale.

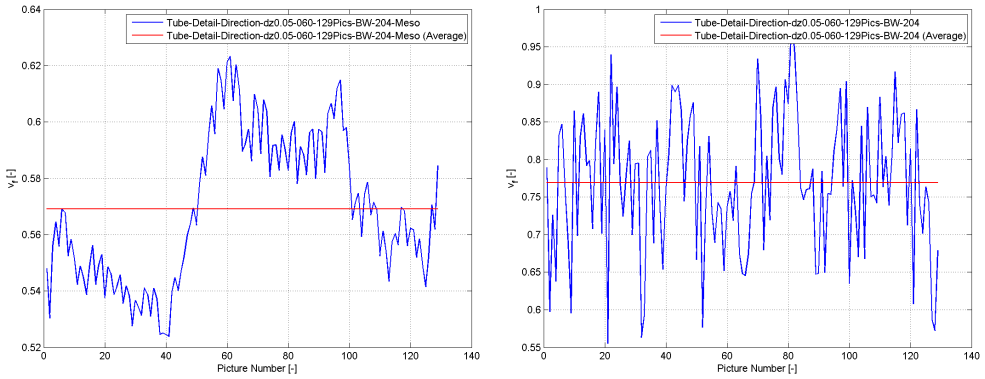

Figure 3.15: Fibre volume content (v_f) distribution on meso-scale (lhs) and micro-scale (rhs).

diagram reveals directly that the fibre volume content, which is assigned to the ordinate in the diagram, changes with respect to the evaluated image, which is assigned to the abscissa. Furthermore a stronger scatter can be observed in terms of the meso-scale analysis. This is related to locally occurring resin mould cavities, which are also captured by the analysis. In order to get appropriate values for the fibre volume content of each scale, a mean value of each graph is calculated.

In order to prove the quality of the applied method, a second export and analysis of the same area with different rendering settings have been conducted. Both evaluation results and the corresponding average values are summarised in Table 3.7. In addition, Table 3.7 contains a value for the fibre volume content determined by a different experiment. Within the scope of the investigation of the mechanical behaviour of the component under static loading, described

in the following section, also a global fibre volume content determination has been conducted for one specimen. Here, the weight of the component has been recorded before and after a matrix combustion procedure. In combination with the known individual densities as well as the masses, the fibre volume content has been determined. Comparing the results of both methods provides a good correlation between the different approaches. This proves the accuracy of the applied method for the determination of the fibre volume content by image analysis based on CT records. In addition, Table 3.7 shows the benefit of the CT analysis, where in contrary to the combustion analysis, fibre volume content values for different scales can be provided.

Fibre Volume Content v_f	Micro Scale	Meso Scale
CT Export Analysis Configuration A	0.769	0.569
CT Export Analysis Configuration B	0.776	0.578
CT Export Analysis Mean Value A,B	0.773	0.574
Combustion Analysis	n/a	0.586

Table 3.7: Summary v_f values - configuration A and B based on method shown in Fig. 3.14.

3.2.3 Static Testing

In this section the manufactured composite structure is analysed in the case of static loading. As a consequence of a very slow velocity such tests are often called quasi-static. Here the behaviour of the component for compression and tension with a velocity v=2 mm/min is considered. All experiments have been conducted on a standard measurement device (Zwick 1475, max. F=100 kN) and have been performed at the Technical University Dresden within a joint research project in 2009. During this test series all specimens have been loaded up to a total failure of the composite structure. Thereby the forces and displacements have been recorded by the machine in a frequency of 1 Hz. All of the used specimens belong to the first manufactured charge of components.In contrast to the specimens for the dynamic tests this charge possess a reinforcement in the load transmission domain (four layers instead of two layers). This procedure is necessary in order to prevent localisation effects within the fixation range. Each of the investigated specimens has a total height of 250 mm which can be sub-divided into two domains: the clamping domain and the characteristic test length.

Figure 3.16: Example of specimen for static component tests.

Taking into account a length of 50 mm for each clamping domain, the remaining characteristic height is h_0=150 mm. In Fig. 3.16 the final shape of one component for the static tension and compression tests is illustrated. As can be seen in Fig. 3.16 the outer shape of the testing domain varies. Based on a constant inner diameter d_1=39.87 mm (no differences in mandrel diameter) in combination with an average outer diameter, d_2, of all specimens, an average thickness t=1.14 mm can be calculated. The summary of all measured and derived geometrical data is shown in Table 3.8. It also points out the remarkable differences of the outer diameter d_2. The lowest value amounts to 41.87 mm, the highest one to 42.78 mm. With respect to the average thickness this implies a local maximum deviation of about 30%. This is mainly related to the necessary reinforcements at the end of the specimen and the corresponding difficulties for the manufacturing process in the transition zones.

Specimen Identifier	d_1 [mm]	d_2 [mm]	t [mm]	A_0 [mm^2]	h_0 [mm]
ZW-CO-GRP-001	39.87	42.78	1.46	188.90	150.00
ZW-CO-GRP-004	39.87	42.30	1.22	156.82	150.00
ZW-CO-GRP-009	39.87	41.98	1.06	135.64	150.00
ZW-CO-GRP-011	39.87	41.92	1.03	131.69	150.00
ZW-TE-GRP-002	39.87	42.43	1.28	165.47	150.00
ZW-TE-GRP-006	39.87	41.92	1.03	131.69	150.00
ZW-TE-GRP-007	39.87	41.87	1.00	128.40	150.00
ZW-TE-GRP-008	39.87	41.93	1.03	132.35	150.00
Mean Value	39.87	42.14	1.14	146.37	150.00

Table 3.8: Geometrical properties of specimens for static compression and tension component tests.

The measured quantities of the quasi-static test series are represented in Fig. 3.17 and in Fig. 3.18, respectively. In the left diagram of Fig. 3.17 the results for the compression tests are shown, in the right one those for the tension. In Fig. 3.18 a comparison between both load cases is illustrated. In all diagrams the forces are depicted with respect to the displacements. It can be observed that the behaviour of the composite structure is very similar for the different load cases in the first phase. All tests show nearly the same initial slope which refers to an identical initial stiffness under both loading conditions. Since the stiffness is mainly provided by the fibres this indicates that the local deviation in thickness is due to matrix variation and the relevant fibres are not varying. A significant difference between the load cases can be detected for a force level greater than about F=5 kN. In terms of compressive loading, the force level further increases and the failure of the complete structure abruptly occurs by reaching the maximum force. Under tensile loading the force level slightly decreases by a strong increase of the displacements up to the total failure. Consequently, the maximum occurring force is less in tension than in compression. However, the maximum displacement is significantly higher for tensile loading,

which refers to a more ductile answer of the composite structure, here. The differences in the behaviour of the components in the second phase are related to the appearing fracture modes due to the loading condition. As mentioned in Chapter 1 various fracture modes can occur within a composite structure. Based on the observed phenomena following hypothesis is given. The sudden total failure of the structure is related to an inter fibre fracture of matrix under compressive loading [47]. In contrary, the degradation of the structure under shear loading and the inter fibre failure under tension is responsible for the behaviour under tension loading [47]. In addition, it seems that a load redistribution to the fibres occurs and finally a fibre failure leads to the complete failure of the structure.

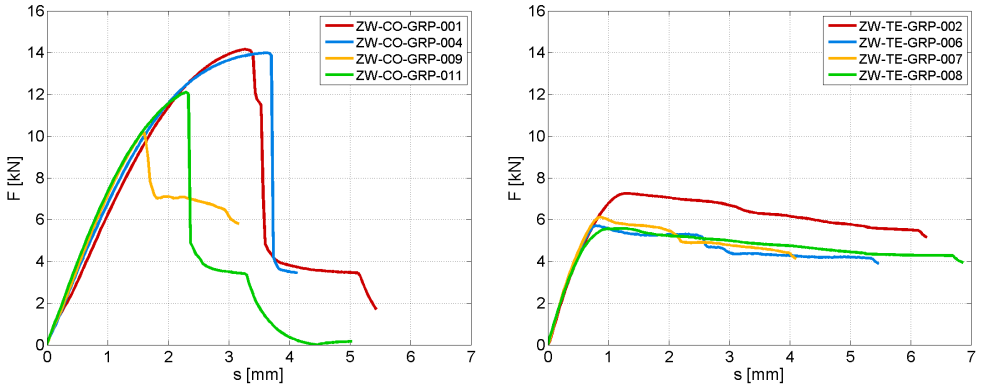

Figure 3.17: Force-displacement diagrams for a) static compression and b) tension tests of wound tube component.

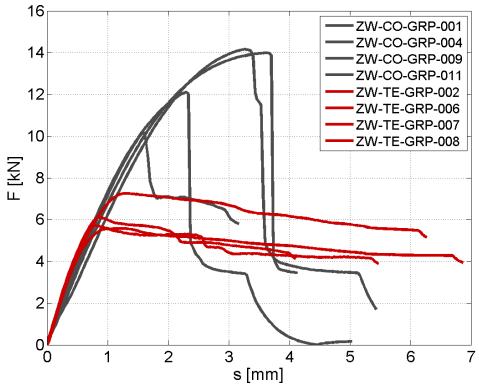

Figure 3.18: Comparison of static compression and tension tests of wound tube component.

A further examination of the individual tests points out a wide scatter of the results. In particular a strong divergence for the ultimate failure can be observed in both load cases. Taking into account the geometrical properties of the specimens from Table 3.8 the relation between thickness and maximum force becomes apparent. As mentioned above the difference in geometry is caused by the special manufacturing procedure for the clamping domains. Despite scattering due to failure these experiments provide a sufficient base for the assessment of the structure concerning its global stiffness and failure in terms of static loading. In addition the study foregrounds the influence of the geometrical properties to the failure of the component.

3.2.4 Impact Testing

In case of high dynamic loading the interaction of various failure modes is more complex as discussed in Section 1.2. To capture these effects and to demonstrate the potential of composite materials regarding their energy dissipation, impact tests have been performed. In order to ensure a sufficient energy transmission, a drop tower facility has been used whose general setup and design is illustrated in Fig. 3.19.

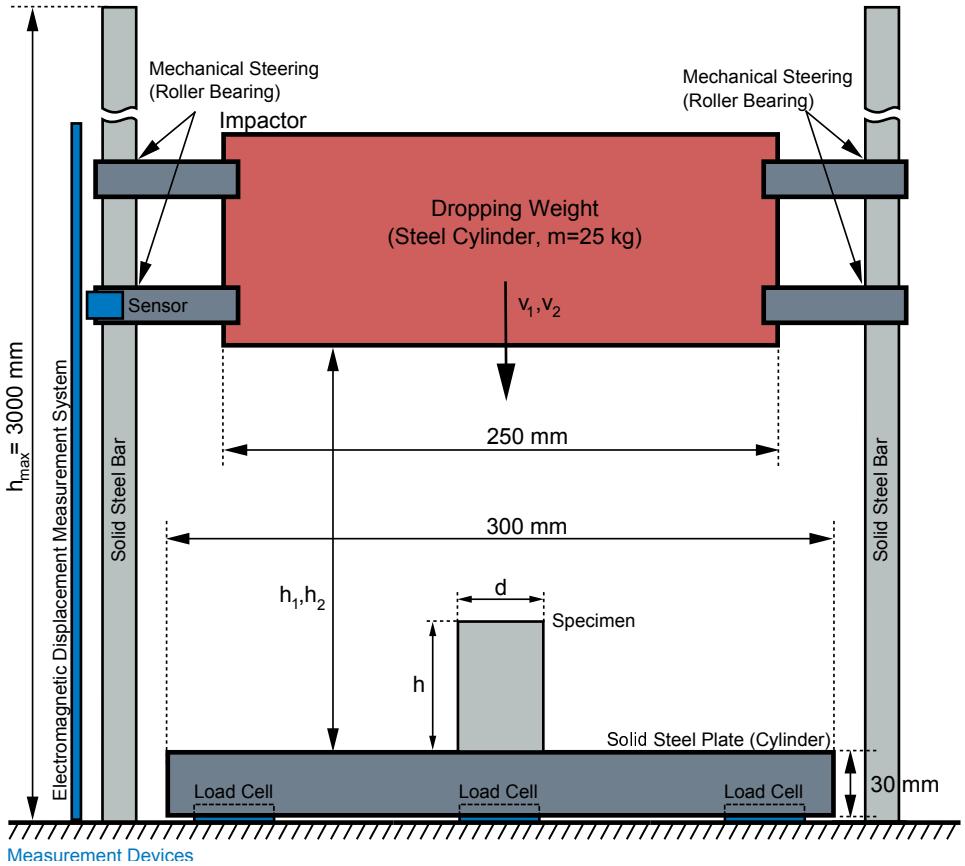

Figure 3.19: Test setup for dynamic component tests.

It is equipped with a dropping weight, three piezoelectric load cells and an electromagnetic displacements measurement system. The load cells are located between a massive steel bottom plate and the ground of the test device. The displacements are captured by a permanent magnet located on the dropping weight in combination with a mounted bar at the side of the drop tower construction. Both, loads and displacements, have been measured with a frequency of 500 kHz. In addition all tests have been recorded by a high speed camera (15000 frames per second) in front of the region of interest. Finally, a semiconductor light source in form of a LED has been installed within the specimen to improve the high speed record quality.

The specimens for the impact tests have been additionally generated and prepared in a second manufacturing series. In comparison to the static component tests a reinforcement for the load transmission domain is not necessary in this case. All specimens have a height of h=60.5 mm and a special preparation of the load transmission zone (45°chamfer). Both have been chosen in order to impose a crushing deformation and avoid buckling. The shape of one specimen is shown in Fig. 3.20. It has to be mentioned, that the chamfer has been introduced manually and could not been investigated in detail. Consequently, a possible deviation of the tested specimen with respect to this geometrical property cannot be excluded.

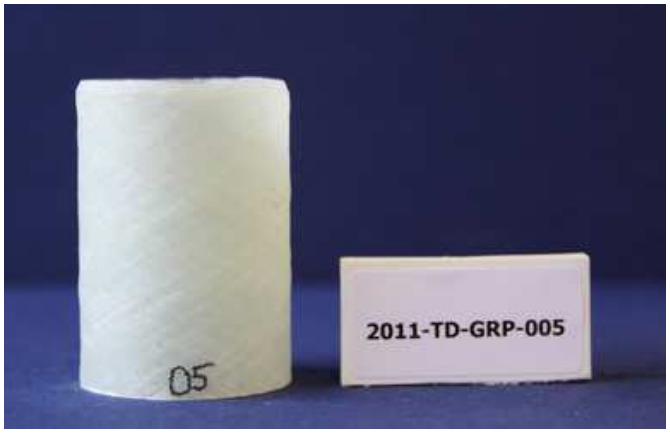

Figure 3.20: Example specimen for dynamic component tests.

Considering Fig. 3.20 more detailed also reveals the variation of the outer shape of the component. Comparison of all original unloaded specimens has shown a variation of the outer diameter at the top from 41.80 mm to 42.10 mm and at the bottom from 41.80 mm to 42.20 mm. The average amounts to 41.98 mm and 42.02 mm, respectively. Due to a constant diameter of the mandrel, the inner diameter shows no divergence (40.00 mm). This implies an average thickness of the component at the top of 0.99 mm and the bottom of 1.00 mm. In Table 3.9 all geometrical properties of the investigated specimens are summarised. Here d_1 and d_2 represent the evaluated inner and outer diameter at the top of each sample and d_3, d_4 at the bottom. Furthermore t_t and t_b refer to the thickness at the measured location (top and bottom).

Specimen Identifier	d_1 [mm]	d_2 [mm]	t_t [mm]	d_3 [mm]	d_4 [mm]	t_b [mm]	h [mm]
TD-GRP-002	40.00	42.10	1.05	40.00	42.00	1.00	60.50
TD-GRP-003	40.00	41.90	0.95	40.00	42.10	1.05	60.50
TD-GRP-004	40.00	41.80	0.90	40.00	41.80	0.90	60.50
TD-GRP-005	40.00	42.10	1.05	40.00	41.90	0.95	60.50
TD-GRP-006	40.00	41.95	0.98	40.00	42.20	1.10	60.50
TD-GRP-007	40.00	42.00	1.00	40.00	41.90	0.95	60.50
TD-GRP-008	40.00	42.00	1.00	40.00	42.00	1.00	60.50
TD-GRP-010	40.00	42.00	1.00	40.00	42.10	1.05	60.50
Mean Value	40.00	41.98	0.99	40.00	42.00	1.00	60.50

Table 3.9: Geometrical properties of specimens for dynamic impact component tests.

The impact tests have been performed with a constant mass of the dropping weight (m=25.0 kg) and two different dropping heights h with respect to the bottom plate (h_1=1500 mm, h_2=2000 mm). Taking into account the height of the specimen this implies an impact velocity of v_1=5.31 m/s and v_2=6.17 m/s, respectively. During the tests the forces at the ground plate and the displacements of the impactor in loading direction have been recorded. In the following the results are discussed for one test in detail. However, most of the given statements are also valid for all other results of the conducted test series.

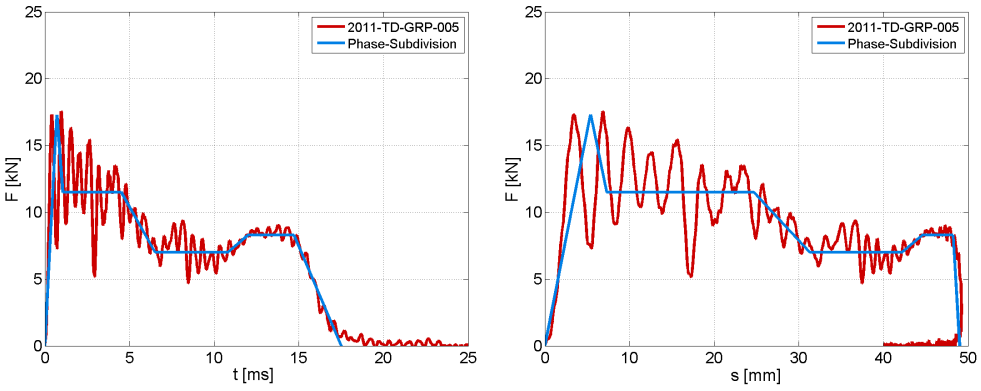

Figure 3.21: Results specimen TD-GRP-005 for dynamic component test.

In Fig. 3.21 the occurring forces with respect to time and displacements, respectively, are depicted for specimen TD-GRP-005. The corresponding velocity is v_1. Consideration of the graphical representation on the left-hand side of the figure permits the subdivision of the curve in five main phases. Firstly, a high peak of the force can be observed (phase (1)), followed by a subsequent constant lower level of the force (phase (2)). In the next phase (phase (3)) the force strongly decreases again, to remain constant for the following time (phase (4)). In the last section (phase (5)) the force slightly increases to a constant

level and finally decreases to zero. The five phases have been adapted to the displacements and are represented with respect to the force on the right-hand side of Fig. 3.21 as well. In summary the five phases can be delineated as follows:

Phase (1):	0.00 ms	-	1.05 ms
Phase (2):	1.05 ms	-	4.50 ms
Phase (3):	4.50 ms	-	6.50 ms
Phase (4):	6.50 ms	-	10.80 ms
Phase (5):	10.80 ms	-	17.50 ms

In order to investigate the reason for the existing characteristics of the individual curves and the related deviation to a perfect energy dissipation the corresponding states of deformation are considered. Hence, Fig. 3.22-3.31 represent an extraction of the high speed record, also here for the test TD-GRP-005. The time interval Δt between the shown states is 1 ms. Studying the single states, following effects can be observed.

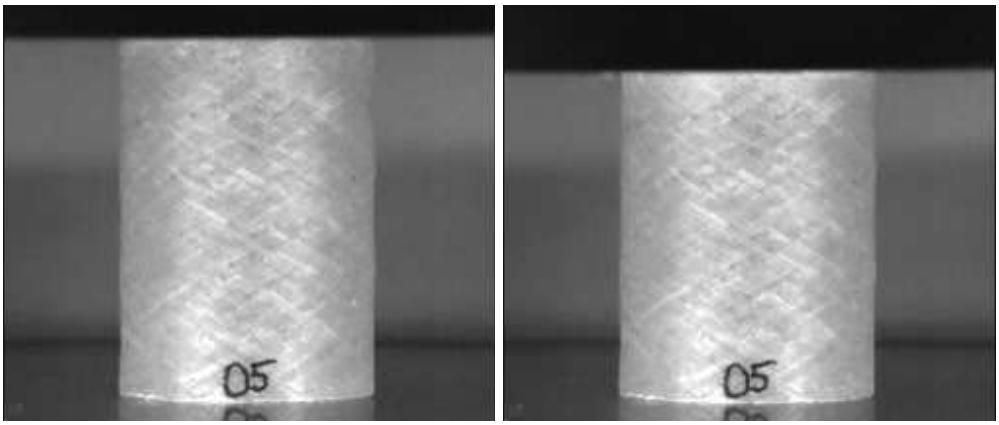

Figure 3.22: Deformation of component in dynamic tests at t=0 ms and t=1 ms.

In phase (1) the specimen is strongly compressed by the impactor without any failure of the structure (Fig. 3.22). Afterwards, the structure starts to fail and the force decreases, but remains constant on a certain level. This effect is related to phase (2) (Fig. 3.23) and well known as crushing, a significant property of fibre reinforced plastics. Furthermore this effect is responsible for the ability of high energy dissipation. In the considered example the first and second phase capture nearly half of the complete deformation path (see Fig. 3.21). However, afterwards another second failure mode occurs abruptly and can be observed in Fig. 3.24-3.25. The sudden fracture of the structure here is probably related to a delamination of the single layers of the composite. This effect is responsible for the decrease of the force in phase (3). If the structure is able to interrupt this process, as the considered example shows, a second crushing period can be observed and the force remains constant during this phase (Fig. 3.26-3.27).

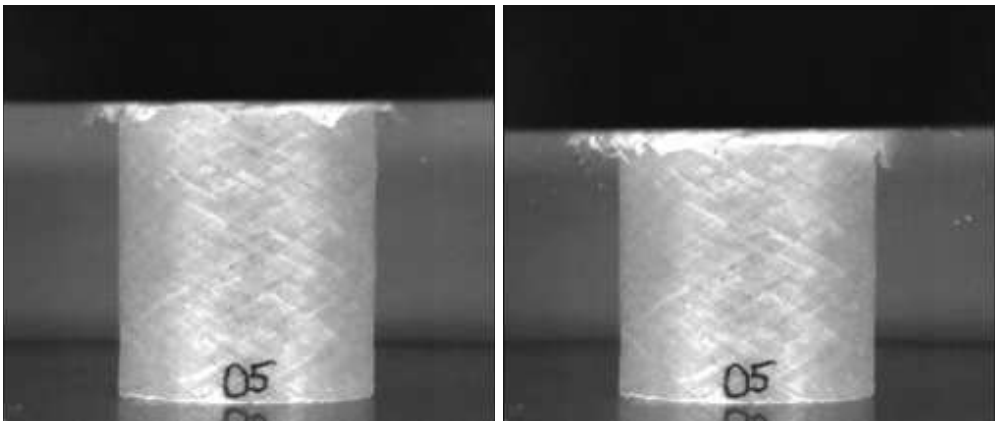

Figure 3.23: Deformation of component in dynamic tests at t=2 ms and t=3 ms.

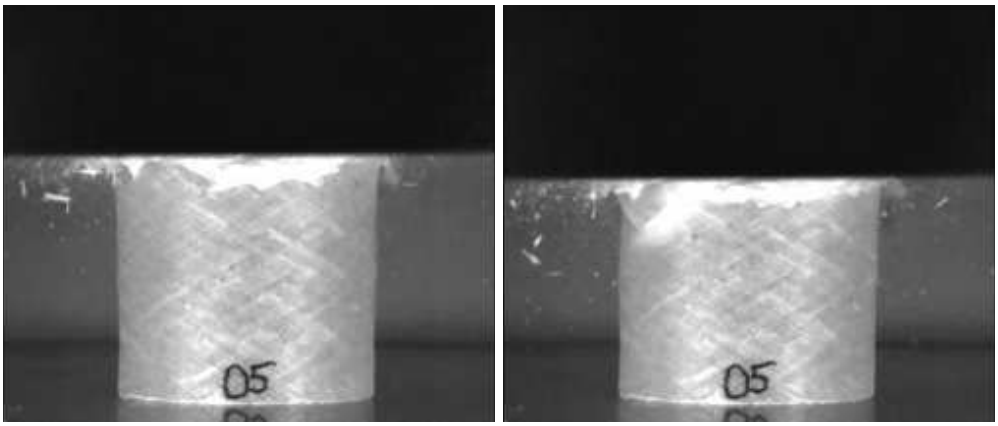

Figure 3.24: Deformation of component in dynamic tests at t=4 ms and t=5 ms.

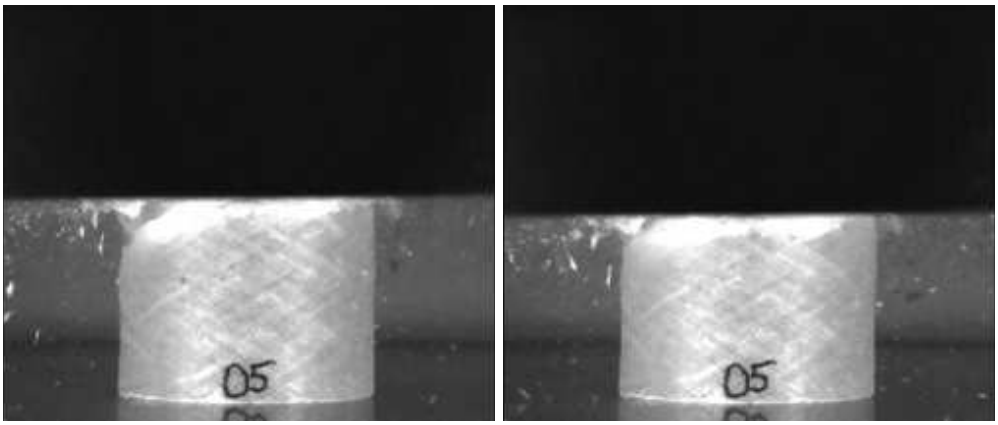

Figure 3.25: Deformation of component in dynamic tests at t=6 ms and t=7 ms.

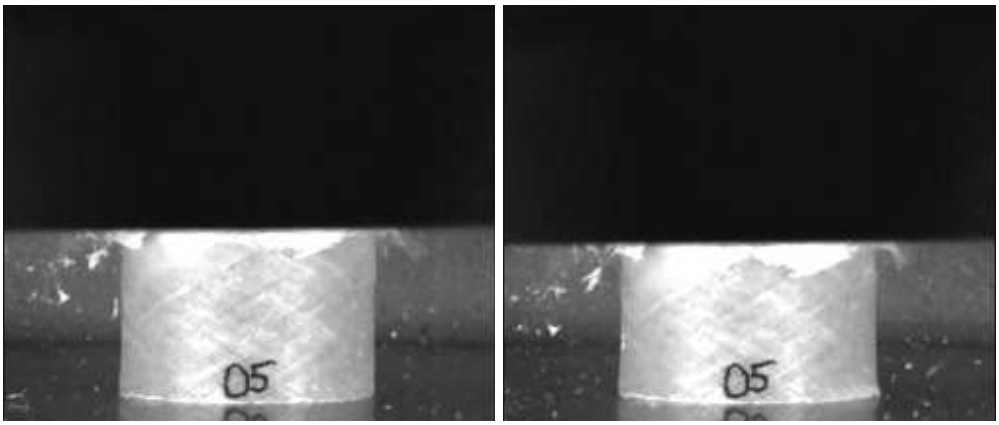

Figure 3.26: Deformation of component in dynamic tests at t=8 ms and t=9 ms.

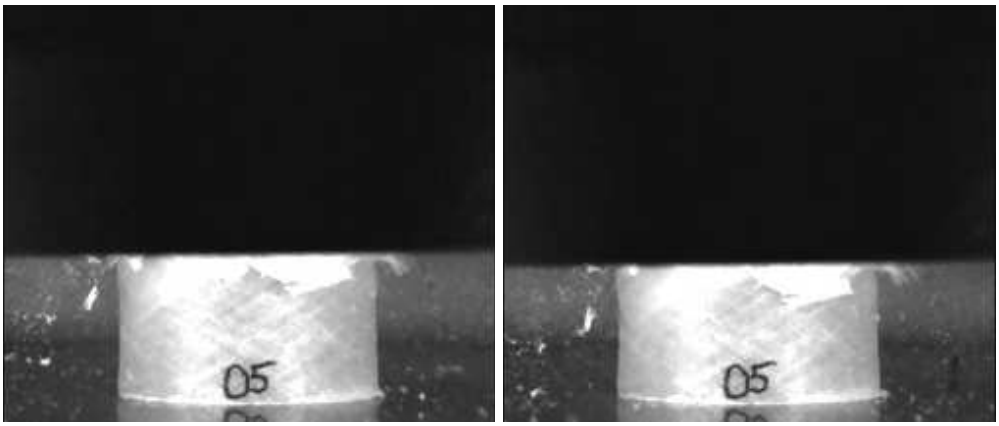

Figure 3.27: Deformation of component in dynamic tests at t=10 ms and t=11 ms.

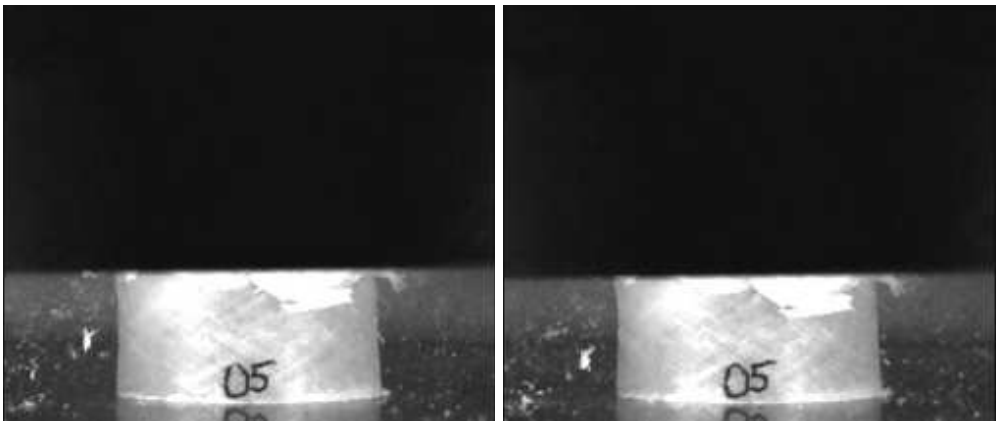

Figure 3.28: Deformation of component in dynamic tests at t=12 ms and t=13 ms.

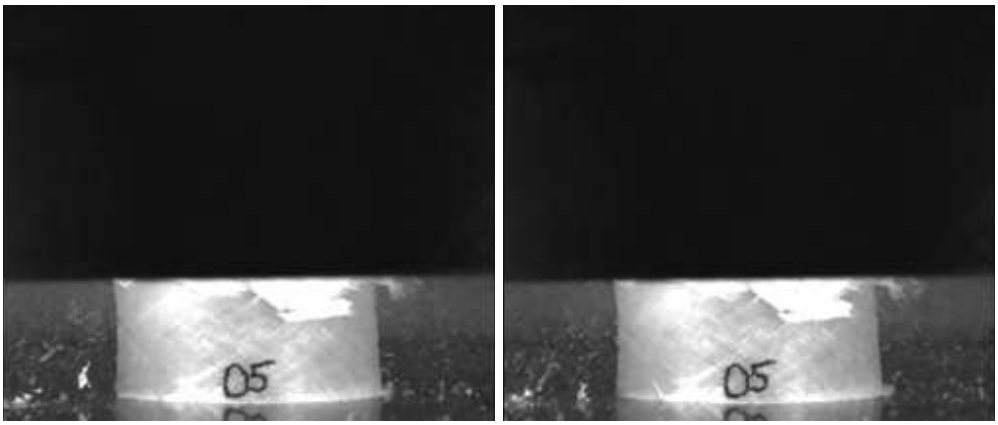

Figure 3.29: Deformation of component in dynamic tests at t=14 ms and t=15 ms.

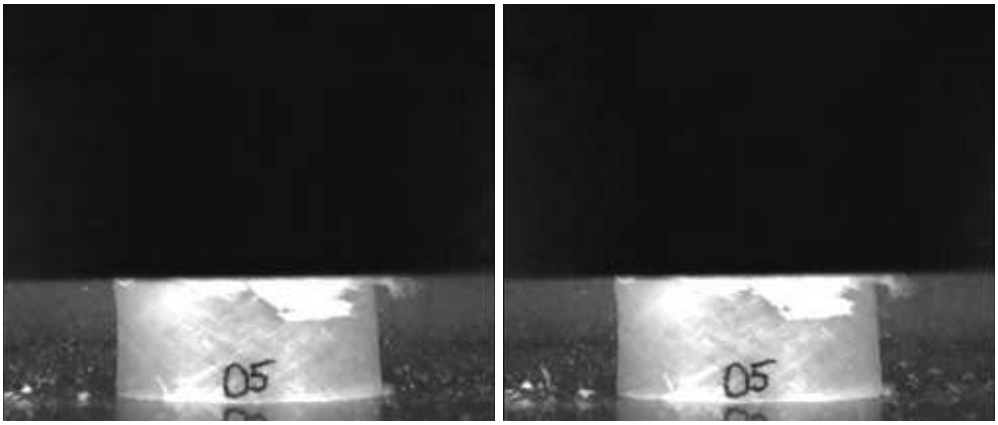

Figure 3.30: Deformation of component in dynamic tests at t=16 ms and t=17 ms.

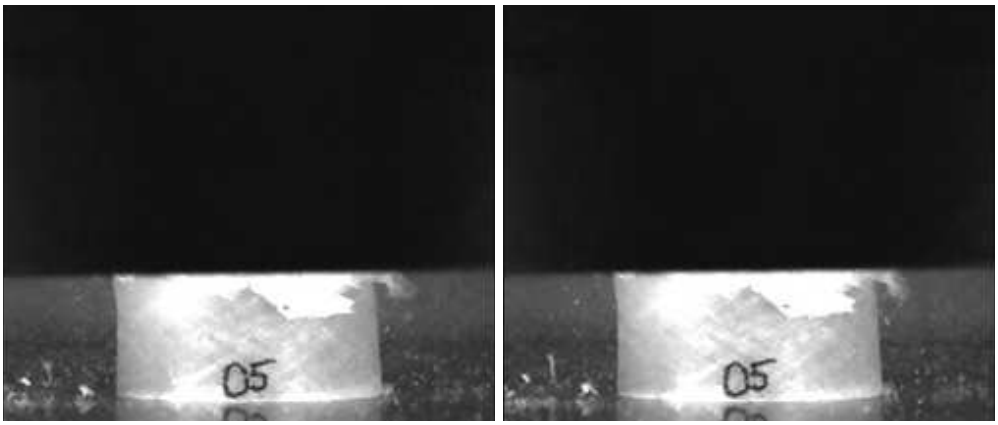

Figure 3.31: Deformation of component in dynamic tests at t=18 ms and t=19 ms.

Finally, in phase (5) the remaining structure is able to stop the impactor without any more failure (Fig. 3.28-3.30). To complete the evaluation of deformation in Fig. 3.30-3.31 the rebound of the impactor due to the stored internal elastic energy is shown. In addition, Fig. 3.32 shows the specimen after the test in front and back view, respectively.

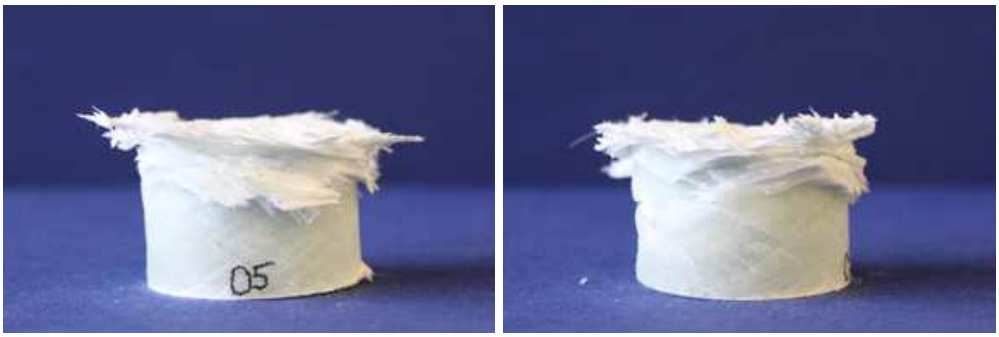

Figure 3.32: Example specimen for dynamic component test after impact.

A further examination of the idealised force-displacement curve in Fig. 3.21 with respect to the energy dissipation expresses the drawback of the failure mode in phase (3). The crushing mode in phase (2), which implies a perfect energy dissipation, is disrupted by this effect. The occurrence of such an undesired failure mode can be observed frequently in fibre reinforced plastics and is related to inhomogeneities of the composite structure (e.g. nested resin pockets). However, to ensure a high level of energy dissipation such effects should be avoided, in particular in terms of industrial crash absorbing elements.
In the demonstration example this effect is not really a drawback. Rather, this phenomena provides additional information about the mechanical behaviour of the composite structure. It directly points out the possibility of the initiation and interruption of different failure modes during a crash scenario.
The described phases above have been observed in all of the conducted tests. The differences between the individual tests concern only time intervals and amplitudes. In Fig. 3.33-3.35 the results for all tests are summarised. Thereby, each figure consists of two diagrams which refer to the force-time (left-hand side) and to the force-displacement relation (right-hand side), respectively. Fig. 3.33 shows the results for the tests with the low velocity, in Fig. 3.34 the high velocity results are given and Fig. 3.35 depicts a comparison of both. The strong increase of the forces in the last phase for the high velocity tests is related to an impact on bumpers made by rubber. These have been installed on the bottom plate of the test device in order to protect the load cells from an undesired impact. Consequently, these slopes do not reflect the properties of the composite structure. In addition, it points out that the considered wound tube is not able to dissipate the whole kinetic energy of the impactor in this configuration.

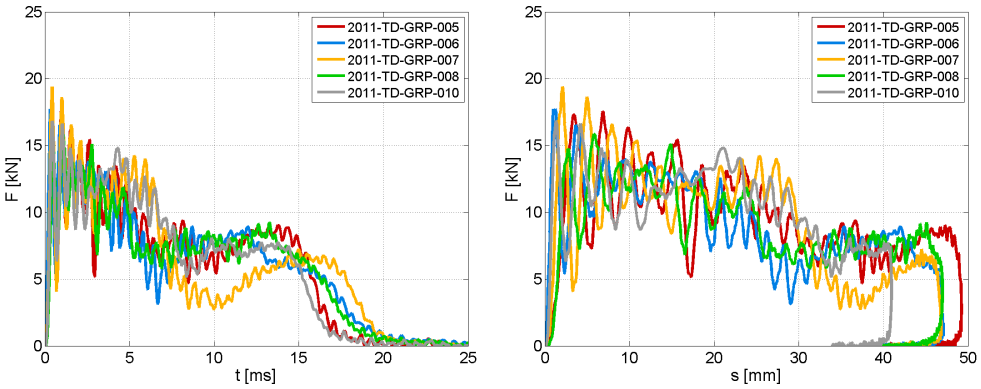

Figure 3.33: Results of dynamic component tests for v_1 a) force-time b) force-displacement.

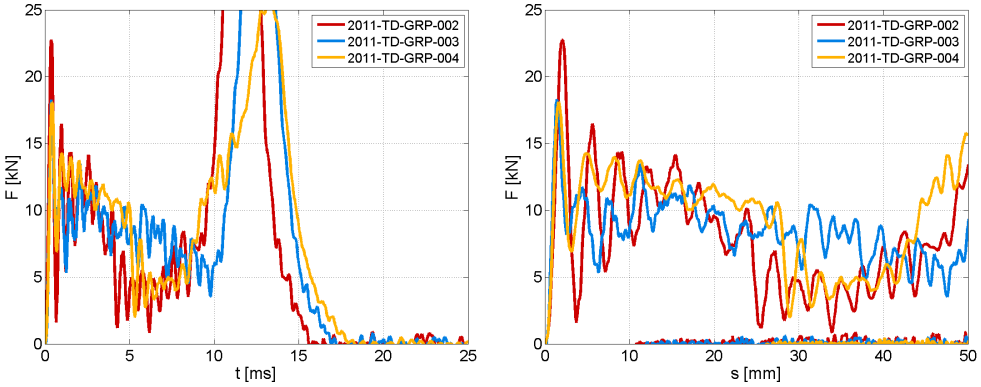

Figure 3.34: Results of dynamic component tests for v_2 a) force-time b) force-displacement.

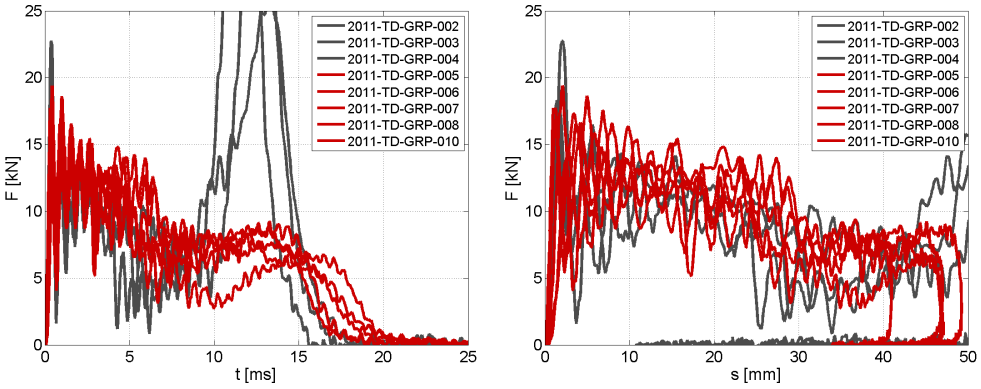

Figure 3.35: Comparison of results v_1,v_2 a) force-time b) force-displacement.

Comparing the results of the two impact velocities shows only minor differences. In both load cases the maximum peak force is about F=17 kN in average. Also the crushing force level is very similar (about F=12.5 kN). Consequently, no strain rate dependency can be detected for the composite structure within the investigated velocity range. However, in case of high velocity testing the height of the specimen is not sufficient to capture the transmitted energy. Finally, the results of test TD-GRP-003 are discussed briefly, where a different behaviour in comparison to the other tests can be observed. Here, the second failure mode already occurs in a very early state (t=1.1 ms) and doesn't appear any more afterwards. Consequently, the subsequent phase shows a constant force level and an improved crushing behaviour. It is assumed that the differences in the behaviour are based on deviations in geometry (e.g. thickness at certain points, manually generated chamfer). However, a non-ambiguous proof cannot be given, but it emphasises the influence of the occurring failure modes with respect to the global answer of the filament wound tube.

3.2.5 Application of Experimental Data

The experimental investigations described above constitute a major role in the subsequent chapters. On the one hand these results provide the input for the definition of appropriate material models in the simulation. On the other hand the results are used for the experimental validation of the simulations and consequently provide the base for a judgement for the proposed approach here after. Therefore, the following items summarise the role of each conducted test in this work.

(1) Material Modelling

  (a) Epoxy Resin L1100 EPH294
    - Static stress-strain curve for tension and compression
    - Tensile and compressive strength
    - Young's modulus
    - Poisson's ratio
    - Density
  (b) E-Glass EC 1200-315
    - Young's modulus
    - Tensile strength
    - Poisson's ratio
    - Density

(2) Component Modelling

  (a) Input
    - Fibre volume content on micro- and meso-scale
  (b) Validation
    - Real geometrical structure on meso-scale (CT tests)
    - Static force over displacement curves (quasi-static tests)
    - Dynamic force over displacement curves (impact tests)

Chapter 4

Meso-model Generation

This chapter represents the most important part of this work. It is concerned with the generation of a finite element meso-scale model of the wound tube based on a manufacturing simulation of the filament winding process. Thereby, the denotation "meso-scale" is related to the level of detail which is used for the geometrical representation of the composite structure and amounts to about 0.2 mm within this work. As a consequence the fibre architecture of the filament wound tube will be characterised on this level which claims appropriate material models and properties. Using a multi-scale approach, effective material properties are provided in the second part of this chapter. The complete generated finite element model finally constitutes the base for the simulation of the component test of the filament wound tube shown in Section 3, captured in the subsequent Chapter 5.

4.1 General Simulation Approach

The general approach for the generation of the meso-scale finite element model can be subdivided into two major steps: (A) the geometrical characterisation of the filament wound tube and (B) the determination of effective material properties. In step (A), a novel finite element simulation of the winding process of the tube is conducted to determine the fibre placements. Based on the obtained results, a three-dimensional fibre architecture is derived and an automatic matrix implementation procedure is used to complete the geometrical part of the finite element model. The main objective of this step is the gain of detailed geometrical information of the composite structure. In particular, information about fibre orientation, fibre placement and undulation as well as the fibre volume content are of high interest. In the second step (B) the pure base materials, fibre and resin, are used to derive effective material properties by multi-scale analysis. Thus, high level validated finite element material cards for the individual materials are obtained. Based on those, stiffness and strength of the meso-scale roving structure are derived from micro-scale data. The combination of (A) and (B) provides a very detailed finite element model on meso-scale which is able to represent the geometrical situation as well as strength and stiffness of the roving and matrix based on the properties of the

original materials. The following Fig. 4.1 illustrates the approach described above in detail.

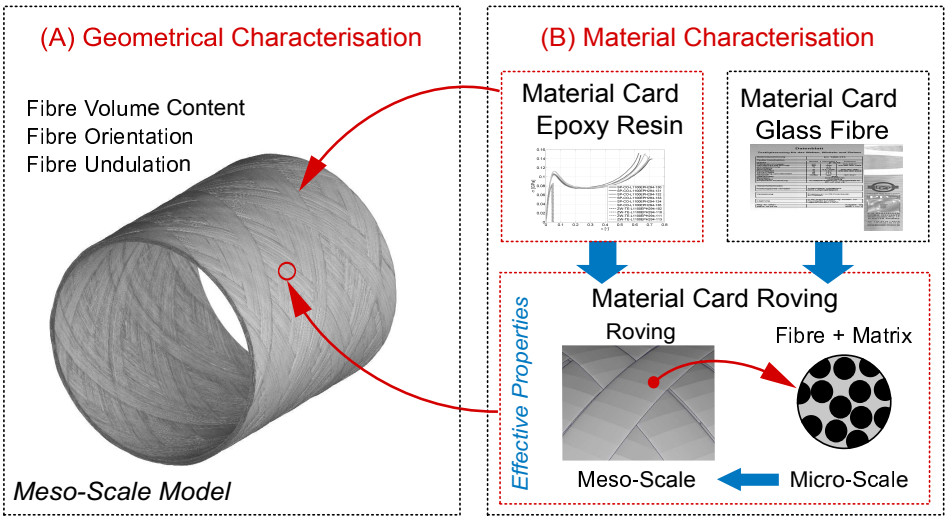

Figure 4.1: General approach for the finite element meso-scale model generation procedure.

4.2 Geometrical Characterisation

4.2.1 Simulation of the Manufacturing Process

The filament winding can be defined as an automated fibre placement process in which continuous fibres are wound on a mandrel. The process is performed by drawing the filaments from one or more spools, collecting and bundling them to rovings in the feed eye and the final placement by winding under a defined tension. In terms of a wet winding process the filaments additionally pass through a resin bath before the placement on the mandrel. The roving placement is controlled by the movement of the feed eye which is mounted on the carriage unit. In dependency of the type of the winding machine, the carriage unit, the feed eye as well as the mandrel can have various degrees of freedom. As a consequence the creation of complex wound structures with different predefined pattern can be realised. In Fig. 4.2, the general construction of a filament winding machine is illustrated.
After the desired number of layers have been wound, the structure is cured by a certain temperature. Opposed to the wet winding process, non pre-treated filaments have to be injected with resin after the fibre placement procedure. This is mostly realised by a resin transfer moulding process (RTM). Since this work concerns only the wet winding procedure, RTM is not further considered. A comprehensive description of the existing filament winding techniques can be found in [61].
Considering the manufacturing process of the demonstrator tube shown in the introduction (Chapter 1, Fig. 1.1) provides the following conclusion. A two

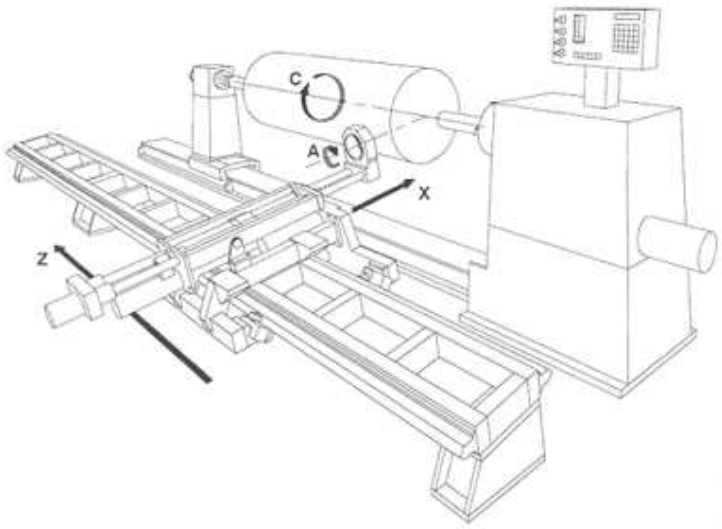

Figure 4.2: Basic scheme of a four degree of freedom winding machine - carriage unit (translation in X and Z), feed eye (rotation about A), mandrel (rotation C) from [18].

degree of freedom filament winding machine is sufficient to realise the desired winding pattern on the applied target geometry. Consequently, this implies a fixed feed eye on a carriage unit which is only able to move parallel to the mandrel in a constant distance. The solely existing degree of freedom for the mandrel is the rotation about its centre axis parallel to the carriage unit. By variation of the velocity of the carriage unit and the rotational velocity of the mandrel the desired fibre angle is generated. In the considered wound tube a fibre angle of 60° with respect to the longitudinal tube axis is used. It has to be mentioned, that this fibre angle provides less strength in comparison to the optimal 45° configuration for an axially loaded component. However, the lower strength is intended for the demonstrator component, in order to capture as many effects as possible in case of high dynamic loading. Finally, the manufacturing process of the considered tube can be completely characterised by the main 3 items:

- Translation of the carriage unit (incl. feed eye);
- Rotation of the mandrel and
- Prestressing of the filaments.

Due to the computerised numerical control (CNC) of winding machines all of the data mentioned above is available in a digital format. Consequently, the movements of the individual involved parts can be clearly represented by a known number of parameters.

Remark 4.1 *A roving is defined as a bundle of continuous, untwisted filaments. From a certain magnitude of filaments (gt 70 tex) this denotation is used instead of yarn. The used glass fibre has a tex of 1200.*

Numerical Representation

The parameterised information of the manufacturing process constitutes an important base for the numerical model. It provides the boundary conditions for the individual finite element components. Therefore, the CNC data obtained by the real process are converted to appropriate functions usable in finite element simulation. These functions, representing the translation and rotation in space, are directly imposed on the respective parts. The finite element simulation model consists of three main parts: the mandrel, the roving and a point which represents the feed eye. Contrary to the real manufacturing process all movements are applied directly to the mandrel in the simulation model. This implies a fixed feed eye in space, a rotation of the mandrel about its centre axis as well as a translation in the direction of the rotational axis. In Fig. 4.3 the scheme of the simulation approach is shown.

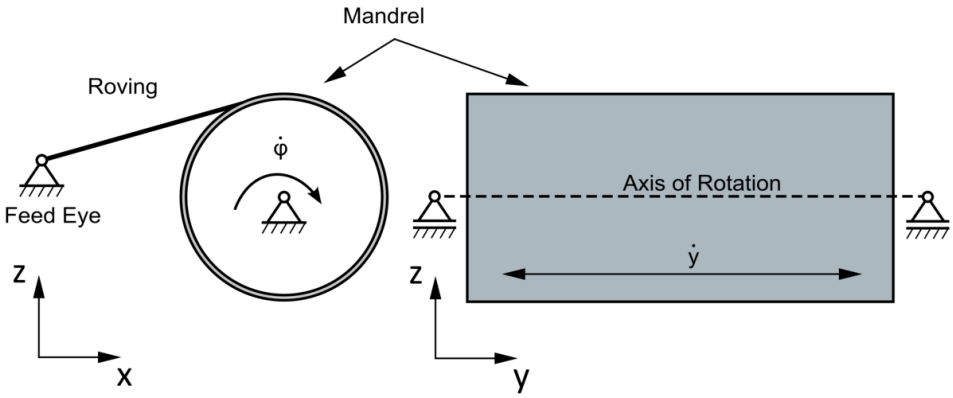

Figure 4.3: Basic scheme of the winding simulation model.

Since the mandrel consists of a strong solid block and its stiffness is much higher than the roving's, this part is represented by a rigid body built by finite elements. Moreover, this simplifies the imposing of the required boundary conditions. The roving is represented by finite bar elements which can only transmit forces in tension. As a consequence the elements have no stiffness in compression or in bending. Due to the pre-stress of the roving and its resulting tangential position regarding the mandrel surface, the bending stiffness can be neglected for the winding simulation. To ensure the representation of large rotations without any loss of accuracy a finite bar element with a *Total Lagrange Formulation* is used. In addition an isotropic elastic material is associated with the roving in order to reflect the properties of the glass fibres. As the matrix in fluid form provides no stiffness, it is not taken into account for the simulation of the winding process. However, it has a strong influence concerning the friction behaviour and must be taken into account for the contact definition of the fibres within the finite element model.
The roving is connected to the mandrel surface on the one side and to the feed eye on the other. The numerical model of the feed eye consists of a stack of bar elements to represent the drawing of the continuous fibres. In addition a special

belt option (RETRA element [24]) is directly defined at the feed eye to enable the pre-stressing of the roving. Between the mandrel and the roving as well as for the roving itself, penalty contact formulations are used [20, 22]. The contact height is given by the roving height. For the first one, a node-to-segment contact for smooth surfaces is applied. In the second case an edge-to-edge contact is used. Within the contact definition the friction between the respective materials is defined. The use of a special smooth surface contact is necessary to avoid mesh dependencies caused by the modelling of the mandrel by finite elements. Alternatively, the mandrel can be represented by a very fine finite element mesh and the smooth surface contact can be replaced by a standard node-to-segment contact. In the following Table 4.1 the model set up is briefly summarised.

	Roving	Mandrel
Element Properties		
Type	Bar	Shell
Average Length	2.0 [mm]	2.0 [mm]
Preload	0.05 [kN]	-
Material Model		
Type	Isotropic Elastic	Rigid Body (Null Material)
Density	2.54e-06 [kg/mm^3]	7.90e-06 [kg/mm^3]
Young's Modulus	75.0 [kN/mm^2]	
Boundary Conditions		
Fixation	Feed Eye/Mandrel	Rotational Axis
Imposed Functions	-	$\dot{y}$, $\dot{\varphi}$
Translational Velocity	-	$\dot{y}$ - Function [mm/ms]
Rotational Velocity	-	$\dot{\varphi}$ - Function [rad/ms]
Contacts		
Type	Edge-Edge (Self Contact)	Node-Segment (Master-Slave Smooth Surface)
Parts	Roving	Mandrel-Roving
Friction	0.3	0.3

Table 4.1: Main properties of the finite element model for the winding simulation.

The filament winding simulations are conducted with the explicit solver (PAM-CRASH) of Virtual Performance Solution (VPS) [21], a commercial finite element code which is widely used in the automotive industry. Due to the use of an explicit time integration scheme, the stable time step for the winding simulation with respect to the model properties from Table 4.1 becomes very small ($\Delta t \approx 0.33 \mu s$). In combination with the real manufacturing time of about t=51 s for one layer the computational effort for the winding simulation is very time consuming. In addition, the related number of calculation steps (cycles) can be critical for an explicit time integration scheme. As a consequence, insta-

bilities which may end in an abort of the calculation can occur. To overcome this issues, the finite element model is modified in the following way. In a first step the original speed of the manufacturing process is increased by a factor of ten. The influence of the related inertia effects is investigated for the first part of the filament winding process (two turns). Therefore, simulations with the original and increased manufacturing speed are compared with respect to the fibre placements. As a result of this preliminary investigation, the pretension of the roving needs to be increased by factor two. This is the minimum required increase to get almost identical results. The related maximum deviation, between the node positions of the bar elements of the two models, amounts to less than 1% and is hence acceptable. The increase of the pretension should be kept as small as possible to avoid undesired artificial strains in the bar elements. The second modification is conducted on material property level. Due to the high stiffness of the glass fibre roving the elongation of the bar elements is very small ($\epsilon \approx 0.1\%$). By reducing the Young's modulus by a factor of three and the application of the increased pretension force, this value still remains small ($\epsilon \approx 0.8\%$). As a consequence the stable time step will also increase by about three times ($\Delta t \approx 1.0 \mu s$). Under the assumption of a constant time step during the calculation this leads to a total of 5.1e+06 cycles (1.5e+08 cycles before) which corresponds to efficiency gain of a factor thirty. Finally, the computational time for the filament winding simulation of the tube with a length of 300mm is approximately 13h for one layer on a 16 CPU machine.

Results of the Winding Simulation

In Fig. 4.4 the results of the simulation of the winding of one layer (1 layer = 21 turns of the carriage unit according to CNC data) are depicted. The first illustration shows the initial configuration of the finite element model. In the following pictures intermediate states of the virtual manufacturing process are represented. At the end, the final configuration of the virtual winding process is shown. In each of the figures the end of the roving represents the feed eye. It can be seen that the rovings are not directly located side by side within one turn. This is related to the desired fibre angle and the corresponding movement of the individual machine components. However, at the end of the 21 turns the rovings are arranged side by side. Caused by this procedure undulations occur between the rovings. This fundamental property of wound structures is covered by the applied numerical method. An example of the occurring undulations between the rovings is illustrated in detail in Fig. 4.6. Thereby, the space between the bar elements is related to the defined contact distance in the finite element model which corresponds to the roving height. In addition the magnitude of the undulation is not constant within the structure. This is related to the tangential forces which depend on the relative position between feed eye and the roving placement position on the mandrel.

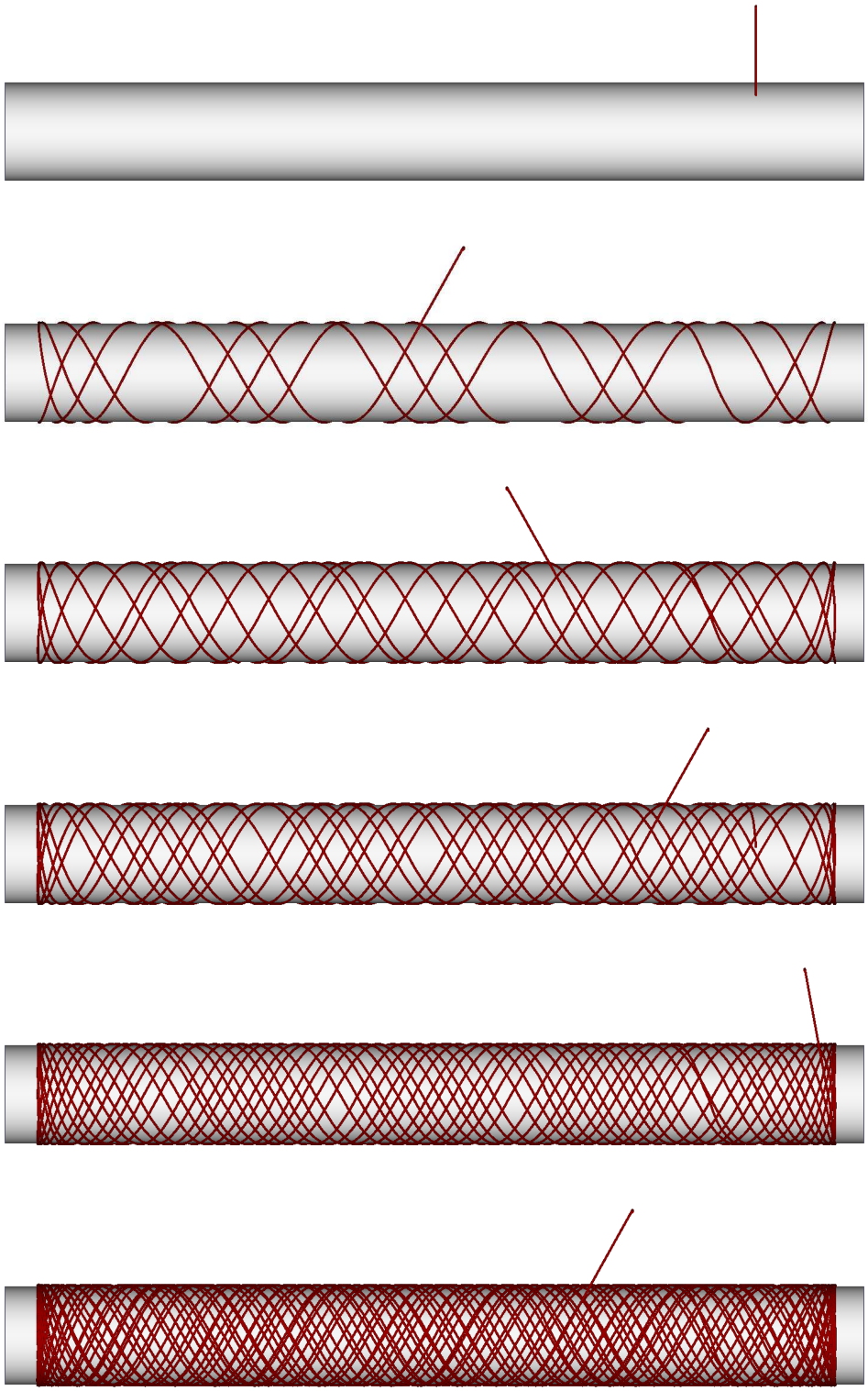

Figure 4.4: Simulation of the manufacturing process from the initial to the final configuration (A).

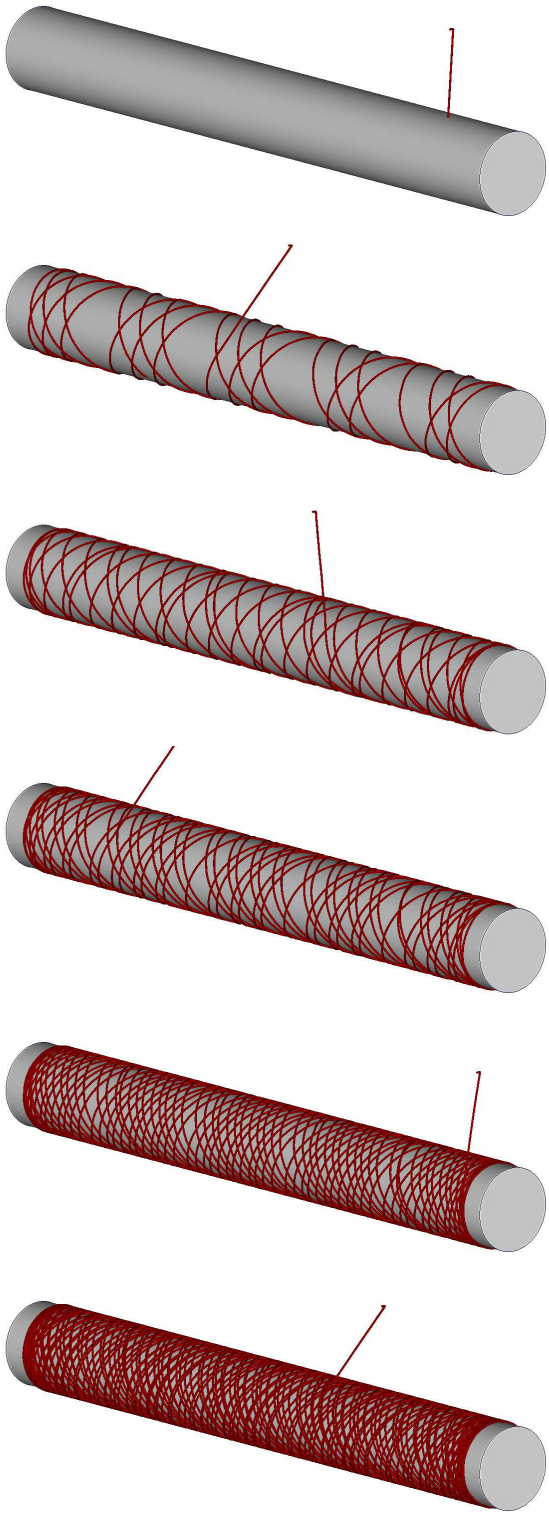

Figure 4.5: Simulation of the manufacturing process from the initial to the final configuration (B).

However, by taking into account the mechanical properties of the fibres in combination with the contact definitions including friction, this effect can also be represented by the simulation. Another region of interest within a wound structure is the area of turning points. As can be seen in the last illustration of Fig. 4.4 a high concentration of fibres can be observed in this domain. As a consequence the fibre volume content is different in such areas. In the considered component this effect has a minor importance since the boundary areas are removed to ensure a homogeneous structure for components. However, in terms of complex components e.g. a wound nose cone of a turbine it is impossible to remove such areas and therefore the simulation must be able to cover these effects. Finally, the simulation of the winding process provides the position of the 1D bar elements in space which in turn represents the individual roving placement and orientation.

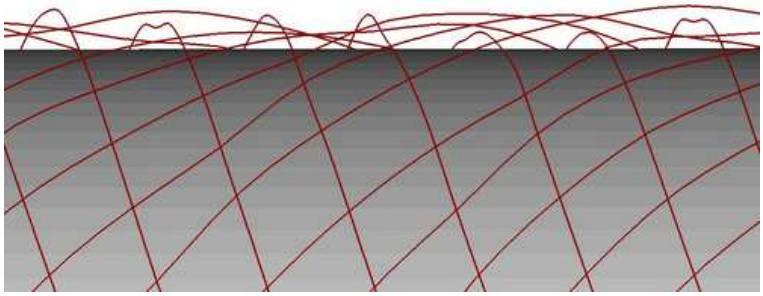

Figure 4.6: Fibre undulations of the 1D bar elements in detail for one layer.

The generation of the winding simulation model is realised by a procedure which automatically generates the spool including feed eye and fibre as well as the fixation at the mandrel. Thereby, the main model properties such as pre-tension, roving cross-sectional area, friction values or feed eye position can be defined by a given user interface. In combination with a given finite element mesh of the mandrel and the description of the individual machine movements, the method can be easily applied to other geometries (e.g. tubes with non constant radius, domes or cones).

Limitations of the Winding Simulation

The approach presented above is not able to take into account taper and twisting effects of the roving during filament winding. Such effects can be mainly observed in the domain of turning points in combination with small fibre angles. In particular, components having a non constant radius like domes or cones are affected by these effects. They are caused by different tangential forces related to the relative feed eye - mandrel surface position. Since the cross-section of the roving is represented here by bar elements, it is not possible to cover 2D taper effects by the current method. In addition, the use of bar elements for the roving representation avoids the transmission of moments and consequently also the consideration of twisting effects. However, the applied method is open

for an extension to cover these effects. Another restriction of the simulation model is the neglect of a detailed feed eye modelling. Due to shape and surface texture of the feed eye the roving may be tapered or twisted by friction effects already at this point. In the numerical model the roving is fixed to the feed eye without any possibilities to cover slipping effects.

4.2.2 Derivation of the 3D Fibre Architecture

In the second step of the virtual manufacturing approach, the 3D fibre architecture of the rovings is determined. Basically, the proposed method can be subdivided into two main parts: a geometrical mapping and a correction procedure based on finite element simulations. The base for this method is provided by the final configuration of filament winding simulation discussed in Section 4.2.1.

Numerical Method

Due to the automatic generation of the finite element roving data for the winding simulation, the arrangement of the bar elements is known. Consequently, also the order of the connected nodes and their position in global coordinates can be determined for the final state. Based on this information the orientation vector for each bar element can be calculated. In combination with a predefined cross-section the 3D roving architecture is created. The cross-section can be arbitrary, but should approximately match the shape of the existing roving geometry. Here an elliptical cross-section is used, since it is assumed that an ellipse will be the best fit for the flat roving. Based on the roving width provided by the fibre manufacturer as well as the cross-sectional area, the height of the ellipse can be calculated. Thereby the cross-sectional area is obtained by the number of filaments in the roving and the individual filament diameter. In Fig. 4.7 the basic scheme of the method is illustrated.

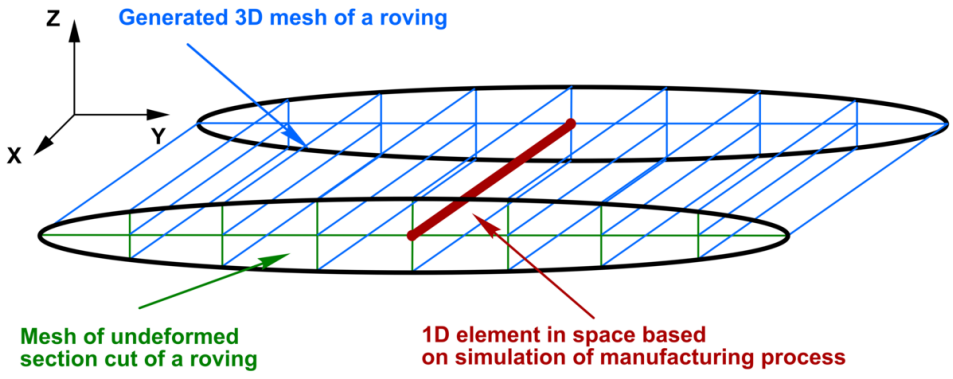

Figure 4.7: Basic scheme of the 3D roving creation.

The cross-section of the roving is modelled by finite shell elements in the origin of a global coordinate system and subsequently mapped to the first node of the respective bar element. Under the assumption that the bar element itself defines the normal vector of the cross-section plane, the transformation matrix for each node can be defined. Finally, each node of the bar elements is connected to an individually orientated cross-section. Due to the known order of the bar elements also the order of all new generated nodes belonging to a cross-section are defined. Thus, the nodes of the individual cross-sections can be easily used to generate the finite element solid structure. The drawback of this pure geometrical approach is the generation of penetrations between the rovings. The issue is mainly caused by the non-consideration of tapering and twisting effects during the winding simulation. To overcome this, the second step of the method consists of a finite element analysis for the penetration removal which is schematically shown in Fig.4.8.

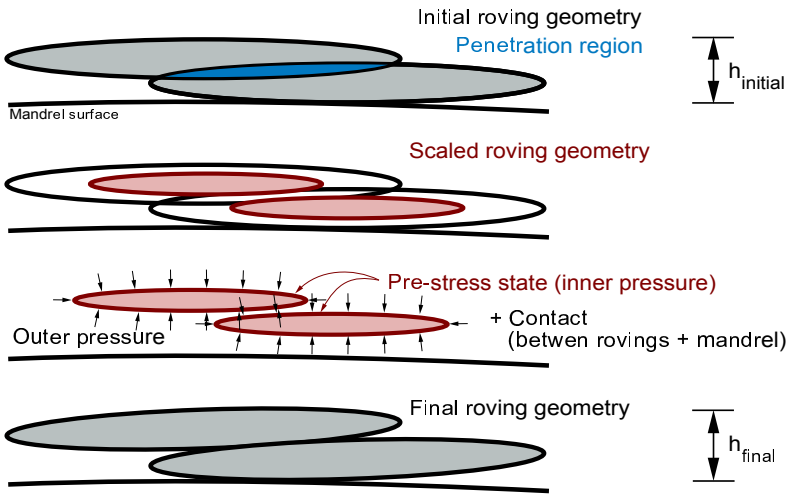

Figure 4.8: General scheme for penetration removal procedure.

Within this procedure, the solid elements are scaled down by a factor ensuring a penetration free state between all rovings. In addition the original geometry is kept as reference for the calculation of initial stresses caused by this artificial deformation. Moreover, the outer surface of the deformed solid elements is loaded by a certain pressure. The magnitude of this pressure must be in equilibrium with the internal forces caused by the artificial scaling. During the initialisation of the finite element analysis the internal forces of the scaled rovings are calculated based on the undeformed reference geometry. Reducing the applied outer pressure by a defined function to zero, in combination with a contact definition between the rovings, provides a penetration free state of the structure.

This simulation is also conducted with the explicit finite element code of VPS. Thereby the initial metric option is used to get the internal forces of the artificially deformed geometry at the initial state. Contrary to the winding simulation, an isotropic hyperelastic material model is used here for the representation of the mechanical behaviour of the roving. This is related to two main reasons: a) the occurrence of large deformations due to the scaling of the roving geometry and b) the need of a path independent material law due to the use of the initial metric option. Both requirements are satisfied by a hyperelastic material law [8]. The mechanical properties for the solid elements are in accordance to Table 4.1.

Results of the 3D Fibre Simulation

In Fig. 4.9 the two states of the roving geometry are depicted for an example domain of the demonstrator tube. On the left-hand side of the illustration the structure after the pure geometrical mapping including the occurring penetrations is shown. On the right-hand side the final geometry after the correction procedure by simulation is represented for the same area. There the dotted line circles mark the regions of main interest.

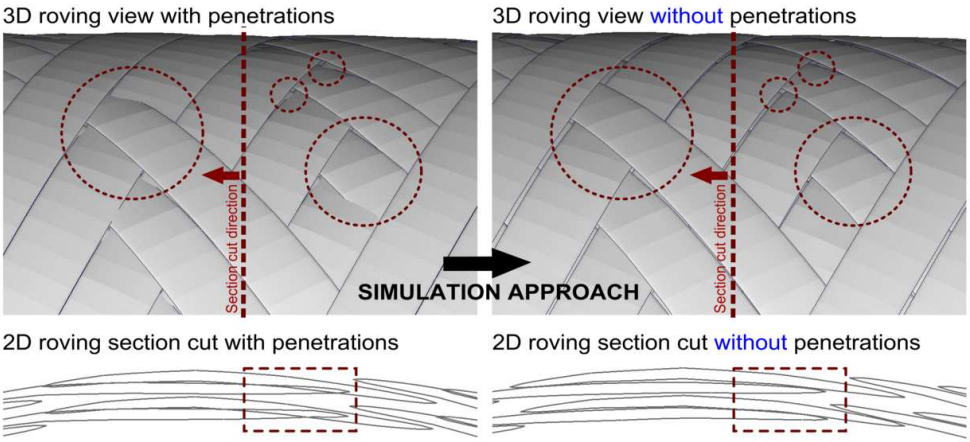

Figure 4.9: Roving mesh before and after the penetration removal procedure - upper row 3D representation, lower row 2D section cut.

In the lower part of Fig. 4.9 a roving section cut for the same states is given. Thereby, the normal direction of the section plane is coincident with the longitudinal axis of the component. This illustration emphasises the necessity of the applied correction method. It can directly be seen that the rovings are modified with respect to shape and position due to the applied simulation procedure. In Fig. 4.10 the result of the 3D fibre architecture generation method for the complete component structure is shown. Finally, Fig. 4.11 illustrates a comparison of the initial and final state of the 3D fibre architecture generation procedure. The initial state refers to the 1D fibres in space provided by the winding simulation, the final state to the newly generated solid fibre structure.

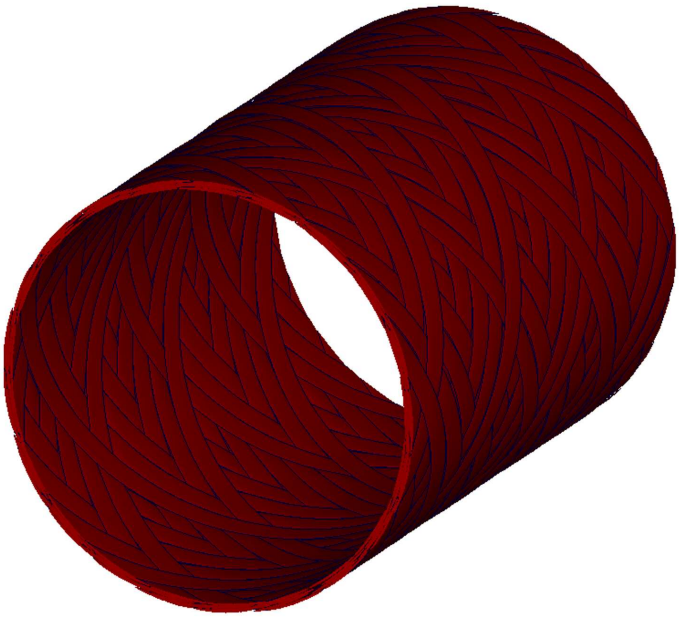

Figure 4.10: Virtually generated 3D fibre architecture of the tube component.

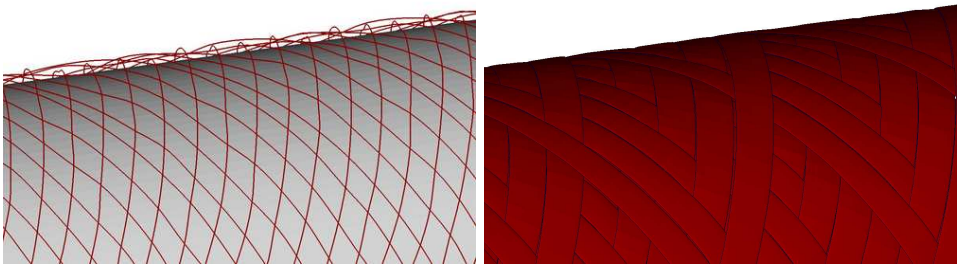

Figure 4.11: Initial and final state of the inner layer for the roving generation method.

Experimental Verification

In order to assess the quality of the virtual model a comparison to the real wound tube is conducted. The evaluated CT records of the real structure for the different resolutions from Section 3.2.1 are used to discuss the quality of the provided 3D fibre architecture. Firstly, the coarse CT resolution is compared to the generated fibre architecture for the complete component. To assess the global quality of the numerical model an overlay of both structures, virtual and real, is realised. In Fig. 4.12 the result of this overlay is illustrated by a subdivision in six different states. The first picture, in the upper left of the figure, represents only the real structure. In the following images of Fig. 4.12 the real structure is overlaid by the results of the simulation model in small geometrical steps.

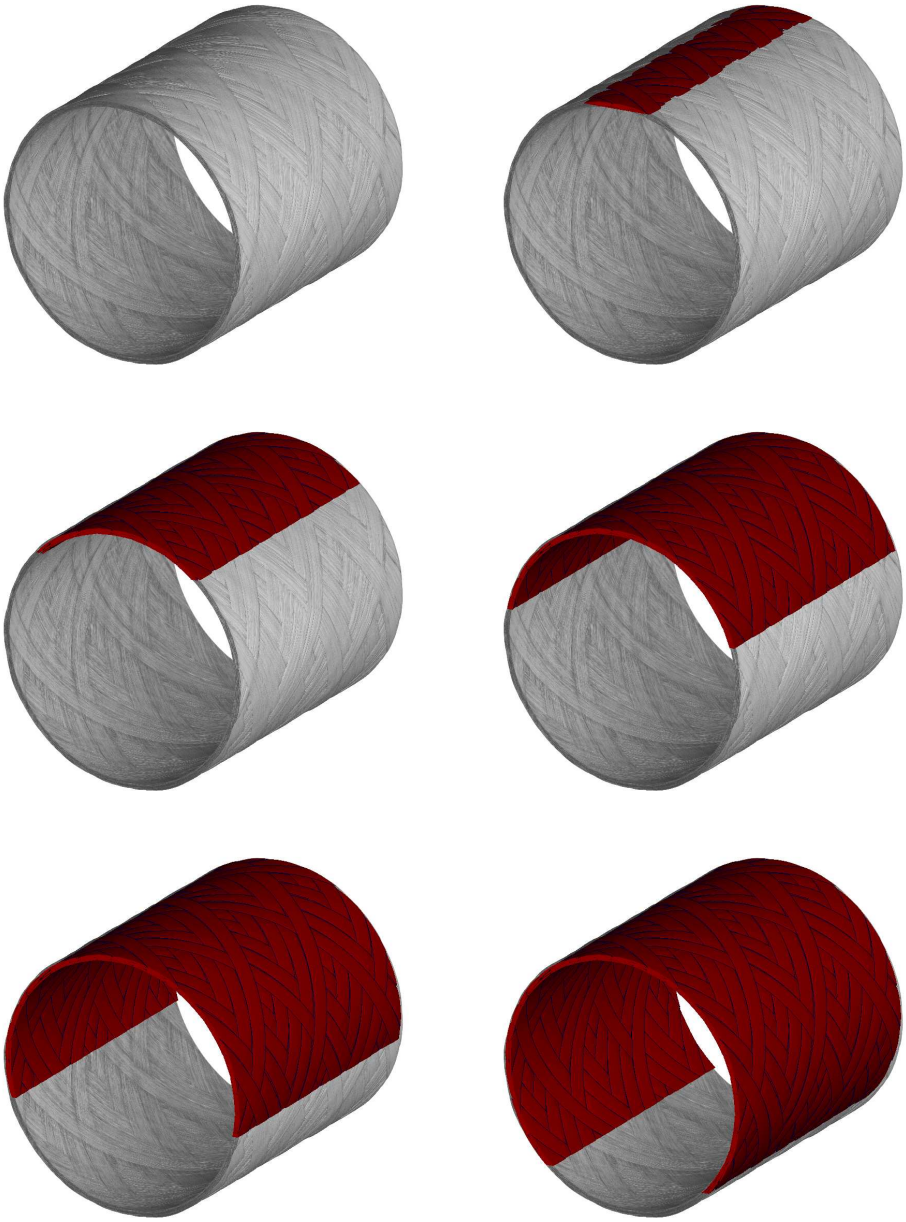

Figure 4.12: Comparison of the CT record for the complete wound tube from Section 3.2.1 to virtually generated 3D fibre architecture - 3D overlay in six steps.

In Fig. 4.13 the section cut perpendicular to the roving direction of the sub domain A shown in Fig. 3.13 from Section 3.2.1 is compared to the virtually generated layer stack. Thereby, the consideration is separated to the inner and outer layer of the complete structure, respectively. Comparing the inner layer it can be seen that the simulation, which is depicted by the white solid lines, correlates very well with the global shape of the existing structure. Both orthogonally and skew cut rovings are captured. However, it can be also seen that the roving lying directly on the mandrel (left-hand-side of upper picture) is

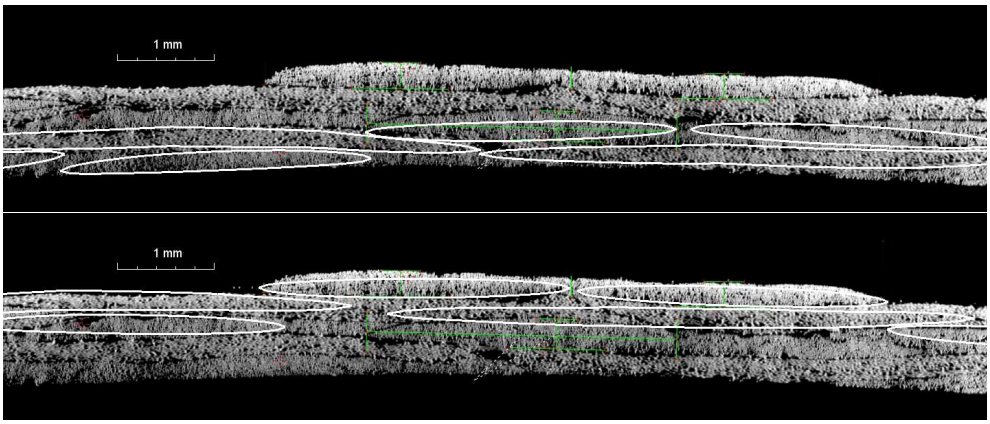

Figure 4.13: Comparison of the CT record to the numerical model - section cut, a) CT record in comparison to first layer and b) CT record in comparison to second layer.

more compressed than the simulation predicts. The shape of this roving in the numerical model is not as wide as the real one. This may be related to higher pressure inside the composite structure during manufacturing. Furthermore the distance between some rovings is closer in the real structure. This point is related to the modelling by solid elements and contact formulations which do not allow any penetration of the structure. In contrast, this may happen in the real composite tube due to the heterogeneous roving structure. However, the deviation is less than 0.5 mm and most of the rovings are represented very well by the simulation.
The statements mentioned above can be directly transmitted to the comparison of the outer layer where the same behaviour can be observed. Finally, it can be summarised that the numerical solution based on the manufacturing process can represent the real structure of the wound tube very well. This includes not only the outer shape but also the inner structure as well as complex roving undulations.

Limitations

The applied method is depending on the discretisation of the roving in longitudinal direction. The increase of the element size for the 1D bars will also increase the occurring penetration. This may lead to situations where it is not anymore possible to generate a penetration free state by constant geometrical scaling. In addition a very coarse mesh of the roving can provide sharp angles between two bar elements due to the occurring undulations in the winding process. This may lead to not acceptable finite elements for the solid structure. In the considered case a bar element length of 2mm is used by a mandrel radius of 20mm. The related ratio of ten between those quantities is a proper choice for the applied method. However, minor difficulties at some locations could already be observed in this configuration. Consequently, a ratio of ten should be considered as limit value for a successful application of the method.
On the other hand a very small contact height for the calculation of the penetration free roving geometry is needed to avoid artificial gaps between the

individual rovings. To ensure a working contact a nonlinear contact stiffness has to be used. In addition the outer pressure must be removed slowly and smoothly to keep the roving deformations small during one time step.

4.2.3 Matrix Implementation

The existence of a finite element mesh of the 3D fibre architecture constitutes an important contribution for the mechanical description of a fibre reinforced composite structure. However, without finite elements representing the surrounding matrix, the model is improper to represent a composite in simulation. In order to complete the existing finite element roving model a method for the matrix implementation is developed. Thereby, the following predefined requirements are considered:

- The surrounding matrix has to be generated automatically;
- The interface regions between fibre and matrix must be identified;
- The method must be independent of the given fibre architecture.

Taking into account the above restrictions, the number of possible solutions for a matrix implementation procedure is quite limited. One option is the use of meshless methods such as *Smoothed Particle Hydrodynamics* or *Finite Point Method* [89]. These methods are well suited for the geometrical filling of the space between the rovings. However, the definition of the interaction between the solid roving elements and the matrix particles is difficult. In addition it is currently not possible to represent sufficiently well a solid structure by one of the approaches mentioned above within the explicit solver of VPS, as these methods are primarily developed for fluids and gases. Another possibility is the use of highly sophisticated meshing tools, embedded in automatic procedures. However, in spite of the high quality of the implemented algorithm these methods will not be able to capture all occurring geometrical issues e.g. the close or near zero distance of the rovings. Even if it is possible to generate a standard finite element mesh for such domains, the element quality will be poor. As a consequence instabilities may occur and the accuracy of the finite element approach will strongly decrease.
To ensure a regular, homogeneous mesh, independent from the roving geometry, an approach based on the *Voxel Method* is used. A voxel (volumetric pixel) is similar to a pixel of a 2D image. Contrary to a pixel it represents a single finite volume in 3D space. In accordance with a pixel a voxel has the same length for each edge. Thus, a voxel grid consists of a number of cubes with the same size. Due to its geometrical properties (e.g. aspect ratio, internal angles) a voxel represents a perfect finite solid element. In combination with the high potential of automation the voxel method is an appropriate approach for the realisation of the requirements defined above.

Matrix Generation Algorithm

In Fig. 4.14 the general scheme of the matrix implementation algorithm is illustrated. Thereby, only a small section of a roving is considered to reveal the major concept of the approach.

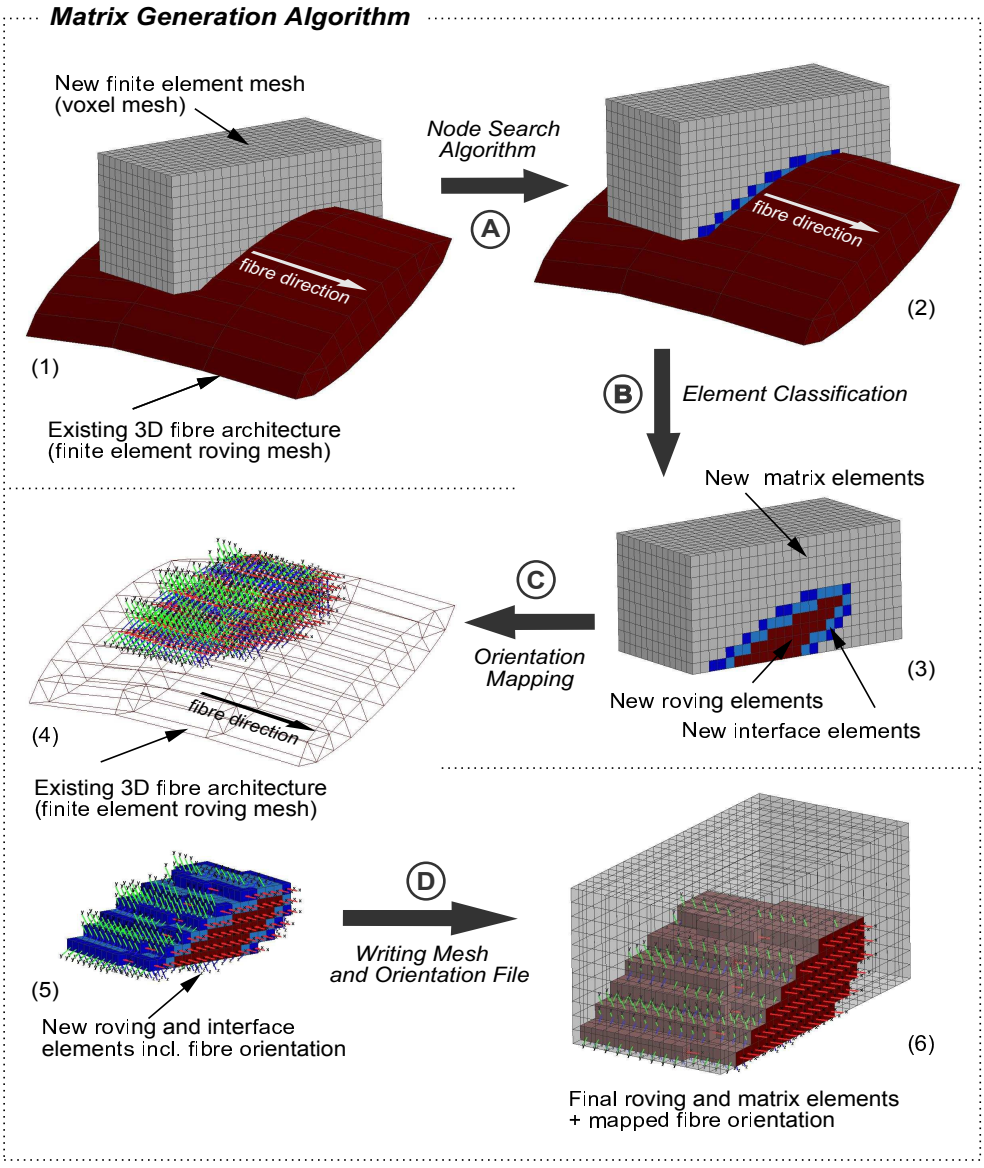

Figure 4.14: Scheme of the matrix implementation algorithm.

At the beginning a finite element mesh consisting of voxels and representing the complete matrix is automatically generated and overlaid to the existing 3D fibre architecture. This preliminary step is depicted in (1) of Fig. 4.14. Here the red colour elements represent the roving and the grey ones the new mesh. In the subsequent step A of the procedure, an algorithm determines the

nodes of the new mesh located inside of the existing roving structure. Based on this information the corresponding elements are identified. Dependent on the occurring number of nodes inside the roving, these elements are classified in various groups within step B. This implies that e.g. elements, having two nodes in the roving structure, are addressed to group number 2 or elements with five nodes inside to number 5. Since all newly generated elements have exactly eight nodes, a maximum of nine groups can exist. Each group corresponds to an individual part which in turn is assigned to an appropriate material. Elements having eight nodes inside the roving structure are assigned to the fibre material. Elements whose nodes do not belong to any group are assigned to matrix material. All other existing groups are defined as interface layer elements. It is not mandatory to assign these elements to different materials, they can also be assigned to the matrix or the fibre material. However, due to this classification the possibility for the definition of one or more interface layers is given. In (3) of Fig. 4.14 the classification of the new mesh with respect to the defined groups is shown. Thereby, the grey colour elements represent the matrix, the red ones the fibres and the two blue groups define the interface layer elements. It becomes apparent that fibre, interface layer and matrix of the new mesh are directly connected. This connectivity is realised by the geometrical mapping of the original roving architecture to the new mesh. To maintain the fibre direction of the roving, a frame with the corresponding orientation is assigned to each new fibre element in step C of the procedure. In (4) and (5) of Fig. 4.14 the fibre orientations of the new roving elements are shown with respect to the original and the new mesh, respectively. Since the interface layer elements can be assigned also to the fibre material, a frame is attached to these elements as well. In the last step D of the procedure, the new finite element input deck containing fibre, matrix and interface elements is written to a file. In addition a second file consisting of two vectors for each element is stored. This file, representing the fibre orientation, can be used for the initialisation of anisotropic material frame axis in the constitutive law. Finally, (6) in Fig. 4.14 represents the last state of the considered example, demonstrating the matrix implementation algorithm in terms of the interface elements assigned to the fibre material.

Application on Component Level

The method described above is now applied to the complete 3D fibre architecture of the considered demonstrator tube from Fig. 4.10. Based on the definition of the inner and outer radius, a centre point as well as the length of the component, the surrounding matrix shape is created. In combination with the target element size the voxel mesh is generated. Thereby, the number of nodes for the inner circle is given by diameter and target length. Due to the voxel approach the outer shape must have the same number of nodes. As a consequence the elements do not match the ideal voxel geometry.

However, Eq. (4.1) shows, that only a minor deviation can occur between the minimal and maximal element length for thin walled structures.

$$\frac{r_2}{r_1} = \frac{l_{max}}{l_{min}} \tag{4.1}$$

Here r_1 and r_2 are the inner and outer radius, respectively. l_{min} represents the target element length and l_{max} the resulting maximum. For the considered wound tube the maximal possible deviation amounts to 5% (r_1=20 mm, r_2=21 mm). Since the edge length of the used voxel is much less than the wall thickness t=1 mm, the real value is significantly less. It has to be mentioned that a strict voxel geometry of the elements is not mandatory. The main objective is the generation of a very accurate mesh without any distorted elements.

In accordance to the general approach described in Fig. 4.14 each element of the newly generated mesh is assigned to the respective material, fibre or matrix. Since the interface between fibre and matrix shall not be treated by a separate material model within this work, all elements of the voxel mesh are assigned either to the matrix or to the fibre material. The individual steps of the matrix generation approach with respect to the complete tube are illustrated in Fig. 4.15 and 4.16. In Fig. 4.15 the generated smooth 3D fibre architecture is depicted on the left-hand side. On the right-hand side of Fig. 4.16 this smooth roving structure is surrounded by the voxel based matrix mesh (grey colour). The new detected fibre elements (blue colour) in comparison to the original roving structure (dark red colour) can be seen in Fig. 4.16 on the left-hand side. In order to precise the illustration and improve the visibility of the different roving meshes, the matrix elements are made transparent here. Finally, the complete composite mesh including the connected fibre and matrix domains is represented on the right-hand side of Fig. 4.16. To illustrate the distribution between fibre and matrix elements the final composite structure is decomposed in its individual constituents in Fig. 4.17, in which the fibre mesh is depicted on the left-hand side and the matrix mesh on the right-hand side. Referring to the initially imposed conditions, the requirements are hence satisfied by the proposed approach for the matrix implementation.
It has to be mentioned that due to the applied approach for the matrix incorporation, the local thickness change related to the fibre stack disappears. In contrast to the real structure the complete tube composite has a constant thickness after the procedure which becomes more apparent in Fig. 4.18.

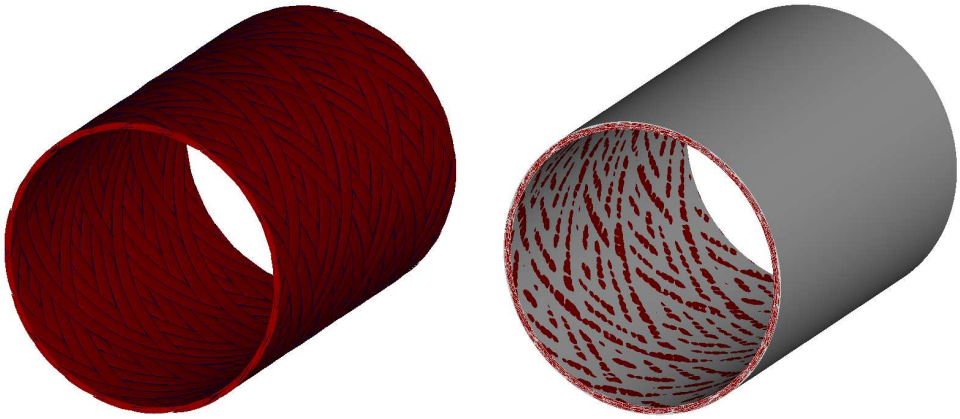

Figure 4.15: Virtual component composite generation - A) original smooth roving structure and new matrix voxel mesh overlay.

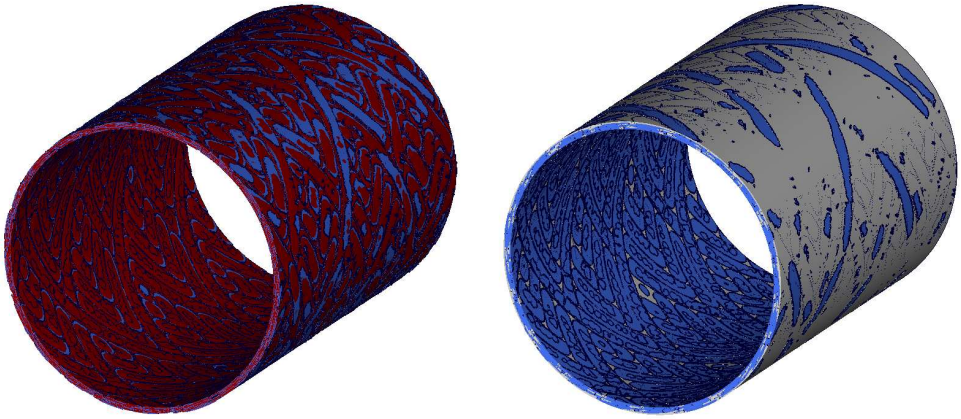

Figure 4.16: Virtual component composite generation - B) comparison of the smooth roving structure to the new voxel fibre elements and the final complete composite mesh.

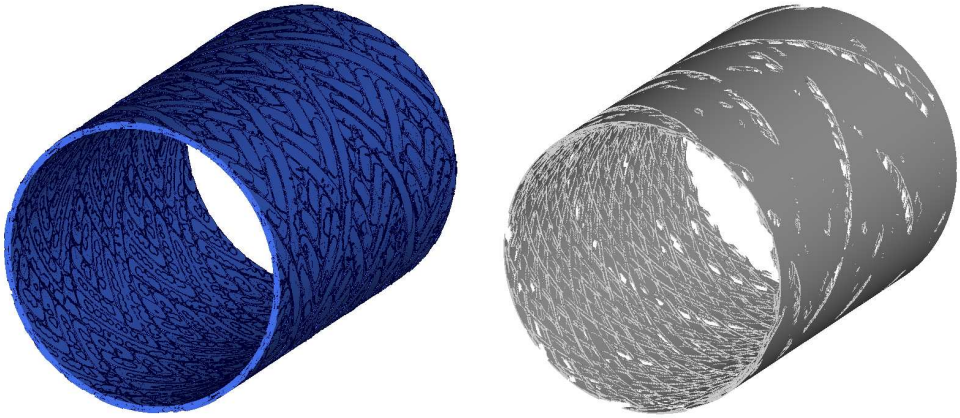

Figure 4.17: Virtual component composite model - decomposition of complete voxel mesh in fibre and matrix domains.

The procedure combined with a parameterised voxel mesh generation tool for tubes is implemented in a programme to enable the generation of various voxel mesh discretisations in a convenient way. This is necessary, since the voxel approach provides a loss of geometrical accuracy. The quality of the representation of the smooth roving structure strongly depends on the voxel size resolution. In order to assess this issue two different voxel mesh resolutions are considered for the wound tube composite: (A) a voxel mesh size l_{xyz}=0.1 mm and (B) a voxel mesh size l_{xyz}=0.2 mm. The choice of these two configurations is related to geometrical conditions given by the 3D fibre architecture. Fig. 4.18 reveals that due to the undulation of the rovings a stack of five layers can exist. In order to capture accurately the fibre orientation of each layer, at least five elements over the thickness are necessary. Consequently, the upper bound of the voxel size amounts l_{xyz}=0.2 mm. The lower bound is restricted by modelling and handling issues. Here, a half of the upper limit is chosen.

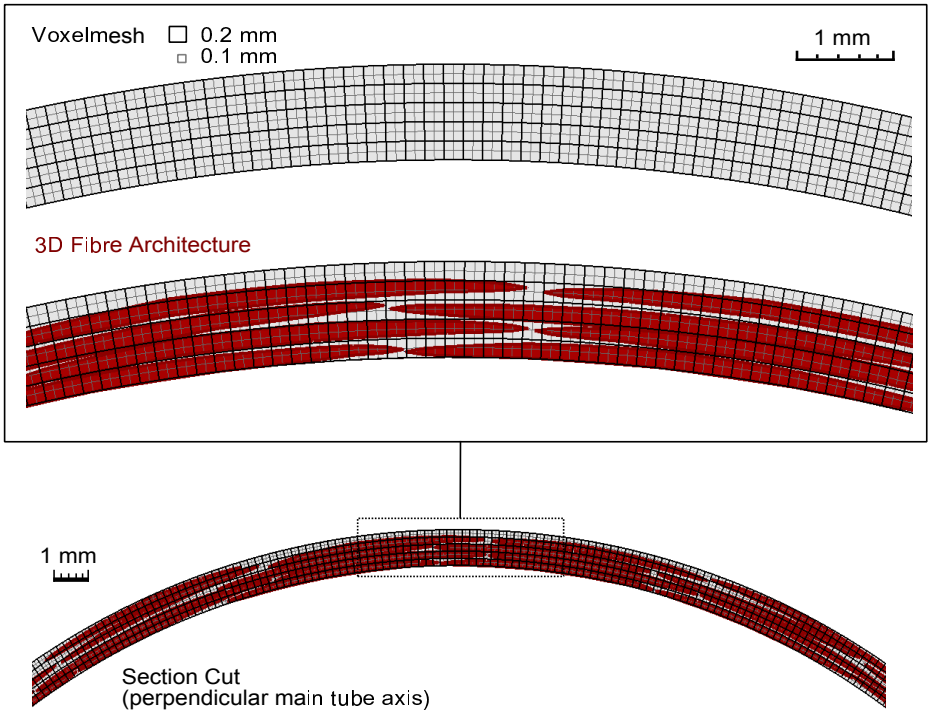

Figure 4.18: Comparison of voxel mesh resolution l=0.1 mm and l=0.2mm with respect to the smooth roving structure.

In Fig. 4.18, a section cut of both voxel mesh resolutions is illustrated in comparison to the smooth roving structure. Thereby, the coarser mesh resolution is represented by dark grey solid lines. It can be seen that this mesh size is sufficient to capture the individual composite layers. However, it becomes also apparent that the representation of the roving structure is rather rough in comparison to the higher resolution. In Fig. 4.19 and Fig 4.20 the results of the matrix generation procedure for both configurations are depicted (two views).

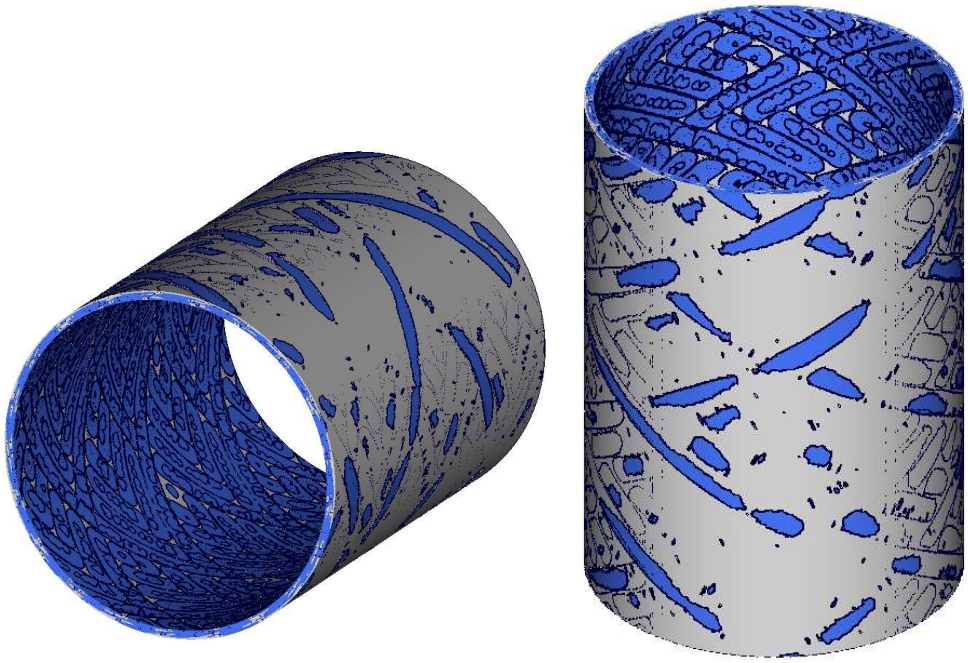

Figure 4.19: Finite element meso-model of the wound tube - voxel size l=0.1 mm.

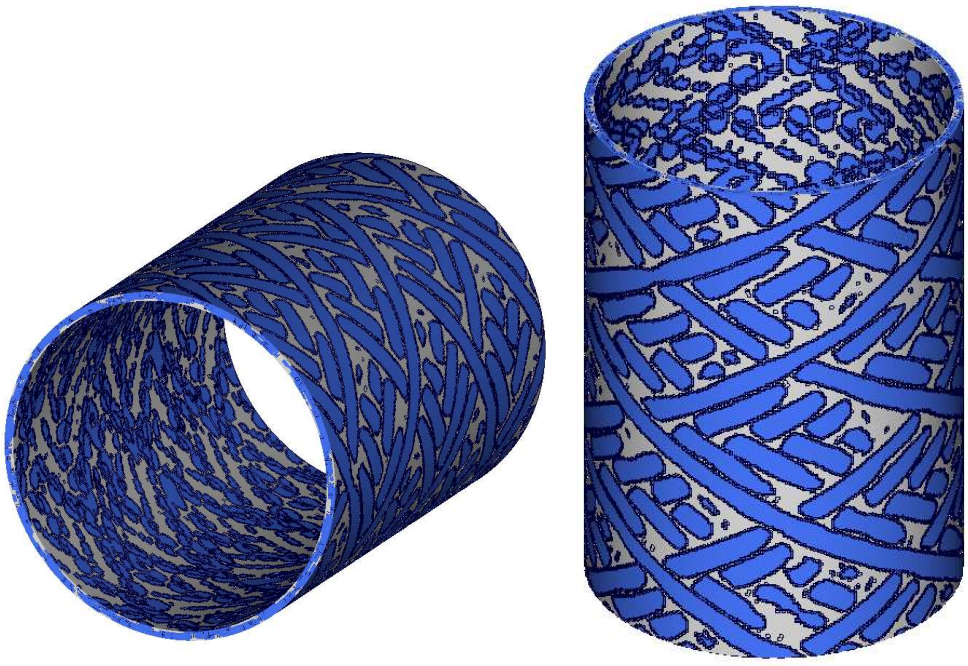

Figure 4.20: Finite element meso-model of the wound tube - voxel size l=0.2 mm.

Fig. 4.19 represents the finite element meso-model (A) and Fig. 4.20 model (B). Model (A) has already been used to demonstrate the application of the method on component level. Consequently, this image is identical to the one on the left-hand side of Fig. 4.16. The difference between the two models can be directly seen. In model (A) the outer roving layer is widely covered by matrix elements, whereas in model (B) most of the rovings are directly visible. This is related to the assignment of the voxel elements as fibre which in turns is controlled by the number of nodes of the respective voxel element, located in the roving structure. In order to provide a comparable fibre volume content for both models this adjustment differs. For model (A) elements with at least four nodes inside the roving structure are assigned as fibre, for model (B) this value amounts to two. Considering the outer layer in Fig. 4.18 reveals the corresponding impact to the fibre-matrix distribution.

	FE-Model A	FE-Model B
Target Element Length [mm]	0.1	0.2
Number of Elements over Thickness	10	5
Total Number of Elements	7,536,000	942,000
Total Number of Nodes	8,303,416	1,134,168

Table 4.2: Summary of the individual finite element models of the wound tube.

However, apart from accuracy also the related model size has to be taken into account. In Table 4.2 this is summarised for the respective configuration. It can be seen, that representing the fibre and matrix architecture of the wound tube by the voxel approach provides a large number of finite elements. The upper bound mesh size provides a meso-scale model with about one million elements. Increasing the resolution by factor two, increases the number of elements by factor eight. In combination with the related time step reduction of a half, this implies an computational effort which is sixteen times higher for model (A) than for model (B). Since model (B) can correctly represent the occurring layer stack including the orientations and because the computational effort is significantly lower, this model will be used within this work.

Limitations

The matrix implementation algorithm can provide local imprecision for the orientation of the new fibre elements. In the particular case, that four of the eight nodes of a voxel element are located in two different elements of the smooth roving structure, the relation of the fibre orientation is ambiguous. In this case the mapped fibre orientation is related to the last considered roving element. Increasing the voxel resolution can reduce this effect. In addition, as described above, the accuracy level depends on the voxel resolution. In order to reduce the occurring discontinuities, mesh refinements can be used. Apart from the

constant method shown here, also the possibility of selective or adaptive mesh refinements algorithm exist [84]. Also the X-FEM technology can be used to avoid this drawback [54]. However, in this work only the proposed approach is used.

Finally, the complete virtual manufacturing procedure, providing the geometry for the finite element meso-scale model of the wound tube can be summarised by the following steps:

(1) Simulation of the parameterised winding process,

(2) Derivation and simulation of the solid fibre architecture based on the results of the winding simulation and

(3) Generation of the final finite element composite model on meso-scale by using the voxel approach and fibre mapping.

It has to be mentioned that the chain is not complete from real manufacturing point of view since the final curing procedure of the composite structure is not included. However, since the simulation of the curing procedure constitutes a separate topic, the effects of this manufacturing step are not taken into account in this work. Consequently, no initial stress or strain conditions are applied to the meso-scale model.

4.3 Determination of Material Properties

As described in the General Approach Section 4.1 at the beginning of this chapter the base constituents of the composite, glass fibre and epoxy resin, are used in combination with a multi-scale approach to supply the geometry of the generated meso-model with appropriate material properties. In Fig. 4.21 this approach including the individual relations between scales and materials is depicted.

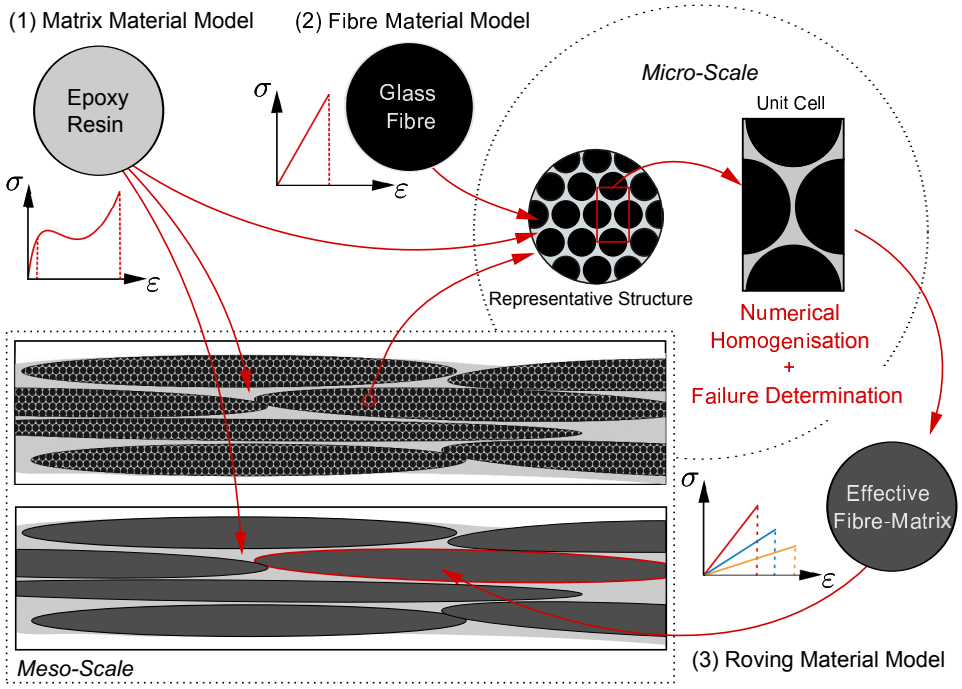

Figure 4.21: Multi-scale approach for the determination of appropriate material properties of the meso-scale model.

Based on calibrated simulation models for the epoxy resin and the glass fibre, effective properties of the roving structure are determined by micro-scale calculations for a representative structure of the roving. This includes a numerical homogenisation as well as a method for the determination of failure parameters. Thus, properties of a homogeneous roving structure are available. This is illustrated in the lower left part of Fig. 4.21 by two different images of a small roving domain on meso-scale in terms of a section cut. Consequently, in total three different material models are necessary for the meso-scale model:

(1) Material model for the glass fibre,

(2) Material model for the epoxy resin,

(3) Material model for the roving structure.

The proposed multi-scale approach combines micro- and meso-scale and is restricted to one direction. As a consequence, it represents an unidirectional

two-scale method without interaction of the individual scales. Thus, the mechanical behaviour of the meso-scale is defined by given states of deformation of the representative structure on micro-scale. Since the complete geometrical information of the component is available on meso-scale, the consideration on two scales is sufficient to describe the mechanical properties of the wound tube. In addition, this enables directly the use of unidirectional layer considerations on micro-scale for failure determination. Layer interaction and load distribution due to fibre undulation and orientation are captured by the geometrical representation of the roving structure on meso-scale. The derived effective material properties in combination with the constitutive law, presented in Section 2.3, are finally used to describe the mechanical behaviour of the roving structure. Accordingly, in the next sections firstly the individual material modelling and subsequently the effective properties determination are discussed. Apart from the numerical homogenisation, in which the implicit solver of VPS is used, all finite element simulations as well as the corresponding material modelling are conducted in VPS explicit (PAM-CRASH) [21].

4.3.1 Individual Material Modelling

Glass Fibre

Opposed to carbon fibres, the properties of glass fibres (or filaments) are isotropic which is related to the three-dimensional network structure of glass [50]. In addition the given material properties of E-Glass EC 1200-315 of Table 3.6 in Section 3.1.2 are restricted to the linear elastic domain and the glass fibres are represented by solid elements within this section. Consequently, a 3D isotropic linear elastic material model can be used to represent the mechanical behaviour of the glass fibre. This is given by MATERIAL TYPE 16 [23] which enables also the possibility to define element failure. The base properties, Young's modulus, Poisson's ratio, density and tensile strength, can directly be incorporated in the material model. Due to the simplicity of the material modelling for the glass fibres no further discussion is done here.

Epoxy Resin

In comparison to the glass fibre, the epoxy resin material modelling is significantly more complex. Reviewing the experimental investigations of Epoxy Resin L1100 EPH294 from Section 3.1.1 reveals that the matrix material is characterised by the following main items:

- Nonlinear stress-strain relation in compression and tension,
- Differences in tensile and compressive yielding,
- Differences in tensile and compressive strength.

A material model representing all of these properties is currently not available in VPS. Consequently, either simplifications have to be accepted or an appropriate user defined material model must be developed. Due to the complexity of the

mechanical behaviour of the resin and the related amount of work for such a development, the first possibility is realised in this work. In addition, due to weighting of the importance of material properties, the deviation can be kept in an acceptable range. Considering the stress-strain relation for compressive and tensile loading in Fig. 3.8 from Section 3.1.1 reveals that the nonlinearity for high compression and the sign dependence of the strength are essential for the characterisation of the epoxy resin. Hence, the tension-compression differences in yielding constitutes a proper way of simplification. In Fig. 4.22 the proposed approach is illustrated in which the red and blue curves schematically referring to an average of the measured compressive and tensile stress-strain relation, respectively.

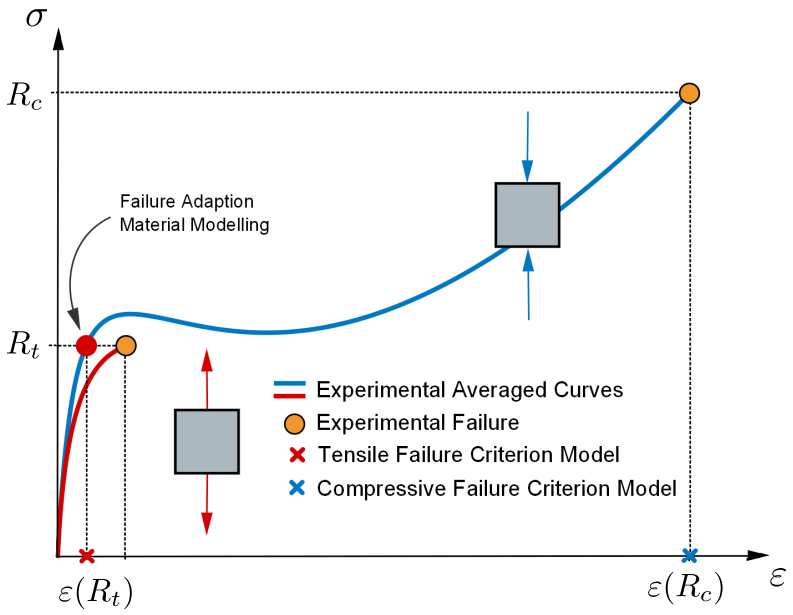

Figure 4.22: Schematic stress-strain relation for epoxy resin in terms of compressive and tensile loading.

It has been shown in Section 3.1.1, that the initial slope of the stress-strain curve under compressive and tensile loading captures a comparable range. Neglecting the difference in yielding, the behaviour in tension can be hence represented by the compression treatment. Consequently, the number of stress-strain curves reduces to one for all loading directions. However, this also implies that the experimentally determined tensile failure value has to be converted to the compressive loading function. Under the condition that the tensile strength R_t remains on the same level, the corresponding new failure strain $\varepsilon(R_t)$ can be calculated. This is illustrated in Fig. 4.22 in which the orange colour circle depicts the measured tensile value, the red colour circle the adaption to the compression function and the red cross the corresponding new tensile failure strain. In addition the blue cross represents the compressive failure strain $\varepsilon(R_c)$.
Due to the reduction to one common stress-strain curve the requirement to

the material model decrease to: nonlinear behaviour for large deformation and differentiation of compressive and tensile failure. The possibility to represent these characteristics in VPS is given by MATERIAL TYPE 52. It is an elastic-plastic solid material model with a failure criterion based on a formulation of Kolmogorov [23]. The model is using a linear hypoelastic stress rate relation, a decomposition of the rate of deformation tensor $\mathbf{d}$ into elastic and plastic parts as well as an isotropic yield criterion and an associative flow rule [20, 23]. It expects the stress-strain relation in terms of plastic strains over true stresses in combination with the definition of Young's modulus E and Poisson's ratio ν. Consequently, the experimentally determined strains ε from Section 3.1.1 have to be separated in elastic strains ε_e and plastic strains ε_p by

$$\varepsilon = \varepsilon_e + \varepsilon_p \quad . \tag{4.2}$$

Expression of the elastic part by Young's modulus and current stress σ provides a relation for the plastic strains based on the total strains ε and the corresponding stresses σ by

$$\varepsilon_p = \varepsilon - \frac{\sigma}{E} \quad . \tag{4.3}$$

Thereby, the beginning of the curve is given by the yield stress. The scope before the yield stress is covered by the Young's modulus and consequently represents linear elastic material behaviour. For the material modelling of the epoxy resin a mean stress-strain relation based on the average of all compressive curves from Section 3.1.1 is defined and subsequently converted to the required input by Eq. (4.3), a Young's modulus of 3.152 GPa and a yield stress of 0.050 GPa.

As mentioned above MATERIAL TYPE 52 incorporates the possibility of failure treatment based on a formulation of Kolmogorov. Thereby, the main feature is given by a weighted integral of the effective plastic strains [23]. For the objective of differentiation between tensile and compressive failure, it is sufficient to define the effective plastic strains as a function of the triaxiality factor η. Consequently, the weighted integral is be given by

$$\psi = \int_0^{\varepsilon_p} \frac{d\varepsilon_p}{\varepsilon_p(\eta)} \quad . \tag{4.4}$$

The fracture will occur if the critical value of $\psi = 1$ is reached. The triaxiality factor η for a state of deformation is defined in VPS by the trace of the stress tensor σ_{ii} divided by the equivalent von Mises stress σ_{eq} and can be expressed by

$$\eta = \frac{\sigma_{11} + \sigma_{22} + \sigma_{33}}{\sqrt{\sigma_{11}^2 + \sigma_{22}^2 + \sigma_{33}^2 - \sigma_{11}\sigma_{22} - \sigma_{22}\sigma_{33} - \sigma_{33}\sigma_{11} + 3(\sigma_{12}^2 + \sigma_{23}^2 + \sigma_{13}^2)}} \quad . \tag{4.5}$$

Considering, Eq. (4.5) for an uniaxial and an equivalent biaxial stress state, given by σ_0, directly reveals the relation between η and the occurring stresses.

$$[\sigma_{ij}] = \begin{bmatrix} \sigma_0 & 0 & 0 \\ 0 & 0 & 0 \\ 0 & 0 & 0 \end{bmatrix} \Rightarrow \eta = \begin{cases} 1 & \text{if } \sigma_0 > 0 \\ -1 & \text{if } \sigma_0 < 0 \end{cases} \tag{4.6}$$

$$[\sigma_{ij}] = \begin{bmatrix} \sigma_0 & 0 & 0 \\ 0 & \sigma_0 & 0 \\ 0 & 0 & 0 \end{bmatrix} \Rightarrow \eta = \begin{cases} 2 & \text{if } \sigma_0 > 0 \\ -2 & \text{if } \sigma_0 < 0 \end{cases} \tag{4.7}$$

In terms of uniaxial unrestricted loading the triaxiality factor becomes $\eta = 1$ for tension and $\eta = -1$ for free compression. The same differentiation between tensile and compressive loading can been seen for the equivalent biaxial stress state in which the value becomes $\eta = 2$ and $\eta = -2$, respectively. Consequently, this measure can be used to distinguish tensile and compressive failure for the resin material modelling. Using the mean failure strains provided by the experimental investigations of Section 3.1.1 a ε_p-η relation can be defined.

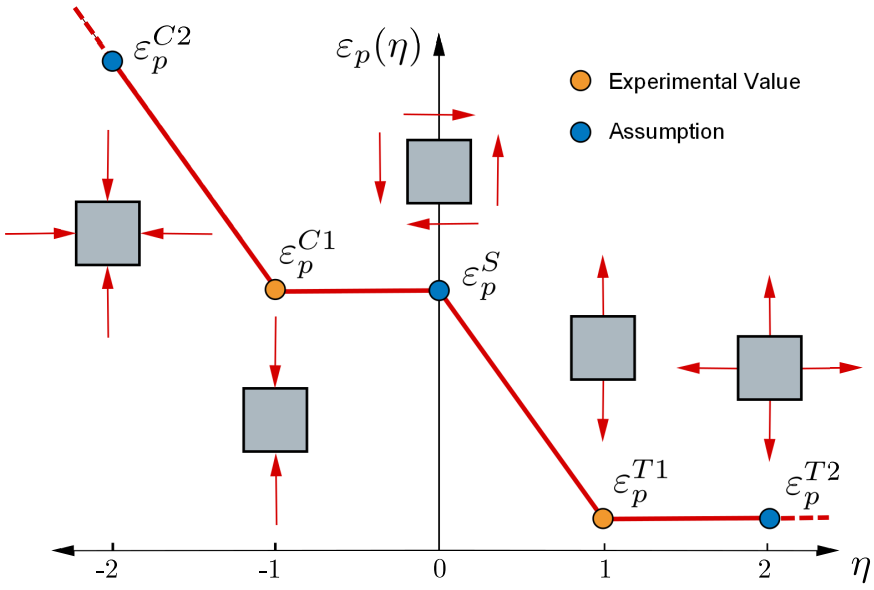

Figure 4.23: Failure modelling for epoxy resin based on ε_p-η relation.

In Fig. 4.23 the defined ε_p-η dependency for the epoxy resin is illustrated in which the experimental determined failure strains are marked by orange colour circles. As mentioned in Section 3.1.1 the evaluation of the experimental failure strains are based on the assumption of a homogeneous state of strain for the tension as well as for the compression tests. As a consequence, these values can directly be assigned to $\eta = 1$ and $\eta = -1$, respectively, after the conversion to plastic strains. In the following, a plastic strain failure value referring to $\eta = 1$ is denoted by ε_p^{T1} and a value referring to $\eta = -1$ by ε_p^{C1}.

In addition, three assumptions (blue colour marked) are made to enhance the ε_p-η relation. Firstly, a strain failure value for $\eta = 0$, which is related to a pure shear loading, is defined and set to the value for uniaxial compression. In [29] epoxy resin investigations have shown that the failure strain under shear loading is significantly higher than in uniaxial compressive loading. Since no detailed information of shear failure for the used epoxy resin is available, it is assumed for this work, that the epoxy cannot fail under shear loading due to a strain lower than the uniaxial compressive limit. The plastic strain limit related to $\eta = 0$ is denoted by ε_p^S. Furthermore, it is assumed that the failure strain increases for multiaxial compressive loading. Therefore, a linear progression based on the slope gained by ε_p^S and ε_p^{T1} is used to define a strain limit for an equivalent biaxial compressive stress state. In terms of an equivalent biaxial tensile stress state, no influence shall appear for the resin in this work. In accordance to the denotation above the values related to $\eta = 2$ and $\eta = -2$, are ε_p^{T2} and ε_p^{C2}, respectively. Finally, a linear extrapolation rule is used to cover possible stress states out of the defined range shown in Fig. 4.23.

Thus, all necessary parameters for the epoxy resin material modelling based on MATERIAL TYPE 52 are given and summarised in Table 4.3.

Material Modelling Epoxy Resin L1100 EPH294			
Stiffness Properties			
Young's Modulus	E	3.152	[GPa]
Poisson's Ratio	ν	0.39	[-]
Density	ρ	1.34e-6	[kg/mm^3]
Yield Stress	σ_y	0.050	[GPa]
σ-ε_p Relation	Averaged mean compression curve		
Failure Properties			
Compressive Plastic Failure Strain (η=-2)	ε_p^{C2}	0.979	[-]
Compressive Plastic Failure Strain (η=-1)	ε_p^{C1}	0.657	[-]
Shear Plastic Failure Strain (η=0)	ε_p^{S0}	0.657	[-]
Tensile Plastic Failure Strain (η=1)	ε_p^{T1}	0.013	[-]
Tensile Plastic Failure Strain (η=2)	ε_p^{T2}	0.013	[-]

Table 4.3: Finite element material model properties for epoxy resin L1100 EPH294 based on MATERIAL TYPE 52.

In order to assess the quality of the approach, the experiments from Section 3.1.1 are simulated, based on the material modelling strategy described above. Thereby, all boundary conditions are imposed according to the real test set up and the specimens are modelled by finite solid elements with an average element length of about 1 mm. The comparison of experiments and simulation, in terms of force-displacement relation, is given in Fig. 4.24 in which the left-hand-side diagram refers to the tension tests and the right-hand-side one to the compression tests. The experimental data are depicted by grey solid lines

and the results of the simulation by red solid lines. The additional green curve for the tensile loading shows the influence of the simplification to one common stress-strain function. For this assessment a material card based on the tensile stress-strain relation has been generated and simulated by applying the same boundary conditions.

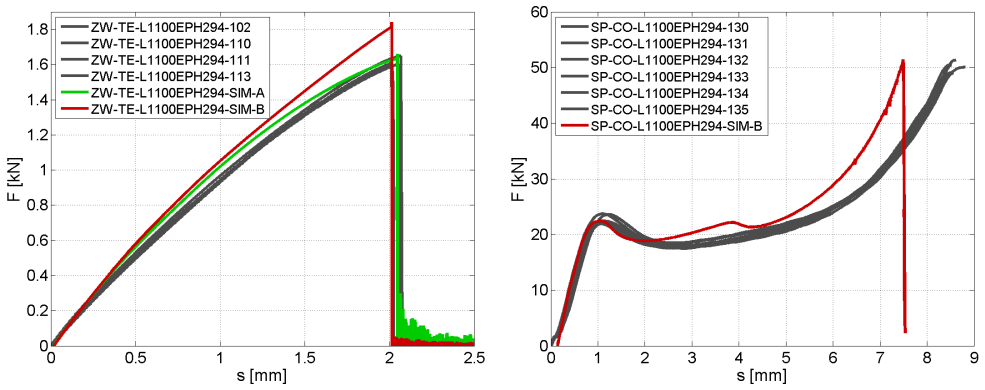

Figure 4.24: Force-displacement comparison of simulation and experiment under a) tensile loading and b) compressive loading.

It becomes apparent that using the original curve a very good approximation by the simulation is given. However, comparing both curves makes the stiffening due to the simplification of the material model approach visible. In total an error of about 10% with respect to the occurring forces, until tensile failure, is introduced by using the proposed approach.
Consideration of the force-displacement behaviour for compressive loading in Fig. 4.24 shows a good correlation of the material model to the experimental data. In particular the initial domain is approximated very well by the simulation. This quality decreases by increasing deformation and is most likely related to the assumption of an homogeneous strain state. Based on this assumption the current cross-section is calculated in the experimental data evaluation procedure which directly affects the stress calculation. In terms of high strains this assumption seems not to be sufficient to represent exactly the resin behaviour. As a consequence the simulation model shows a stiffer prediction in this domain. However, the force level for the specimen fracture is captured well and thus the overall approximation of the material by the proposed modelling approach is satisfying. The intermediate slope of the simulation curve is related to the mesh size and disappears in terms of a very fine mesh (see Fig. 4.25). This is related to the difference in distribution of plastic deformation for various mesh sizes which is smoother for finer meshes.

Finally, the influence of the element size with respect to the failure behaviour is considered. Therefore, additional simulations of the tension and compression tests with an element length of about 0.5 mm have been conducted. The influence of the mesh size on the fracture is given in Table 4.4 in which the validated failure values for the smaller mesh size are represented in comparison to those obtained for the reference element size of 1 mm. As can be seen, the values

Element Size	ε_p^{C2}	ε_p^{C1}	ε_p^{S0}	ε_p^{T1}	ε_p^{T2}
1.0 mm (Reference)	0.979	0.657	0.657	0.013	0.013
0.5 mm (Validated)	0.989	0.664	0.664	0.011	0.011
0.1 mm (Extrapolation)	0.997	0.669	0.669	0.009	0.009

Table 4.4: Influence of element size for fracture modelling of epoxy resin.

need to be increased for compressive and decreased for tensile loading. The necessary decrease of the failure limit for tension is related to a redistribution of the load to more elements which reduces the strains in the local domain of the specimen. In contrast the full solid compression specimen behaves softer for a smaller element size which provides higher local strains and consequently needs an increase of the failure limit. However, the correction in terms of compression is minor. In order to provide limits for smaller element sizes a linear extrapolation of the validated values is done. This procedure shall minimise the influence of the element size on the fracture of the resin material in simulation. To verify the assumption of linear extrapolation one simulation with a very fine mesh (element size about 0.1 mm) of the compression specimen has been conducted in which the extrapolated values from Table 4.4, last row, are used. The corresponding force-displacement relation is depicted in Fig. 4.25. In the diagram all mesh sizes are compared to the experimental data. SIM-B corresponds to the reference mesh size of 1mm, SIM-C and SIM-D to 0.5 mm and 0.1 mm, respectively. The force level is captured well with the fine mesh, which proves the assumption of linear extrapolation. In addition the aforementioned influence of the mesh size on the curve progression is visible. In order to emphasise the quality of the material modelling, finally the deformation with respect to the very fine mesh is considered. In Fig. 4.26 a comparison between simulation and experiment is shown for three different states. The upper row is referring to the initial configuration, the second line represents an intermediate state and the last two images show the specimen directly before the total failure. It can be seen that using this fine mesh in combination with the adapted values, the failure and the deformation mode under high compressive loading can be captured well by the simulation. This reveals the quality of the applied approach for the resin material modelling. In following sections the resin failure values corresponding to the individual mesh size are used.

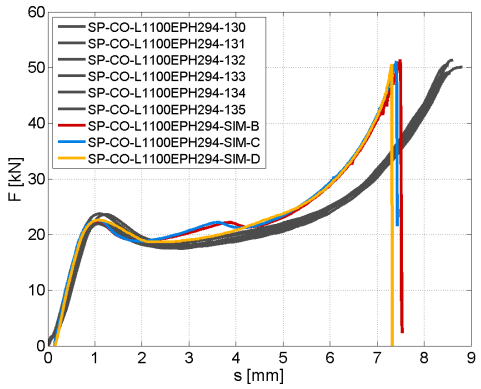

Figure 4.25: Force-displacement comparison of simulation and experiment under compressive loading for different element sizes (B- 1mm, C-0.5mm, D-0.1mm.

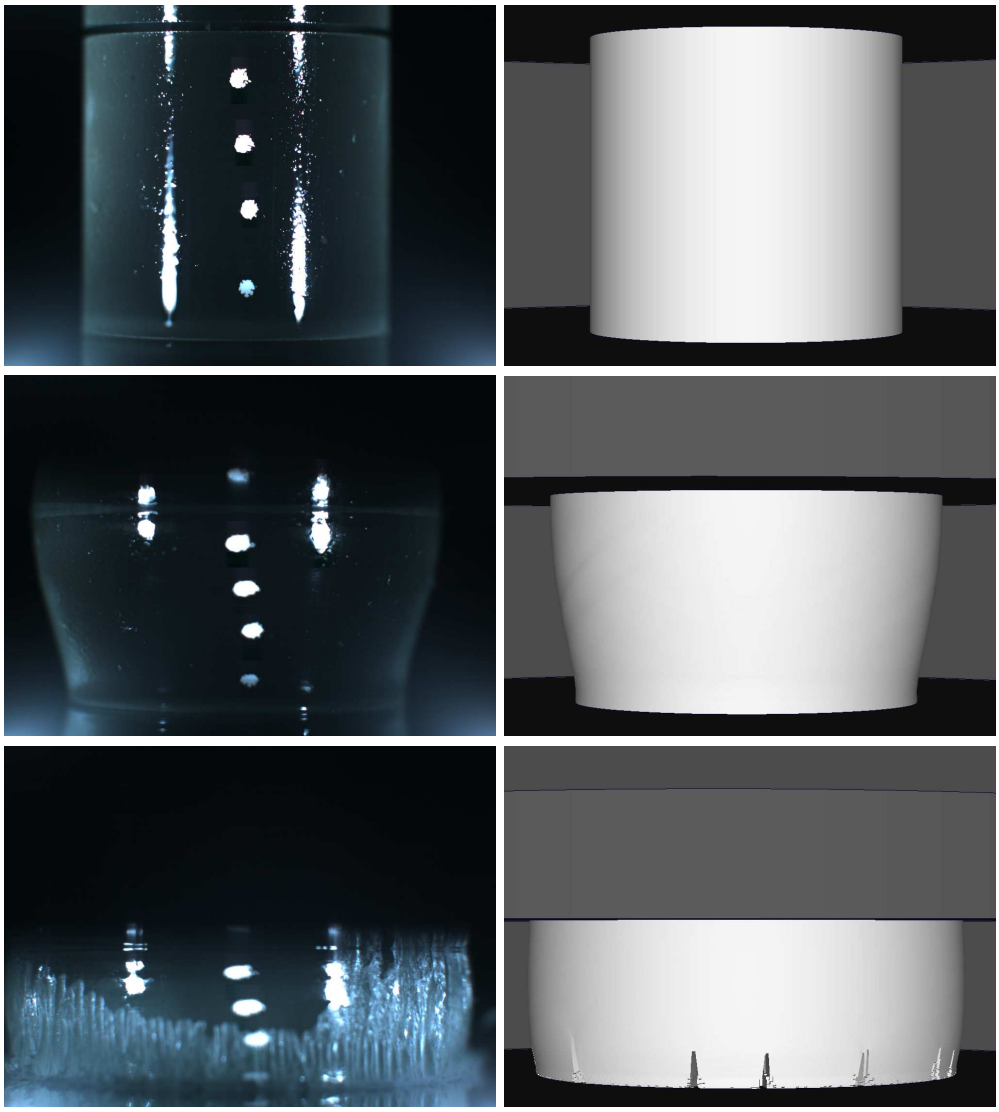

Figure 4.26: Comparison of simulation (0.1 mm mesh) and experiment for different states of deformation.

Limitations

The proposed approach provides an error in tension behaviour due to the use of one common stress-strain relation. Assumptions are incorporated for the prediction of fracture in terms of shear as well as of multiaxial tensile and compressive loading. In addition, the material modelling does not take into account strain rate dependency which is related to the missing of material data as mentioned in Section 3.1.1. However, the incorporation of strain rate dependent stress-strain relations and failure definitions is possible with MATERIAL TYPE 52.

4.3.2 Effective Material Properties of Roving Structure

The determination of the effective properties of the roving structure is based on micro-scale calculations. As mentioned in Section 2.4 two main conditions have to be satisfied in order to get an appropriate approximation of the effective quantities by multi-scale considerations. The heterogeneous base structure must be representative for the considered domain and the ratio of the small scale length to the large scale length must be much less than one [36]. In order to fulfil the former requirement it is assumed that the fibre-matrix distribution of the roving structure on micro-scale can be represented by a unidirectional hexagonal arrangement of the fibres. This is illustrated in Fig. 4.27 in which a small subdomain of the roving structure is depicted and the white line hexagon emphasises the type of arrangement.

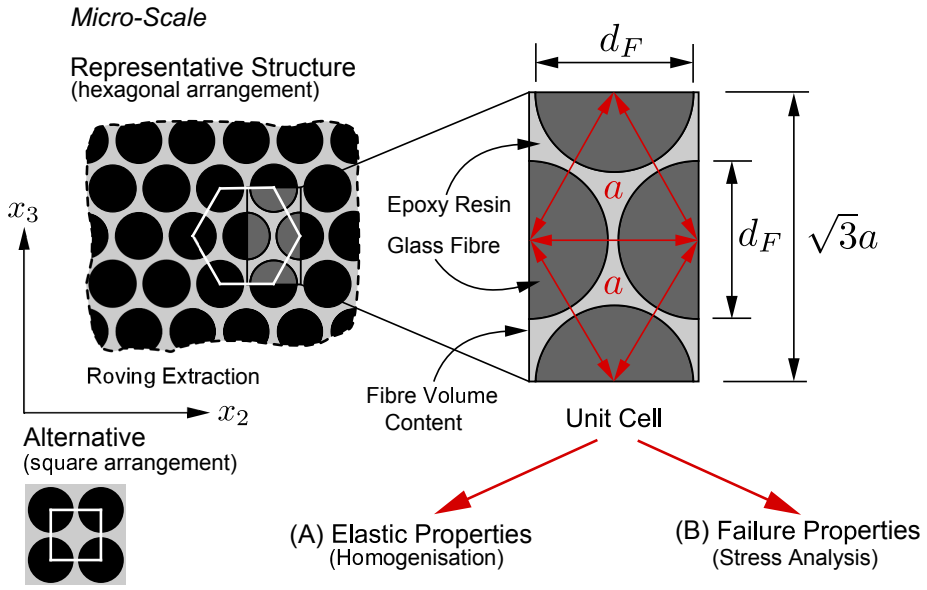

Figure 4.27: Hexagonal unit cell of the representative roving structure on micro-scale.

The choice of this type is based on the fibre volume content provided by the experimental investigations of Section 3.2.2 in which a value of v_f=0.773 for the micro-scale is given. This value can only be well represented by a hexagonal arrangement. In terms of a square fibre arrangement, which is exemplarily shown in the lower left part of Fig. 4.27, the maximum possible fibre volume content is limited to $\frac{\pi}{4}$. However, this already implies a touch of the individual fibres. Consequently, the square arrangement is not suited to represent fibres completely surrounded by matrix in terms of high fibre volume content.
The hexagonal representative structure can be reduced to a unit cell shown on the right hand-side of Fig. 4.27. Due to the hexagonal arrangement and the related constant distance a between all fibres, the geometry of the unit cell can be completely characterised by the fibre diameter d_F and the fibre volume content v_f. In combination with the voxel mesh method the generation of finite

element unit cell models can be completely automatised.
The potential of this method for micro-scale unit cells of textile composites for finite element analysis has been shown by Swan et al. [84]. Rolfes et al. [77] and Ernst et al. [19] use the voxel mesh in damage mechanics of unit cells within the scope of multi-scale consideration. And Mishnaevsky [68] proposes an automated voxel mesh generation procedure to analyse composite structures on micro-scale. The main advantage of the voxel mesh method is here the minimisation of mesh dependency and the high potential of automation. In addition, the method simplifies the application of periodic boundary conditions. Therefore, the voxel mesh approach is used for the determination of effective properties in this work. The voxel mesh creation is incorporated in a programme which enables the generation of unidirectional 3D unit cells based on fibre volume content, fibre diameter and voxel element size in a convenient way. Thereby, the third dimension is given by the fibre direction and is equal to a. Furthermore, it is defined that for unidirectional layer considerations the fibre direction corresponds to the first axis of a Cartesian coordinate system. In Fig. 4.28 the finite element model of a hexagonal unit cell is illustrated in frontal view.

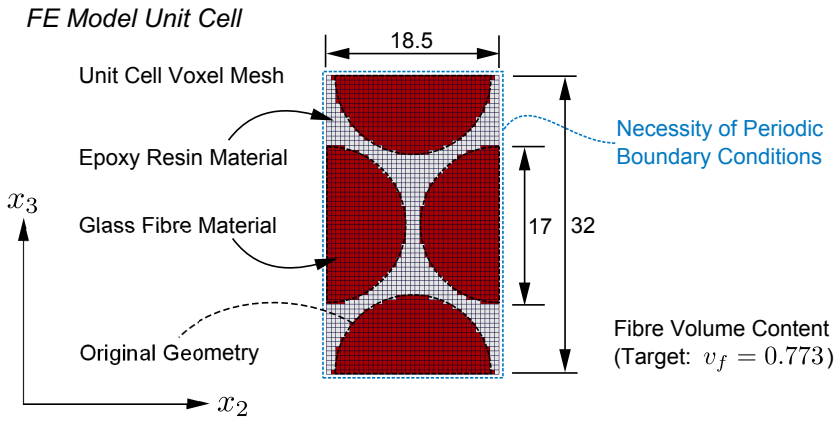

Figure 4.28: Hexagonal unit cell of the representative roving structure on micro-scale (all length dimensions in μm).

Thereby, d_F and v_f have been applied according to the experimental values from Section 3.1.2 and Section 3.2.2, respectively. The mesh size in the shown example amounts to 0.5 μm. In addition, the ideal circular geometry is depicted to demonstrate the loss of accuracy by using this approach. The fibre-matrix assignment is based on geometrical check procedure of real fibre surface within the voxel mesh. As a consequence the target and reached fibre volume content can vary in dependency of the voxel mesh. In Table 4.5 the influence of the voxel size to the nominal fibre volume content of 0.773 is summarised.
It is visible that fibre volume V_F and matrix volume V_M may change with the voxel size. Moreover a deviation of the total volume V_{TOT} can be seen. This is related to the voxel mesh generation algorithm which is advised to exactly keep the imposed element size. Consequently, the height, width and depth of the

Voxel Size [μm]	V_{TOT} [μm^3]	V_F [μm^3]	V_M [μm^3]	v_f [-]	Δ v_f [%]
1.0	10368	8064	2304	0.7778	0.62
0.9	10206	8048	2158	0.7886	2.01
0.8	10834	8314	2520	0.7674	-0.72
0.7	10666	8133	2533	0.7625	-1.36
0.6	11001	8410	2591	0.7645	-1.10
0.5	10951	8352	2599	0.7627	-1.34

Table 4.5: Reached fibre volume content v_f of hexagonal voxel mesh unit cells and its deviation to the nominal defined fibre volume content of 0.773.

unit cell can only be an integer number of the voxel size which provides slight geometric differences. For the considered mesh sizes the maximum deviation to the perfect geometry (a=18.41 μm) amounts to 3% in maximum.
Finally, the length scale ratio between unit cell dimensions and roving size is evaluated to assess the second requirement for using the multi-scale approach. Considering the average width b_{meso} of the roving obtained from Section 3.2.1 and the width of the unit cell b_{micro} from Fig. 4.28 provides

$$\frac{b_{\text{micro}}}{b_{\text{meso}}} = \frac{0.0185}{3.17} \approx 0.01 \ll 1 \quad \text{and} \quad \frac{h_{\text{micro}}}{h_{\text{meso}}} = \frac{0.032}{0.28} \approx 0.11 \ll 1 \tag{4.8}$$

for the respective heights h_{meso} and h_{micro}. Consequently, the conditions for the multi-scale analysis are satisfied.

Elastic Properties

The numerical homogenisation approach shown in Section 2.4 is applied to the unit cell to provide elastic constants for the roving structure. Therefore, firstly the effective stiffness tensor $\bar{C}_{ijkl}$ is calculated and subsequently inverted to derive nine elastic engineering constants, namely

- E_{11}, E_{22}, E_{33} - the elastic moduli in the three main directions,
- G_{12}, G_{23}, G_{13} - the shear moduli in the three main planes and
- ν_{12}, ν_{23}, ν_{13} - the Poisson's ratios in the three main planes.

Thereby, the first index refers to normal direction of the acting plane and the second one indicates the acting direction. The obtained engineering constants can be directly incorporated in the explicit USER MATERIAL routine proposed in Section 2.3.3.

The calculation of $\bar{C}_{ijkl}$ is based on finite element analyses of the unit cell for the six deformation modes and Eq. (2.68) as described in Section 2.4. Since elastic constants are of interest, an implicit linear static analysis is appropriate to determine the state of stress due to a prescribed deformation. Consequently, the calibrated resin and fibre materials are degenerated to pure elastic behaviour without failure. The resulting material properties for the numerical homogenisation are shown in Table 4.6.

Material Properties Homogenisation	E [GPa]	ν [-]	ρ [kg/mm^3]
Epoxy Resin	3.152	0.39	1.34e-6
Glass Fibre	75.0	0.25	2.54e-6

Table 4.6: Finite element material model properties for numerical homogenisation.

In order to impose periodicity at the outer surfaces of the unit cell, additional equations for opposing nodes are integrated in the finite element model. The principal scheme for the definition of such linear constraints is exemplarily shown in Fig. 4.29.

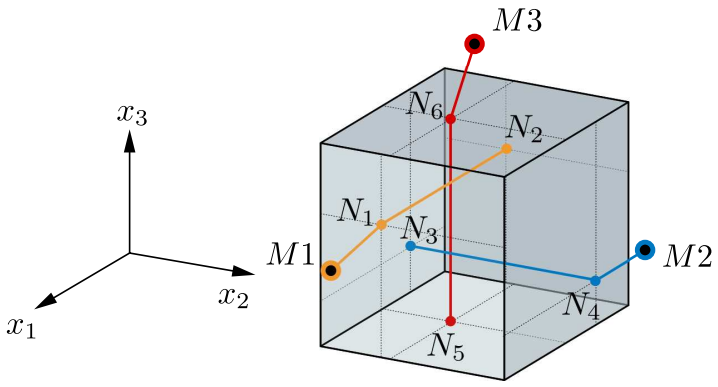

Figure 4.29: Scheme of definition of linear constraint equations to ensure periodic boundary conditions.

Here N_1, N_4 and N_6 represent arbitrary nodes of the finite element mesh located on the positive surfaces (outward normal in main direction) of the unit cell. N_2, N_3 and N_5 are the corresponding nodes on the opposing surfaces satisfying

$$N_2(x_2) = N_1(x_2) \quad , \quad N_2(x_3) = N_1(x_3) \quad , \tag{4.9}$$

$$N_4(x_1) = N_3(x_1) \quad , \quad N_4(x_3) = N_3(x_3) \quad , \tag{4.10}$$

$$N_5(x_1) = N_6(x_1) \quad , \quad N_5(x_2) = N_6(x_2) \quad . \tag{4.11}$$

In addition, one free master M node is defined for each positive surface. The location of the master nodes $M1$, $M2$, $M3$ can be arbitrary, but are set close to the respective surface here. The displacements u_i of the node on the positive surface are now expressed by the displacements of the opposing node and the respective master node. For the considered example this implies:

$$u_i^{(N_2)} = u_i^{(N_1)} + u_i^{(M1)} \quad , \tag{4.12}$$
$$u_i^{(N_4)} = u_i^{(N_3)} + u_i^{(M2)} \quad , \tag{4.13}$$
$$u_i^{(N_6)} = u_i^{(N_5)} + u_i^{(M3)} \quad . \tag{4.14}$$

Using the master nodes to impose prescribed boundary conditions the periodicity is given. For instance the strain field $\bar{\varepsilon}_{11}^0$ can be represented by the displacement mode

$$\vec{u}^{\,(M1)} = \begin{pmatrix} \alpha \\ 0 \\ 0 \end{pmatrix} \quad , \quad \vec{u}^{\,(M2)} = \begin{pmatrix} 0 \\ 0 \\ 0 \end{pmatrix} \quad , \quad \vec{u}^{\,(M3)} = \begin{pmatrix} 0 \\ 0 \\ 0 \end{pmatrix} \quad . \tag{4.15}$$

in which α is the scalar value for the imposed displacement. Accordingly, $\bar{\varepsilon}_{23}^0$ is given in the same manner by

$$\vec{u}^{\,(M1)} = \begin{pmatrix} 0 \\ 0 \\ 0 \end{pmatrix} \quad , \quad \vec{u}^{\,(M2)} = \begin{pmatrix} 0 \\ 0 \\ \frac{\alpha}{2} \end{pmatrix} \quad , \quad \vec{u}^{\,(M3)} = \begin{pmatrix} 0 \\ \frac{\alpha}{2} \\ 0 \end{pmatrix} \quad . \tag{4.16}$$

Applying the linear constraints to each node of the positive surfaces of the unit cell mesh, in combination with the three master nodes, provides all necessary boundary conditions to impose the six strain fields as well as ensures periodicity for the entire finite element model.

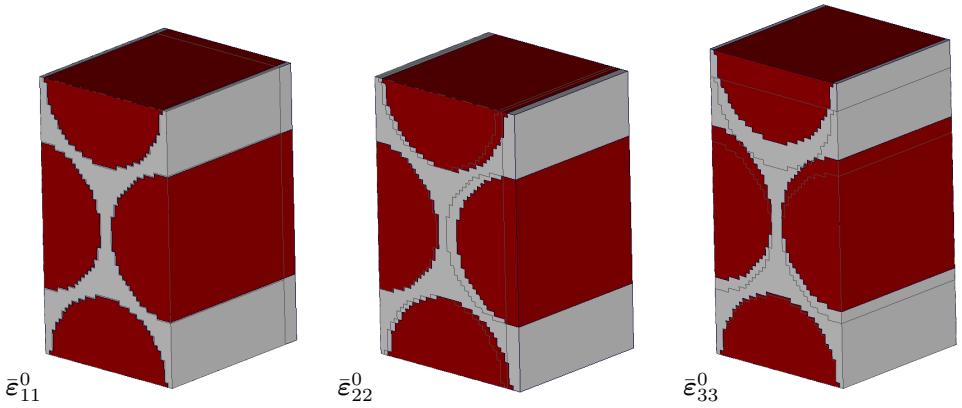

Figure 4.30: Deformation of unit cell for imposed strain fields $\bar{\varepsilon}_{11}^0$, $\bar{\varepsilon}_{22}^0$ and $\bar{\varepsilon}_{33}^0$.

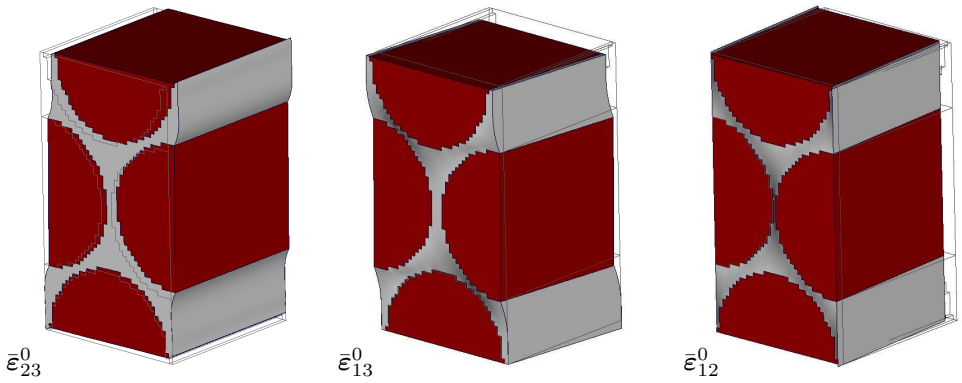

Figure 4.31: Deformation of unit cell for imposed strain fields $\bar{\varepsilon}^0_{23}$, $\bar{\varepsilon}^0_{13}$ and $\bar{\varepsilon}^0_{12}$.

In Fig. 4.30 and Fig. 4.31 the resulting deformation for the six applied strain fields $\bar{\varepsilon}^0_{11}$, $\bar{\varepsilon}^0_{22}$, $\bar{\varepsilon}^0_{33}$, $\bar{\varepsilon}^0_{23}$, $\bar{\varepsilon}^0_{13}$, $\bar{\varepsilon}^0_{12}$ are illustrated. These simulations are based on a voxel mesh size of 0.5 μm, the material properties of Table 4.6 and a nominal imposed strain of 0.1 and 0.05, respectively. In addition, the undeformed shape is depicted by grey thin lines in each figure. Fig. 4.30 shows the three normal modes and Fig. 4.31 represents the three shear modes. In particular, the latter reveals the effect of applying periodic boundary conditions to the structure.

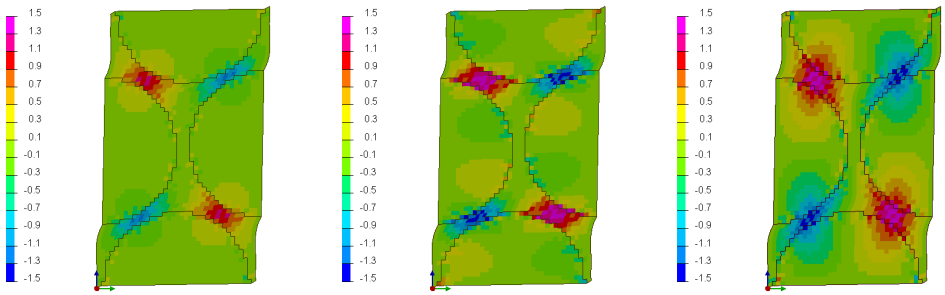

Figure 4.32: Stress results σ_{11}, σ_{22} and σ_{33} due to prescribed strain field $\bar{\varepsilon}^0_{23}$

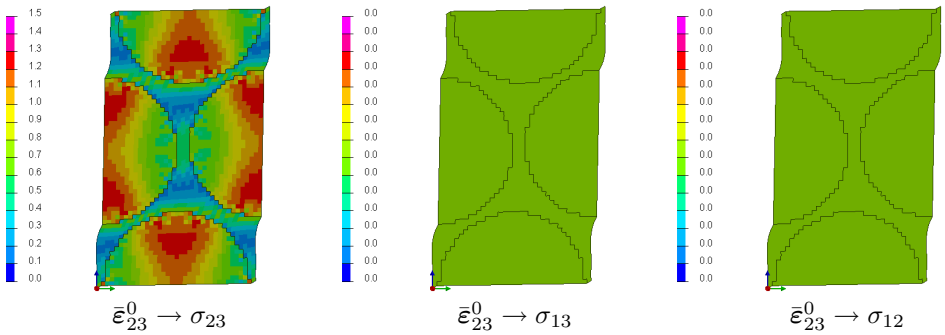

Figure 4.33: Stress results σ_{23}, σ_{13} and σ_{12} due to prescribed strain field $\bar{\varepsilon}^0_{23}$

In order to verify the periodicity, the results due to the strain field $\bar{\varepsilon}^0_{23}$ are exemplarily evaluated. In Fig. 4.32 and Fig. 4.33 the six components of the stress tensor σ_{ij} are depicted for the final deformed state in $x_2 - x_3$-plane. Thereby, the maximum occurring element stresses are illustrated. Considering the deformation it is visible that an entire structure can be represented by any composition of the unit cell. In addition, also each stress component shows periodicity at the boundary. This is related to the additional constraint equations which impose constant displacements u_i between nodes for opposing surfaces and can be interpreted as a condition for stress relaxation on boundary. Thus, the applied boundary conditions ensure a periodic, representative behaviour of the unit cell.
The corresponding element stresses due to the prescribed strain field are collected in a post evaluation procedure for the individual load cases. Thereby, also the volume of each finite element is calculated. Thus, the related component of $\bar{C}_{ijkl}$ is given by the volume average of the stresses and the applied strain by Eq. (2.68) from Section 2.4. Hence, $\bar{C}_{ijkl}$ is completely determined by the six deformations modes and becomes, using the Voigt notation for matrix representation:

$$\bar{C}_{ijkl} = \begin{bmatrix} 63.9633 & 10.9035 & 10.7894 & 0.0000 & 0.0000 & 0.0000 \\ 10.9035 & 28.0081 & 11.3764 & 0.0000 & 0.0000 & 0.0000 \\ 10.7894 & 11.3764 & 27.5260 & 0.0000 & 0.0000 & 0.0000 \\ 0.0000 & 0.0000 & 0.0000 & 7.9776 & 0.0000 & 0.0000 \\ 0.0000 & 0.0000 & 0.0000 & 0.0000 & 7.2946 & 0.0000 \\ 0.0000 & 0.0000 & 0.0000 & 0.0000 & 0.0000 & 7.3862 \end{bmatrix} \quad [\text{GPa}] \quad .$$

It can be seen that the homogenisation procedure provides a symmetric effective stiffness tensor. Since e.g. $\bar{C}_{1122}$ and $\bar{C}_{2211}$ are calculated twice due to $\bar{\varepsilon}^0_{11}$ and $\bar{\varepsilon}^0_{22}$, respectively, this reveals also the plausibility of the obtained results. In addition it becomes apparent that the homogenisation procedure of the unidirectional unit cell provides an effective stiffness tensor which characterise orthotropic material behaviour. Moreover, the hexagonal arrangement of the fibres further simplifies this to transversal isotropic behaviour. However, due to the minor differences between $\bar{C}_{2222}$ and $\bar{C}_{3333}$ as well $\bar{C}_{1212}$ and $\bar{C}_{1313}$ the condition for such a behaviour is not exactly given. This is related to the approximation of the geometry by the voxel method. Comparable calculations with a standard finite element mesh show almost identical results for the same components. Due to the orthotropic material behaviour a non-ambiguous relation between $\bar{C}^{-1}_{ijkl}$ and the engineering constants is given. Inverting $\bar{C}_{ijkl}$ yields to the effective compliance matrix $\bar{N}_{ijkl}$ given by:

$$\bar{N}_{ijkl} = \begin{bmatrix} 0.0173 & -0.0048 & -0.0048 & 0.0000 & 0.0000 & 0.0000 \\ -0.0048 & 0.0442 & -0.0164 & 0.0000 & 0.0000 & 0.0000 \\ -0.0048 & -0.0164 & 0.0450 & 0.0000 & 0.0000 & 0.0000 \\ 0.0000 & 0.0000 & 0.0000 & 0.1254 & 0.0000 & 0.0000 \\ 0.0000 & 0.0000 & 0.0000 & 0.0000 & 0.1371 & 0.0000 \\ 0.0000 & 0.0000 & 0.0000 & 0.0000 & 0.0000 & 0.1354 \end{bmatrix} \quad \frac{1}{[\text{GPa}]} \quad .$$

According to [2] the relations between the engineering elastic constants and $\bar{N}_{ijkl}$ are given by

$$\bar{N}_{ijkl} = \begin{bmatrix} \frac{1}{E_{11}} & \frac{-\nu_{21}}{E_{22}} & \frac{-\nu_{31}}{E_{33}} & 0 & 0 & 0 \\ \frac{-\nu_{12}}{E_{11}} & \frac{1}{E_{22}} & \frac{-\nu_{32}}{E_{33}} & 0 & 0 & 0 \\ \frac{-\nu_{13}}{E_{11}} & \frac{-\nu_{23}}{E_{22}} & \frac{1}{E_{33}} & 0 & 0 & 0 \\ 0 & 0 & 0 & \frac{1}{G_{23}} & 0 & 0 \\ 0 & 0 & 0 & 0 & \frac{1}{G_{13}} & 0 \\ 0 & 0 & 0 & 0 & 0 & \frac{1}{G_{12}} \end{bmatrix} \quad , \tag{4.17}$$

which provide the elastic effective constants represented in Table 4.7. In addition, the symmetry of $\bar{N}_{ijkl}$ and Eq. (4.17) give the following relation for the Poisson ratios

$$\nu_{21} = \frac{E_{22}\nu_{12}}{E_{11}} \quad , \quad \nu_{32} = \frac{E_{33}\nu_{23}}{E_{22}} \quad , \quad \nu_{31} = \frac{E_{33}\nu_{13}}{E_{11}} \quad . \tag{4.18}$$

Thus, the definition of ν_{12}, ν_{23} and ν_{13} is sufficient to completely determine the material behaviour. Consequently, the number of elastic constants reduce to nine.

E_{11} [GPa]	E_{22} [GPa]	E_{33} [GPa]	G_{23} [GPa]	G_{13} [GPa]	G_{12} [GPa]
57.9374	22.6091	22.2272	7.9777	7.2945	7.3861
ν_{23} [-]	ν_{13} [-]	ν_{12} [-]	ν_{32} [-]	ν_{31} [-]	ν_{21} [-]
0.3710	0.2775	0.2764	0.1067	0.3645	0.1085

Table 4.7: Effective elastic constants for the roving structure for mesh size 0.5 μm.

Finally, the influence of the voxel mesh size is investigated for the different element lengths given in Table 4.5. The related results for the elastic and shear moduli are illustrated in Fig. 4.34 in terms of diagrams. The voxel size is assigned to the abscissa and the elastic and shear moduli to the ordinate, respectively. The dependency of the individual moduli to the voxel size becomes directly apparent. In particular, for voxel sizes in the range of 1.0 μm - 0.8 μm a strong influence is visible. This is related to the connection of the fibres due to the element size which appears for mesh size greater than 0.8 μm. It points out the drawback of the voxel mesh, which requires finer resolution in comparison to standard meshes due to the loss of geometrical accuracy. Comparing the mesh sizes lower than 0.9 μm and taking into account the deviation in fibre volume content, shown in Table 4.5, a convergence for a voxel size of 0.5 μm can be assumed. The assumption is based on the observation, that the voxel sizes of 0.7 μm and 0.5 μm are directly comparable with respect to the fibre

volume content and the differences between E_{22} and E_{33} as well as G_{12} and G_{13} becomes small (less than 2%) with the use of 0.5 μm. Consequently, the results shown in Table 4.7 represent the effective elastic constants of the heterogeneous roving structure based on the numerical homogenisation approach.

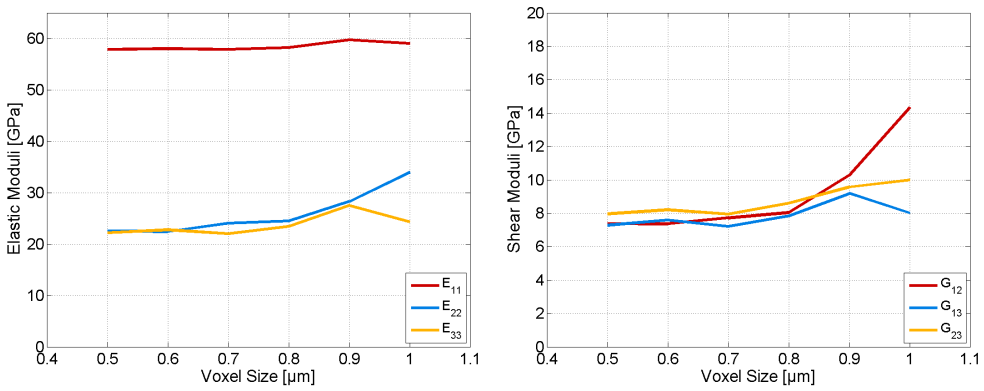

Figure 4.34: Influence of voxel element size to a) elastic moduli and b) shear moduli.

The quality of the applied homogenisation procedure has been evaluated by an example from literature [58] in which an asymptotic homogenisation approach for the determination of elastic properties is used. The comparison of the results of both methods, which can be found in the Appendix B, shows a good agreement and proves the quality of the applied approach.

Failure Properties

In the second step of the micro-scale considerations effective failure parameters for the roving structure are determined. Thereby, the hexagonal unit cell voxel model described above is used. In order to capture the failure mechanisms of the epoxy resin the nonlinearities as well as the differences in tensile and compressive strength must be taken into account. In addition the glass fibre failure has to be considered. Both can be realised by the use of the calibrated materials from Section 4.3.1. However, this causes major adaptions of the finite element model which are mainly related to the change of the analysis type from implicit to explicit. The use of implicit analyses for the representation of nonlinear material behaviour is coupled to convergence criteria which causes iterations to solve the system of equations. In particular, in combination with element elimination this is almost impossible to satisfy. Explicit analysis allow the treatment of highly nonlinear problems due to the small time step. In addition they are not restricted to any convergence criteria and does not have to solve a system of equations. As a consequence this time integration scheme is used for the consideration of failure for the unit cell here. However, there are also drawbacks obtained by the change: the very small time step due to the element size and the non-existence of the linear constraint equations in identical

form used for the implicit analyses.
In order to provide periodicity without using linear constraint equations, the unit cell is considered within an embedded domain for the explicit analyses. Thereby, the unit cell is surrounded by a defined fraction of the same structure. This is illustrated in Fig. 4.35 in which such a model is shown for the undeformed state on the left-hand side and under shear loading on the right-hand side. To improve the visibility the surrounding domain is made transparent in the latter.

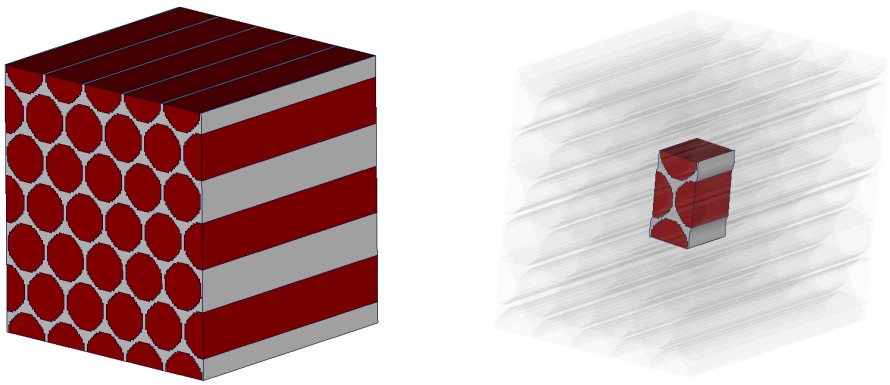

Figure 4.35: Embedded unit cell in 5x5x3 patch.

Since the distance between the unit cell inclusion and the free boundary will affect the periodicity and consequently the results, the size of the surrounding domain must be well defined. Therefore, different sizes of the surrounding domain are considered and the results in the unit cell are compared to the one provided by the homogenisation approach. However, in order to efficiently conduct this and to enable subsequent failure investigation, an improvement for the explicit time step is necessary. Therefore, the mesh size of the unit cell is uniformly scaled by a factor of one thousand. Using the same material properties this implies a direct increase of the time step by this factor. As a consequence the mass of an element increases by factor of one billion. Since stress and strain are dimension-related measures only inertia effects due to the mass increase can influence the results. The inertia effects are directly related to the imposed velocity-time function. Since no strain rate dependency is taken into account in this work, the load application function can be used to control the inertia effects. Using a smooth and sufficiently slow load application, inertia effects are eliminated. This is realised by imposing an average velocity of v=0.1 mm/ms in terms of a sinusoidal time-displacement function. Consequently, the time step can be increased by applying this procedure. In addition, the enlargement of the mesh size enables the direct use of the calibrated material models for the epoxy resin for a mesh size of 0.5 mm given in Section 4.3.1.
The unit cell generation tool enables also the possibility to create cell arrangements, in the following denoted as patches. A patch can be defined by a number of unit cells in the three main directions. For example a 5x5x3 patch corresponds

to five unit cells in x- and y-direction and three unit cells in z-direction and consists of 75 unit cells. Thereby, the unit cell itself is located in the centre of the structure. This procedure has already been shown in Fig. 4.35, the patch on the left-hand side and the unit cell inclusion on the right-hand side. In order to determine the influence of the distance s to the boundary, three different patch sizes are investigated under the six deformation modes in terms of linear elastic material behaviour for fibre and resin. The properties of the individual patches are summarised in Table 4.8 in which s_x, s_y and s_z represent the distance from the unit cell to the patch boundaries in x, y and z-direction, respectively. In addition the number of elements and the time step are given.

	s_x [mm]	s_y [mm]	s_z [mm]	Δt [ms]	No.of Elements
Voxel Size 0.5 mm					
Patch 3x3x2	18.50	18.50	16.00	1.00e-05	1,577,088
Patch 4x4x3	27.75	27.75	32.00	1.00e-05	4,205,568
Patch 5x5x3	37.00	37.00	32.00	1.00e-05	6,571,200
Voxel Size 0.7 mm					
Patch 3x3x2	18.20	18.00	16.10	0.71e-04	559,728
Patch 4x4x3	27.30	27.00	32.20	0.71e-04	1,492,608
Patch 5x5x3	36.40	36.00	32.20	0.71e-04	2,332,200

Table 4.8: Properties of unit cell patches for different element sizes.

It is obvious that the use of the embedded cell approach provides large finite element models and small time steps. Even, after the improvement procedure the time step for the 0.5mm mesh is about fifty times smaller than the time step currently used in the automotive industry (Δt=0.5e-03 ms). For this reason and due to the lower number of elements the patch size assessment is conducted with a voxel mesh size of 0.7 mm. The results of the study are listed in Table 4.9 in which the last row represents the results of the numerical homogenisation for the same element size.

Moduli in [GPa]	E_{11}	E_{22}	E_{33}	G_{23}	G_{12}	G_{13}
Voxel Size 0.7 mm						
Patch 3x3x2	56.67	23.00	20.80	7.62	7.93	7.60
Patch 4x4x3	56.59	22.97	20.93	7.85	7.80	7.16
Patch 5x5x3	56.83	23.06	20.94	7.60	7.63	6.94
Homogenisation	57.94	24.13	22.05	7.96	7.73	7.23

Table 4.9: Effective elastic moduli and shear moduli based on explicit patch analysis

Considering the results reveals, that almost no influence of the patch can be detected for the elastic moduli. In general the explicit analysis provides a softer

behaviour. This is mainly related to the difference in the used element formulation between the implicit and explicit analysis. In the explicit analysis an one point integration rule is used, whereas in the implicit solver a selective reduced integration rule is applied which is the mandatory default in VPS. In addition an influence of the patch size can be seen for the shear moduli. Here, a dependency of the distance to the boundary is visible. The results become closer to the homogenisation approach if the differences between s_x, s_y and s_z are small. This is given by the first and second patch size shown in Table 4.9. Since the improvement gained by the increase of patch size is small in comparison to the computational effort, the patch size 3x3x2 is used for the failure analyses. It is considered to provide sufficiently periodicity for the embedded unit cell.

Since the maximum stress criteria is used within the USER MATERIAL, the maximum occurring failure stresses due to the prescribed deformation modes have to be calculated. The use of this criteria is based on its simplicity. As detailed geometrical information for the load transfer is given by the meso-scale model, the objective within this work is to determine the failure for an unidirectional composite layer in the simplest way. This also implies that any stress interaction is not taken into account. In order to get a failure stress value for the complete unit cell for the respective deformation mode, an appropriate evaluation procedure is needed. Here, a stress evaluation based on occurring section forces is used.

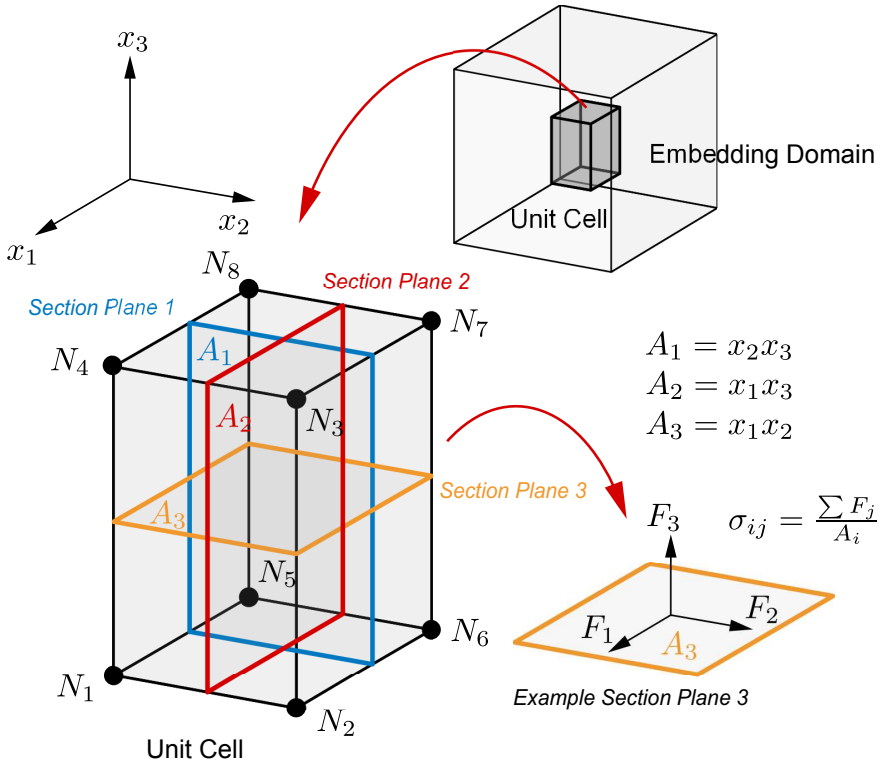

Figure 4.36: Stress evaluation scheme for embedded unit cell calculations.

In Fig. 4.36 a scheme of the unit cell including three section force planes is depicted. Thereby, the normal of a plane corresponds with the respective main axis of a Cartesian coordinate system. In addition each plane is located in the middle of the respective unit cell dimension. The nodal forces of the finite elements, which are cut by the plane in the undeformed state, are accumulated for defined states of the simulation. Using the sum of the respective force components F_j in combination with the initial cross-section A_i the stress σ_{ij} can be calculated by

$$\sigma_{ij} = \frac{\sum F_j}{A_i} \quad . \tag{4.19}$$

For example, the failure stress for tensile or compressive loading in x_3-direction is calculated by

$$\sigma_{33} = \frac{\sum F_3}{A_3} \quad \text{and} \quad \sigma_{32} = \frac{\sum F_2}{A_3} \quad , \tag{4.20}$$

provides the shear stress due to a load in x_2-direction acting on A_3. In addition the displacements between the unit cell corner nodes N_1-N_8, shown in the same figure, are evaluated to determine the occurring strains by

$$\varepsilon_{ij} = \frac{1}{2}(u_{i,j} + u_{j,i}) \quad . \tag{4.21}$$

In each load case four line segments represented by two nodes are evaluated. Since only a minor deviation of the individual strains have been observed, the mean value is subsequently determined. For example the strain ε_{11} due to tensile or compressive loading in x_1-direction is given by

$$\varepsilon_{11}^{N_1N_5} = \frac{((N_1^{(1)}(x_1) - N_5^{(1)}(x_1)) - (N_1^{(0)}(x_1) - N_5^{(0)}(x_1)))}{(N_1^{(0)}(x_1) - N_5^{(0)}(x_1))} \quad , \tag{4.22}$$

$$\varepsilon_{11}^{N_2N_6} = \frac{((N_2^{(1)}(x_1) - N_6^{(1)}(x_1)) - (N_2^{(0)}(x_1) - N_6^{(0)}(x_1)))}{(N_2^{(0)}(x_1) - N_6^{(0)}(x_1))} \quad , \tag{4.23}$$

$$\varepsilon_{11}^{N_3N_7} = \frac{((N_3^{(1)}(x_1) - N_7^{(1)}(x_1)) - (N_3^{(0)}(x_1) - N_7^{(0)}(x_1)))}{(N_3^{(0)}(x_1) - N_7^{(0)}(x_1))} \quad , \tag{4.24}$$

$$\varepsilon_{11}^{N_4N_8} = \frac{((N_4^{(1)}(x_1) - N_8^{(1)}(x_1)) - (N_4^{(0)}(x_1) - N_8^{(0)}(x_1)))}{(N_4^{(0)}(x_1) - N_8^{(0)}(x_1))} \quad , \tag{4.25}$$

$$\varepsilon_{11} = \frac{\varepsilon_{11}^{N_1N_5} + \varepsilon_{11}^{N_2N_6} + \varepsilon_{11}^{N_3N_7} + \varepsilon_{11}^{N_4N_8}}{4} \tag{4.26}$$

in which the superscripts (0) and (1) refer to the initial and current configuration, respectively. Both proposed evaluation methods are based on the assumption of small displacements and have already been used to evaluate the influence of the patch size discussed above.
By applying the deformation modes at the outer surfaces of the patch, the strain fields for determination of the failure stresses are defined. Contrary to the homogenisation procedure the deformations in normal direction have to distinguish between tensile and compressive loading here. Consequently nine, instead of six, load cases and failure stresses exists. The applied deformation modes are depicted in Fig. 4.37 in which the first two lines show the normal tension and compression modes and the last one illustrates the shear loading.

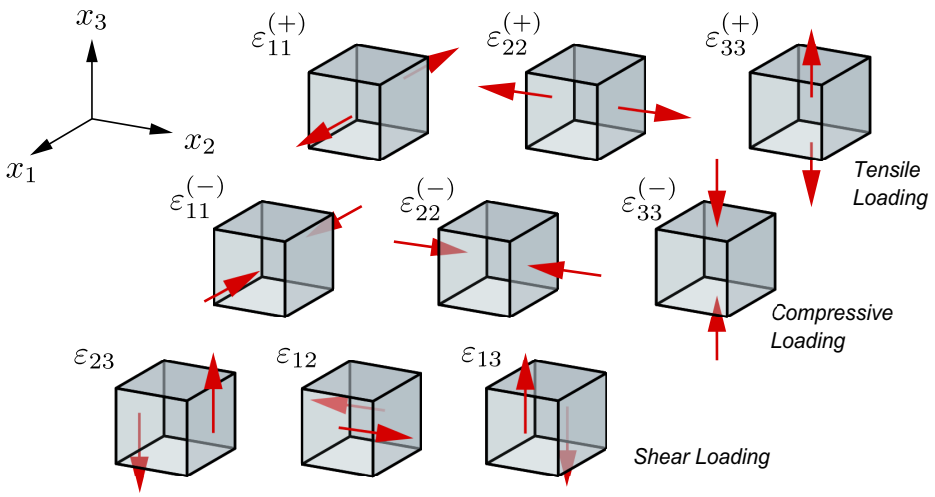

Figure 4.37: Patch deformation modes for failure stress determination.

The corresponding stress-strain relations are given in Fig. 4.38 by the red colour curves. The diagrams of the left column represent the normal modes and the right column depicts the shear answer of the embedded unit cell. In the normal mode diagrams tensile and compressive behaviour are considered together. The latter are illustrated by dotted lines and have been transformed to positive stress and strain ranges for comparing purpose. In addition the elastic and shear moduli provided by the numerical homogenisation procedure are represented by the blue dashed line. The simulations have been conducted with a voxel element length 0.5 mm and the respective calibrated materials in which only the unit cell inclusion can represent failure. Comparing the elastic constants and the initial slope of the stress-strain curves shows a very good correlation which proves the choice of the patch size for the explicit analysis. Furthermore, an almost elastic behaviour of the unidirectional composite layer is visible for normal deformations in fibre direction. This is coupled to a sudden fracture of the structure caused by fibre failure.

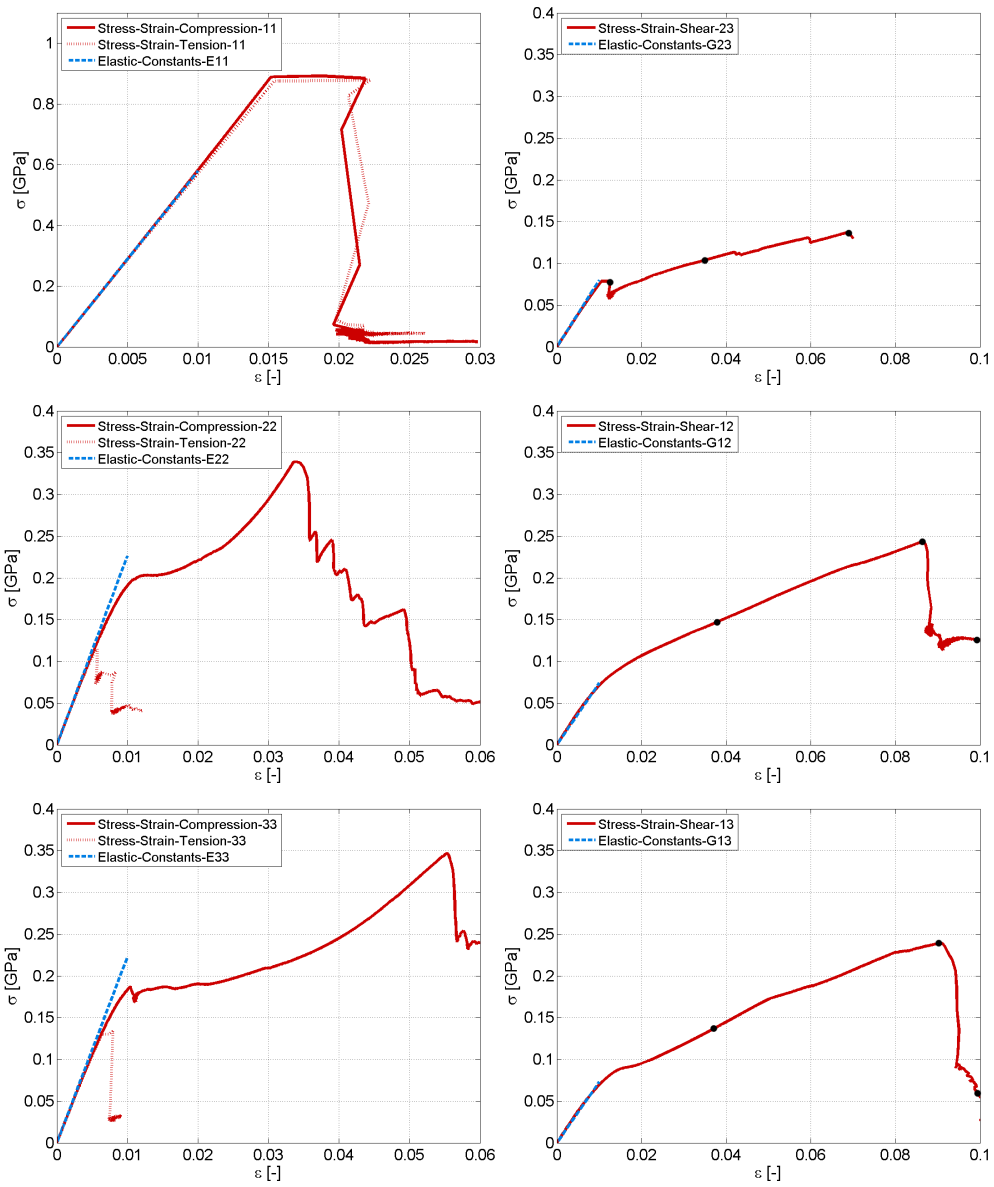

Figure 4.38: Stress-strain relations of embedded unit cell under normal and shear loading (markers on shear curves with respect to states of deformation in Fig. 4.39, Fig. 4.40 and Fig. 4.41, respectively).

The plateau visible in the upper left diagram is related to the evaluation procedure and reflects not the material behaviour. It is based on strong oscillations occurring with the abrupt failure due to the high stored elastic energy. Since no filter treatment is applied on the evaluated node coordinates this effect appears. However, since only the maximum failure stresses are of interest in this work this can be neglected. In addition the normal loading in fibre direction shows almost no difference between compressive and tensile behaviour. In contrast, a significant influence can be observed for the loading perpendicular to

the fibres. In terms of tension the structure behaves almost linear up to the fracture whereas in compression a strong nonlinear stress-strain relation is visible. The brittle answer in tension is related to the matrix tensile failure (inter fibre failure). In terms of compression the fracture is controlled by the matrix compressive strength. A nonlinearity in stress-strain relation is also visible in terms of shear loading, shown in the right column of Fig. 4.38. Additionally, here and also in terms of compression transverse to the fibre, the fracture is not anymore a sudden event. Moreover, it is a gradual process which is exemplarily shown in Fig. 4.39 for three states of strain under shear load $\bar{\varepsilon}^0_{23}$.
It is visible that the unit cell fibre arrangement is different to that obtained by the numerical homogenisation. This is caused by the even number of unit cells used for the patch size generation and the centre positioning procedure of the generation tool. However, since this is also a representative structure the results are not affected by this difference. Considering the three given states, a continuous crack propagation around the fibres (inter fibre failure) can be observed. Comparing further the state of crack initiation to the stress-strain relation of Fig. 4.38 (black markers) directly reveals the influence. Moreover the shear loading of the resin elements at the top and bottom of the centre fibre becomes apparent.

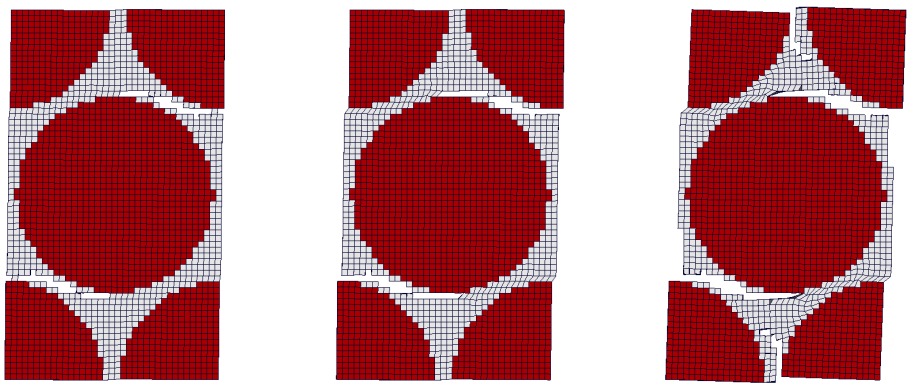

Figure 4.39: Deformation of embedded unit cell for imposed strain field $\bar{\varepsilon}^0_{23}$ at state a) $\varepsilon_{23} = 0.017$ b) $\varepsilon_{23} = 0.036$ and c) $\varepsilon_{23} = 0.069$.

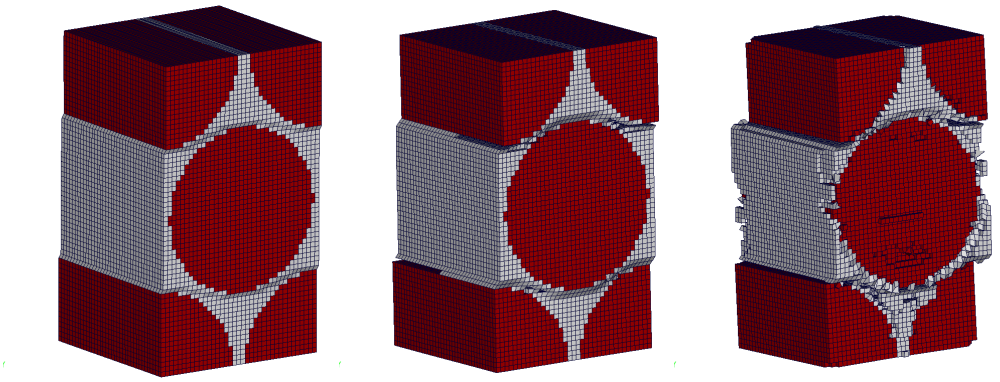

Figure 4.40: Deformation of embedded unit cell for imposed strain field $\bar{\varepsilon}^0_{13}$ at state a) $\varepsilon_{13} = 0.038$ b) $\varepsilon_{13} = 0.089$ and c) $\varepsilon_{13} = 0.103$.

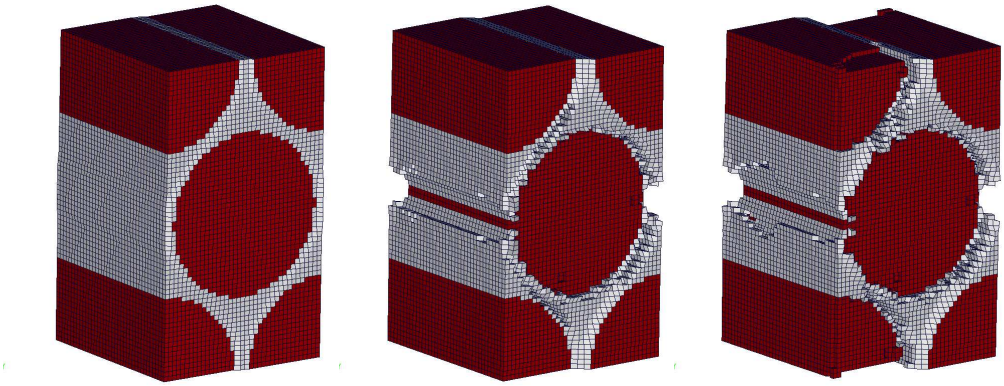

Figure 4.41: Deformation of embedded unit cell for imposed strain field $\bar{\varepsilon}^0_{12}$ at state a) $\varepsilon_{12} = 0.039$ b) $\varepsilon_{12} = 0.086$ and c) $\varepsilon_{12} = 0.102$.

Similar effects can be observed for the other two shear modes which are depicted in Fig. 4.40 and Fig. 4.41, respectively. However, since the element failure occurs for higher strains the shear resistance of the resin is more dominating. It has to be mentioned that the use of the embedded unit cell approach is well suited for the representation of the stiffness of the embedded structure. With the onset of failure the crack propagation is represented well within the unit cell, but is impeded at the boundary due to the embedding domain in which the failure of the elements is deactivated. However, the onset of failure does not represent the complete fracture of the unit cell structure. A complete fracture can only occur if a crack propagates complete from one to the other side within the micro structure. Therefore, it is stated for this work that the unit cell failure is indicated by a significantly drop of the occurring stresses in loading direction. Even if the crack pattern of the unit cell is deviating from the real micro structure this approach ensures a similar assessment with respect to the ultimate fracture of the unit cell.

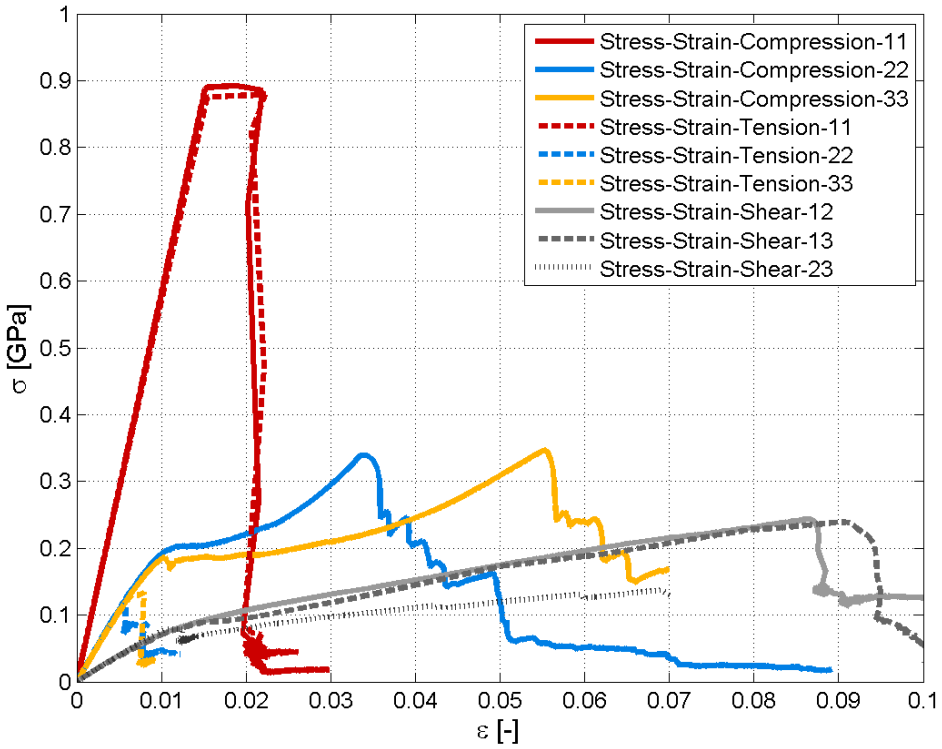

Figure 4.42: Comparison of stress-strain relations for embedded unit cell under normal and shear loading.

Finally, all stress-strain relations based on the embedded unit cell approach are represented in Fig. 4.42. The diagram reveals the differences in resistance under nine prescribed deformation modes: a brittle behaviour in tension and apart from compressive loading in fibre direction, a strong nonlinear behaviour under shear and compression. Determining the maximum of each curve provides the individual failure stresses of the respective stress-strain relation. Consequently, the effective failure of the unit cell structure is defined by nine independent stress values which are summarised in Table 4.10.

$\sigma_{11+}^{\mathrm{FAIL}}$ [GPa]	$\sigma_{22+}^{\mathrm{FAIL}}$ [GPa]	$\sigma_{33+}^{\mathrm{FAIL}}$ [GPa]	$\sigma_{23}^{\mathrm{FAIL}}$ [GPa]	$\sigma_{12}^{\mathrm{FAIL}}$ [GPa]	$\sigma_{13}^{\mathrm{FAIL}}$ [GPa]
0.879	0.115	0.134	0.135	0.239	0.239
$\sigma_{11-}^{\mathrm{FAIL}}$ [GPa]	$\sigma_{22-}^{\mathrm{FAIL}}$ [GPa]	$\sigma_{33-}^{\mathrm{FAIL}}$ [GPa]			
0.892	0.339	0.348			

Table 4.10: Effective failure stresses due to embedded unit cell approach.

Thus, the heterogeneous roving structure can be characterised by the effective material properties. Consequently, the parameters given in Table 4.11 are used to supply the orthotropic USER MATERIAL for an unidirectional composite

layer which finally characterise the roving structure within this work.

Material Modelling Roving Structure			
Stiffness Properties			
Elastic Moduli	E_{11}	57.9374	[GPa]
	E_{22}	22.6091	[GPa]
	E_{33}	22.2272	[GPa]
Shear Moduli	G_{23}	7.9777	[GPa]
	G_{12}	7.3861	[GPa]
	G_{13}	7.2945	[GPa]
Poisson's Ratios	ν_{23}	0.3710	[-]
	ν_{12}	0.2764	[-]
	ν_{13}	0.2775	[-]
Density	ρ	2.272e-6	[kg/mm^3]
Failure Properties			
Compressive Failure Stresses	$\sigma_{11-}^{\mathrm{FAIL}}$	0.892	[GPa]
	$\sigma_{22-}^{\mathrm{FAIL}}$	0.339	[GPa]
	$\sigma_{33-}^{\mathrm{FAIL}}$	0.348	[GPa]
Tensile Failure Stresses	$\sigma_{11+}^{\mathrm{FAIL}}$	0.879	[GPa]
	$\sigma_{22+}^{\mathrm{FAIL}}$	0.115	[GPa]
	$\sigma_{33+}^{\mathrm{FAIL}}$	0.134	[GPa]
Shear Failure Stresses	$\sigma_{23}^{\mathrm{FAIL}}$	0.135	[GPa]
	$\sigma_{12}^{\mathrm{FAIL}}$	0.243	[GPa]
	$\sigma_{13}^{\mathrm{FAIL}}$	0.239	[GPa]

Table 4.11: Finite element material model properties for roving structure based on USER MATERIAL model.

Limitations

The determination of stresses and strains in the evaluation procedure for the failure determination is based on the assumption of small displacements. This becomes critical in terms of shear loading and may affect the results of the strain evaluation. Since the cross-section remains almost constant during loading, the stress evaluation is not affected. In addition, the failure determination procedure cannot take into account micro buckling due the size of the unit cell. The defined failure criteria can represent well the stress failure level. However, in combination with the elastic constants the corresponding strain is always underestimated in terms on nonlinear stress-strain relations. Finally, the computational effort for the embedded unit cell approach has to be mentioned. In average each of the nine load cases of the conducted example takes about six hours on 16 CPU's which is not an issue for the industrial environment, but may become a bottleneck for research activities.

Chapter 5

Numerical Analysis of Component Structure and Experimental Validation

After the comprehensive description of the model generation procedure in the previous chapter, this chapter finally deals with the simulation of the wound tube component tests presented in the experimental Section 3.2.3 and 3.2.4 of this work. Therefore, in total three finite element simulations with the VPS explicit solver (PAM-CRASH) are conducted: a quasi-static compression as well as a quasi-static tension analysis and a crash analysis. Thereby, the static tests are mainly used to prove the applied approach for plausibility, since the main objective remains the crash simulation and the prediction of the crushing behaviour of a wound tube. The corresponding model setups including common and load case specific settings are presented in the subsequent section, followed by the representation of the results for the meso-scale simulations of the individual load case including the comparison to the experiments.

5.1 Model Description

The core model for all simulations is based on the geometrical representation of the wound tube structure by finite elements on meso-scale provided by Section 4.2. In order to match the fibre volume content of the complete composite given by the experimental analysis (see Table 3.7), the assignment of the voxel elements belonging to the roving structure is adjusted. This is possible, since a separation of the elements with respect to the number of nodes inside the roving structure has been conducted during the matrix generation procedure. In combination with the value obtained from micro-scale (0.773), a global fibre volume content of $v_f = 0.565$ can be reached by assigning all elements having at least two nodes in the roving structure to the roving material. The comparison to the experimental value of $v_f = 0.574$ shows a good agreement between numerical model and the real existing structure.

The USER MATERIAL model proposed in Section 2.3.3 in combination with the fibre direction obtained by the manufacturing simulation and the effective material properties provided by Table 4.11 finally complete the numerical description of the roving structure. In accordance the surrounding pure matrix is represented by the numerical modelling approach shown in Section 4.3.1 and is supplied by the properties given in Table 4.3. The explicit stable time step Δt, related to the material properties and the mesh size of 0.2 mm, amounts to 0.334e-04 ms. For all calculations underintegrated finite solid elements are used. In Fig. 5.1 the aforementioned properties and relations are summarised.

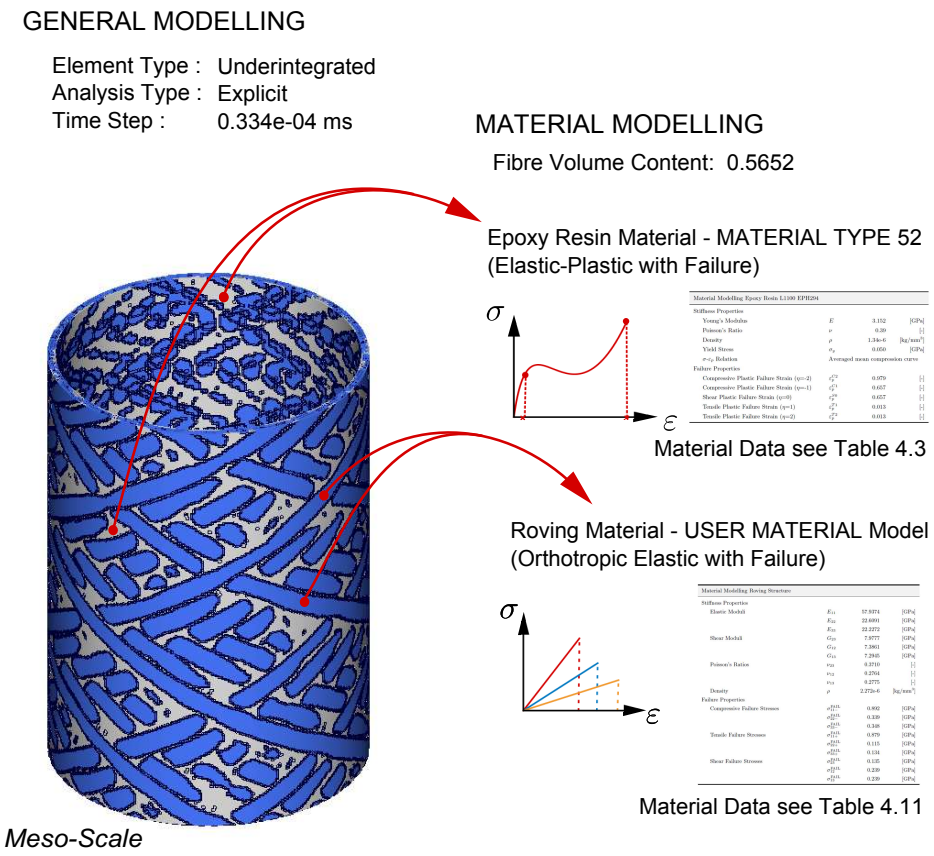

Figure 5.1: Finite element wound tube model setup - general modelling.

The major differences between static and crash simulation model are model size and load application based on the boundary conditions existing in the experiments. The former is directly visible in Fig. 5.2 in which the load case specific modelling properties are given. In accordance with the real given structure the static testing model (left-hand side) has a greater height which implies a significant higher number of nodes and elements. This is also visible in the data size. In contrast to the real structure the reinforced clamping domains are not represented in the simulation. The load is applied at the top of the specimen. Therefore, all nodes having the maximum positive z-coordinate are collected in

a rigid body. Its centre of gravity (COG) is used to apply the load by a time-displacement function in z-direction which also implies the only translational degree of freedom of this node. On the bottom the same technique is applied to fix the model in space. Contrary to the top, all translational degree of freedoms are fixed and no load is applied.

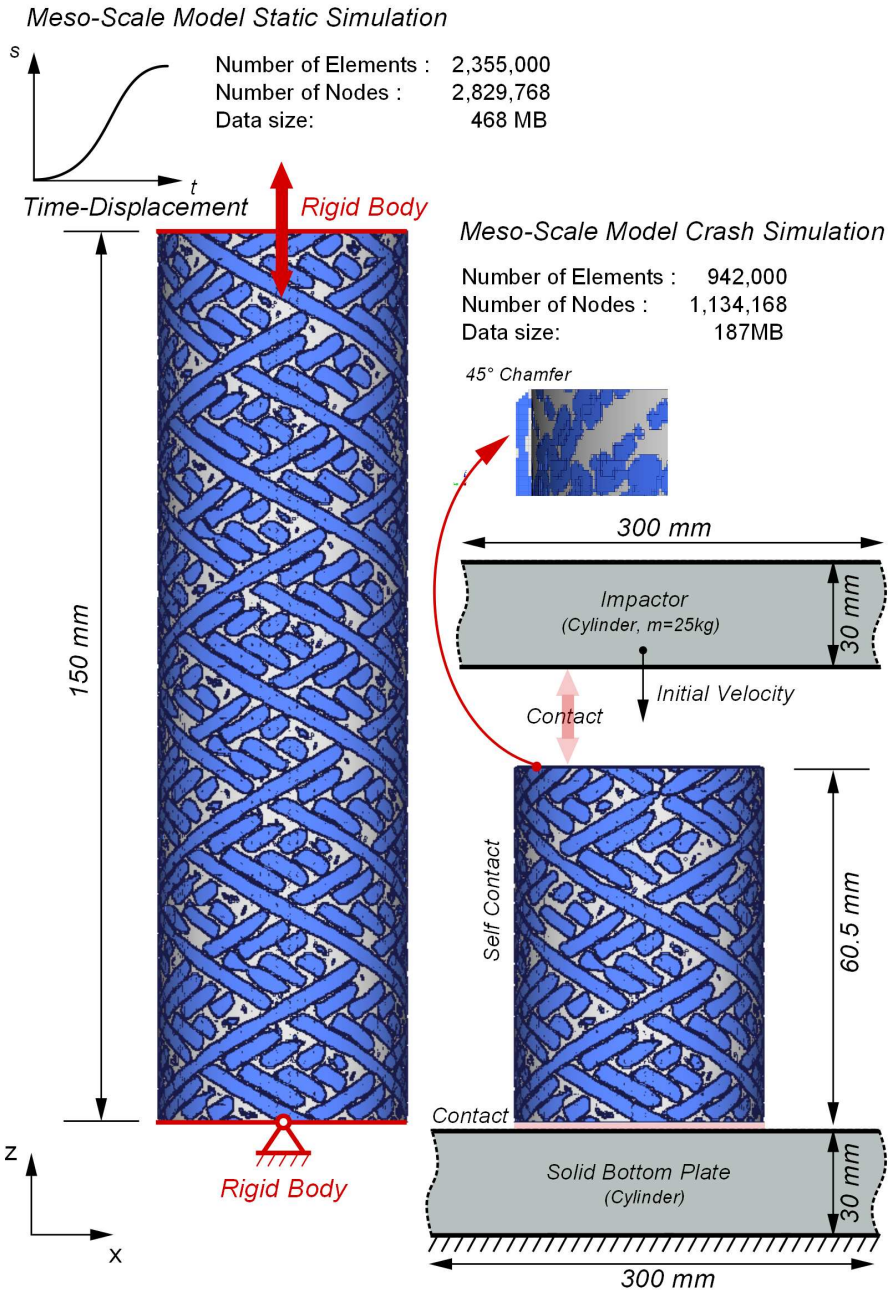

Figure 5.2: Finite element wound tube model setup - load case specific modelling.

The meso-scale crash model is depicted on the right-hand side of Fig. 5.2. The load is given by an impactor with an imposed initial velocity. In addition the model is constraint by the definition of contacts between the tube, ground and the impactor. Furthermore, a self contact for the complete tube structure constitutes a major difference to the static model. There, a self contact is neglected due to the huge model size, the related computational effort and the assumption of a very low influence to the results. Finally, in accordance to the real tested structure, the 45° chamfer is modelled to trigger the crushing behaviour of the virtual wound crash tube.

5.2 Wound Tube under Quasi-static Loading

Using explicit analyses for quasi-static simulations provides high computational effort. In particular in terms of small time steps and huge models as presented here. In order to get acceptable responding times the load has to be applied faster than in reality. The static tests from Section 3.2.3 have been conducted with a velocity of v=2 mm/min which implies v=0.03e-03 mm/ms. In the simulation a velocity of 0.1 mm/ms is applied which corresponds to an increase by factor 3,000. However, since the mass of the tube is very low (0.040 kg) and no strain rate dependency exists, the effects related to this increase are low. Applying additionally the load by a sinusoidal time-displacement function, which ensures a smooth velocity increase, almost eliminates the inertia effects.

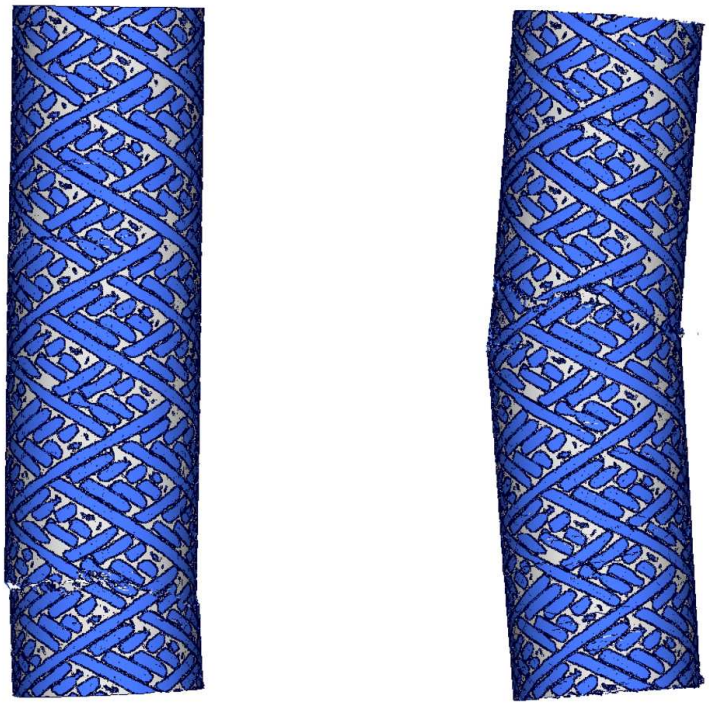

Figure 5.3: State of deformation of wound tube under quasi-static tensile (left) and compressive loading (right) at failure.

The ordinate values of this function correspond with the z-direction and are positive in terms of tension and negative for compressive loading. In order to evaluate the numerical analysis, the z-displacements of the COG at the top and the occurring reaction forces in z-direction at the COG of the bottom are recorded during simulation. The deformation results obtained by the simulation are depicted in Fig. 5.3 in which the left-hand side represents the tensile loading and the right-hand side the compressive loading. Both refer to the time of complete structural failure. It is visible that simulation predicts a failure under tensile loading near the bottom whereas for compression failure occurs in middle of the wound composite structure. Since no image records are available for this test series a validation of failure location and visual appearance is not possible.

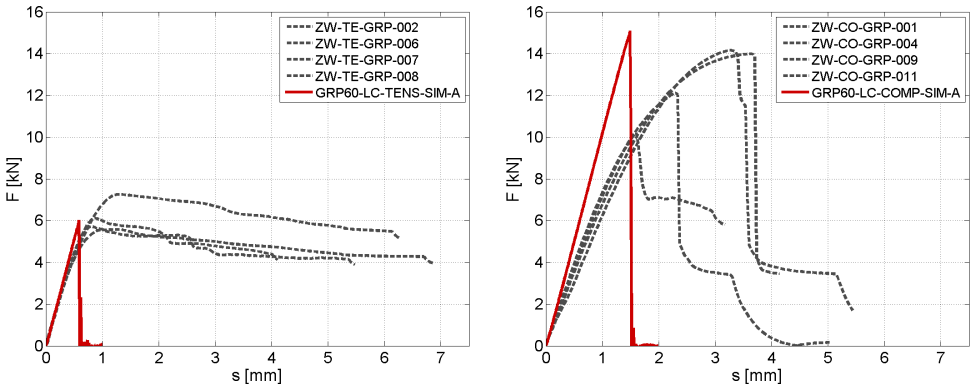

Figure 5.4: Comparison of simulation (red) and experiments (grey) for force-displacement behaviour of wound tube under a) tensile loading b) compressive loading.

The corresponding force-displacement relations are given in Fig. 5.4 in which also the left-hand side is referring to tensile loading and the right-hand side to compressive loading. In each diagram the results of the simulation are represented by red colour curve and compared to the experiments from Section 3.2.3 which are illustrated by grey dashed lines. In addition all forces and displacements are presented by absolute values for comparison. Considering firstly the behaviour in tension, it can be seen that the initial stiffness of the composite structure is captured well by the simulation. In addition a good agreement between virtual and real specimen can be stated for the failure force level. However, the difference in the displacement behaviour is also obvious. A comparable judgement can be given for the results of the compression tests in which the quality is slightly lower. Also here the difference in terms of displacement is visible.
Representing all curves in one common diagram shown by Fig. 5.5 reveals an almost identical behaviour of the simulation model under compressive and tensile loading in the initial domain. Furthermore, it can be seen that the simulation model predicts a linear response whereas the experiments shows a nonlinear behaviour. Hence it can be concluded that the roving structure is the dominating part in the simulation model and the contribution of the nonlinear pure matrix material is low. Due to the linear behaviour the occurring displacements

obtained by simulation are significantly less. Since the roving material is represented by effective properties the predictability of strains in terms of transverse compressive and shear loading is limited.

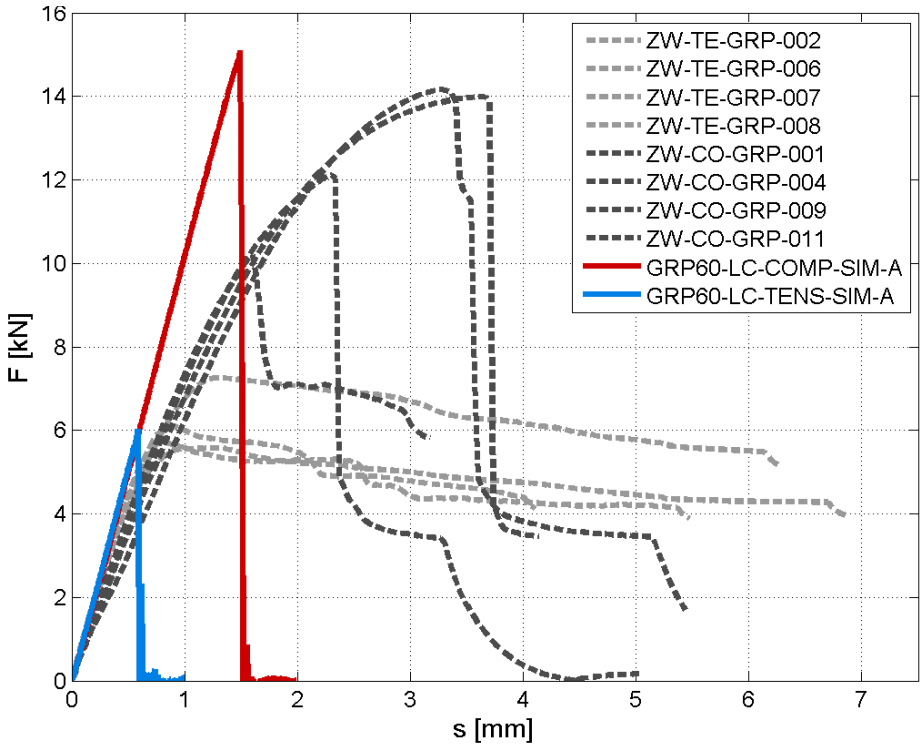

Figure 5.5: Comparison of simulation (red,blue) and experiments (grey) for force-displacement behaviour of wound tube under static loading.

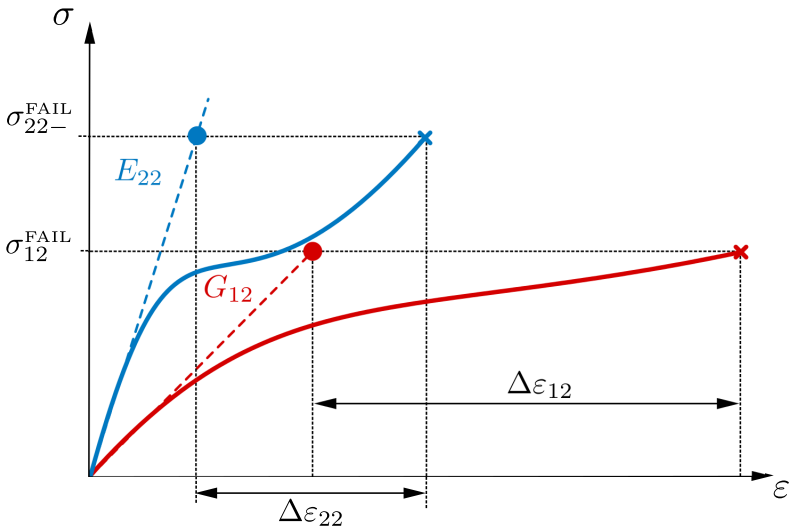

Figure 5.6: Deviation in strain prediction by using effective properties for the roving structure.

The unit cell investigations on micro-scale have shown nonlinear responses for these quantities (see Fig. 4.42 of Section 4.3.2) which cannot be represented by the roving material. In order to reveal the related influence, the dependency between stress-strain curves on micro-scale and derived effective properties are exemplarily illustrated for shear and transverse compressive loading in Fig. 5.6. The scheme points out the possible stiffer response of the roving material in the simulation for these loading conditions. For comparable stresses, smaller strains are predicted and consequently lower displacements are obtained by the virtual model. Thereby, the effect is significantly higher in terms of shear loading. The obtained results lead to the conclusion that the observed nonlinearity in the tension experiments is strongly related to the shear response of the composite on micro-scale. Moreover, the nonlinearity in compression seems to be caused by the transverse compressive response on micro-scale.
Finally, a closer consideration of the virtual failure appearance for the initially presented state of deformation is conducted. Therefore, in Fig. 5.7 and Fig. 5.8 detailed image records of the fracture state are given for tensile and compressive loading, respectively.

Figure 5.7: Fracture of wound tube under tensile loading.

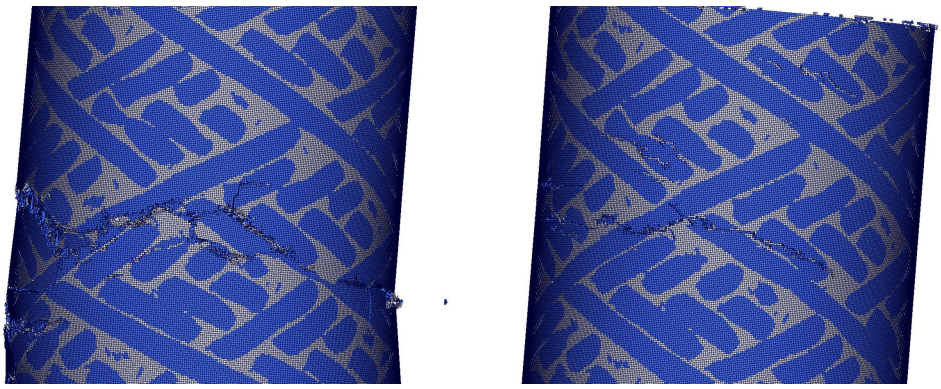

Figure 5.8: Fracture of wound tube under compressive loading.

In Fig. 5.7 it can been seen that the occurring failure in the virtual wound tube model is dominated by a fracture of the roving perpendicular to the roving direction. In order to reveal this, the considered domain is further reduced by section cuts above and under the crack location in the illustration on the right-hand side of the same figure. In terms of compressive loading the model shows a crack propagation mainly parallel to the roving placement which is visible in Fig. 5.9. Here, two different domains are illustrated: the location of the main fracture in the middle of the structure on the left-hand side and a region at the top showing the crack initiation on the right-hand side. However, also under this condition finally a roving fracture results in a fracture of the complete structure. Comparing both load cases, the differences in the failure appearance are visible. An exemplarily examination of the given loading in Fig. 5.9 shows the differences between tension and compression behaviour for the roving structure of the wound tube. In both load cases the shear component is acting in fibre direction whereas the loading transverse to the fibres is different. Taking into account the differences in strength for these load states the reason for the different behaviour becomes apparent.

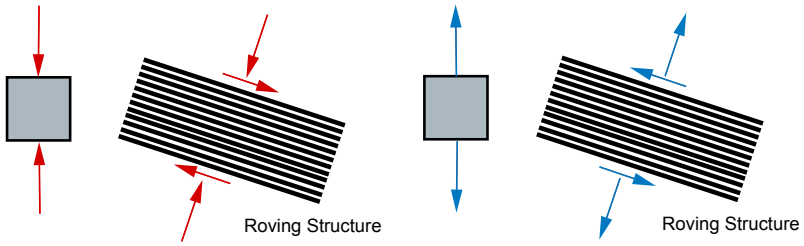

Figure 5.9: Loading of roving structure under compressive and tensile loading.

Summarised it can be stated that the simulation model consisting of the detailed representation of the geometry in combination with an uncoupled maximum stress criteria based on micro-scale considerations is able to capture the force level under quasi-static tensile and compressive loading. However, due to the restriction of the material model for the roving structure to linear elasticity, nonlinear effects cannot be represented which causes an underestimation of the displacements. The computational effort for the conducted analyses amounts to about 6h hours for the wound tube under tension and 12h under compression loading (64 CPU).

5.3 Wound Tube under Crash Loading

The final consideration of this work is related to the simulation of the impact test of the filament wound tube presented in Section 3.2.4. In accordance to the test environment the impactor has a mass of m=25 kg and an initial velocity of v_1=5.31 m/s. Since no strain rate behaviour is taken into account in this work only this load case is analysed. However, as mentioned in the experimental section the tests have not shown any strain rate dependency within the investigated range of velocity. The solid ground plate is represented by a rigid block (h=30 mm) with a density related to steel. It is spatially fixed and used for the measurement of the reaction force at the bottom according to the tests. The impactor is also modelled by a solid rigid body and its COG is used to record the occurring z-displacements during simulation. The contact formulation for the tube represents a self contact with activated eroding option [22]. This option ensures, that additionally all internal element faces are taken into account for the contact treatment which is necessary for the crushing behaviour. This implies that each node is a potential contact partner for each contact segment defined by an element face. As a consequence the applied contact thickness must be much smaller than the element size to avoid artificial internal forces. In the meso-scale model of the tube a self contact height of 0.05 mm is applied by an element size of 0.2 mm and satisfies this condition. In addition a value of μ=0.3 is assumed for the inner friction of the composite structure. This value is additionally applied to the contacts acting between steel impactor and tube as well as tube and steel plate.
The results of the crash simulation in terms of deformation are illustrated in Fig. 5.10-5.23, in which a constant time interval of Δt=1 ms between two figures is chosen. In addition each state of deformation is depicted in two different views. The left-hand side image of the respective figure corresponds to an isometric view in space. The right-hand side images illustrate a longitudinal cut of the tube in x-z view in which the section cut is foreground by black colour and a slight transparency is applied to the structure. In order to improve the visibility of occurring effects, the impactor as well as the ground plate are not depicted.

Figure 5.10: Deformation of the wound tube in crash loading obtained by simulation t=0 ms.

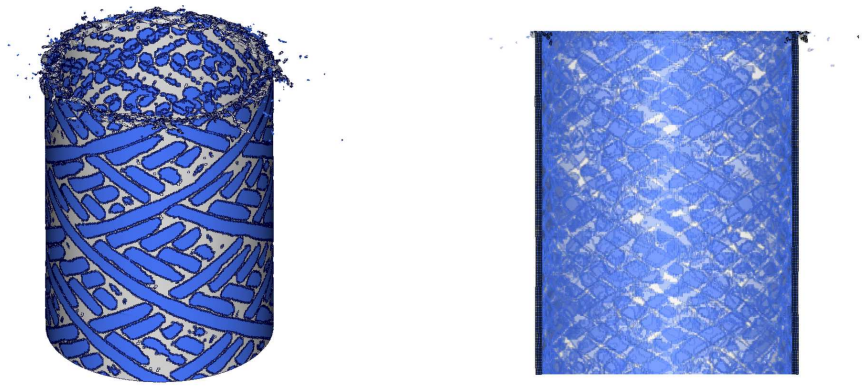

Figure 5.11: Deformation of the wound tube in crash loading obtained by simulation t=1 ms.

Figure 5.12: Deformation of the wound tube in crash loading obtained by simulation t=2 ms.

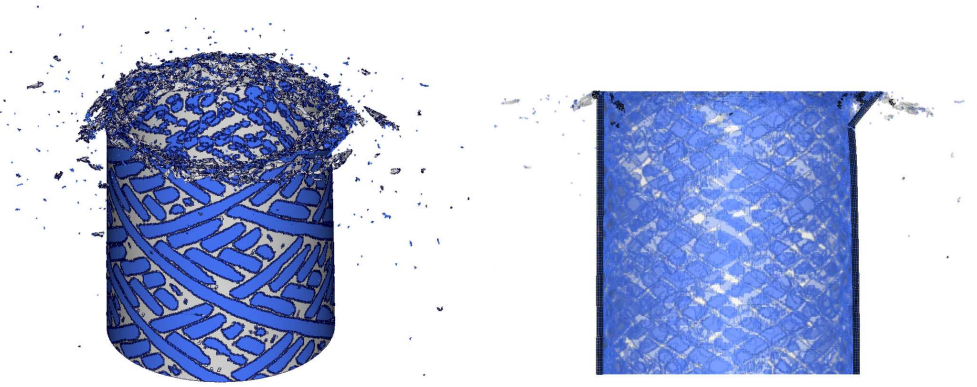

Figure 5.13: Deformation of the wound tube in crash loading obtained by simulation t=3 ms.

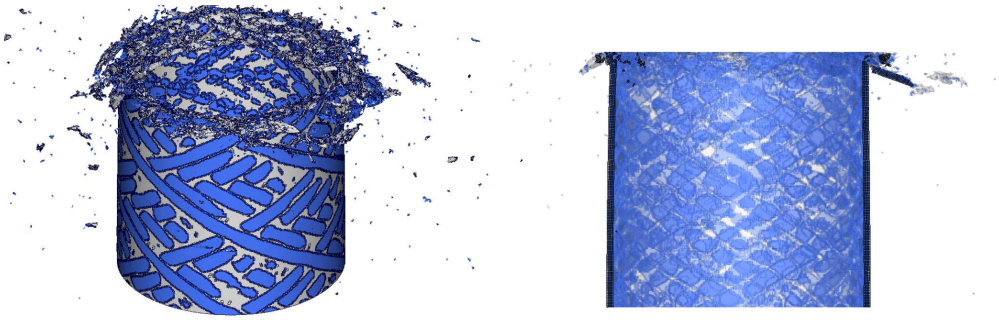

Figure 5.14: Deformation of the wound tube in crash loading obtained by simulation t=4 ms.

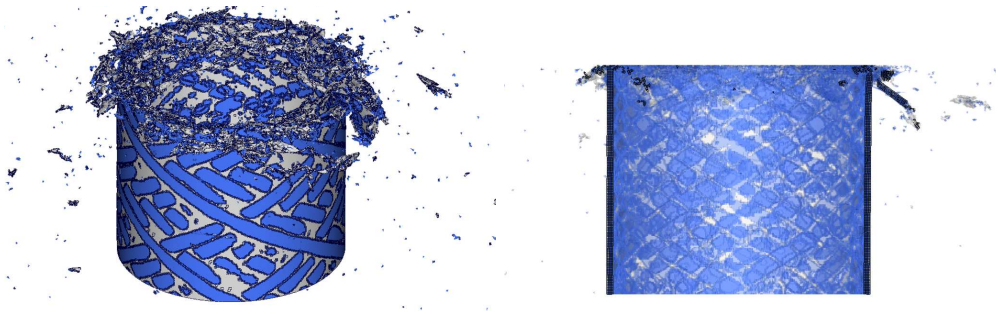

Figure 5.15: Deformation of the wound tube in crash loading obtained by simulation t=5 ms.

Figure 5.16: Deformation of the wound tube in crash loading obtained by simulation t=6 ms.

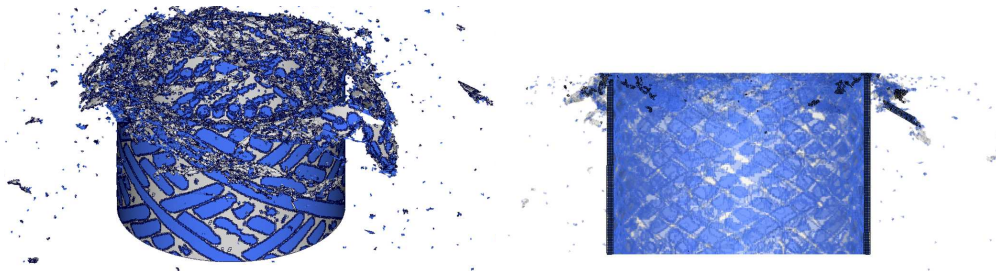

Figure 5.17: Deformation of the wound tube in crash loading obtained by simulation t=7 ms.

Figure 5.18: Deformation of the wound tube in crash loading obtained by simulation t=8 ms.

Figure 5.19: Deformation of the wound tube in crash loading obtained by simulation t=9 ms.

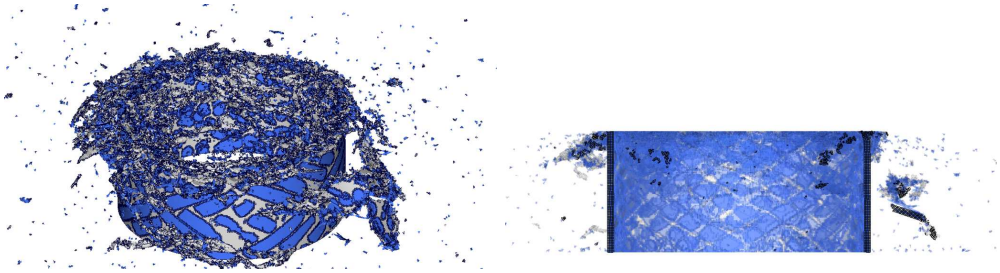

Figure 5.20: Deformation of the wound tube in crash loading obtained by simulation t=10 ms.

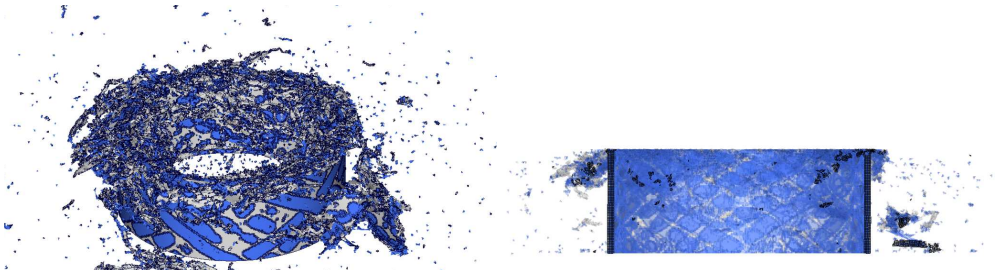

Figure 5.21: Deformation of the wound tube in crash loading obtained by simulation t=11 ms.

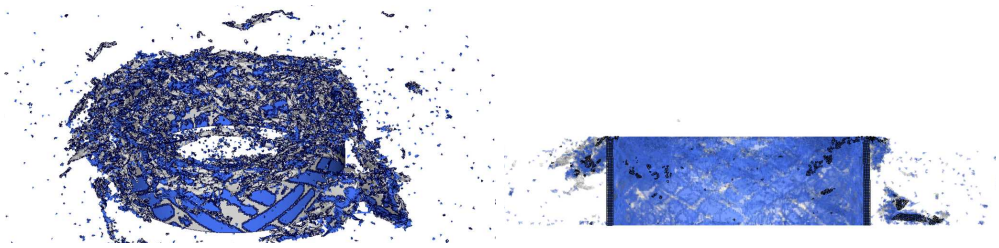

Figure 5.22: Deformation of the wound tube in crash loading obtained by simulation t=12 ms.

Figure 5.23: Deformation of the wound tube in crash loading obtained by simulation t=13 ms.

Consideration of the individual states of deformation reveals that the simulation model is able to predict the crushing behaviour of the wound composite structure. It becomes apparent that the finite elements located near the impactor are strongly distorted. Furthermore flying particles and small releasing parts can be observed over the whole crushing period. Although the elements are partly strongly deformed in the crushing zone, no stability issue has been detected during the numerical analysis. This indicates a robust numerical model.

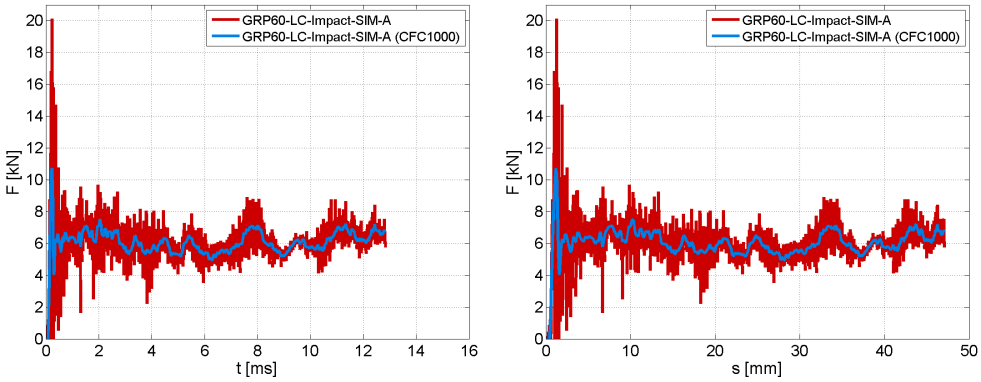

Figure 5.24: Force-time and force-displacement relation for wound tube in crash loading.

The corresponding force-time and force-displacement relation are shown in Fig. 5.24 in which the red colour curve represents the signal directly obtained from the simulation. In order to smooth the occurring oscillations a filter of type CFC1000 has been applied to the original numerical data. The resulting curve is depicted in blue solid line. Consideration of the force-displacement curve

reveals that the simulation can also represent the typical crushing behaviour: a peak value in force at the beginning followed by an almost constant force level. Additionally, a detailed analysis of the force-time function shows a small force drop at $t \approx 3$ ms. The corresponding state of deformation on the right-hand side of Fig. 5.13 shows a partial collapse of the structure at the top of the tube. This points out that the crushing process in the simulation is not a complete uniform procedure. In addition, it shows that also suddenly appearing events due inner roving loading may be captured by the meso-scale model. Similar effects have been detected in higher extend for the real structure in the experimental investigations.
In order to assess the quality of the simulation the results are compared to experiments from Section 3.2.4. Firstly, the states of deformation are considered and depicted in Fig. 5.25-5.38. Thereby, the left-hand side illustrations show the test and the right-hand side represent the numerical results in a comparable view. The used test example corresponds to the one discussed in Section 3.2.4. The time interval Δt between the individual figures amounts to 1 ms.

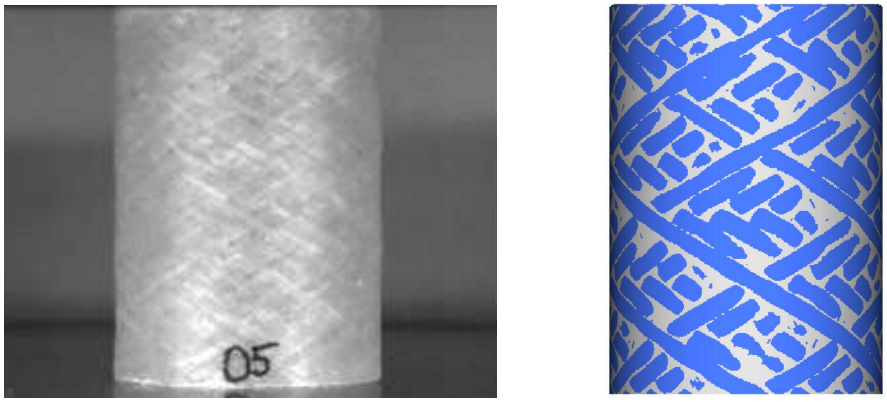

Figure 5.25: Comparison of deformation of real test to simulation for the wound tube in crash loading at t=0 ms.

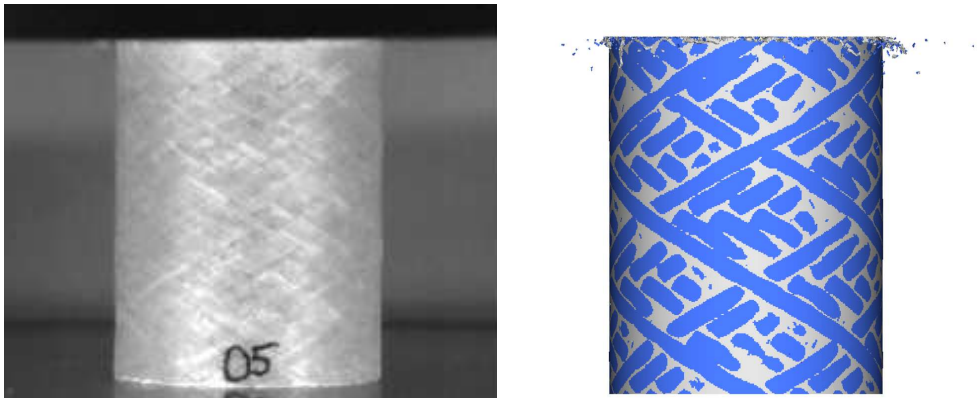

Figure 5.26: Comparison of deformation of real test to simulation for the wound tube under crash loading at t=1 ms.

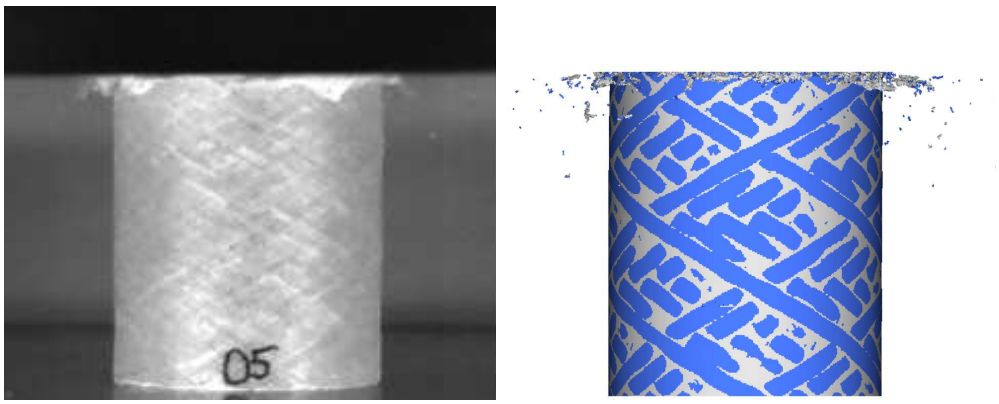

Figure 5.27: Comparison of deformation of real test to simulation for the wound tube in crash loading at t=2 ms.

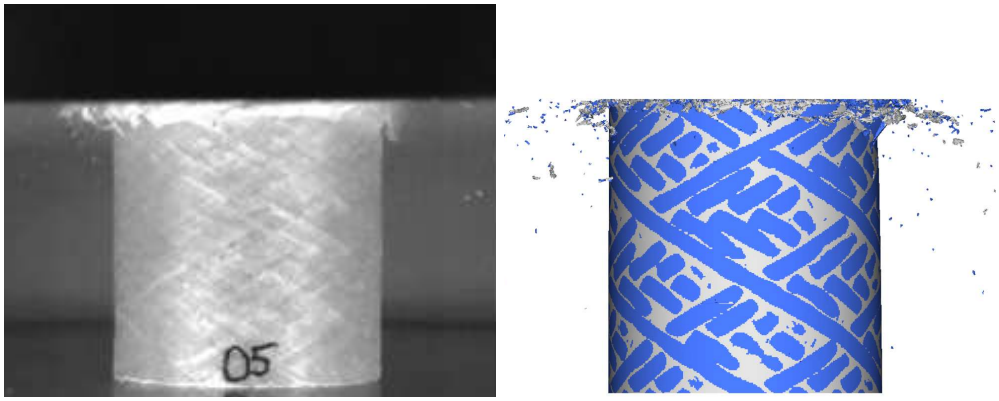

Figure 5.28: Comparison of deformation of real test to simulation for the wound tube in crash loading at t=3 ms.

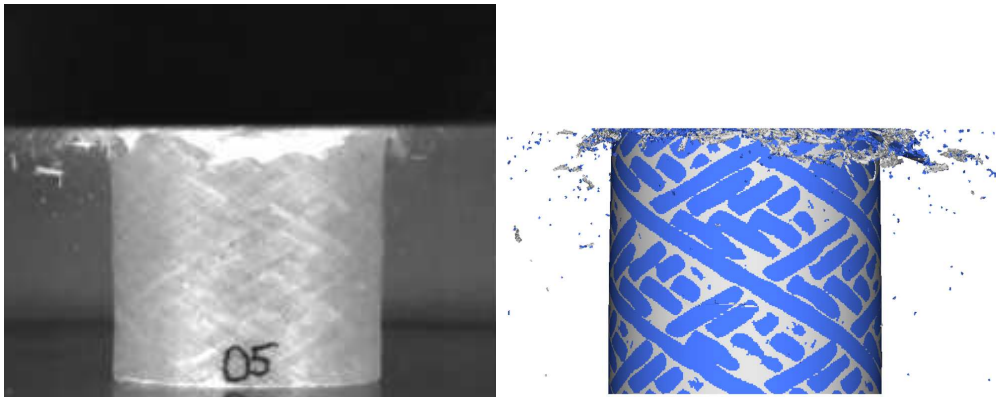

Figure 5.29: Comparison of deformation of real test to simulation for the wound tube in crash loading at t=4 ms.

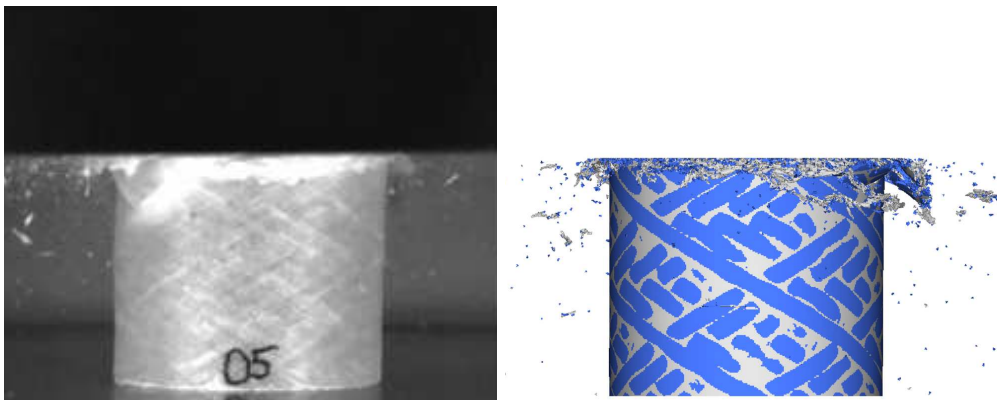

Figure 5.30: Comparison of deformation of real test to simulation for the wound tube in crash loading at t=5 ms.

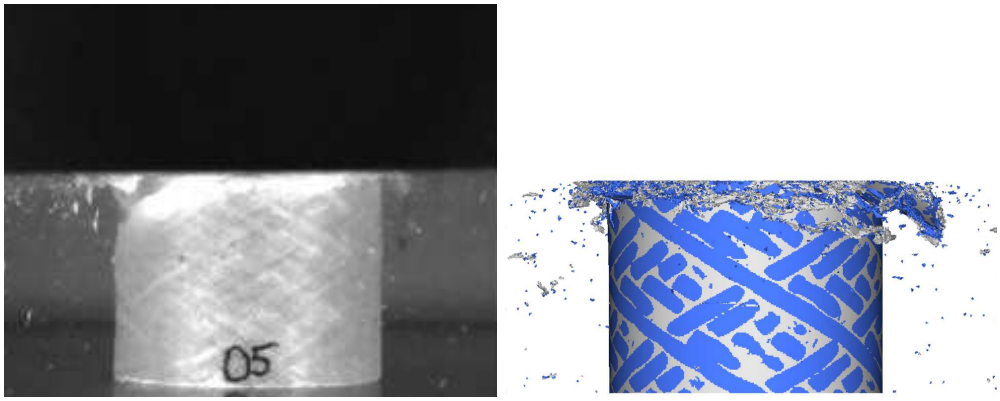

Figure 5.31: Comparison of deformation of real test to simulation for the wound tube in crash loading at t=6 ms.

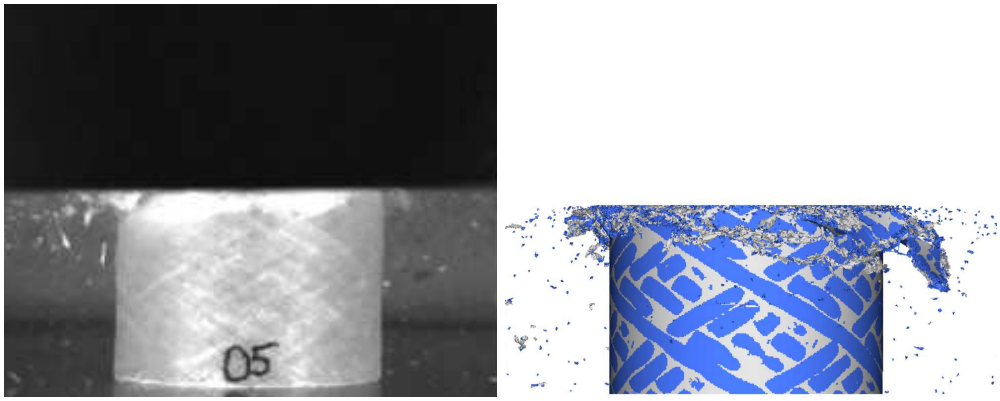

Figure 5.32: Comparison of deformation of real test to simulation for the wound tube in crash loading at t=7 ms.

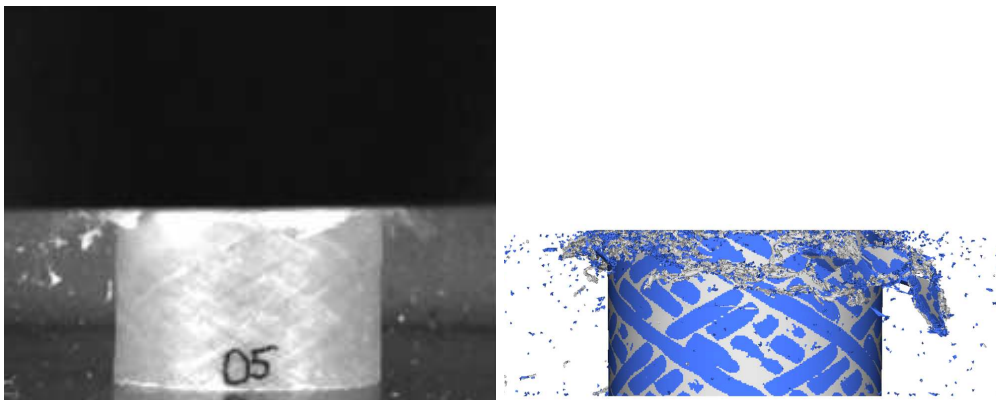

Figure 5.33: Comparison of deformation of real test to simulation for the wound tube in crash loading at t=8 ms.

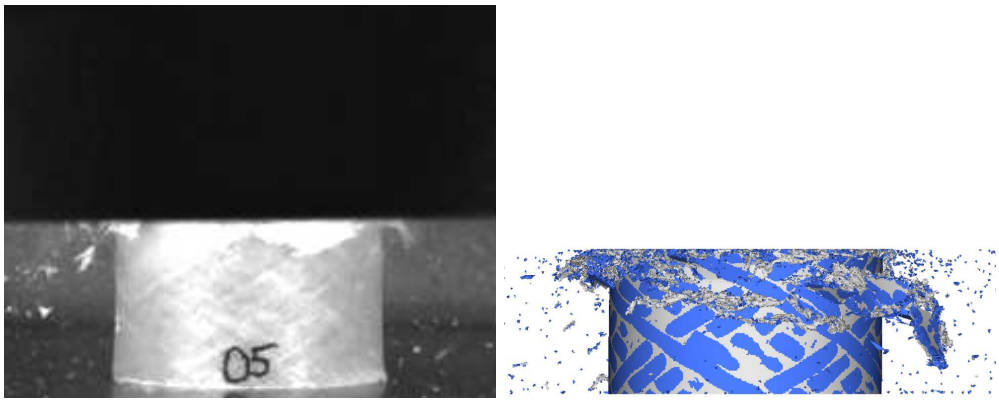

Figure 5.34: Comparison of deformation of real test to simulation for the wound tube in crash loading at t=9 ms.

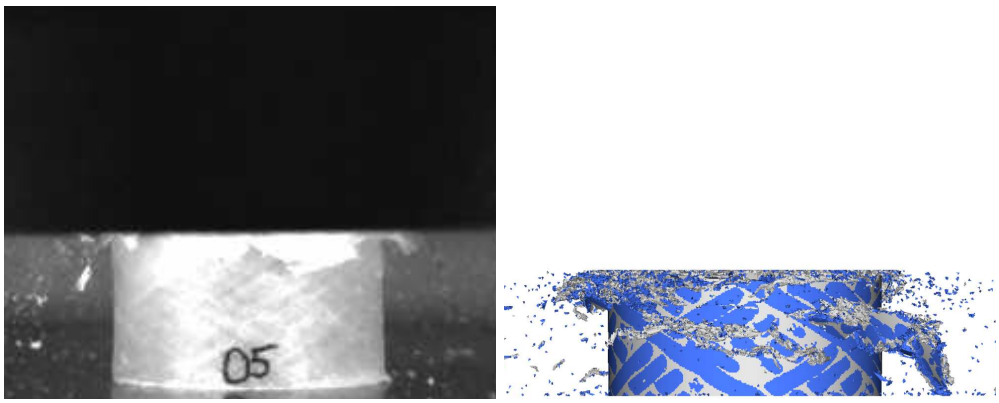

Figure 5.35: Comparison of deformation of real test to simulation for the wound tube in crash loading at t=10 ms.

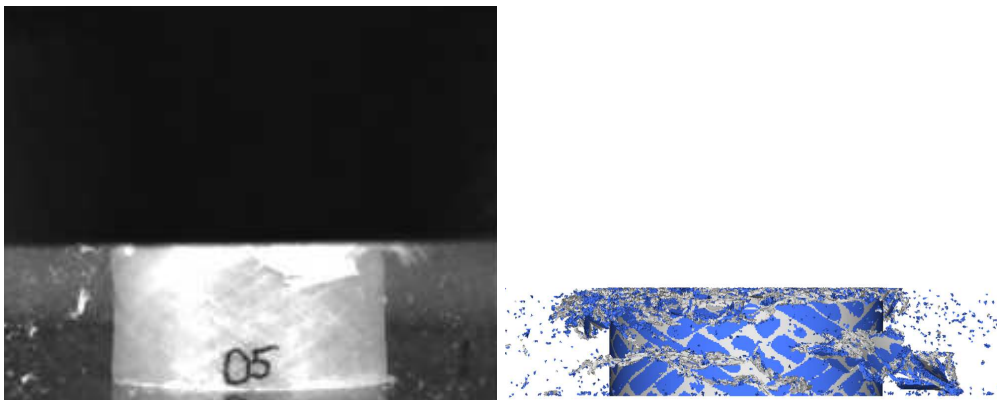

Figure 5.36: Comparison of deformation of real test to simulation for the wound tube in crash loading at t=11 ms.

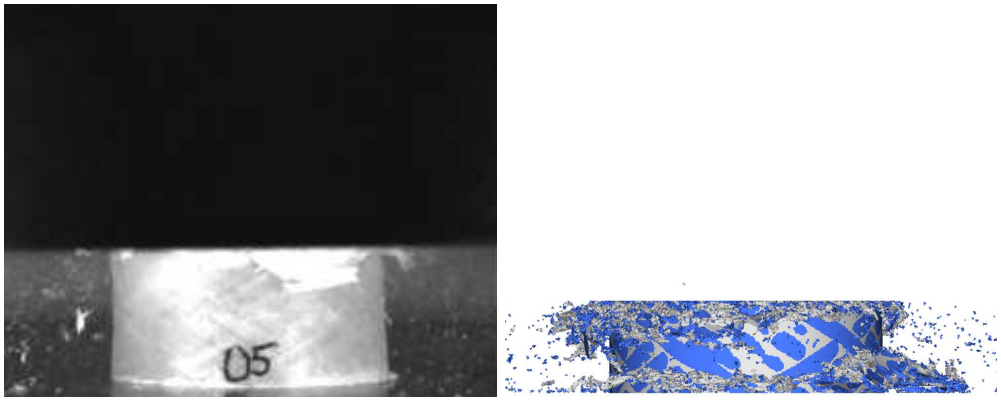

Figure 5.37: Comparison of deformation of real test to simulation for the wound tube in crash loading at t=12 ms.

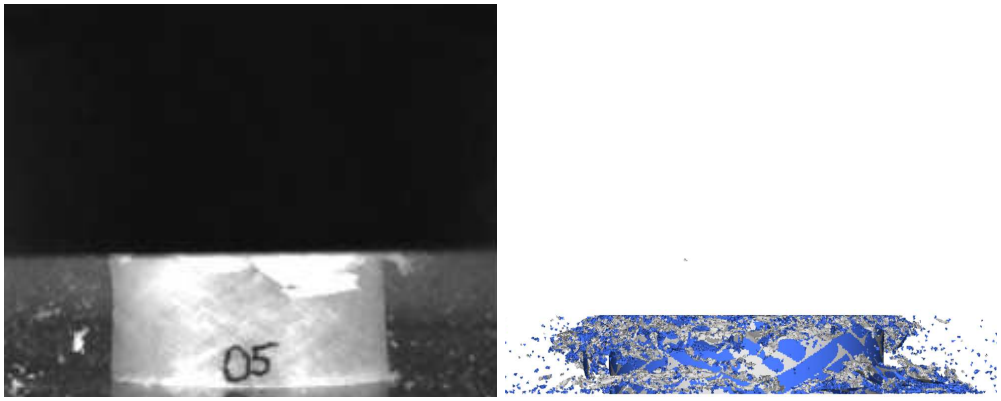

Figure 5.38: Comparison of deformation of real test to simulation for the wound tube in crash loading at t=13 ms.

It becomes apparent by the individual images that a very good correlation is obtained for the crushing behaviour until t=5 ms. From this point differences are visible and growing with increasing time. The simulation predicts larger displacements than the test provides and is finally not able to stop the impactor. The reason can be seen directly by consideration of the corresponding force-time and force-displacement curves depicted in Fig. 5.39. Here, experimental results are represented by grey dashed lines and the simulation by the blue solid line. Additionally, the original signal of the simulation is depicted.

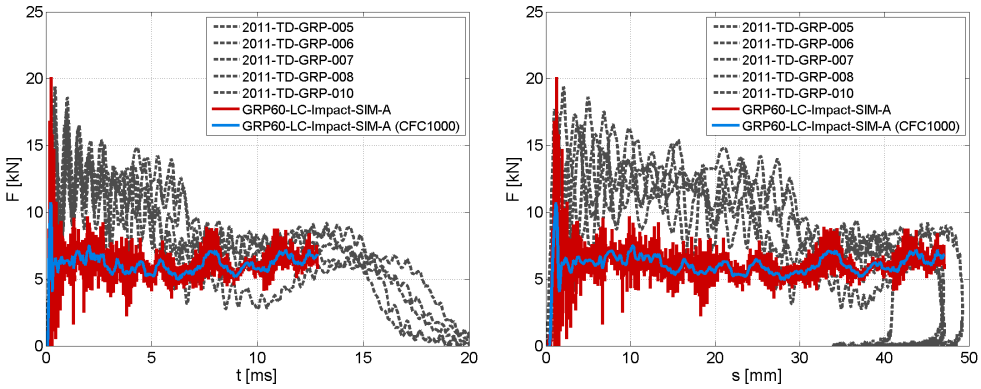

Figure 5.39: Comparison of real test to simulation for force-time and force-displacement relation for wound tube in crash loading.

The occurring crushing force level in the experiments is higher than the simulation predicts. As a consequence the energy dissipation is higher for the same displacements in the experiments which explains the difference to the simulation observed in the states of deformation. In addition this causes a higher remaining kinetic energy in the simulation which finally cannot be captured by the structure. This is the reason that the simulation stops earlier in comparison to the experiment in the force-time diagram in Fig. 5.39.
It is also visible that the original signal of the simulation shows a good match of the maximum force. Due to the short appearance in time, the peak is significantly reduced by the filtering procedure. It is assumed that the brevity of this period is also related to the facts discussed for compressive and tensile loading: the lower strain by capturing the correct failure stress in terms of nonlinearities. An increase of this period will affect directly the initial peak. However, since filtering constitutes a standard application procedure in the scope of numerical analyses, the original curve has been presented only for discussion. Consequently, the final results of the crash simulation in terms of force-displacement relation are given by the filtered signal and shown in Fig. 5.40 in comparison to the results obtained by the tests.
It is visible that the initial peak as well as the crushing force level are lower in the curve provided by simulation. Consequently, the imposed kinetic energy of the impactor cannot completely be dissipated by the numerical model. Since the global crushing behaviour is captured well by the virtual model, it is assumed that the differences in force are related to the representation of the micro-mechanical effects. This may contain the discussed influence of nonlin-

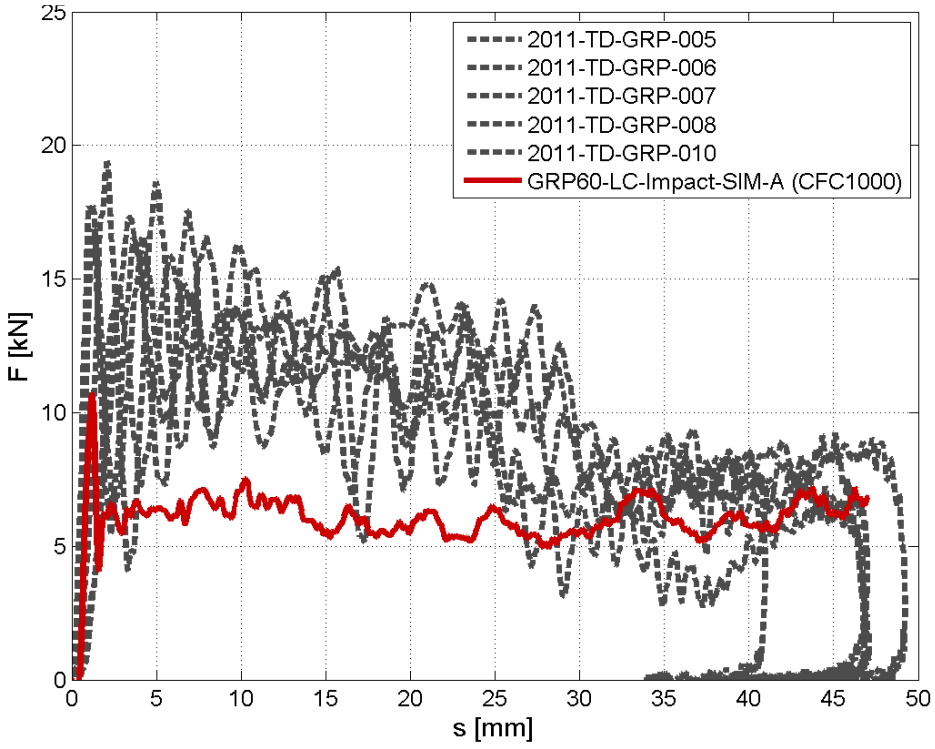

Figure 5.40: Comparison of real test to simulation for force-displacement relation for wound tube in crash loading.

earities, a different strength of the unit cell under multiaxial loading or the representation of the failure by individual maximum stresses.
Finally, the phase subdivision conducted exemplarily for one experiment in Section 3.2.4 is compared to the simulation, see Fig. 5.41. The diagrams illustrate the force-time as well as the force-displacement relation for one test (grey dashed curve), its approximation by straight lines (blue dashed curve) and the numerical response. Since the individual phases have been discussed in detail in the experimental section, the assessment is given for the virtual model here.

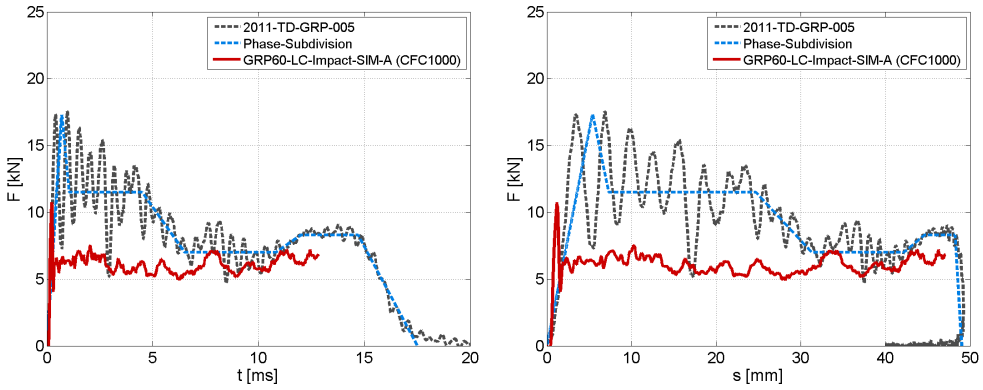

Figure 5.41: Comparison of simulation to test TD-GRP-005 for force-time and force-displacement relation.

After the initial peak the model shows an almost constant force level until $t \approx 3$ ms. At this point a slight drop of the force is visible. Remaining on this level the force starts to increase slightly from $t=7$ ms onwards. Thereby, the force drop is related to the collapse of structure as discussed above. The mentioned periods reflects the same general behaviour observed in the experiments, not in the distinct form and on lower level, but visible. This proves the quality of the virtual approach, using a detailed geometrical model on the meso-scale model. Even with the related model size and the low time step the calculation can be performed over night (10h) on 64 CPUs.

Chapter 6

Conclusion

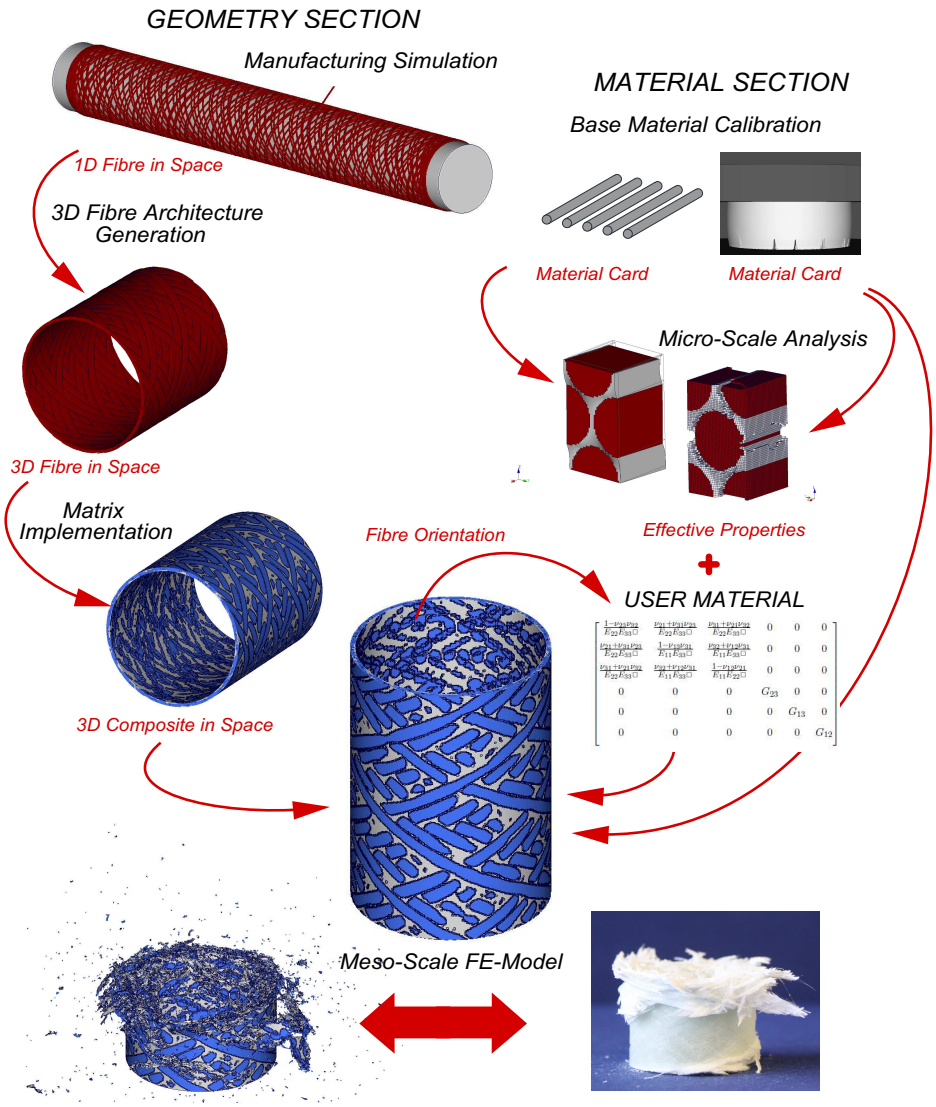

Figure 6.1: Virtual chaining procedure for meso-model generation of a filament wound tube.

Within this work a virtual approach for the prediction of the mechanical behaviour of a filament wound tube under crash and quasi-static loading has been presented. The individual chaining steps for the generation of a finite element model on meso-scale are summarised in Fig. 6.1. Two main threads, geometry and material, have been defined to represent the fibre reinforced composite. The generation of the meso-scale geometry is based on the manufacturing simulation of the filament winding process. As a result one-dimensional fibre orientations in space are available which are subsequently used to create the three-dimensional roving structure. The geometrical thread is completed by the implementation of the matrix based on a voxel mesh approach. During the virtual chain the information of the fibre orientation is also transferred. Within the second thread the material properties for the composite are provided. Material models for the base constituents are calibrated and subsequently used in micro-scale analyses to determine effective properties. A USER MATERIAL model, taking into account the respective fibre orientation and incorporating the effective properties, completes the material section. Thus, the finite element meso-scale model is finally described by the voxel mesh, the pure matrix material and the effective material properties for the roving structure. It is used to determine the virtual mechanical response of filament wound tube under quasi-static and crash loading.

6.1 Critical Reflection

The importance of an appropriate description of the epoxy resin has become apparent within the scope of this work. Major improvements of the results on component level have been reached by the incorporation of the compressive stress-strain relation. However, the behaviour under shear loading, in particular the shear failure, requires further investigations. In this work an assumption has been made for the shear failure based on literature. As a consequence, the results may be affected by the incorporation of additional experimental investigations. In addition, the difference in yielding for tension and compression are not considered in the simulation due to a lack of appropriate material models. Hence, this material property is not captured by the approach.
The properties of the epoxy resin directly influence the effective parameters of the roving structure based on micro-scale considerations. The used approach represents a basic level in terms of failure determination. The investigations are restricted to unit cells and only consider separated stress-strain relations without any interaction. The former, is based on the use of an embedding domain for the representation of periodicity and the related computational effort. Due to the small size of the unit cell e.g. micro-buckling cannot be captured by the approach. The use of a simple failure criteria for the unidirectional layer was intended. Due to the high detail of geometrical information on meso-scale, including e.g. fibre undulations and directions, the material model for the roving should be easy to use and its properties easy to define. However, the combination of the maximum stress failure criteria with the linear elastic approach

of the USER MATERIAL is not sufficient to represent the fracture of unidirectional composite layer for all load conditions. In particular, in terms of the nonlinear behaviour under transverse compressive and shear loading the occurring strains are underestimated by the used approach which limits the results. Furthermore, a visible influence of the nonlinear behaviour of the pure matrix was expected for the quasi-static load case. Since this effect does not appear it has been concluded that the roving is the dominating part in the numerical model.
The use of the voxel mesh approach for the final geometrical representation of the wound tube has shown many advantages for the automation of the approach. The inherent loss of geometrical accuracy seems to be not a drawback. In addition the computational responding time for the crash simulation is acceptable for the considered component mesh size of 0.2 mm. The further increase in computational resources will offer the possibility to consider more problems on finer scales. However, in this study another issue has been encountered: the handling of the huge model (voxel size 0.1 mm) in terms of preparation and evaluation. As a consequence the limit for the voxel size seems to be given rather by the pre- and post-processing programmes than by computational response time, today.

6.2 Summary

The three-dimensional fibre geometry of the filament wound tube, obtained by the virtual manufacturing, has been compared to real existing structure which has been investigated by Computer Tomography (CT). It has been shown that the virtual prediction correlates well with the real structure from global point of view. An additional local comparison for the geometry of single rovings has also given a good agreement with respect to height and width. Due to the availability of detailed geometrical information on meso-scale, the mechanical description of the roving structure could be reduced to unidirectional layer consideration on micro scale. Based on the calibrated material models for the epoxy resin and glass fibre, effective elastic constants and maximum failure stresses have been derived on this scale. The proposed USER MATERIAL formulation for orthotropic elastic deformation incorporates these properties in combination with the fibre orientation obtained by the manufacturing process and is used to determine the resistance of the roving structure.
It has been shown that combining the different material models with the finite element mesh on meso-scale, a crushing behaviour of the filament wound tube structure can be predicted by the simulation. Thereby, also occurring experimental phenomena have been captured by the virtual model. However, the crushing force level is lower than identified in the experimental investigations. It has been concluded that the lower force level is related to the applied failure criteria in combination with the restriction of the numerical roving material model to linear elasticity. The simulations of the quasi-static load cases have demonstrated, that the experimentally defined force level can be captured

by the simulation in terms of compressive and tensile loading. However the corresponding displacements are underestimated by the finite element model. The same phenomenon occurs in the crash simulation. This causes a fracture for smaller strains and finally provides a lower force level. Nevertheless, the proposed approach, of taking into account the geometry on meso-scale for the complete structure, shows a high potential for the prediction of composite tubes under impact loading. Using in addition existing methods for the direct coupling of high-resolution models with a standard finite element model e.g. Multi-Model Coupling option in VPS [21] allows the use in industrial environment.
In addition the virtual method provides the possibility to improve a component from two different sides. On the one hand the chaining procedure of the material section can be used to investigate the influence of different materials keeping the same roving geometry. On the other hand, the geometry of the component can be modified by changing the properties of the manufacturing process. Even a complete change of the manufacturing process for the continuous fibre reinforced composite e.g. from winding to braiding could be possible if the simulation of the process can be conducted in the same manner.

6.3 Outlook

The work also provides new topics, questions and problems which require deeper investigations in the future. One of them is related to the manufacturing simulation. In order to capture twisting and tapering effects of the roving, the simulation approach of the filament winding has to be extended to a second dimension. A further topic in the scope of manufacturing is the influence of the curing procedure to the initial strain and stress state of the meso-scale model. A subsequent study should also investigate the application of existing unidirectional failure approaches to the meso-scale model. Furthermore new methods e.g. based on micro-mechanics can be applied to the detailed available roving structure. But also a study on the influence of fibre-matrix interface properties could be a possibility. With respect to the resin material modelling the influence of the difference in yielding for compression and tension has to be investigated. And finally the influence of the consideration of nonlinearities within the USER MATERIAL of the roving structure requires a further study.

Appendix A

Derivation of Equations

A.1 Calculation of Current Cross-Section

In terms of isotropic material behaviour and uniaxial unrestricted loading the occurring strains in the plane perpendicular to the loading direction are equivalent. This property can be used to derive a relation between the initial and current cross-section.

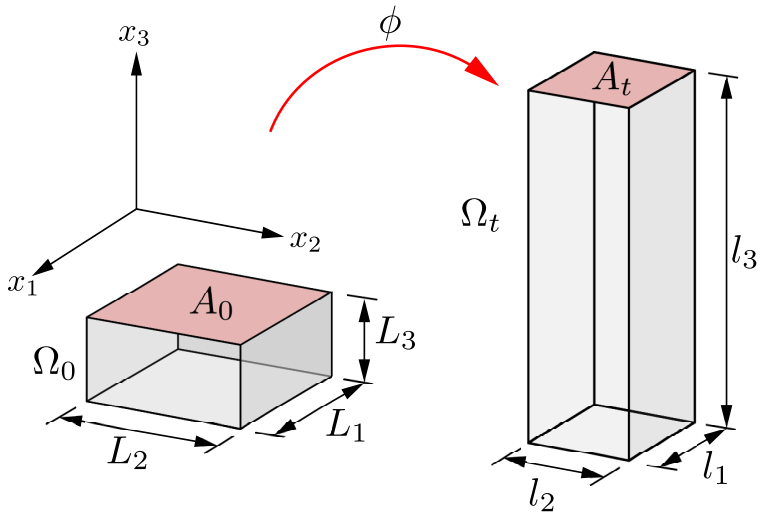

Figure A.1: Initial and current configuration Ω in case of unrestricted tensile loading.

Let Ω be a cuboid in Cartesian coordinates in case of uniaxial loading. Thereby, Ω_0 refers to the initial undeformed configuration and Ω_t to the current unrestricted deformed configuration, as illustrated in Fig. A.1. In each configuration the cuboid is explicitly defined by L_1, L_2, L_3 and l_1, l_2, l_3, respectively.

As a consequence the occurring strains ε_{11}, ε_{22}, ε_{33}, in global direction can be calculated by

$$\varepsilon_{11} = \ln\left(\frac{l_1}{L_1}\right) \quad , \quad \varepsilon_{22} = \ln\left(\frac{l_2}{L_2}\right) \quad , \quad \varepsilon_{33} = \ln\left(\frac{l_3}{L_3}\right) \quad . \tag{A.1}$$

In terms of tensile loading in global x_3-direction, as shown in Fig. A.1, the initial and current-cross section in $x_1 - x_2$-plane A_0 and A_t can easily be determined by

$$A_0 = L_1 L_2 \quad , \quad A_t = l_1 l_2 \quad . \tag{A.2}$$

Rewriting Eq. (A.1) with respect to the current configuration for l_1, l_2 and l_3, yields to

$$l_1 = e^{\varepsilon_{11}} L_1 \quad , \quad l_2 = e^{\varepsilon_{22}} L_2 \quad , \quad l_3 = e^{\varepsilon_{33}} L_3 \quad . \tag{A.3}$$

Substitution of l_1 and l_2 in Eq. (A.2) and some algebra provides the following expression

$$A_t = L_1 L_2 \cdot e^{(\varepsilon_{11}+\varepsilon_{22})} \quad . \tag{A.4}$$

Under the condition of isotropic material behaviour, the following relations between the strains are given for the considered case:

$$\nu = -\frac{\varepsilon_{11}}{\varepsilon_{33}} \quad , \quad \varepsilon_{11} \equiv \varepsilon_{22} \quad . \tag{A.5}$$

Taking into account Eq. (A.5) in Eq. (A.4) and replacing $L_1 L_2$ by A_0 yields to

$$A_t = A_0 \cdot e^{(-2\nu\varepsilon_{33})} \quad , \tag{A.6}$$

and finally gives an expression for the current cross-section based on the initial cross-section and in dependency of the Poisson's ratio as well as the occurring strain in loading direction.

Appendix B

Comparison of Results

B.1 Numerical Homogenisation Procedure

In order to assess the quality of the results obtained by the numerical homogenisation procedure from Section 4.3.2 the method is applied to an example provided by Lukkassen et al. [58]. In their work they use the asymptotic homogenisation approach to determine effective properties for unit cells. One example, which is used for the comparison here, is shown in Fig. B.1 on the left-hand side and denoted by model (A). The unit cell is represented by a voxel mesh of 0.5 μm to provide results for the approach used in this work. The corresponding model (B) is illustrated on the right-hand side of the same figure. In addition the unit cell consists of a glass fibre surrounded by epoxy resin with following properties:

$$\begin{array}{lcll} \text{Epoxy resin} & : & E = 3.5 \text{ GPa} & \nu = 0.35 \ , \\ \text{Glass fibre} & : & E = 75.0 \text{ GPa} & \nu = 0.20 \ , \end{array}$$

by a nominal fibre volume content v_f=0.45. The reached fibre volume content of the voxel mesh amounts to v_f=0.443.

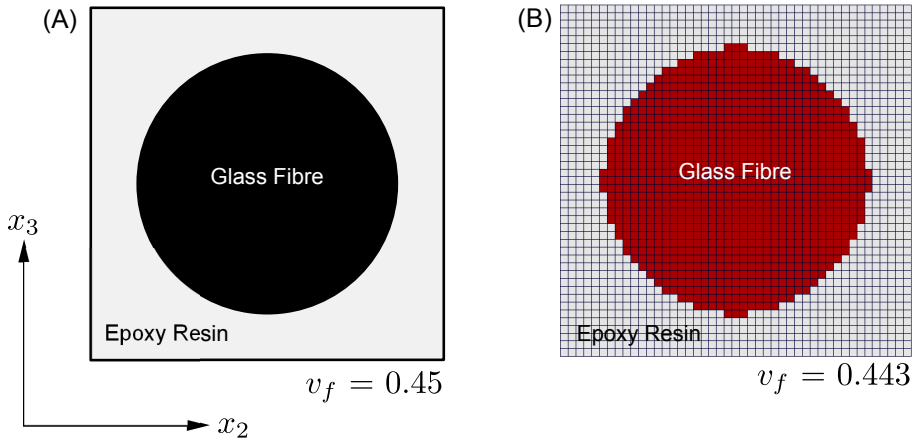

Figure B.1: Circular glass fibre inclusion (A) real geometry (B) voxel representation.

Since only a two-dimensional consideration of the cell in x_3-x_2 plane has been conducted in the reference example, the effective stiffness tensor can be reduced to

$$\bar{\mathbf{C}} = \begin{bmatrix} \bar{C}_{2222} & \bar{C}_{2233} & 0 \\ \bar{C}_{3322} & \bar{C}_{3333} & 0 \\ 0 & 0 & \bar{C}_{2323} \end{bmatrix} \quad .$$

The effective stiffness tensor components provided by the respective method of model (A) and (B) are

$$\bar{\mathbf{C}}^A = \begin{bmatrix} 11.7 & 4.5 & 0 \\ 4.5 & 11.7 & 0 \\ 0 & 0 & 2.4 \end{bmatrix} \quad [\text{GPa}] \quad , \quad \bar{\mathbf{C}}^B = \begin{bmatrix} 11.73 & 4.41 & 0 \\ 4.41 & 11.73 & 0 \\ 0 & 0 & 2.47 \end{bmatrix} \quad [\text{GPa}] \quad .$$

It is visible that the results for the components in main direction are almost identical and only minor differences occur in the shear component and for the secondary diagonal, the maximum deviation is less than 3%. Consequently, the applied numerical homogenisation procedure provides a good quality with respect to the reference example.

Bibliography

[1] L. Aktay. *Improved Simulation Techniques for Modelling Impact and Crash Behaviour of Composite Structures*. PhD thesis, Universität Stuttgart Germany, 2009.

[2] H. Altenbach. *Kontinuumsmechanik - Einführung in die materialunabhängigen und materialabhängigen Gleichungen*. Springer Verlag, 2 edition, 2012.

[3] H. Altenbach, J. Altenbach, and W. Kissing. *Mechanics of Composite Structural Elements*. Springer Verlag, 2010.

[4] D. Aragonés. Fracture micromechanisms in c/epoxy composites under transverse compression. Master's thesis, Universidad Politécnica de Madrid Spain, 2007.

[5] T. Belytschko, W.K. Liu, and B. Moran. *Nonlinear Finite Elements for Continua and Structures*. John Wiley, 2000.

[6] T.A. Bogetti, C.P.R. Hoppel, V.M. Harik, J.F. Newill, and B.P. Burns. Predicting the nonlinear response and progressive failure of composite laminates. *Composites Science and Technology*, 64:329–342, 2004.

[7] T.A. Bogetti, C.P.R. Hoppel, V.M. Harik, J.F. Newill, and B.P. Burns. Predicting the nonlinear response and progressive failure of composite laminates: correlation with experimental results. *Composites Science and Technology*, 64:477–485, 2004.

[8] J. Bonet and R.D. Wood. *Nonlinear Continuum Mechanics for Finite Element Analysis*. Cambridge University Press, 2 edition, 2008.

[9] T.S. Butalia and W.E. Wolfe. Strain energy based non-linear failure criterion: comparison of numerical predictions and experimental observations. *Composites Science and Technology*, 62:1695–1710, 2002.

[10] P. P. Camanho, C.G. Dávila, S.T. Pinho, and J.J.C. Remmers, editors. *Mechanical Response of Composites*, volume 10 of *Computational Methods in Applied Sciences*. Springer Verlag, 2008.

[11] D. Cohen. Influence of filament winding parameters on composite vessel quality and strength. *Composites: Part A*, 28(A):1035–1047, 1997.

[12] D. Cohen, S.C. Mantell, and L. Zhao. The effect of fiber volume fraction on filament wound composite pressure vessel strength. *Composites: Part B*, 32:413–429, 2001.

[13] R.G. Cuntze. The predictive capability of failure mode concept - based strength criteria for multidirectional laminates. *Composites Science and Technology*, 64:343–377, 2004.

[14] R.G. Cuntze. The predictive capability of failure mode concept - based strength criteria for multidirectional laminates - part b. *Composites Science and Technology*, 64:487–516, 2004.

[15] R. de Borst and T. Sadowski, editors. *Lecture Notes on Composite Materials - Current Topics and Achievements*, volume 154 of *Solid Mechanics and its Applications*. Springer Verlag, 2008.

[16] J. de Carvalho, M. Lossie, D. Vandepitte, and H. Van Brussel. Optimization of filament-wound parts based on non-geodesic winding. *Composites Manufacturing*, 6:79–84, 1995.

[17] H. M. Deuschle. *3D Failure Analysis of UD Fibre Reinforced Composites: Puck's Theory within FEA*. PhD thesis, Universität Stuttgart Germany, 2010.

[18] P. Ermanni. *Composite Technologien, Skriptum zur gleichnamigen Vorlesung*. Centre of Structure Technologies, ETH Zürich Switzerland, 2007.

[19] G. Ernst, M. Vogler, C. Hühne, and R. Rolfes. Multiscale progressive failure analysis of textile composites. *Composites Science and Technology*, 70:61–72, 2010.

[20] ESI Group. *PAM-CRASH, PAM-SAFE Theory Notes Manual*, 2000.

[21] ESI Group. *Virtual Performance Solution 2011 - Solver Reference Manual - Volume I - General Simulation Procedure*, 2011.

[22] ESI Group. *Virtual Performance Solution 2011 - Solver Reference Manual - Volume II - Core Modeling*, 2011.

[23] ESI Group. *Virtual Performance Solution 2011 - Solver Reference Manual - Volume III - Material Modeling 3D*, 2011.

[24] ESI Group. *Virtual Performance Solution 2011 - Solver Reference Manual - Volume VI - Multi-Applications/Physics Modeling*, 2011.

[25] G. L. Farley and R. M. Jones. Crushing characteristics of continuous fiber-reinforced composite tubes. *Journal of Composite Materials*, 26(1):37–50, 1992.

[26] N. Feindler. *Charakterisierungs- und Simulationsmethodik zum Versagensverhalten energieabsorbierender Faserverbundstrukturen*. PhD thesis, Technische Universität München Germany, 2012.

[27] J. H. W. Fender. *Solution Spaces for Vehicle Crash Design*. PhD thesis, Technische Universität München Germany, 2014.

[28] F. Feyel and J.-L. Chaboche. Fe2 multiscale approach for modelling the elastoviscoplastic behaviour of long fibre sic/ti composite materials. *Computer Methods in Applied Mechanics and Engineering*, 183:309–330, 2000.

[29] B. Fiedler, M. Hojo, S. Ochiai, K. Schulte, and M. Ando. Failure behavior of an epoxy matrix under different kinds of static loading. *Composites Science and Technology*, 61:1615–1624, 2001.

[30] J. Fish, V. Belsky, and M. Pandheeradi. Composite grid method for hybrid systems. *Computer Methods in Applied Mechanics and Engineering*, 135(3-4):307–325, 1996.

[31] J. Fish and K. Shek. Multiscale analysis of composite materials and structures. *Composites Science and Technology*, 60:2547–2556, 2000.

[32] J. Gosse and S. Christensen. Strain invariant failure criteria for polymers in composite materials. *American Institute of Aeronautics & Astronautics*, 2001-1184:45–55, 2001.

[33] K. Gramoll and S. Ramaprasad. Effects of band weaving on fiber strength in filament-wound composite structures. *Composites Engineering*, 5(4):363–373, 1995.

[34] L. Greve, A.K. Pickett, and F. Payen. Experimental testing and phenomenological modelling of the fragmentation process of braided carbon/epoxy composite tubes under axial and oblique impact. *Composites: Part B*, 39:1221–1232, 2008.

[35] D. Gross, W. Hauger, W.Schnell, and P. Wriggers. *Technische Mechanik 4 - Hydromechanik, Elemente der Höheren Mechanik, Numerische Methoden*. Springer Verlag, 5th edition, 2004.

[36] D. Gross and Th. Seelig. *Bruchmechanik mit Einführung in die Mikromechanik*. Springer Verlag, 4th edition, 2007.

[37] J. Hapke, F. Gehrig, N. Huber, Schulte, and E.T. Lilleodden. Compressive failure of UD-CFRP containing void defects: In situ SEM microanalysis. *Composites Science and Technology*, 71:1242–1249, 2011.

[38] L.J. Hart-Smith. Predictions of the original and truncated maximum strain failure models for certain fibrous composite laminates. *Composites Science and Technology*, 58:1151–1178, 1998.

[39] L.J. Hart-Smith. Expanding the capabilities of the ten-percent rule for predicting the strength of fibre-polymer composites. *Composites Science and Technology*, 62:1515–1544, 2002.

[40] R. Hill. Elastic properties of reinforced solids: Some theoretical principles. *Journal of the Mechanics and Physics of Solids*, 11:357–372, 1963.

[41] M.J. Hinton, A.S. Kaddour, and P.D. Soden, editors. *Failure Criteria in Fibre Reinforced Polymer Composites: The World Wide Failure Exercise*. Elsevier, 2004.

[42] M. Hori and S. Nemat-Nasser. On two micromechanics theories for determining micro-macro relations in heterogeneous solids. *Mechanics of Materials*, 31:667–682, 1999.

[43] H. M. Hsiao and I. M. Daniel. Effect of fiber waviness on stiffness and strength reduction of unidirectional composites under compressive loading. *Composites Science and Technology*, 56:581–593, 1996.

[44] http://www.bmw.de/de/topics/faszination-bmw/bmw i/konzept.html. BMW i3 Konzept, 2013.

[45] http.//www.material.be/. CADWIND.

[46] http://www.volkswagen xl1.com/. Volkswagen XL1 Web Page, 2013.

[47] W. Hufenbach, V. Ulbricht, R. Böhm, B. Grüber, F. Cichy, A. Hornig, I. Koch, R. Füßel, M. Zscheyge, K. Thielsch, V. Pham, M. Kästner, and S. Blobel. Praxisgerechte Simulationsmodelle zur virtuellen Entwicklung neuartiger Textilverbundwerkstoffe für Crash- und Impactanwendungen unter Berücksichtigung von Mikro-Meso-Makro-Interaktionen - SIMOTEX. Technical report, Technische Universität Dresden Germany, 2011.

[48] D. Hühn and T. Pyttel. Experimentelle Untersuchungen am Harzsystem L1100 EPH294. Technical report, Technische Hochschule Mittelhessen Germany, 2013.

[49] C. Kim, J. Kang, C. Hong, and C. Kim. Optimal design of filament wound structures under internal pressure based on the semi-geodesic path algorithm. *Composite Structures*, 67:443–452, 2005.

[50] J.-K. Kim and Y.-W.Mai. *Engineered Interfaced in Fibre Reinforced Composites*. Elsevier, 1 edition, 1998.

[51] S. Koussios, O.K. Bergsma, and A. Beukers. Filament winding part 1: Determination of the wound body related parameters. *Composites: Part A*, 35:181–195, 2004.

[52] S. Koussios, O.K. Bergsma, and A. Beukers. Filament winding part 2: Generic kinematic model its solution. *Composites: Part A*, 35:197–212, 2004.

[53] S. Koussios, O.K. Bergsma, and A. Beukers. Filament winding: kinematics, collision control and process optimisation through application of dynamic programming. *Composites: Part A*, 37:2088–2104, 2006.

[54] M. Kästner. Homogenisierung von Faserverbundwerkstoffen unter Nutzung von X-FEM und Netzüberlagerung. Master's thesis, Technische Universität Dresden Germany, 2004.

[55] C. Laval. Cadwind 2006 – 20 years of filament winding experience. *Reinforced Plastics*, 50(2):34–37, 2006.

[56] J. LLorca and C. González. Mechanical behavior of unidirectional fiber-reinforced polymers under transverse compression: Microscopic mechanisms and modeling. *Composites Science and Technology*, 67:2795–2806, 2007.

[57] J. LLorca, F. Sket, R. Seltzer, J.M. Molina-Aldareguía, and C. Gonzalez. Determination of damage micromechanisms and fracture resistance of glass fiber/epoxy cross-ply laminate by means of x-ray computed microtomography. *Composites Science and Technology*, 72:350–359, 2011.

[58] D. Lukkassen, L.-E. Persson, and P. Wall. Some engineering and mathematical aspects on the homogenization method. *Composites Engineering*, 5(5):519–531, 1995.

[59] J. Mackerle. Finite element analyses and simulations of manufacturing processes of composites and their mechanical properties: a bibliography (1985–2003). *Computational Materials Science*, 31:187–219, 2004.

[60] J. S. Marsolek. *Energieabsorptionsverhalten zylinderschalenförmiger Strukturelemente aus Metall und Faserverbundwerkstoff.* PhD thesis, RWTH Aachen Germany, 2002.

[61] S. K. Mazumdar. *Composites Manufacturing - Materials, Products and Process Engineering.* CRC Press, 2002.

[62] L.N. McCartney. Predicting transverse crack formation in cross play laminate. *Composites Science and Technology*, 58:1069–1082, 1998.

[63] L.N. McCartney. Predicting ply crack formation and failure in laminates. *Composites Science and Technology*, 62:1619–1632, 2002.

[64] P. Mertiny and F. Ellyin. Influence of the filament winding tension on physical and mechanical properties reinforced composites. *Composites: Part A*, 33:1615–1622, 2002.

[65] L. Mishnaevsky. *Computational Mesomechanics of Composite.* John Wiley, 2007.

[66] L. Mishnaevsky, M. Dong, S. Hönle, and S. Schmauder. Computational mesomechanics of particle-reinforced composites. *Computational Materials Science*, 16:133–143, 1999.

[67] L. Mishnaevsky, N. Lippmann, and S. Schmauder. Computational modeling of crack propagation in real microstructures of steels and virtual

testing of artificially designed materials. *International Journal of Fracture*, 120:581–600, 2003.

[68] L. L. Mishnaevsky. Automatic voxel-based generation of 3d microstructural fe models and its application to the damage analysis of composites. *Materials Science and Engineering A*, 407:11–23, 2005.

[69] M. Morthorst. *Modellierung des Crashverhaltens konischer Faserverbundstrukturen*. PhD thesis, Technische Universität Braunschweig Germany, 2006.

[70] S. P. Pai and D. W. Jensen. Influence of fiber undulations on buckling of thin filament-wound cylinders in axial compression. *Journal of Aerospace Engineering*, 14(1):12–20, 2001.

[71] J.-S. Park, C.-S. Hong, C.-G. Kim, and C.-U. Kim. Analysis of filament wound composite structures considering the change of winding angles through the thickness direction. *Composite Structures*, 55:63–71, 2002.

[72] F. París, E. Correa, and J. Canas. Micromechanical view of failure of the matrix in fibrous composite materials. *Composites Science and Technology*, 63:1041–1052, 2003.

[73] T. P. Philippidis and D.J. Lekou. Probabilistic failure prediction for FRP composites. *Composites Science and Technology*, 58:1973–1982, 1998.

[74] A. Puck and H. Schuermann. Failure analysis of FRP laminates by means of physically based phenomenological models. *Composites Science and Technology*, 58:1045–1068, 1998.

[75] A. Puck and H. Schuermann. Failure analysis of FRP laminates by means of physically based phenomenological models - part b. *Composites Science and Technology*, 62:1633–1662, 2002.

[76] J. Qu and M. Cherkaoui. *Fundamentals of Micromechanics of Solids*. John Wiley, 2006.

[77] R. Rolfes, G. Ernst, D. Hartung, and J. Teßmer. Strength of textile composites - a voxel based continuum damage mechanics approach. Technical report, Institute for Structural Analysis, University of Hannover Institute of Composite Structures and Adaptive Systems, DLR Braunschweig, 2006.

[78] A. Rotem. Prediction of laminate failure with the Rotem failure criterion. *Composites Science and Technology*, 58:1083–1094, 1998.

[79] A. Rotem. The Rotem failure criterion theory and practice. *Composites Science and Technology*, 62:1663–1672, 2002.

[80] E. Sanchez-Palencia. Non-homogeneous media and vibration theory. In *Lecture Note in Physics*, volume 127. Springer Verlag, 1981.

[81] P. J. Schilling, B. R. Karedla, A. K. Tatiparthi, M. A. Verges, and P. D. Herrington. X-ray computed microtomography of internal damage in fiber reinforced polymer matrix composites. *Composites Science and Technology*, 65:2071–2078, 2005.

[82] R.A. Shenoi and H.K. Jeong. Probabilistic strength analysis of rectangular FRP plates using Monte Carlo simulation. *Computers & Structures*, 76:219–235, 2000.

[83] S. Sriramula and M.K. Chryssanthopoulos. Quantification of uncertainty modelling in stochastic analysis of FRP composites. *Composites: Part A*, 40:1673–1684, 2009.

[84] C.C. Swan and H. J. Kim. Voxel-based meshing and unit-cell analysis of textile composites. *International Journal for Numerical Methods in Engineering*, 56:977–1006, 2003.

[85] N. Takano and Y.Okuno. Three-scale finite element analysis of heterogeneous media by asymptotic homogenization and mesh superposition methods. *International Journal of Solids and Structures*, 41:4121–4135, 2004.

[86] S. W. Tsai and E. W. WU. A general theory of strength of anisotropic materials. *Journal of Composite Materials*, 5:58–80, 1971.

[87] S.W. Tsai, A. Kuraishi, and K.-S. Liu. A progressive quadratic failure criterion, part b. *Composites Science and Technology*, 62:1682–1696, 2002.

[88] S.W. Tsai and K.-S. Liu. A progressive quadratic failure criterion of a laminate. *Composites Science and Technology*, 58:1023–1032, 1998.

[89] M. von Nida. *Meshfree Methods for the Dynamics of Solids*. PhD thesis, Technische Universität Kaiserslautern Germany, 2005.

[90] W.E. Wolfe and T.S. Butalia. A strain energy based failure criterion for nonlinear analysis of composite laminates subjected to biaxial loading. *Composites Science and Technology*, 58:1107–1124, 1998.

[91] P. Wriggers. *Nichtlineare Finite-Element-Methoden*. Springer Verlag, 2001.

[92] www.pd fibreglass.com/. Pd fibreglass group.

[93] S.P. Xiao and T. Belytschko. A bridging domain method for coupling continua with molecular dynamics. *Computer Methods in Applied Mechanics and Engineering*, 193:1645–1669, 2004.

[94] X. Xiao, C. McGregor, R. Vaziri, and A. Poursartip. Progress in braided composite tube crush simulation. *International Journal of Impact Engineering*, 36:711–719, 2009.

[95] D. Yadav, A.K. Onkar, and C.S. Upadhyay. Probabilistic failure of laminated composite plates using the stochastic finite element method. *Composite Structures*, 77:79–91, 2007.

[96] L. Zhao, S. C. Mantell, D. Cohen, and R. McPeak. Finite element modeling of the filament winding process. *Composite Structures*, 52:499–510, 2001.

[97] D. Zindel and Ch. E. Bakis. Nonlinear mircromechanical model of filament-wound composites considering fibre undulation. *Mechanics of Composite Materials*, 47(1):103–132, 2011.

[98] P. A. Zinoviev, S. V. Grigoriev, O. V. Lebedeva, and L. P. Tairova. The strength of multilayered composites under a plane-stress state. *Composites Science and Technology*, 58:1209–1224, 1998.

[99] P. A. Zinoviev, S. V. Grigoriev, O. V. Lebedeva, and L. P. Tairova. Coupled analysis of experimental and theoretical results on the deformation and failure of laminated composites under a plane state of stress. *Composites Science and Technology*, 62:1171–1724, 2002.

[100] T.I. Zohdi, P. Wriggers, and C. Huet. A method of substructuring large-scale computational micromechanical problems. *Computer Methods in Applied Mechanics and Engineering*, 190:5639–5656, 2001.

[101] L. Zu, S. Koussios, and A. Beukers. Design of filament–wound domes based on continuum theory and non-geodesic roving trajectories. *Composites: Part A*, 41:1312–1320, 2010.

[102] L. Zu, S. Koussios, and A. Beukers. Shape optimization of filament wound articulated pressure vessels based on non-geodesic trajectories. *Composite Structures*, 92:339–346, 2010.

List of Tables

List of Figures